Modelling gap junction-coupled networks of olfactory bulb mitral cells

PhD Thesis

Simon O'Connor

simon.oconnor@btinternet.com

Supervisor – Prof. Tim Jacob

Internal Examiner – Prof. Vincenzo Crunelli

External Examiner – Dr. Peter Brennan

ProQuest LLC
789 East Eisenhower Parkway
P.O. Box 1346
Ann Arbor, MI 48106-1346

Student ID Number:	**0432411**
Title:	**Please circle appropriate value** **Mr/ Miss/ Ms/ Mrs/ Dr/ Rev/ Other, please specify .....**
Surname:	**O'CONNOR**
First Names:	**SIMON**
School:	**SCHOOL OF BIOSCIENCES**
Title of Degree:	**Please circle appropriate value** **EdD, EngD, DSW, DClinPsy, DHS, MCh, Md, MPhil, MPhil/PhD, MScD by Research, PhD/ Other, please specify .....**
Full Title of Thesis	MODELLING GAP JUNCTION-COUPLED NETWORKS OF OLFACTORY BULB MITRAL CELLS

Student ID Number:	**0432411**

Summary of Thesis: The olfactory bulb forms the first level of input integration for olfactory receptor neurons that receive stimuli from odorant molecules in the nose. The olfactory bulb is multi-channel in nature, with each channel containing its own populations of mitral cells. These channels each handle the input from neurons expressing a single type of olfactory receptor protein tuned to a unique range of odorant structures. I have constructed a mitral cell gap-junction network model with morphologically accurate mitral cells to study the behaviour of mitral cells in a channel population. The passive parameters of each of the mitral cells were determined by fitting to *in vitro* recordings. Sodium and potassium channels were added to the mitral cells to give the ability to generate action potentials. Gap-junctions were placed in the apical dendrite tufts of the mitral cells and their conductance adjusted to give a coupling ratio between mitral cells consistent with experimental findings. Firing was induced with twenty current injections randomly located in the apical dendrite tuft of two of the mitral cells, mimicking the multiple inputs from the olfactory receptor neurons. A protocol was used to promote an initial asynchrony in firing which was transmitted across the gap-junctions to all six mitral cells. I found that the mitral cell population would overcome this asynchrony, rapidly tending to synchronous firing. Adding calcium and calcium dependent potassium channels to the mitral cells produced burst firing patterns that were different for each of the cells. The gap-junctions did not have enough influence to overcome the asynchrony of the different burst firing patterns. The addition of calcium concentration threshold dependant glutamate release and AMPA auto receptors to the apical dendrite tuft of each mitral cell allowed the burst firing to promote self propagating synchronised firing after an initial period of asynchrony.

In memory of

Ian Brendan O'Connor

1936-2008

Contents

Acknowledgement

First of all, I would like to extend my gratitude to Professor Tim Jacob for his supervision of my research. He would step in and steer me in the right direction when it looked like I was getting entrenched in work that did not necessarily further my research. But he gave me the space to explore modelling as much as I needed. He has patiently corrected my misuse of English and journalistic style of reporting scientific experiments which has enabled me to reach the required standard of accuracy and rigour needed for a thesis. This process was continued by my two examiners Peter Brennan and Professor Vincenzo Crunelli who painstakingly reviewed the thesis. They not only highlighted those areas that needed clarification and development, but also pointed out areas that required further investigation and then guided me through the correction process. I was encouraged to compare the simulations with experimental recordings and use cross correlation analysis to compare the levels of synchronisation in simulated networks with those published in experimental studies. They pointed out that action potentials were longer than normal and that burst firing would be expected to recur under a constant current injection. Investigation of these points revealed that experimental measurements of the kinetics of some of the ion channels in the model are needed from mitral cells to refine the accuracy of the model.

Next I would like to thank my wife Ilaria for providing our family with an income while I was carrying out my research. She has always provided a sympathetic ear and all the support I needed when the path got difficult. My elder daughter Morgaine kept me company during the earlier stages of my exploratory reading and my younger daughter Tess as a baby sat on my lap and helped with the typing. Tess is now four and continues to keep me company while I am writing up the thesis, occasionally letting out a yell when she wants another DVD putting on or another drink making.

When I reached the morphology and passive parameter fitting stage Arnd Roth at UCL explained to me how he had carried out his work in the Purkinje cell and the key points that need to be consider when carrying out this work. He also introduced me to Troy Margrie (also at UCL) who runs a lab working on mitral cells. Troy first suggested that I work with Diogo Pimentel in his lab. Diogo provide me with mouse morphology reconstructions that were used for the exploratory models in Chapter 3. Later when I made it clear the type of protocol I was aiming at for fitting passive parameters Troy suggested that I work with Kamilla Angelo who also worked in his lab. Kamilla taught me how to use the microscope in conjunction with the Neurolucida software for reconstructing cell morphology. I used her fixed slides of biocytin filled mitral cells for all the mitral cell reconstructions in my network model. Kamilla also provided me with all the experimental data for fitting the passive parameters in Chapter 4. I had many discussions with Kamilla during the development of the passive model. I am very grateful to Arnd, Troy, Diogo and Kamilla for getting me started on the road to my mitral cell model. But special thanks must go to Kamilla Angelo such a sophisticated model would not have been possible without her experimental work and slides. Andreas Schaefer a modeller working in Troy's lab also gave good advice at these earlier stages, as did Tibor Toth at Cardiff University.

Three people must be thanked for helping me to develop my understanding of the techniques of modelling and providing the software that I have made so much use of. I started with the *Genesis* simulator; I avidly consumed the contents of the "Book of Genesis" (Bower and

Beeman 1998) but still needed further instruction. Dave Beeman came to my rescue and explained what was missing in my understanding of how the KCa channel script in the Bhalla and Bower model (Bhalla and Bower 1993) worked using a vdep channel object and what I needed to do to rewrite it as a tab2dchannel. Later on my work shifted to the *Neuron* simulator and Michael Hines gave me a tutorial on the finer points of the built in parameter fitting tools on the steps of a building in Edinburgh after the building had been shut up for the evening after the 2006 CNS conference. Michael has also been quick to suggest ways I might go about improving my hoc scripts when they refused to do exactly what I wanted them to do. Finally the larger proportion of my modelling has been carried out using neuroConstruct that allows all the parameters including ion conductance channels to be set, then writes scripts to function in either the *Genesis* or *Neuron* simulators. Padraig Gleeson at UCL was in the later stages of developing neuroConstruct in Angus Silver's lab while I was developing my model. So while I was one of his beta testers he was advising how I could use the program to best effect and even modifying parts of it so that it could actual do the things that I was demanding of it. These continual discussions developed my understanding of what was needed and helped with my programming skills. The development of neuroConstruct is an ongoing project with many conflicting priorities. Where neuroConstruct lacked the capabilities in particular areas and that functionality could not be fitted into the development program, Padraig was always there with suggestions of ways to achieve the same ends by such means as editing script files that neuroConstruct had produced.

As I proceeded with the fitting of passive parameters I had useful discussions with Christina Weaver, Andrew Davidson, Arnd Roth, and Michael Hines about optimisation and getting the best out of specific fitting algorithms. Guy Major at Cardiff University shared his views on errors involved in passive parameter fitting and provided a useful critique of an early version of Chapter 4. I also had useful discussion with Ted Carnevale about reciprocity in passive cells and visualising the electrotonic shape of cells. When I started trying to assess the level of synchronisation of oscillations in my network model Professor Krishna Persaud at Manchester University suggested that this could be easily done using principle component analysis in Minitab. This saved considerable time as I was considering learning about Fourier transforms in order to carry out this analysis. During the correction process it became clear that cross correlation analysis was needed to compare the degree of synchronisation with other experimental studies. At Professor Crunelli's recommendation François David from his team in Cardiff stepped in at almost the final hour to guide me through matlab syntax and the complexities of cross correlation. I could never have learned and applied the techniques needed to carry out this analysis in the time available without François' guidance.

All the people mentioned deserve my thanks, but I would also like to thank James Bower and Dave Beeman for organising the WAM-BAMM conference in San-Antonio, Texas in 2005 and 2006. This meeting facilitated my introduction into Computational Neuroscience and allowed me to meet the majority of the people mentioned.

Chapter 1 Introduction

While olfaction is not a dominant sense for humans, this does not mean that it is an unimportant sense for human perception. It is however, difficult to easily quantify the importance of olfaction in our daily lives. Olfaction can operate by direct perception; when somebody is peeling an orange we know instantly what is happening without seeing or hearing the action. This is an example of the many odour cues that we have learned the significance of. The argument for inherent rather than learned odour discrimination is more controversial. Clear examples of an inherent response are the many invertebrate pheromones that consist of a unique chemical structure eliciting a defined behavioural response. However the vertebrate olfactory system is geared to learned responses. While the topographical map of processing unit at the first synapses within the olfactory system of mammals is relatively consistent (Mori et al. 1999, Bozza and Mombaerts 2001), the ultimate attributed meaning is dependent on synaptic plasticity (e.g. Coopersmith and Leon 1984, Coopersmith et al. 1986). Even with reproductive cues the response is provoked by familiarity with the odour of a mate rather than unique chemical structures (e.g. Brennan et al. 1990).

Usually we are less aware of our experience with odours than the example of orange peeling. Odorants often influence us without our having fully registered their perceptions in our conscious thought. In fact, odours can imperceptibly modify our perception in general and influence the choices we subsequently make. The ability of odours to evoke memories was famously described by Marcel Proust in an experience of a returning memory provoked by consuming a certain variety of French sponge cake soaked in lime tree flower tea, in the first book of his classic "A la recherche du temps perdu" 1913-1927.

The fact that olfactory perception is by nature not completely definable and usually operates in the background escaping our full attention could be considered to be a result of its not being a primary sense. However a little more thought reveals olfactory perception to be more complicated. Fragrance industry professionals expend much effort in training their sense of smell. Assigning a vocabulary to the perception of odour helps in the identification, memory and communication of the olfactory experience. Nevertheless perception of odour still retains a subjective element that any amount of experience only allows us to take account of but not remove. The strength of emotion, both positive and negative, that we have with many foods (the richness of our experience of food is enhanced by its olfactory components and is one of our most noticeable everyday olfactory experiences), and that we can instantly imagine, illustrates the subjectivity of this sensory modality. But our personal tastes although not always so polarised are formed by our experiences and guide our perception. Perception of odour is also modified by adaptation/habituation and physiological changes such as hunger or cycles in the reproductive system.

The reason that the olfactory system evokes a more emotional response than the other senses, is its early appearance in evolution. The rhinencephalon in primitive vertebrates comprises most of the cerebrum and is closely coupled to the limbic system. As the brain evolves to encompass more systems and processing in vertebrates with a larger range of sensory modalities, the olfactory system keeps its original pathways. Most other senses are gated by the thalamus, while the first level of processing for olfactory system is the olfactory bulb (OB). The other main exception is the allied vomeronasal organ which has its first level of processing in the accessory olfactory bulb (AOB). The OB therefore offers the researcher the advantage that it represents an opportunity to access, in isolation, the first level of processing of sensory input (Shepherd and Greer, 1998).

However the fact that olfactory system is found in primitive vertebrates does not suggest that the olfactory system can be considered as simple. Its complexity has already been alluded to in our discussion of its links to other brain regions and its capacity to evoke memory and emotion. At this stage of our understanding of olfactory perception, trying to model the system as a whole would be futile if it is to be considered on a data processing level. For this reason I am narrowing the focus of my research and considering the OB in line with the suggestion of Shepherd and Greer (1998) - in isolation as the first level of processing of sensory input – as mentioned in the previous paragraph. This removes much of the higher function including hedonic judgement that would be handled by the olfactory cortex. It also removes the signal transduction step at the olfactory receptors at the olfactory epithelium so that I need not consider the nature of the chemical structures that stimulate receptors. We can then consider the OB as a multi-channel processing unit.

In Chapter 2 I review the neuro-pharmacology and all the complexities of the modulatory systems that are found in the olfactory bulb. So far I have been discussing olfaction from a human perspective, but henceforth most references will be to the rat as the only practical model for research into the workings of the OB.

A research project needs to be finite, so after the complexities of Chapter 2 I need to scale back the focus to consider just the mitral cells. The mitral cells[1](MCs) are the principle output cells of the olfactory bulb (Figure 1.1), and in this role they both receive the sensory input from the olfactory receptor neurons and output the processed signal to the olfactory cortex. An understanding of how input and output are related in the MC is therefore the key to understanding the first level of processing of sensory input in the olfactory system.

[1] A fuller description of mitral cells is given in Chapter 2.

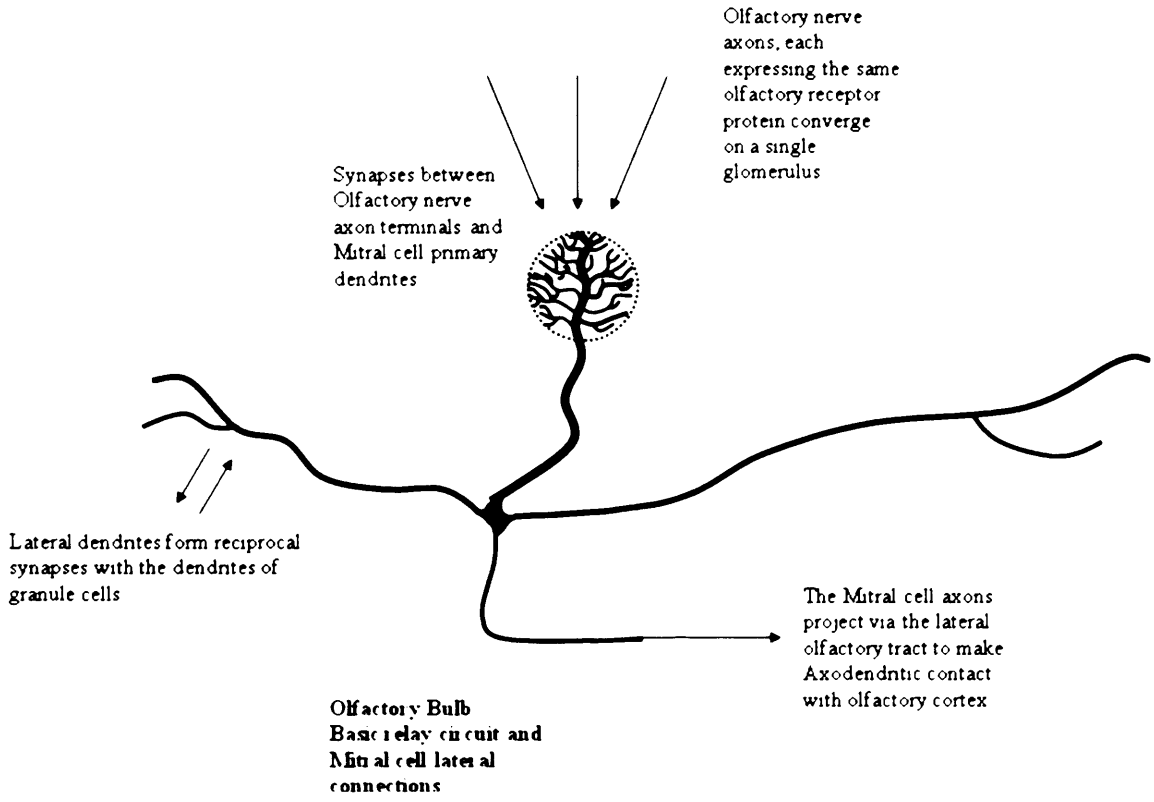

Figure 1.1: Mitral cells are the principle cells of the olfactory bulb.

Taking this narrower focus of just the MCs should strip away the modulatory effects of hunger and reproductive cycles, together with the higher level association that I have discussed. In Chapter 2, I give details of centrifugal inputs to the MCs from the olfactory cortex, locus coeruleus, Raphe nuclei etc., that are involved with the modulatory control of MCs, but they will not form an element of the model. The aim is to keep the underlying mechanisms of the MCs intact so as to gain an understanding of the basis on which MCs process data.

I will take what is now refered to as a "detailed biophysical" approach to the construction of these research models of MCs. The alternative is the "reduced model" approach in which the morphology can be reduced to various levels of complexity and even as far as a point neuron. Reduced models are useful in considering the interactions between large number of cells in networks when not much is known about individual cell morphology and/or properties (for a review of different approaches to modelling the OB see Cleland and Linster 2005). Two earlier MC models that form the precedents for detailed biophysical models are considered in detail in Chapters 3 and 5 (Bhalla and Bower 1993, Migliore et al. 2005). In Chapter 5, I also describe the selection process for choosing components from these models to use as a basis for my own models.

When constructing a model though, the starting point must be the MCs themselves. Any thought of data processing must come later. Chapter 4 covers the process of reconstructing the detailed morphology of a number of MCs, then using experimental recordings to fit their passive parameters.

In Chapter 6, I add the basic Hodgkin and Huxley set of Na, K_{dr} and K_A channel mechanisms (Hodgkin and Huxley 1952a,b,c,d, Hodgkin, Huxley and Katz 1952). This allows depolarising current injection to promote spike initiation. Having functional models of MCs, I need to discuss the aims and objectives of the project. I start by considering some of the characteristics of MCs and their interaction and how I am going to develop the model to gain an understanding of these processes. For this discussion I use some of the detail that will be covered in Chapter 2. The OB is multi-channel in nature and has a separate channel for each odour receptor type (Figure 1.2). Each channel has 50-100 MCs whose apical dendrite tufts (ADTs) connect in the same glomerulus. The ADTs are where the olfactory receptor neurons (ORNs) terminate and pass on their sensory input.

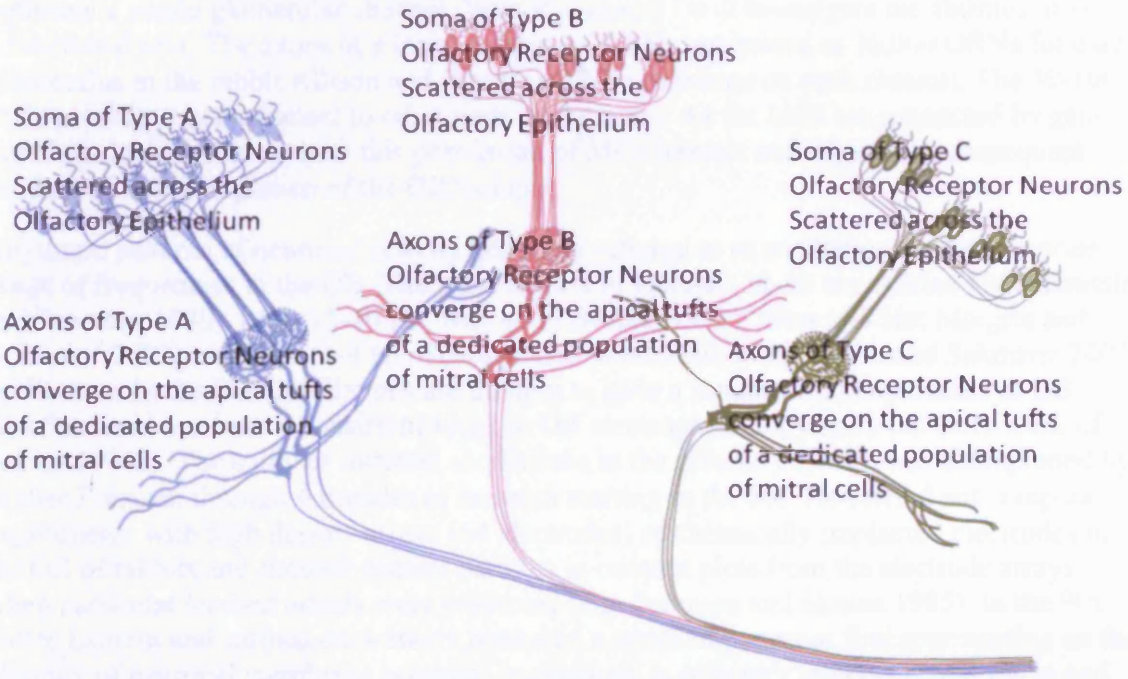

Figure 1.2: Olfactory Receptor Neurons expressing a particular olfactory receptor protein converge on the apical dendrite tufts of a dedicated population of 50-100 mitral cells.

The glomeruli are highly complex foci of modulatory control and feedback regulation which will be covered further in Chapter 2. A single glomerulus consists of the enmeshed ADT branches of the mitral cells that belong to the channel population. This forms a dense neuropil were the axons of the ORNs terminate. The glomerulus is surrounded by up to 2000 periglomerular cells that provide feedback modulation on the mitral cells (see Chapter 2). There are other modulatory mechanisms such as interactions between glomeruli that are mediated by short axon cells that will be reviewed in chapter 2. The modulation that occurs within the glomeruli but external to the MCs must remain outside the scope of this study. There are many subclasses of juxtaglomerular cells that impose this modulation and that would need to be modelled to develop an understanding of the complexities of this interaction. There needs to be a greater understanding of the MCs themselves before such a vast exercise can be undertaken. One detail however needs to be considered in order to make progress with this discussion. The MC's ADTs are connected to each other by gap-junctions and specifically connexin36 has been shown to mediate spike synchrony in the OB glomeruli (Christie et al. 2005, see Chapter 2 for details of the types of gap-junctions found in the OB. I continue Chapter 6 with an account of constructing a model with 6 MCs connected in a network using ADT gap-junctions (GJs).

Equally, the modulation of the MCs that occurs in the external plexiform layer (see Chapter 2) must also remain outside the scope of this study. The centrifugal modulation involves multiple brain areas which does not lend itself to investigation in slice preparations. The MC modulation intrinsic to the plexiform layer is mediated by granule cells. Granule cells form a tangled mass intertwined with MC lateral dendrites. In an OB slice preparation, until biocytin has been injected into an individual granule cell at the end of recording, it is almost impossible to identify more than short lengths of separate granule cells. It would therefore be difficult to insert two electrodes at a distance from each other to carry out current injection recordings in order to fit the passive parameters of granule cells.

So I have decided to focus the modelling on a gap-junction connected network of MCs that represent a single glomerular channel. With this model I will investigate the abilities of such a functional unit. The axons of a large number of ORNs (estimated as 26,000 ORNs for each glomerulus in the rabbit Allison and Warwick 1949) converge on each channel. The 50-100 MCs provide a relay channel to other parts of the brain. As the MCs are connected by gap-junctions I need to know how this population of MCs interact and what is the consequent product of their integration of the ORNs input.

Rhythmic patterns of neuronal activity generally referred to as oscillations occur at a wide range of frequencies in the OB. There are reports of gamma (30-80 Hz; Adrian 1950, Bressler and Freeman 1980), beta (15-30 Hz; Kay and Freeman 1998), theta (4-7 Hz; Margrie and Schaefer[2] 2003) and delta (1-4 Hz; Schoppa and Westbrook 2001, Urban and Sakmann 2002) oscillations in the OB. Oscillations are thought to have a fundamental importance to OB function and have been a consistent focus in OB electrophysiology since the early work of Adrian (1942). The study of intrinsic oscillations in the olfactory system was championed by Walter Freeman through 4 decades of research starting in the 60s. He carried out complex experiments with high density arrays (64 electrodes) of chronically implanted electrodes in the OB of rabbits and showed distinct patterns in contour plots from the electrode arrays when particular learned odours were presented (e.g. Freeman and Skarda 1985). In the 90s Gilles Laurent and various co-workers produced a series of papers at first commenting on the ubiquity of neuronal membrane potential oscillations in olfactory systems across phyla and theorising about odour coding within coherently oscillating neuronal assemblies. Later they showed a clear correlation between synchronised neuronal activity insect antennal lobe and discrimination (Stopher et al. 1997). Since 2000 there has been a more mechanistic approach to understanding the synchronisation of mitral cell activity involving a combination of electrophysiological recordings from pairs of cells and modelling the interactions (Schoppa and Westbrook 2001, 2002, Margrie and Schaefer 2003,Migliore et al. 2005). More recently it has been suggested that oscillations enhance stimulus discrimination by providing a consistent reset that prevents the accumulation of errors (Schaefer et al. 2006). They used tracheotomised mice and controlled sub-threshold mitral cell membrane voltage via current injection. If they produced an oscillating wave in this membrane voltage the Action Potentials (APs) became more time focused in response to pulsed air flow of odoriferous air compared to when the sub-threshold was kept constant. This AP 'precision' was measured by combining all the pulse cycles with the same number of APs then comparing the average distance of each AP from the mean AP time. In an *in vitro* slice preparation they also looked at the ability of mitral cells to discriminate between individual injected stimuli by assessing correlation with AP timing with and without an injected sinusoidal membrane voltage oscillation. For which they found that when physiologically relevant levels of noise are

[2] Margrie and Schaefer (2003) define theta as (2 – 5 Hz) and the example recordings they show are at the lower end of this range, so while their title refers to theta band they are actually talking about delta band.

introduced the discrimination ability of cells without the injected membrane voltage oscillations is significantly reduced ($F_{(14,126)} = 50.7$, $p < 0.001$) while voltage oscillations give almost perfect discrimination ($F_{(1,120)} = 94.2$, $p < 10^{-6}$). In further experiments they showed that this improvement in discrimination in the presence of noise was due to improved AP precision as per the *in vivo* study. The enhanced precision/discrimination is due to the prolonged period of cell hyperpolarisation at the trough of the oscillations removing cumulative membrane voltage fluctuations that are associated with APs so effectively acting as a reset so the membrane voltage responds to the immediate input.

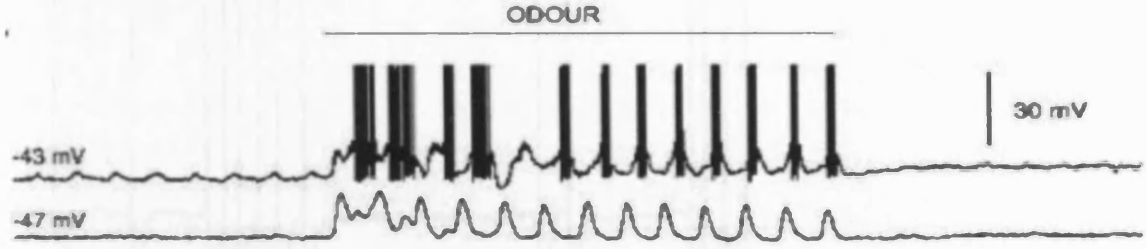

Figure 1.3: **Mitral cell recordings in freely breathing mice showing bursts of firing superimposed on a respiration linked theta rhythm that has been revealed by hyperpolarizing the cell with DC current injection. Membrane potential and AP discharge in a mitral cell in response to overt odour stimulation (1 % amyl acetate), APs are clipped, odour presentation was 5 s (Figure from Margrie and Schaefer 2003).**

Narrowing the focus now to a more detailed look at experimental recordings of MCs, Figure 1.3 shows *in vivo* recordings from mitral cells in freely breathing mice. Holding the cell below AP threshold reveals sub-threshold depolarisations at ~2.6 Hz which are thought to be linked to the odour presentation being linked to the respiration rate. These subthreshold depolarisations drive the the APs. It is likely that calcium channels are involved in promoting bursts of APs and KCa channels in terminating the bursts of firing (see Chapter 7). I have restricted the model to MCs and these MCs have been reconstructed from in vitro slice preparations so I need to also consider recordings made under these conditions. Recordings in slice preparations also allow tests to made under controlled/isolated conditions which reveal more about the components of the reponses. In Figure 1.4 stepped current injections give varying degrees of AP bursts. In the control (Figure 1.4A) there is a short burst of 4 APs with a long latency after the current injection is applied. The application of bicuculline produces a much greater amount APs and a much shorter latency to the response. This suggests that short latency $GABA_A$ receptor inhibition is involved in suppressing the AP response in the control. The addition of APV to the Bicculline in C returns the AP response to a similar response as found in the control. This suggests that NMDA receptors are responsible for the increase in cell excitation which triggers the short latency and robust AP response of MCs evoked by stepped current injection when not inhibited by $GABA_A$ receptors.

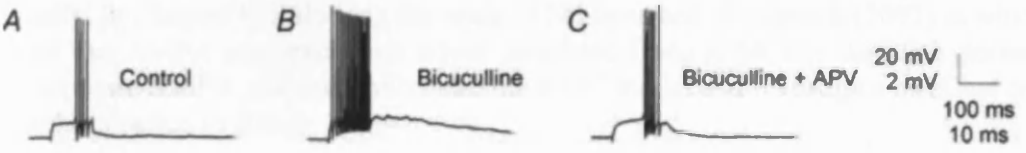

Figure 1.4: **Mitral cell recordings in a mouse OB slice preparation in response to stepped current injections. Comparisons of a control (A) with the effect of introducing (B) 20 µM Bicuculline and (C) 20 µM Bicuculline and 50 µM APV (Figure from Urban and Sakmann 2002, the 20 mV/100 ms scale is the relevant one the 2mV/10 ms scale is for EPSPs in a postsynaptic mitral cell that is not shown here).**

Also it should be noted that spontaneous AP activity in MCs can be recorded in rat OB slice preparations (Figure 1.5).

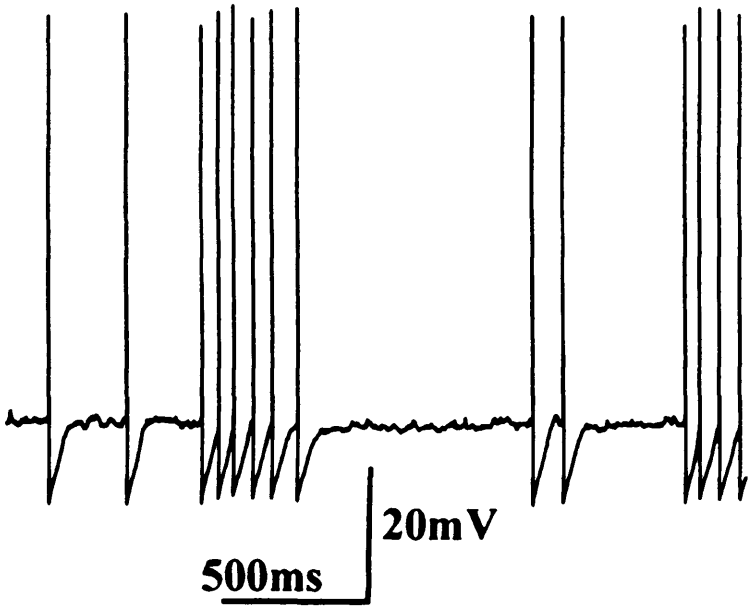

Figure 1.5: Whole cell patch clamp recording of a mitral cell showing spontaneous mitral cell activity in a rat OB slice preparation (Figure from Heyward et al. 2001).

It has been suggested that the MC's ADT GJs synchronise oscillations in populations of mitral cells (Migliore et al. 2005). In the final part of Chapter 6 I extend the Migliore et al. 2005 simulations that were carried out in a pair of identical simple MCs to a 6 MC GJ connected network of morphologically accurate MCs. In this way I investigate the ability of the network to synchronise oscillations so the population of MCs could act as a single unit of input integration. For assessment of synchrony I looked at both principle component analysis (PCA) and spike time differences for comparison between recording from individual cells within the network models to investigate the effect of passive parameter differences. However since absolute synchrony is not found in neuronal circuits, there is a need show that the degree of synchrony achieved in network models is equivalent to experimental measurements. For this I refer to an experimental criterion that has been defined as a test of correlated spiking between pairs of MCs by Schoppa and Westbrook (2002, see Chapter 6).

In Chapter 7, I incorporate calcium channels and KCa channels along with a sub-membrane calcium pool into the 6 MC GJ connected network model and look at how the resultant burst firing effects the ability of the network to synchronise the firing of individual MCs.

Finally, in Chapter 8, following the work of Schoppa and Westbrook (2002) in which they show that AMPA auto-excitation drives correlated firing in MCs of the same glomerulus, I incorporate AMPA auto-excitation into the 6 MC model and investigate its effect on synchronisation of firing.

After this systematic investigation of factors influencing network synchrony in MCs, in Chapter 9 I discuss and summarise how the model helps with the understanding of how MCs with ADTs in the same glomerulus work as a population to integrate input and produce synchronous output. I describe the mechanisms involved and what further work could be undertaken to develop further this understanding.

To summarize, there are 5 phases for the development of my MC model:

Phase 1: The Passive Cell – the morphologies of 6 MCs were reconstructed using Neurolucida from the biocytin filled MCs in fixed OB slice preparations. Then dual pipette recordings made before the biocytin was injected were used for fitting the passive parameters. The value of C_m obtained is probably higher than it should be due mainly to underestimation of the cross sectional area of the apical dendrite trunk. However the C_m values are internally consistent within the model.

Phase 2: Adding ion channels to enable action potentials – sodium and K_{dr} and K_A potassium ion channels from the Migliore et al. (2005) model were converted to ChannelML scripts that neuroConstruct uses to write Neuron scripts. These channels were added to the passive MCs at the densities used in the Migliore et al. (2005) model to produce back propagating action potentials.

Phase 3: Producing a gap-junction connected network of MCs – the 6 MC models were now connected via randomly placed gap-junctions in their apical dendrite tufts. One hundred gap-junctions were used between each pair of mitral cells adding up to a total of 1600 gap-junctions for the 6 MC model (see Figure 6.2 to see the 16 possible pair connections between 6 cells). The script for the gap-junctions is from Migliore et al. (2005) and their conductance was adjusted to give a coupling ratio measured in the soma around the midpoint of the experimental measured range of 0.01-0.08 (Schoppa and Westbrook 2002). An oscillation synchronisation test was developed by Migliore et al. (2005) in which repetitive action potentials were evoked in one of the MCs by a continuous current injection to apical dendrite tuft. In a second MC asynchronous firing is evoked by 10 ms delay in the start of the continuous current injection. Under these conditions the 6 MC gap-junction connected model achieves efficient synchronisation when a larger number of small currents/conductances are used. The apical dendrite tuft is adapted to receive a large number of inputs from the olfactory receptor neurones. To mimic this 20 x 0.06 nA current injections were used, scattered across the apical dendrite tufts. The coupling ratios rather than the number of gap-junction is known so between pairs I tried 1, 10 and 100 gap-junctions with proportionately lower conductances. The model with 100 gap-junctions was able to efficiently synchronise the firing across all 6 MCs unlike the lower numbers of gap-junctions.

Phase 4: Adding calcium channels to produce burst firing in the MCs – high threshold calcium channels along with calcium dependent potassium channels and a sub-membrane calcium pool from the Bhalla and Bower (1993) model were incorporated into the individual mitral cells. The action potentials activate the calcium channels and the resulting depolarisation keeps the MCs above firing potential until the KCa channel repolarises the cell. The result is short repetitive bursts of firing in the MCs.

Phase 5: Adding AMPA auto-receptors to the MCs – a mechanism was developed from scripts of Saftenku (2005) in which quanta of glutamate can be released in response to the $[Ca^{2+}]$ threshold being exceeded. This glutamate release activates AMPA auto-receptors that are incorporated in the same script mechanism. These mechanisms were added to the MC apical dendrite tufts following the suggestion that AMPA auto-receptors drive correlated firing in MCs whose apical dendrite tufts enter the same glomerulus (Schoppa and Westbrook 2002). I found in my model that the $[Ca^{2+}]$ in the apical dendrite tuft remains high for the whole period of the burst firing. It is difficult to see how the correlation of firing could be driven by a relatively constant rate of glutamate vesicle release while the $[Ca^{2+}]$ remains above threshold for the duration of the burst firing. In my model under certain conditions

these mechanisms produce self propagating synchronised firing in all the MCs of the gap-junction network once the initial burst firing has ceased. This would provide an alternative explanation for the presence of AMPA auto-receptors.

Chapter 2 : The olfactory bulb: a complex modulatory environment

In this chapter I give a brief outline of the structure of the olfactory bulb along with some key developments in the understanding of the olfactory bulb. This should allow readers to orientate themselves before a more detailed review is undertaken. Beyond the orientation sections follows a review of the neuropharmacology of the OB. This review has previously been published (O'Connor and Jacob 2009)[3].

When constructing a model it is important to know not only the components that are to be modelled but also the context that the components exist in. For our model the context is the complex modulation provided by neuropharmacology of the OB. I have discussed in the introduction the choices that have been made when selecting the components. In this chapter I review the detail of both what has been included in the model and what have been left out. Both sets of components will interact, so an understanding of these relationships will allow a more realistic interpretation of the resulting simulations and the assumptions that have been made by not including some of the possible interactions.

The olfactory bulb has a tightly packed laminar structure in which many different populations of neurons interact to carry out the integration and processing of the sensory input (Figure 2.1).

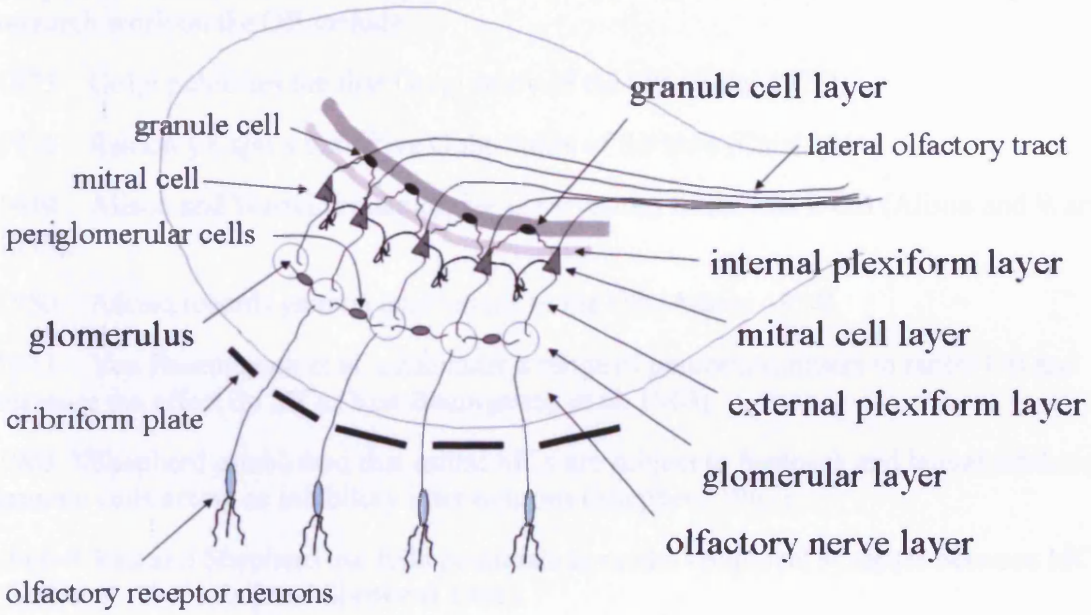

Figure 2.1: The Layers of the Olfactory Bulb (courtesy of Tim Jacob)

[3] http://www.ncbi.nlm.nih.gov/pubmed/20021432

The naming convention for the layers comes from Ramon y Cajal's extensive Golgi study published in 1911 (Cajal 1911). Incoming ORNs synapse with the primary dendrites of the mitral cells – the projection neurons of the olfactory bulb – in the glomeruli. Around 80 mitral cells contribute to each of the 2000 glomeruli per bulb in the rabbit and upwards of 1000 olfactory receptor neurons synapse onto a single glomerulus. Periglomerular cells mediate lateral inhibition at the level of the glomeruli and granule cells mediate inhibition at the level of the mitral cells (see discussion of mitral cells versus tufted cells below in "The first synapse in the olfactory system"). The olfactory nerve layer consists of the unmyelinated fibres of the axons of the olfactory receptor neurons. The glomerular layer contains the primary dendrites of the mitral and tufted cells and the incoming olfactory nerve fibres. The external plexiform layer contains the lateral dendrites of the mitral and tufted cells where they synapse onto the gemmules (swollen spine like projections) of the peripheral processes (dendrites) of granule cells. The mitral cell layer consists of the somata of the mitral cells and the internal plexiform layer is composed of axons and collaterals of the mitral cells. The granule cell layer is composed of the many cell bodies of the granule cells – there are about $3x10^6$ in each rat bulb. The axons of the mitral cells form the lateral olfactory tract that projects to the primary olfactory cortex.

The complex structure of the olfactory bulb has required that researchers use many inventive strategies to isolate the different interactions and interpret the role they serve. Before I get into a detailed survey of the neuropharmacology of the OB, I will pause to mention a few of the pioneers whose work has shaped our understanding of the OB. Some of the highlights of research work on the OB include:

1875 Golgi publishes the first Golgi study of the OB (Golgi 1875).

1911 Ramon y Cajal's definitive Golgi study of the bulb (Cajal 1911).

1949 Alison and Warwick quantitative observations of the rabbit OB (Alison and Warwick 1949).

1950 Adrian records gamma oscillations in the OB (Adrian 1950).

1963 Von Baumgarten et al. administer a range of neurotransmitters to rabbit OB and measure the effect on MCs (Von Baumgarten et al. 1963).

1963 Shepherd established that mitral MCs are subject to feedback and lateral inhibition by granule cells acting as inhibitory inter-neurons (Shepherd 1963).

1966-8 Rall and Shepherd use field potentials to model reciprocal synapses between MCs (Rall et al. 1966, Rall and Shepherd 1968).

1970 Price and Powell's electron microscope studies of rat OB mitral and granule cells (Price and Powell 1970a, 1970b).

1970 Nicholl shows that GABA depresses mitral cell activity (Nicoll 1970 1971).

1979 -1985 Jahr and Nicholl; and Mori, Nowycky and Shepherd using an *in vitro* turtle OB slice preparation characterise the properties and neuropharmacology of mitral cell and granule cell interactions (Mori and Shepherd 1979, Jahr and Nicholl 1980, 1982b, Mori, Nowycky and Shepherd 1981a, 1981b, 1981c, 1982, 1984, Nowycky, Mori and Shepherd 1981a, 1981b, Nicholl and Jahr 1982)

Since this pioneering work, the use of the patch clamp, rodent *in vitro* tissue slices and synthetic agonists/antagonists has allowed ever more sophisticated experiments to isolate components of cellular interactions in the OB. This work has revealed an abundance of sophisticated modulatory systems, which makes olfactory bulb neuropharmacology challenging to interpret and reflects the degree of analytical processing of the sensory input that occurs at this stage of the olfactory system. More recently calcium imaging allows the voltage changes to be viewed at multiple locations using *in vitro* slice preparations to observe what is happening across large sections of a single cell (Margrie et al. 2001, Xiong and Chen 2002, Djrursic et al. 2004). Two photon imaging uses a combination of scanning laser and fluorescent dyes to give a penetration of about 1 mm for calcium imaging allowing *in vivo* imaging to be carried out for a complete apical dendrite including the tuft (Charpak et al. 2001). These newer techniques are being used to make observations that go beyond what one or two patch clamp electrodes can reveal. In this way it can be seen that action potentials can actively propagate along the full length of lateral dendrites (Xiong and Chen 2002, Djrursic et al. 2004) or that when synaptic stimulation of granule cells provokes a long lasting depolarisation that is accompanied by an unusual calcium signal that is dependent on the sequential activation of NMDA receptors, a nonselective cation conductance I(CAN) and T-type voltage-dependent Ca^{2-} channels (Egger 2008). With such new techniques it is possible to get round some of the difficulties of interpretation that measurement of variables by isolation of individual components using pharmacological blockers has created. However there is much that still cannot be assessed or measured with experimental techniques. This is where detailed modelling has a role to play. Models can be developed constrained by experimental measurements which allow further interactions to be investigated or measurements to be made that are not currently possible with the techniques available to experimentalists. A good historical example of this is the interpretation of the reciprocal synapse between MCs and granule cells (Rall and Shepherd 1968).

The first synapse in the olfactory system

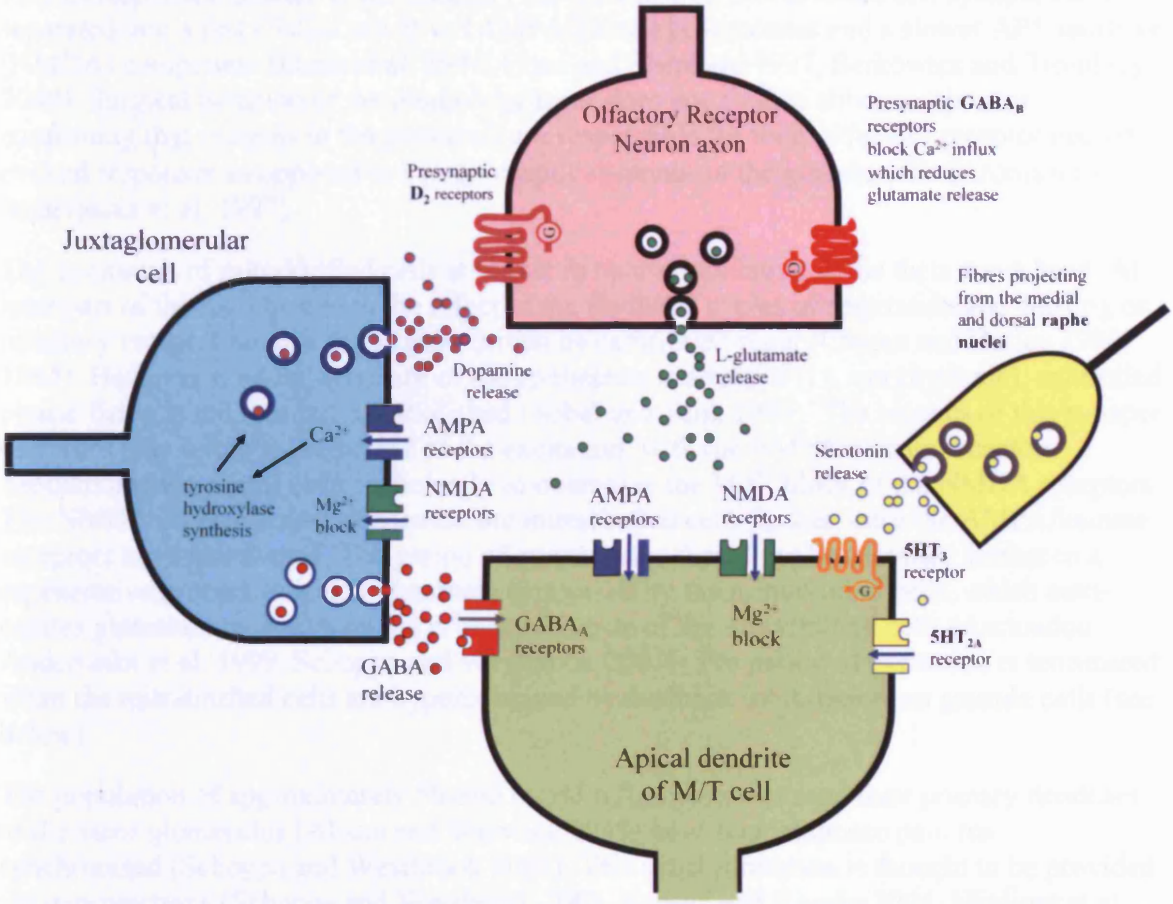

Figure 2.2: Glomerular synapses showing the variety of receptors. The axons from the olfactory receptor neurons form the olfactory nerve which synapses on the primary apical dendrites of the mitral cells. L-glutamate is the primary excitatory transmitter at this synapse which binds to AMPA and NMDA receptors on the postsynaptic membrane. Juxtaglomerular cells are inhibitory GABAergic/dopaminergic interneurons that mediate inhibition between glomeruli. Centrifugal fibres project from the Raphe nuclei to the glomeruli modulating the mitral cell activity *via* postsynaptic 5HT receptors (see text).

The first synapse of the olfactory system occurs at the glomerulus (see Figure 2.2) where upwards of 10,000 axons from olfactory receptor neurons terminate. Glutamate is the main excitatory transmitter of the olfactory system and the mitral/tufted cell (M/TCs) receptors that are stimulated by the release of glutamate from the olfactory receptor neuron axon terminals are a highly heterogeneous population (Horning et al. 2004). External tufted cells can be separated from the mitral cells on functional grounds with a synchronising oscillation (~2Hz) for juxtaglomerular cells being attributed to the external tufted cells (Hayar et al. 2004a). From here on I will use the term "mitral cells" (MCs) to mean those cells whose soma lie in the mitral cell layer and whose size is reasonably uniform. The soma of tufted cells are not part of this distinct layer, but are scattered throughout the external plexiform layer and glomerular layer (see Figure 2.1). The convention in the literature is to refer to "mitral/tufted" cells because it is difficult to be certain that electrodes have been inserted into cells that are completely representative of the narrower definition of MCs. A study has found differences in odour evoked responses between identified mitral and tufted cells in intact animals (Nagayama et al. 2004). However more recent studies failed to find distinct differences between the electrophysiology and response to odours between MCs and tufted cells but did

find differences between M/TCs and external tufted cells (Griff et al. 2008a, 2008b). There is evidence in M/TCs for the presence of AMPA, kainate and NMDA receptors (see Figure 2.2), as responses isolated at the olfactory receptor neuron-mitral/tufted cell synapse can be separated into a fast CNQX sensitive (AMPA/kainate) component and a slower AP5 sensitive (NMDA) component (Ennis et al. 1996, Chen and Shepherd 1997, Berkowicz and Trombley 2000). Surgical isolation of the glomerular layer does not abolish either component, confirming that currents in the glomeruli are responsible for these olfactory receptor neuron evoked responses as opposed to a polysynaptic response in the granule cells (Aroniadou-Anderjaska et al. 1997).

The excitation of mitral/tufted cells is phasic in nature oscillating in the theta wave band. At least part of this will be due to the effect of the rhythmic cycles of respiration and sniffing on olfactory receptor neuron stimulation driven by centrifugal input (Chaput and Holley 1980, 1985). However if odour exposure of the epithelium is artificial (i.e. not rhythmic), controlled phasic firing is reduced but not abolished (Sobel and Tank 1993). The kinetics of this synapse therefore play a role in the period of the excitation, with the AMPA/kainate receptors depolarising the mitral cells sufficiently to overcome the Mg^{2+} block of the NMDA receptors. The NMDA receptors then depolarise the mitral/tufted cells further, once the AMPA/kainate receptors have inactivated. The period of excitation is thought to be extended further in a regenerative process in which glutamate is released by the mitral/tufted cells, which auto-excites glutamate receptors on the primary dendrite of the mitral/tufted cells (Aroniadou-Anderjaska et al. 1999, Schoppa and Westbrook 2001). The period of excitation is terminated when the mitral/tufted cells are hyperpolarized by feedback inhibition from granule cells (see below).

The population of approximately 50-100 mitral/tufted cells that send their primary dendrites to the same glomerulus (Alison and Warwick 1949) have their response patterns synchronised (Schoppa and Westbrook 2001). This synchronisation is thought to be provided via gap-junctions (Schoppa and Westbrook 2002, Kosaka and Kosaka 2004, Migliore et al. 2005). This would explain the complex mechanism slowing mitral/tufted cell oscillations, as slow oscillations facilitate the correlation of signals. The oscillations are slowed by the kinetics of the depolarization of the first synapse in the olfactory bulb. Gap-junctions will synchronise a population of mitral cells with apical dendrites terminating in the same glomerulus (see Chapter 5 in which I use a model of 6 MCs connected by gap-junction between apical dendrite tufts to test action potential synchronisation across gap-junctions) . With slow oscillation the chance of two mitral cells having synchrony by chance firing is much reduced (Schoppa and Westbrook 2002) and the whole process of synchronisation is further enhanced because populations of mitral cells need to work in unison to overcome NMDA block by Mg^{2+}.

The active properties of mitral/tufted cells

The mitral/tufted cells generate action potentials that initiate close to the soma in response to weak olfactory nerve input but with stronger synaptic excitation the site of action potential initiation shifts to the distal dendrites (Chen et al. 1997, Shen et al. 1999). The ability to initiate spikes in the distal dendrites is likely to be due to the higher than normal sodium channel densities to be found in the mitral/tufted cell primary dendrites (90 $pS/\mu m^2$) (Bischofberger and Jonas 1997, Chen et al. 2002). The action potential back propagates into both the primary and secondary dendrites triggering calcium transients in all regions as P/Q- and to a lesser extent N-type calcium channels open (Isaacson and Strowbridge 1998). The action potential attenuates along the secondary dendrites probably due to the hyperpolarizing

affect of an A-type potassium current (Christie and Westbrook, 2003). However no attenuation of the calcium transients is seen along the dendrites, right to the distal tips (Xiong and Chen 2002).

There is evidence that further currents modulate mitral cell activity including:

- A sub-threshold oscillation of the mitral/tufted cell membrane potential, thought to synchronise spike firing in populations of mitral cells and to be mediated by a non-inactivating sodium current I_{NaP} (Desmaisons et al. 1999).
- Spike clustering in mitral/tufted cells which is thought to depend on the interplay between slowly inactivating I_D-like K^+ channels and a sub-threshold TTX-sensitive Na^+ current (Balu et al. 2004).
- Local control of dendritic excitability which has been shown to be mediated by small conductance calcium activated potassium (SK) channels (Maher and Westbrook, 2005).

As well as the delta oscillations (~2Hz) mentioned above, originating in the glomeruli and synchronised for mitral cells projecting to the same glomerulus (Schoppa and Westbrook 2001), spontaneous sub-threshold oscillations in membrane potential have been observed in mitral cells at resting membrane potential (Desmaisons et al. 1999). The frequency was found to be ~10 Hz at a membrane potential of -65 mV and rose to ~20 Hz when the membrane potential was depolarised to -62 mV by constant current injection. At a membrane potential of -62 mV clusters of APs were also observed. Further depolarization of the cell progressively increased the frequency of sub-threshold oscillations up to 40 Hz at -59 mV (Desmaisons et al. 1999). Further to this, task related gamma oscillations in the olfactory bulb have been observed (Chabaud et al. 2000, Beshell, Kopell and Kay 2007, Kay 2003, Ravel et al. 2003, Neville and Haberley 2003) in which the mitral cells are thought to participate.

Intrinsic Modulation in the Glomerulus

Each glomerulus is a functional unit receiving convergent input from olfactory receptor neurons expressing a particular receptor protein (Mombaerts, 2004). In a recent review, Chen and Shepherd (2005) have suggested that the key functional operation of the glomerulus is to act as a signal-to-noise enhancing device in the processing of sensory input.

Modulation of olfactory nerve glomerular input - The output from each functional unit is provided by a population of 50-100 mitral/tufted cells and this output is modulated by a population of 1500-2000 juxtaglomerular cells (Figures 2.1 and 2,2). Based on their response to depolarizing pulses, individual juxtaglomerular cells can be divided into two physiological classes: bursting and standard firing (McQuiston and Katz 2001) of which the former (mainly periglomerular external tufted cells) oscillate spontaneously. Based on their mode of firing and placement in the bulb circuit, these bursting cells are well situated to drive synchronous oscillations in the olfactory bulb and it has been suggested that juxtaglomerular cells are responsible for spontaneous glomerular field layer potentials (sGFLPs) (Karnup et al. 2006) which may represent one level, or sub-system, of processing in the olfactory bulb network (Karnup et al. 2006). Juxtaglomerular cells include periglomerular, external tufted and short axon cells. It is a heterogeneous population that is slowly being broken down into subpopulations that differ chemically, morphologically and physiologically. Much more work needs to be done in characterising these cells and the function they serve (the current extent

of the knowledge of juxtaglomerular cells is reviewed in Kosaka and Kosaka (2005a). Approximately 50% of juxtaglomerular cells that have been partially characterised so far can be divided into the following populations, some of which overlap:

GABAergic periglomerular cells - populations of GABAergic periglomerular cells synapse with both olfactory nerve axon terminals and mitral/tufted cell dendrites in the glomerulus (Shepherd 1971) (see Figure 2.2). The GABAergic population of periglomerular cells in the rat forms about 20% of the cells in the glomerular layer. GABA released from the periglomerular cells, combined with the rapid action of the $GABA_A$ receptors and a postsynaptic position (see Figure 2.2) on the mitral cells (Keller et al. 1998), allows sufficient hyperpolarisation of the mitral/tufted cell apical dendrites to cancel out the effect of remaining L-glutamate in the synaptic cleft. While a presynaptic location (see Figure 2.2) of the slower but longer acting $GABA_B$ receptors on the olfactory nerve terminals (Keller et al. 1998, Aroniadou-Anderjaska et al. 2000) allows the blocking of further L-glutamate release until the $GABA_B$ effects wear off. Only about 20% of periglomerular cells receive monosynaptic olfactory nerve input, and it may be this population that mediates presynaptic inhibition of the olfactory nerve (Hayar et al. 2004b). This presynaptic inhibition appears to extend the dynamic range of the post-synaptic bulbar neurons as well as exerting some feedback control over the very strong excitatory drive from the incoming axons, particularly as increasing odour concentrations drive these thousands of olfactory receptor cells to higher firing frequencies (Chen and Shepherd, 2005).

There is also likely to be interneuron-to-interneuron inhibition as functional $GABA_A$ receptor channels are found in periglomerular cells (Puopolo and Belluzzi 1998). Stimulation of periglomerular cells in the rat olfactory bulb results in self-inhibition as the GABA activates $GABA_A$ receptors on the same neuron as well as spilling over to neighbouring periglomerular cells (Caitlin Smith and Jahr 2002). The periglomerular cells represent the first level of inhibition in the olfactory system and this GABA-mediated self-inhibition will favour mitral/tufted cell excitation during intense olfactory stimulation by reducing inhibition on them by periglomerular cells (Caitlin Smith and Jahr 2002).

Dopaminergic cells - The glomerular layer (see Figure 2.1) of the olfactory bulb contains one of the largest populations of dopaminergic neurons in the brain and dopamine in the olfactory bulb is found exclusively in the juxtaglomerular neurons (Ennis et al. 2001). A subset of GABAergic periglomerular cells were found to contain dopamine and tyrosine hydroxylase (TH) a critical enzyme in dopamine production (Hokfelt et al. 1975, Halasz et al. 1978, Kosaka and Kosaka 2005a). The dopamine released by this population of periglomerular cells is thought to reduce olfactory nerve output, because dopamine application reduced the olfactory nerve evoked response in mitral/tufted cells mediated by a presynaptic D2 receptor (Berkowicz and Trombley 2000). Both D2 and D1 receptors are expressed in the olfactory bulb but D2 receptors are the predominant sub-type and are expressed in the terminals of olfactory nerve axons (see Figure 2.2) and in presynaptic elements of the glomerular neuropil, including mitral/tufted cell dendrites and the dendrites of a subset of GABAergic/dopaminergic periglomerular cells (Gutierrez-Mecinas et al. 2005a). D1 receptors are only sparsely expressed in the rat olfactory bulb (glomerular layer, external plexiform, mitral and granule cell layers) stimulate cAMP and are excitatory, whereas D2 receptors reduce cAMP and are inhibitory.

GABAergic/dopaminergic periglomerular cells and dopaminergic periglomerular cells produce spontaneous rhythmic firing in the theta wave band from the combined effects of a persistent, tetrodotoxin-sensitive sodium current and a T-type Calcium current (Pignatelli et

al. 2005, Puopolo and Belluzzi 1998). TH expression in these cells is reduced following both peripheral deafferentation of the olfactory bulb (Baker et al. 1984) or unilateral naris (nostril) closure (Brunjes et al. 1985). In tissue culture experiments it has been shown that both odour stimulation of ONs and glutamate release by the ONs provokes TH induction; a process mediated by NMDA receptors followed by the activation of L-type Ca^{2+} channels and an increase in intracellular calcium ion concentration (Puche and Shipley 1999). In this way dopaminergic periglomerular cells allow activity-dependent modulation of inhibition over a longer term than the GABAergic periglomerular cells. The purpose of this mechanism appears to be linked with discrimination of odours as it was found that individual mitral/tufted cells were three times more likely to respond to both citral and peppermint after odour deprivation or injection of the dopamine antagonist spiperone (Wilson and Sullivan 1995). Mice in which the D2 receptor, or the dopamine transporter (DAT), had been knocked out displayed an olfactory discrimination deficit but were normal for odour habituation, sensitivity and odour recognition memory (Tillerson et al. 2006) and the doubling of dopaminergic cells in the olfactory bulb may therefore explain the hyposmia that occurs in Parkinson's disease (Huisman et al. 2004). Dopaminergic cells also send dendrites into non-olfactory nerve regions where they contact dendrites from mitral/tufted cells and centrifugal axons (Pignatelli et al. 2005).

NO containing cells - nitric oxide is another transmitter that is slowly revealing a specialised modulatory mechanism amongst periglomerular cells. Being gaseous and with a small molecular weight, nitric oxide diffuses much more readily than other transmitters. It is produced by neuronal nitric oxide synthase, which has been found in a distinct population of periglomerular cells (Kishimoto et al. 1993) thought to be GABAergic (Crespo et al. 2003). It has been suggested that the target of the periglomerular nitric oxide transmitter is another population of periglomerular cells that express the β_1 subunit of soluble guanylyl cyclase, and also mostly appear to express calbindin D28K (Guterrez-Mecinas et al. 2005b). The activation of the soluble guanylyl cyclase by the nitric oxide will result in the production of the intracellular messenger cGMP. The interplay of NO and cGMP triggers molecular mechanisms, including adaptation processes, which enable the olfactory neuroepithelium to cope with strong stimuli (Breer and Shepherd 1993).

External tufted cells – the external tufted cells receive direct input from the olfactory nerve axon terminals and in turn provide intraglomerular monosynaptic excitatory input to many short axon and periglomerular interneurons that do not receive direct olfactory nerve input (Hayar et al. 2004b). External tufted cells express slowly inactivating sodium channels (I_{NAP}), which generate rhythmic spike bursts that are readily entrained by olfactory nerve input (Hayar et al. 2004a). In this way the external tufted cells act as a glomerular synchronising mechanism (Hayar and Ennis 2007). Bursting external tufted cells oscillate spontaneously and their position and electrical activity make them well situated to drive synchronous oscillations in the olfactory bulb (McQuiston and Katz 2001). The oscillatory activity of external tufted cells is finely tuned by endogenous GABA and glutamate (Hayar and Ennis 2007).

Because of their bursting properties external tufted cells may amplify sensory input onto the glomerular network possibly enabling synchronization of the network, including mitral cells, to sensory input, which is in turn synchronised to sniffing (Hayar et al. 2004a).

Short axon cells – the short axon cells send interglomerular axons over long distances to form excitatory synapses with inhibitory periglomerular neurons 20-30 glomeruli away (Aungst et al. 2003). Interglomerular excitation of these periglomerular cells potently inhibits

mitral cells and forms an on-centre, off-surround circuit. This interglomerular centre–surround inhibitory network, along with the well-established mitral–granule–mitral inhibitory circuit, forms a serial, two-stage inhibitory circuit that could enhance spatiotemporal responses to odours (Aungst et al. 2003).

Intrinsic Modulatory Circuits in the External Plexiform Layer

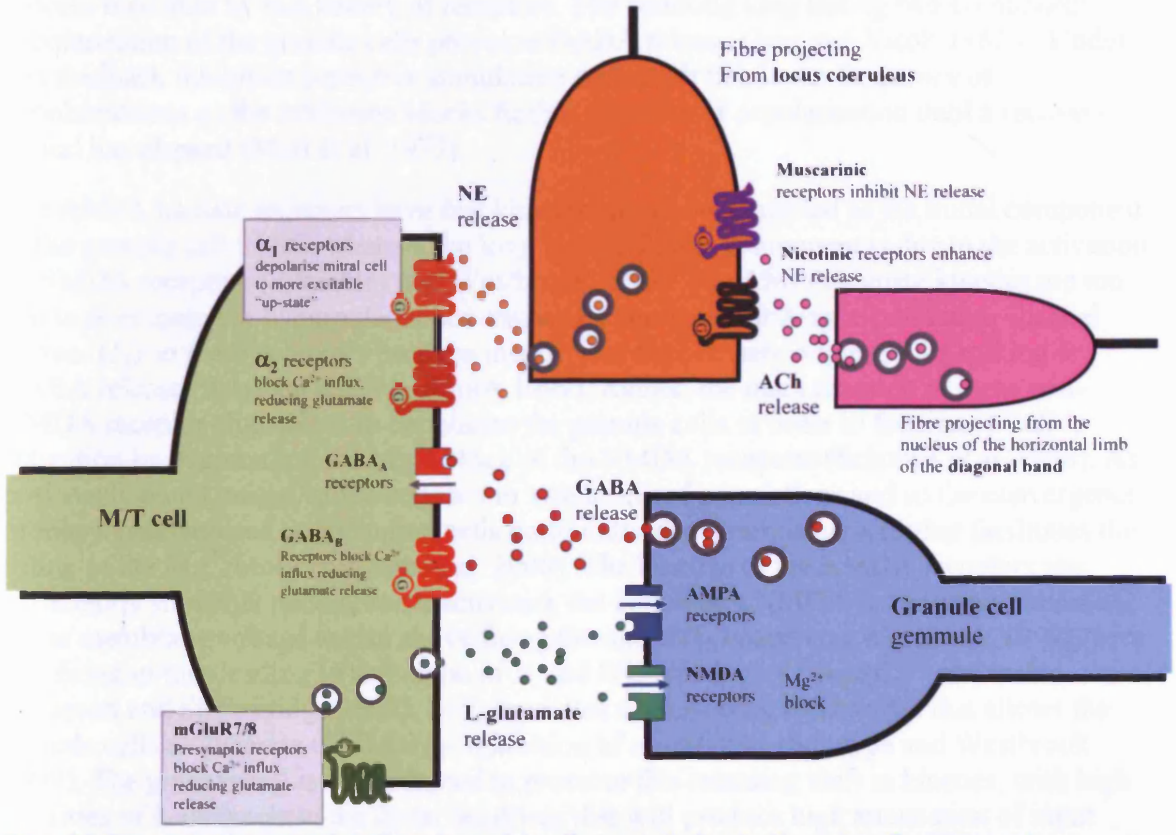

Figure 2.3: Synapses in the external plexiform layer of the olfactory bulb showing the variety of receptors and neurotransmitters. Granule cells mediate feedback and lateral inhibition between mitral cells with which they form reciprocal dendrodendritic synapses. Adrenergic and cholinergic efferent fibres project from the diagonal band and the locus coeruleus respectively (see text for further explanation).

The lateral dendrites of mitral/tufted cells make dendrodendritic reciprocal synapses with granule cells (Figure 2.3). This local synaptic circuit forms the basis for reciprocal dendrodendritic inhibition mediated by ionotropic $GABA_A$ receptors in mitral cells (Isaacson and Vitten 2003). This interaction is responsible for generating the synchronised γ-oscillatory activity (30-70Hz) in the olfactory bulb which is thought to be important in odour detection and discrimination (Halabisky and Strowbridge 2003).

The dendrodendritic synapses are host to a heterogeneous population of AMPA/kainate and NMDA receptors (Trombley and Westbrook 1990, Montigue and Greer 1999). *In situ* hybridization experiments have suggested that mitral/tufted cells express kainate receptors of the type GluR5 and KA2, whereas interneurons (periglomerular and granule cells) express mostly GluR6 and KA2 (Davila et al. 2007). In the accessory olfactory bulb (AOB) that receives input from the vomeronasal organ there is a high concentration of mGluR2/3 staining in the mitral/tufted cell layer. However, in the main olfactory bulb (MOB) that we are considering here strong staining of mGluR2/3 is only found in periglomerular cells

(Sahara et al. 2001). Granule cells also express high levels of metabotropic glutamate receptors. On the basis of inhibitor studies, Heinbockel et al., (2007a) suggest these are mGluR5, the activation of which participates in feed-forward and/or feedback inhibition at mitral/tufted cell to granule cell dendrodendritic synapses, possibly to modulate lateral inhibition and contrast in the olfactory bulb. Dong et al. (2007) show the contribution of both mGluR1 and mGluR5 in granule cells enhancing synaptic inhibition of mitral cells. Release of L-glutamate by the lateral dendrites of mitral/tufted cells stimulates the granule cells in a process mediated by this battery of receptors. The resulting long lasting two-component depolarisation of the granule cells provokes GABA release (Jahr and Nicoll 1982b). Under this feedback inhibition repetitive stimulation will result in a lower frequency of depolarisations as the inhibition blocks further episodes of depolarisation until a recovery period has elapsed (Mori et al. 1977).

The AMPA/kainate receptors have fast kinetics so can be identified as the initial component of the granule cell EPSC, whereas the long lasting slower component is due to the activation of NMDA receptors (Trombley and Westbrook 1990). The AMPA/kainate kinetics are too fast to overcome the hyperpolarisation caused by the transient A-type potassium channel current (I_A) so these receptors produce insufficient depolarisation to provoke spiking or GABA release (Schoppa and Westbrook 1999). Rather, the main function of these non-NMDA receptor channels is to depolarise the granule cells in order to facilitate NMDA activation by overcoming the Mg^{2+} block of the NMDA receptors (Schoppa et al. 1998). As previously noted, mitral/tufted cells act in synchronised populations and so the convergence of many synchronised mitral/tufted cells on to individual granule cells further facilitates the lifting of the Mg^{2+} block (Carlson et al. 2000). The kinetics of the NMDA receptors are sufficiently slow that once I_A has inactivated, the continuing NMDA receptor activation will cause membrane voltage to rise above firing threshold (Schoppa and Westbrook 1999), with this firing in turn leading to activation of N and P/Q type high voltage Ca^{2+} channels (Isaacson and Strowbridge 1998). So I_A mediates a controlling mechanism that allows the granule cells to generate GABAergic inhibition of mitral cells (Schoppa and Westbrook 1999). The granule cell is well adapted to promote this retarding shift in kinetics, with high densities of I_A channels in the distal dendrites that will produce high attenuation of input while the transient I_A is activated and lower attenuation afterwards. This weights the attenuation towards blocking the ability of AMPA receptors to promote spiking while favouring NMDA receptors, and a low densities of somatic sodium channels enhance this effect by lifting the spiking threshold (Schoppa and Westbrook 1999, Isaacson 2001). The rapid kinetics of AMPA receptors, together with the inactivation of I_A , ensures that granule cells have short spike-response times and they are able to synchronize rapidly resulting in phase-locked GABA release on to mitral cells (Schoppa 2006). The elevation of local intracellular Ca^{2+} concentration in granule cells mediated by activation of the N and P/Q channels provokes exocytosis of GABA (Isaacson and Strowbridge 1998).

Recently two functionally distinct excitatory synapses have been found on granule cells (Balu et al. 2007); distal synapses which are the dendrodendritic inputs from mitral cells with slow kinetics, exhibiting paired-pulse depression, and proximal axonal inputs with fast kinetics, exhibiting facilitation (Balu et al. 2004). These proximal synapses originate from two sources, local axon collaterals from mitral cells and centrifugal feedback projections from cortical regions. Thus input, originating from the piriform cortex, synapses onto granule cells and can gate dendrodendritic inhibition onto mitral cells (Balu et al. 2004). The implications of this are that the degree of lateral inhibition in the olfactory bulb after sensory stimulation may be dynamically modulated by activity in the piriform cortex (Balu et al. 2004).

There is evidence for heterogeneity in the inhibition imposed on the lateral dendrites since, as well as the GABA mediated inhibition, glycine and taurine have both been found to inhibit mitral/tufted cells (Trombley and Shepherd 1994, Belluzzi et al. 2004). Also, $GABA_B$ receptors have been found on granule cells which may act as autoreceptors (Isaacson and Vitten 2003).

Extrinsic Modulation of the Glomerulus and Mitral Cells

The projection of serotonergic fibres from the median and dorsal Raphe nuclei passes along the ventromedial surface of the anterior olfactory nucleus and then enters the olfactory bulb from its exterior surface, together with the olfactory nerves (McLean and Shipley 1987). The fibres terminate densely in the glomeruli, and less densely in the infraglomerular layers (McLean and Shipley 1987). Serotonergic fibres in the glomeruli are thicker, contain more numerous and larger varicosities, and are more intensely stained than most infraglomerular fibres (McLean and Shipley 1987). Deafferentation of olfactory bulb serotonergic fibres causes olfactory disturbance in the short term and shrinkage of the glomerulus in the longer term (Moriizumi 1994).

The development of odour memory to conditioned odour training is associated with the phosphorylation of cAMP response element binding protein (CREB) in the rat neonate olfactory bulb (McLean et al. 1999). This type of odour conditioning had also been linked to 5-HT (serotonin) receptors (McLean et al. 1996), and β-adrenoceptors (Sullivan et al. 1989, see extrinsic noradrenergic modulation below). 5-HT receptors of the sub-classes $5\text{-}HT_{2A}$ (Wu et al. 1998) and $5\text{-}HT_3$ (Gehlert et al. 1991) have been found using monoclonal antibody staining and selective antagonist binding respectively. 5-HT receptors are co-localised with β-adrenoceptors on mitral cells (Gehlert et al. 1991). Beta-adrenergic stimulation increases cAMP in mitral cells – an effect that requires 5-HT-induced mobilization of Ca^{2+}. A model of odour induced learning has been suggested in which the convergence of these effects with odour stimulation recruits CREB phosphorylation and induces memory-associated changes in the olfactory bulb (Yuan et al. 2003).

Extrinsic Modulation of Circuits in the External Plexiform Layer and Granule Cell Layer

Extrinsic glutamatergic modulation - Centrifugal fibres from the olfactory cortex (Price 1968) and anterior olfactory nucleus may make excitatory synapses with granule cells. The granule cells will then impose inhibitory output on to mitral/tufted cells. The anterior olfactory nucleus projections pass via the anterior commissure to the contralateral bulb (Mori and Takagi 1978). Another possibility is that these centrifugal fibres have a direct modulatory effect by releasing zinc directly on sites postsynaptic to glutamate release (Jo et al. 2000).

Extrinsic noradrenergic modulation - Noradrenergic fibres project from the locus coeruleus to the granule cell layer via the lateral olfactory tract (Dahlström et al. 1965) (see Figure 2.3). An early study demonstrated that noradrenaline reduces the inhibition exerted by the granule cells on the mitral cells (Jahr and Nicoll 1982a). Evidence has been gathered for the expression of α_1, α_2, and β-adrenergic receptors in relation to the lateral dendrite synapses. Alpha-1 receptors have been found on mitral/tufted cells that cause a G-protein mediated inhibition of a leak potassium current. The resultant depolarisation, although modest, was sufficient to lift the mitral cell to an up state that would make the cell more responsive to olfactory nerve stimuli (Hayar et al. 2001). Alpha-2 receptors have been

demonstrated on the mitral/tufted cell lateral dendrites that block high threshold Ca^{2+} currents via G-protein mechanism. This causes presynaptic blocking of glutamate release and the net result is loss of feedback inhibition from granule cells (Trombley and Shepherd 1992, Trombley 1992).

A β-receptor mediated mitral cell inward current was identified using the agonist isoproterenol. However this current could be abolished by pharmacological isolation with TTX, AP5, CNQX, and gabazine, indicating that it was most likely a circuit effect (Hayar et al. 2001). The β-receptors were found to mediate a sequence that consisted first in a depression of the feedback inhibition imposed on mitral/tufted cells followed by a potentiation of this inhibition (Okutani et al. 1998). The β-receptors have also been implicated in olfactory learning as odour conditioning in young rats that is normally reinforced by tactile stimulation was also found to be reinforced by the β-receptor agonist isoproterenol (Sullivan et al. 1989). This mechanism also appears to involve disinhibition of the mitral/tufted cells from the GABAergic inhibition of the granule cells (Okutani et al. 1999).

It has been shown that association of odour with a surge of noradrenalin from the locus coeruleus to the olfactory bulb is sufficient to produce a subsequent relative preference for that odour in rat pups. Pairing an odour with either direct activation of noradrenergic β-receptors within the olfactory bulb or with putative direct pharmacological stimulation of the locus coeruleus produces a subsequent relative odour preference in a dose-dependent manner (Sullivan et al. 2000).

Extrinsic cholinergic modulation - Cholinergic fibres project to the olfactory bulb from the horizontal limb of the diagonal band (Brashear et al. 1986, Zaborszky et al. 1986). A population of juxtaglomerular cells and a population of cells in the granule cell layer (see Figure 2.1) are amongst the recipients of the cholinergic projection (Nickell and Shipley 1988). The receptors receiving the cholinergic input were found to have distinct areas of expression with nicotinic receptors found mainly in the glomerulus and producing short-lived excitation of a population juxtaglomerular cells and a longer lived excitation of mitral cells (Castillo et al. 1999). Muscarinic receptors were found to inhibit granule cell firing rate while increasing their activity dependent GABA release (Castillo et al. 1999) an effect mediated by pirenzipine-sensitive M1 receptors.

Rats with selective lesions of cholinergic neurons that project to the olfactory bulb and cortex discriminate less well between aliphatic aldehydes with similar carbon chain lengths than do rats that received sham lesions (Linster and Cleland 2002).

The noradrenergic fibres appear to be under the control of the cholinergic fibres as stimulation of muscarinic receptors on the noradrenergic fibres inhibit noradrenaline release and stimulation of nicotinic receptors promotes noradrenaline release (El-Etri et al. 1999). The net effect of acetylcholine administration appears to favour the nicotinic response as the result is noradrenaline release (El-Etri et al. 1999).

Extrinsic modulation by orexin - Fibres originating from lateral and posterior hypothalamus of the rat containing the peptides orexin A and B (molecules that regulate food intake) were found distributed in the glomerular layer, mitral cell layer and granule cell layer layers (see Figure 2.1) of the olfactory bulb (Hardy et al. 2005). Type 1 orexin receptor expression has been found in the rat olfactory bulb from 10 days to adult in periglomerular, mitral/tufted cells and granule cells (Hardy et al. 2005). Depolarisation and hyperpolarisation of mitral

cells has been observed along with changes in mitral cell firing rates and responsiveness to food and non-food odours with the application of orexin A (Hardy et al. 2005, Apelbaum et al. 2005). Apelbaum et al. (2005) suggested that this change in firing activity could underlie a larger scale regulation of the olfactory system, allowing the threshold for odour detection to be modified depending on the nutritional status of the animal and the responses to food and to non-food odours near threshold to become more salient, and they also pointed out that it may be involved in the well-documented changes of responsiveness induced by the nutritional state.

These inhibitory local circuits within the olfactory bulb serve a number of functions in addition to the more conventional lateral inhibition for "centre-surround" sharpening of the response to a given stimulus. For example, they give rise to the generation of bursts in firing frequency and oscillatory activity. They are responsible for the temporal variation in these firing patterns and oscillations and the synchronization and desynchronization of oscillations in mitral/tufted cells. They interconnect mitral/tufted cells that can be some distance apart and underlie the phenomenon of "declustering" (Laurent et al. 2001) that occurs following extended exposure to an odour.

Circadian Modulation of the olfactory bulb

A circadian oscillation in the responsiveness of the olfactory bulb has been observed in rats (Amir et al. 1999) and mice (Granados-Fuentes et al. 2006). In mice the peak responsiveness of mitral cells to odour stimulation occurred during the subjective night and persisted under constant dark conditions as well as following lesions in the suprachiasmatic nucleus suggesting that the olfactory bulb comprises a master circadian pacemaker (Granados-Fuentes et al. 2006). In humans, odor-evoked event-related potentials peak during the day, being largest at around 16:00 and smallest at 04:00 (Nordin et al 2003).

Endocrine Modulation of the olfactory bulb

Oxytocin - Maternal behaviour in rats appears to be promoted by an odour imprinting mechanism that involves oxytocin mediated changes in the olfactory bulb (Yu et al. 1996). The effect of oxytocin appears to be mediated by a presynaptic mechanism affecting GABA release from granule cells (Osako et al. 2000). Microiontophoretic administration of oxytocin had a pre-synaptic effect on mitral cells increasing glutamate release and post-synaptic effect on granule cells increasing their responsiveness to glutamate. The combined pre and post synaptic effects produce an augmentation of the glutamatergic transmission in the mitral/granule cell reciprocal synapses. This may enhance the self-inhibition of active mitral/tufted cells or their lateral inhibition on less active neighbours through the reciprocal dendrodendritic synapses, thereby mediating several aspects of maternal and social behaviour which could rely on the gating of olfactory input (such as odour imprinting and nipple search behaviour) (Osako et al. 2001).

It has also been shown that in rat OB oxytocin can activate α adrenoceptors (Dluzen et al. 2000).

Insulin and brain derived neurotrophic factor - Insulin has been shown to suppress the voltage dependent outward current in cultured olfactory bulb mitral and granule cells, an effect that is mimicked by Src tyrosine kinase (Fadool and Levitan 1998). This modulation was thought to be mediated by tyrosine kinase phosphorylation of potassium Kv1.3 channels

(Fadool and Levitan 1998). It is possible that insulin in the brain could also be used as a satiety factor. After a meal, blood insulin levels would rise in response to increased serum levels of glucose but, in the olfactory bulb, insulin levels are low after a meal. As mentioned above, the threshold for odour detection is dependent upon nutritional status thus mitral cell firing rates, influenced by insulin levels, could represent a potential mechanism (Fadool et al. 2000).

Chronic exposure to brain derived neurotrophic factor increased the magnitude of Kv1.3 current mediated by a Trk receptor kinase (Tucker and Fadool 2002). Mitral cells in Kv1.3 null mice failed to show normal modulation of currents by these tyrosine kinase mediated mechanisms, but also there were other side effects including an increased ability to discriminate between odorants (Fadool et al. 2004).

Gap-Junctions

Connexins (Cx) are a family of trans-membrane proteins that mediate electrical coupling between cells. They have been associated with synchronising firing throughout the central nervous system (Bennett and Zukin 2004, Connors and Long 2004, Hormuzdi et al. 2004). A range of techniques are used to define their distribution, including freeze fracture electron microscopy, immuno-gold labelling and in situ hybridisation. In the OB and ORNs this has lead to a degree of conflicting results (Rash et al. 2005).

Working through the OB from the surface: no gap-junctions have been found be ORNs and any other neuronsl types of the OB (Rash et al. 2005, Kosaka and Kosaka, 2003, 2004, 2005b, Christie et al 2005). Cx43 was found in the pia mater, ORN axon bundle ensheathing cells and astrocytes but none of the neurons forming the glomeruli (Rash et al. 2005). Cx36 and to a lesser extent Cx45 was found co-localized with AMPA and NMDA receptors of large dendrites (presumably mitral cells) of the glomeruli (Rash et al. 2005, Christie et al 2005). Periglomerular cells have been observed to share gap-junctions with mitral cells (Kosaka and Kosaka 2005b) and Cx36 has been observed on the margins of the glomeruli where these gap-junctions might be located (Rash et al. 2005). In another study it was shown that Cx36 was expressed in a subset of inter-neurons in the periglomerular region that rarely express calbindin, calretinin or tyrosine hydroxylase (Kosaka et al. 2005).

In the granule cell layer, inter-neurons expressing Cx36 were a subset that were rarely positive for calretinin (Kosaka et al. 2005).

Connexins have been shown to exhibit voltage gating properties (e.g. Gonzalez et al 2007, Bukauskas and Verselis 2004). However in studies involving electrophysiological assessment of gap-junctions in the OB, there has so far been no attempt to investigate these voltage gating properties of gap-junction (Schoppa and Westbrook 2001, 2002, Christie et al. 2005, Christie and Westbrook 2006, Maher et al. 2009). The assessment that was made of these gap-junctions involved looking at coupling ratios of paired cells in response -250 to -400 pA current injections into the soma of one of the cells while recording from the soma of the other cell (Schoppa and Westbrook 2001, 2002, Christie et al. 2005, Christie and Westbrook 2006, Maher et al. 2009).

Knockout models of the olfactory bulb

Another method for examining the function of specific mechanisms in the olfactory bulb is to delete the gene of interest. This is a relatively new field that is providing some interesting insights. The importance of the granule cells in odour discrimination was clearly

demonstrated in a neural cell adhesion molecule-deficient mouse model. In these mice the rostral migratory stream is interrupted resulting in a 40% size reduction of the olfactory bulb. This reduction was restricted to the granule cell layer, a layer that contains the GABAergic interneurons. The mice with this deficit had a reduced odour discrimination ability but their detection threshold for odours and their short-term odour memory were unimpaired, demonstrating that the granule cells are crucial only for odour discrimination but not for general olfactory functions (Gheusi et al. 2000). In the normal olfactory bulb the mitral cells within a particular glomerulus exhibit synchronised activity, knocking out the gap-junction gene Cx36 completely eliminated this synchronised activity (Christie et al. 2005). Correlated spiking between mitral cells is a mechanism for maintaining the fidelity of the glomerular activation map induced by a particular odorant.

Receptor knockouts have been used to investigate the role of the D2 dopamine receptor (Huisman et al. 2004, see above under "Dopaminergic cells"), the $GABA_A$ receptor (Nusser et al. 2001), the insulin receptor (Das et al. 2005), group 1 metabotropic glutamate receptors (Heinbockel et al. 2007a, 2007b) and the rho 1 subunit of the GABA-C receptor (Chen et al. 2007).

$GABA_A$ receptor β3 subunit deficient mice resulted in mitral/tufted cells with increased mIPSCs (control β3 +/+ vs β3 -/- frequency reduced ~80% from 1.16 ± 0.30 Hz to 0.24 ± 0.04 Hz, n = 7, P = 0.01 amplitude reduced 43% from 74.8 ± 11.9 pA to 42.9 ± 8.2 pA, n = 7, P = 0.02) and significant decreases in theta[4] (normalised power spectra: 0.41 ± 0.08 for control, n = 4 and 0.75 ± 0.09 in β3 -/- n = 3, P = 0.02, unpaired t-test for 2.5 ± 0.3 Hz, n = 4 in control and 4.3 ± 0.9, n = 3 in β3 -/- P > 0.05) and gamma (normalised power spectra: 0.36 ± 0.13 for control, n = 4 and 1.00 ± 0.10 in β3 -/- n = 3, P < 0.01, unpaired t-test for 52 ± 5 Hz in control and 52 ± 3 in β3 -/-) oscillations. In odour discrimination tasks, the knockout mice became better that their wild type counterparts in distinguishing closely related monomolecular alcohols. However, the null mice were initially better and became worse than control mice at distinguishing closely related mixtures of alcohols. Disruption of $GABA_A$ receptor mediated synaptic inhibition of GABAergic interneurons and the augmentation of IPSCs in the mitral/tufted cells result in increased network oscillations in the olfactory bulb with complex effects on olfactory discrimination related to the size or power of oscillating networks (Nusser et al. 2001). Knockout of $GABA_C$ rho 1 subunit resulted in increased smell sensitivity (Chen et al. 2007) and knockout of the metabotropic glutamate receptor, mGluR5, demonstrated that activation of mGluR5 participates in feed-forward and/or feedback inhibition at mitral cell to granule cell dendrodendritic synapses, possibly to modulate lateral inhibition and contrast in the olfactory bulb (Heinbockel et al. 2007b).

Transgenic technology, in which genes are deleted (knockouts), either completely or conditionally, or are knocked in, offers a powerful method for investigating the contribution of specific mechanisms to the function of the whole olfactory bulb. The consequences of such genetic manipulations can then be observed at the cellular, organ, system or behavioural level. However, to interpret the results of such interventions requires the development of accurate models of olfactory bulb function. It is therefore the future partnership of genetic and computer modelling technologies that will begin to provide the integrated solution to the problem of how we smell.

[4] Nusser et al. (2001) define theta band as 2-12 Hz which normally would be separted into delta band (1-4 Hz), theta band (4-7 Hz) and alpha band (8-12 Hz).

The Purpose of this complexity?

The immediate impression that one gains when considering the complexities of the neuropharmacology of the olfactory bulb is that each system employs multiple backups. Does this complexity tell us that the olfactory system is so important to the survival of mammals that an element of redundancy has been built in as a fail-safe? Alternatively, the complexities of the modulation may be part of a highly sophisticated multidimensional processing system which remains to be interpreted.

The answers to these questions are to some extent thwarted by the available methods for research in neuropharmacology where the emphasis is on characterising the components of a system by a process of isolation. In the process interaction between systems is lost. Even exploring the effects of gene-targeted deletion, a technique that aims to side-step the isolation issue, can result in the establishment of a new equilibrium rather than an interpretable system failure. How then is it possible to examine the way the many modulating components interact?

Thesis Aim

A possible answer to the question posed at the end of the last paragraph and something that will inevitably become a greater part of future research in understanding the dynamics of olfactory bulb function is realistic neuronal modelling. In the previous sections, I have highlighted the existing evidence that shows that the OB consists of multiple functional channels that consist of populations of mitral cells and their associated inter-neurons. **The aim of this thesis is to develop a model of a representative small network of mitral cells in order to understand how by interacting as a neuronal population they convert simple current injection input to correlated output across the population.** This process will specifically focus on a detailed biophysical approach in which morphology is reconstructed from individual cells and is fitted with as much experimental recordings as possible. The development will be carried out in a series of steps to assess the contribution of gradually increasing biophysical complexity to the functioning of the mitral cell network.

The following chapter gives an account of initial model development that was carried out to assess the feasibility of using reconstructed morphology with components of Bhalla and Bower (1993) mitral cell model.

Chapter 3 : Preliminary Mitral Cell Models

This chapter gives details of some preliminary modelling experiments carried out to assess the feasibility of using equations for conductances from Bhalla and Bower (1993) with detailed morphology reconstructions. The chapter focuses on MCs and how input from stimulation of the MCs apical dendrite tuft is integrated by them to give output. The output of the MC projects to the olfactory cortex via the MC axon, but for modelling purposes a somatic membrane voltage will suffice.

Any model of a neuronal system needs to have a chosen set of parameters and methods of constraining those parameters. Experimental measurements will form a basis of the constraint of these parameters. But as the model is a simplified system with fewer parameters, the parameters need to be fitted to the experimental data within the model.

An early example of fitting model parameters to experimental data used field potentials measured at various depths in the OB to deduce the reciprocal synapses between MTs and GCs (Rall et al. 1966, Rall and Shepherd 1968). We now have access to whole cell patch clamp recordings that should be much better for constraining individual cell parameters.

Before starting to fit parameters it is necessary to deal with the issue of cell morphology. It is possible to ignore the morphology completely and have neurons that react in a desired manner to input stimuli. Often morphology is created in compartmental models composed of simple units with roughly the right geometric components. A discussion of different approaches in OB models can be found in Cleland and Linster (2005) and a more general discussion of the possible implications of simple threshold models versus detailed biophysical models can be found in Gerstner and Naud (2009).

In the model presented in this thesis I will be looking at how MCs integrate input and the processing involved that produces the MCs output. For this kind of research the detailed biophysical model is most appropriate. However detailed MC morphology reconstructions were not available when earlier MC models were constructed. So I needed to test the existing conductance channel equations and densities to see if they were scalable to reconstructed MC morphology when they were originally fitted in much simpler morphology.

Simulators

In the first few decades of neuron modelling a series of differential equations where used to describe the different properties of the neuron. The spread of charge throughout the neuron had to be modelled using cable equations. To make the models more manageable the branching was abbreviated to an equivalent cylinder but this made assumptions about branching that were not always true (the collected papers of Wilfrid Rall give a good account of neuron modelling in this way Segev, Rinzel and Shepherd 1995). There has now been a move away from this cable modelling to compartmental modelling in which the neuron is broken down into a series of small pieces that are connected by a resistance. Compartmental modelling allows the full complexity of the branching to be modelled by simple differential equation. For compartmental modelling rather than building model simulations completely from the ground up a simulator program is used. These programs contain an interpreter for a structured high level language for specifying all the model parameters for each compartment. Several have been developed over the years but just two have managed to achieve a sufficient following amongst academics to acquire the momentum for continued development. The two

mainstream simulators for detailed biophysical models are the 'Genesis' simulator (Wilson et al. 1989; Bower and Beeman 1998) and the 'Neuron' simulator (Hines and Carnevale 1997, 2000). As these two simulators use incompatible languages and methods, a standards group have been working to produce a standardised language of an XML type (http://www.neuroml.org/). This standardised language can be used by another program called neuroConstruct (Gleeson et al. 2007). This tool automates some of the aspects of model specification which allows a degree of randomisation in synapse location. Its 3D visualisation allows rotation of cells for inspection of their morphology which is not possible in Neuron or Genesis. It then can be used to produce code in either the Neuron or Genesis script languages so the simulations can be run.

I have used it to be able to use combinations of active properties that were written in a mixture of Genesis and Neuron script languages. The files are translated to XML versions then neuroConstruct produces the Genesis or Neuron code depending on which simulator I need to use at the time.

Detailed Biophysical OB Models

As precedents to this work there is the pioneering work of Bhalla and Bower 1993 and the sequence of more targeted studies (Shen et al. 1999; Chen et al. 2001; Migliore et al. 2005). The Bhalla and Bower model (Bhalla and Bower 1993) was created in Genesis from experimental measurements from similar cells in other brain regions and different species according to what was available in the early 1990s. The latter group of simulations were carried out by Gordon Shepherd and collaborators using Neuron and a more tightly constrained approach to model correctly the shift of the action potential from axon to dendrites (Shen et al. 1999; Chen et al. 2001). This was followed by adapting the model to look at intercellular synchronisation via gap-junctions, for which the morphology was modelled as a simple canonical structure (Migliore et al. 2005).

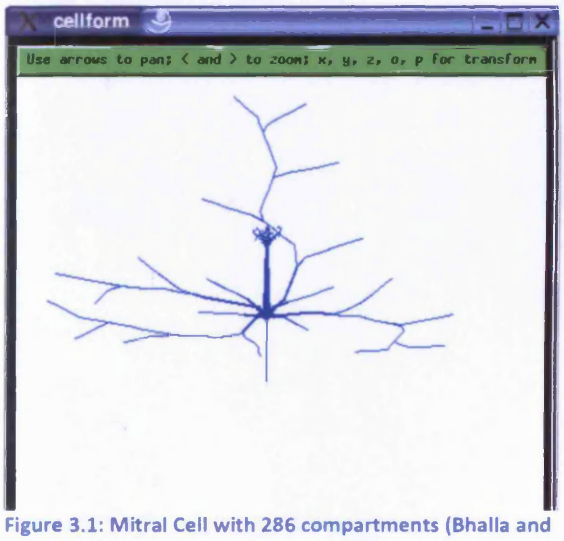

Figure 3.1: Mitral Cell with 286 compartments (Bhalla and Bower 1993)

The Bhalla and Bower model has relatively complex morphology (Figure 3.1) and a large number of parameters including cell mechanism for Na, K_{dr}, K_A, KCa, L-type calcium channels. A series of parameter searches were used to successively fix the distribution patterns and densities of the active properties in which output was fitted to experimental recordings from Jahr and Nicoll (1982b) and Mori et al. (1981a).

The somatic membrane recording of a MC from the Bhalla and Bower model exhibits burst firing (Figure 3.2). It is the calcium mechanisms that impart this burst firing. In the Migliore model Na, K_{dr} and K_A mechanisms only are present and tonic firing is achieved by continuous current injection.

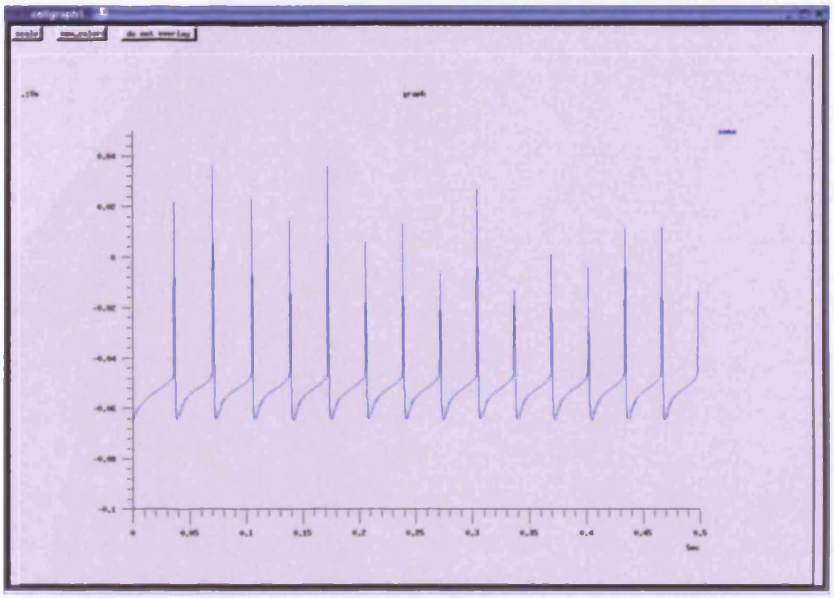

Figure 3.2 Simulated mitral cell somatic membrane potential from the Bhalla and Bower (1993) model.

Bhalla and Bower Synthetic Mitral Cell (286 compartments 712 ion channels) simulation with membrane voltage recording from soma during a continuous 0.5 nA current clamp injection into to soma , L-type calcium channel density in apical tuft compartments = 95 S/m^2 (see Table 3.1 for the other channel densities). Time steps (dt) of 0.005 ms is not short enough to capture all the peaks of the action potentials (APs) leading to variable amplitude on the Vm recording. A shorter dt would give APs of equal height. X axis = Time (seconds, Y axis = Vm (volts).

For an initial experiment I used a Neurolucida (computer software by MicroBrightField, Colchester, VT, USA, that is used in combination with an optical microscope to achieve detailed reconstructions of cell morphology) reconstruction of a mouse MC supplied by Diogo Pimentel (Figure 3.3).

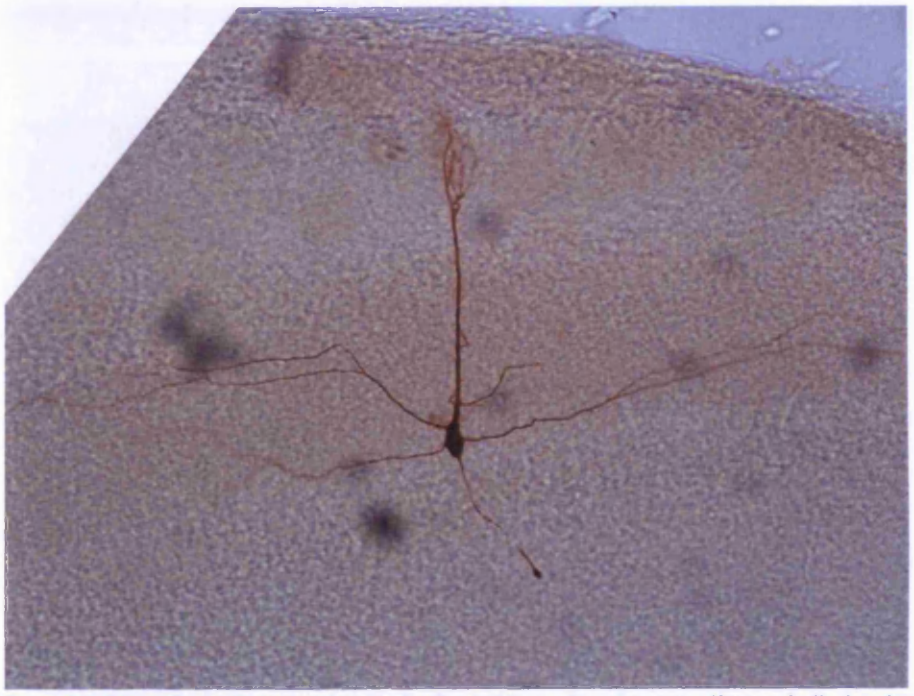

Figure 3.3: 20x optical microscope image of a fixed 300μm slice of mouse olfactory bulb showing a filled mitral cell (Image courtesy of Diogo Pimentel, UCL, London).

The Neurolucida reconstruction was converted for use in Genesis using CVAPP morphology editor (an open source application that is available online[5] for converting and editing morphology files). The basic reconstruction can be seen in Figure 3.4 and after the addition of a spherical soma and an axon in Figure 3.5.

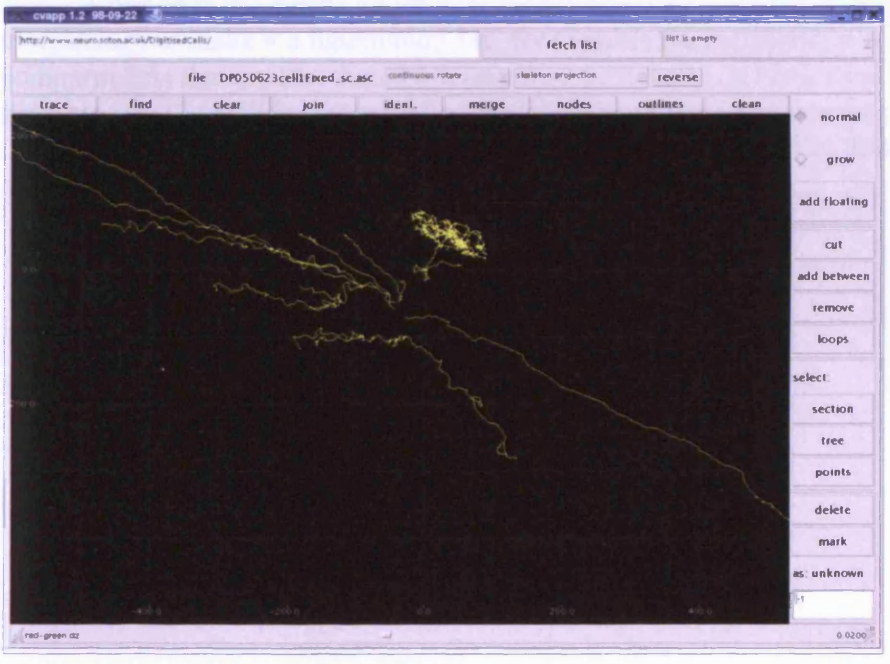

Figure 3.4: The Neurolucida reconstruction is next imported into the cvapp morphology editor. It can be seen that the slice has truncated the glomerulus which is no longer spherical and the lateral dendrites outside of the plane of the slice are torn from the cell.

[5] http://neuron.duke.edu/cells/download.html

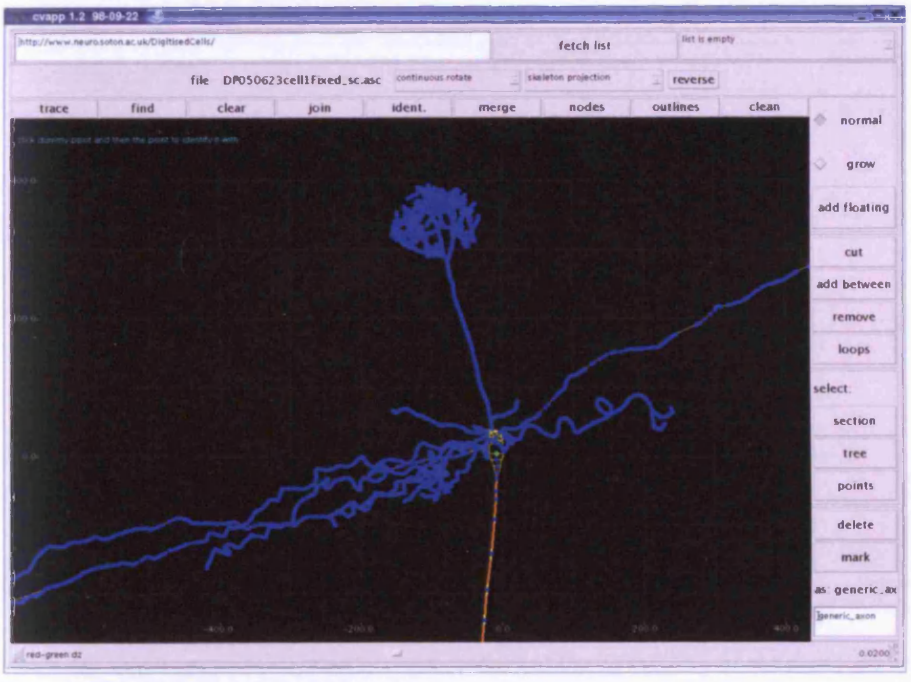

Figure 3.5: The cvapp morphology editor is used to replace the soma polygon with a spherical soma, connect up the dendrites and add a synthetic soma. It is then used to divide the cell up into even compartments (meshing in cvapp1.4.3) and write the Genesis.p file.

Genesis requires a 3D spherical soma rather than the 2D polygon that is generated by Neurolucida. The Bhalla and Bower model specifies channel densities for an axon, while the OB slice preparations for mice rarely have any MC axons present. I therefore added an axon that conformed to the Bhalla and Bower model. Once all these adjustments were made to the morphology to make it a functioning MC for Genesis the morphology was remeshed to give compartments that are less than 0.1 λ (electrotonic length). A Genesis.p file was then generated by CVAPP for the modified morphology (Figure 3.6) and the channel densities for the Bhalla and Bower model were added manually (Figure 3.7). The details of the channel densities and passive parameters are given in Table 3.1 (below).

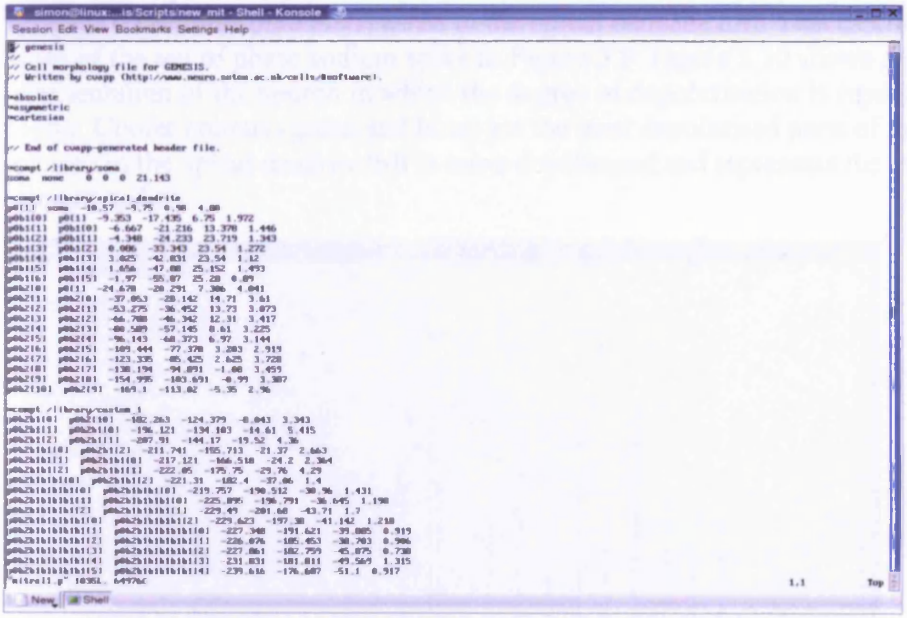

Figure 3.6: The Genesis.p file created by cvapp contains all the 3D coordinates and diameters needed to specify the compartments of the cell.

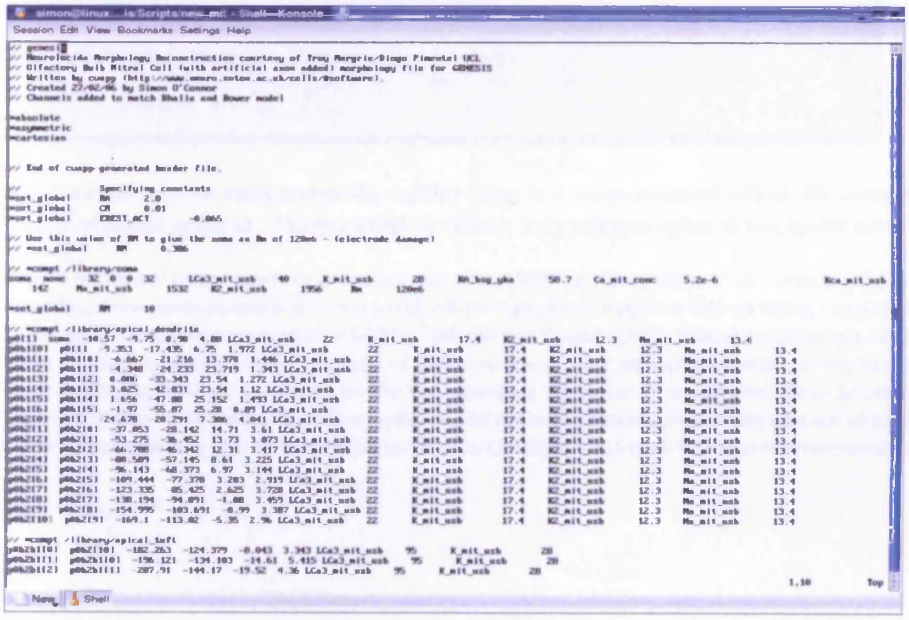

Figure 3.7: The cvapp generated file is then manually edited to add the ion channel densities. I used the same pattern of distribution and implementation of ion channels as used in the Bhalla and Bower model.

Simulations were setup in the Neurokit application in Genesis. With the density for the L-type calcium channel in the apical dendrite tuft set at 95 S/m^2, occasional calcium spikes were observed in the tuft, which disrupt the burst firing. This phenomenon is observable as the L-type calcium channel density is reduced down as far as 64 S/m^2 (Figure 3.8 somatic recording, Figure 3.9 apical dendrite tuft recording, and Figure 3.10 simulation graphic). In Figure 3.8 we see the regular spiking of the soma interrupted by an out of phase spike at ~250 ms. Once the extended refractory period, following the double spike, has finished, spiking returns to the original frequency. The concurrent recording in the apical dendrite tuft (Figure 3.9) shows the depolarisation in the apical tuft that result from the spikes in the soma. At

~250 ms a calcium spike is triggered in the apical dendrite tuft. This calcium spike is the cause of the out of phase sodium spike in Figure 3.8. Figure 3.10 shows a graphical representation of the neuron in which the degree of depolarisation is represented by the colour. Cooler colours (green and blue) are the least depolarised parts of the cell, while the red area in the apical dendrite tuft is more depolarised and represents the extent of the calcium spike.

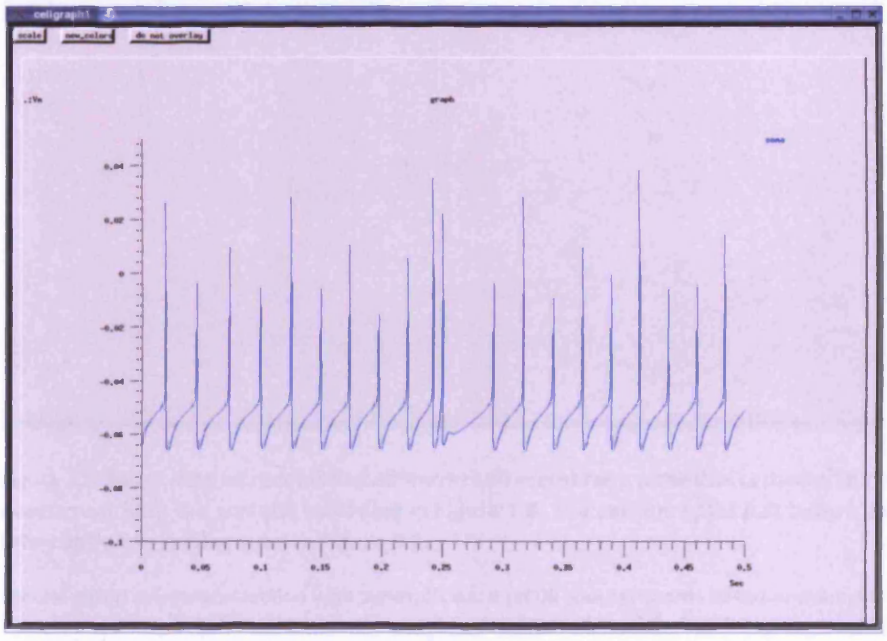

Figure 3.8: Simulation demonstrating regular firing in a reconstructed mitral cell soma that is interrupted by an out of phase spike at ~250 ms which is caused by a calcium spike at the apical dendrite tuft.

Mouse mitral cell reconstruction with synthetic axon (1006 compartments 2646 ion channels) with membrane voltage recording from soma during a continuous 0.5 nA current clamp injection into to soma, L-type calcium channel density in apical dendrite tuft compartments = 64 S/m^2 (Bhalla and Bower (1993) Model ion channels used, see Table 3.1 for the other channel densities). Time steps (dt) of 0.005 ms is not short enough to capture all the peaks of the action potentials (APs) leading to variable amplitude on the Vm recording. A shorter dt would give APs of equal height. X axis = Time (seconds, Y axis = Vm (volts). A calcium spike at 250 ms in the apical tuft provokes an out of phase sodium spike in the soma that causes a longer refractory period before the firing goes back to the same frequency as before.

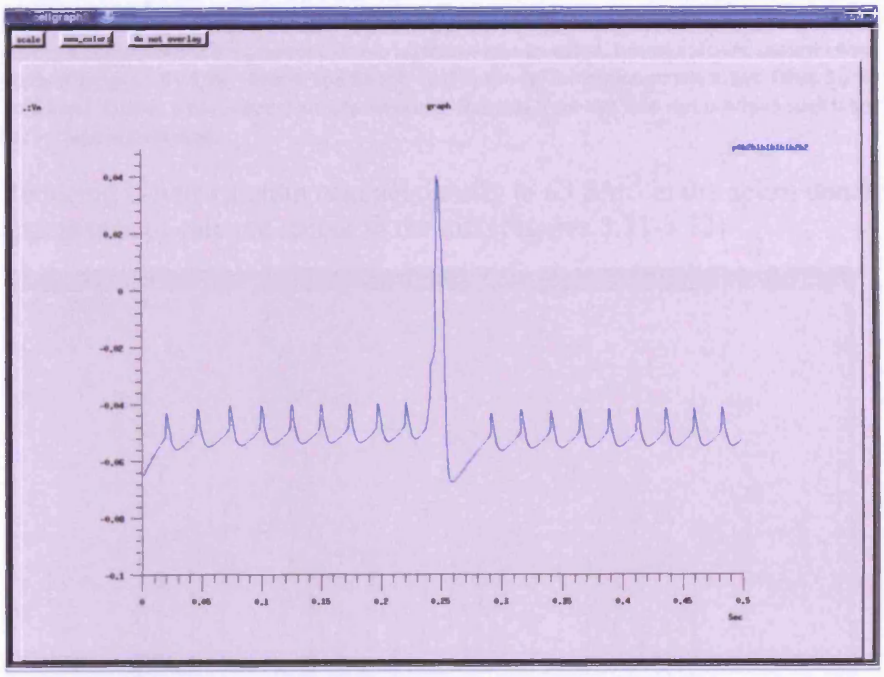

Figure 3.9: Simulation of reconstructed mitral cell membrane potential recorded in the apical dendrite tuft concurrent with the somatic recording in Figure 3.8. The calcium spike just before 250 produces the interruption in spiking seen in Figure 3.8.

Mouse mitral cell reconstruction with synthetic axon (1006 compartments 2646 ion channels) with membrane recording from apical dendrite tuft during a continuous 0.5 nA current clamp injection into to soma, L-type calcium channel density in apical tuft compartments = 64 S/m^2 (Bhalla and Bower (1993) Model ion channels used, see Table 3.1 for the other channel densities). Time steps (dt) of 0.005 ms is not short enough to capture all the peaks of the action potentials (APs) leading to variable amplitude on the Vm recording. A shorter dt would give APs of equal height. X axis = Time (seconds, Y axis = Vm (volts).

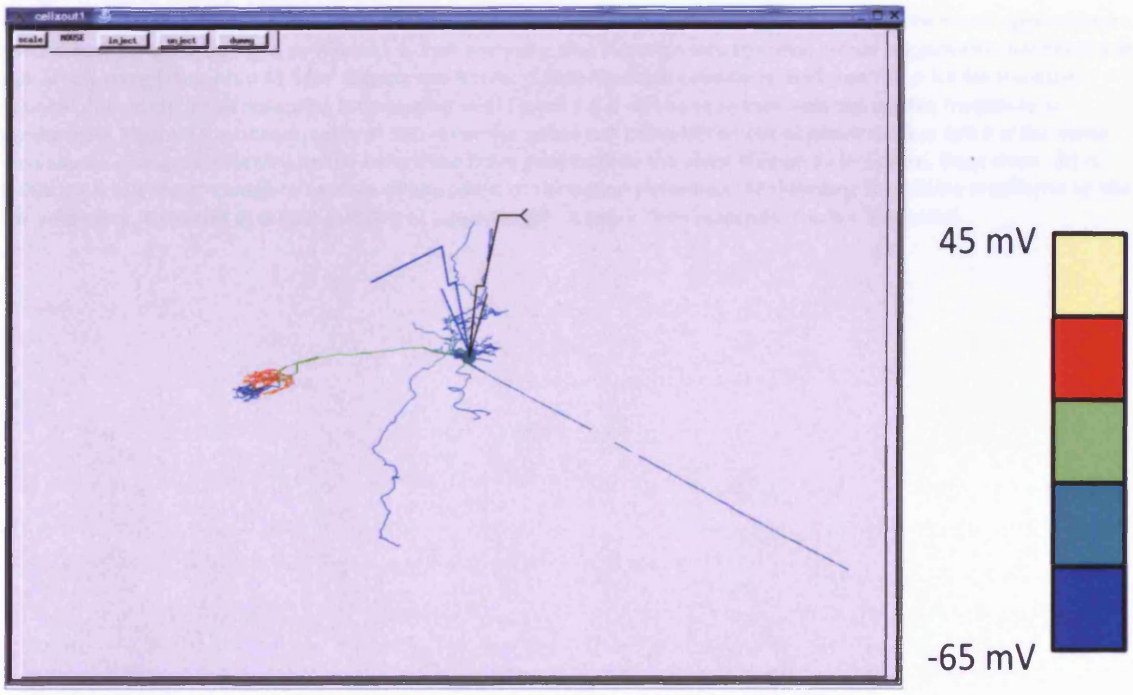

Figure 3.10: Graphic representation of the reconstructed mitral cell in Figures 3.8 and 3.9 using colours to represent the membrane voltage changes during a calcium spike.

Mouse mitral cell reconstruction with synthetic axon (1006 compartments 2646 ion channels) graphic of calcium spike during a continuous 0.5 nA current clamp injection into to soma, L-type calcium channel density in apical tuft compartments = 64 S/m^2 (Bhalla and Bower (1993) Model ion channels used, see Table 3.1 for the other channel densities). Colour scale is approximate because 'Genesis Neurokit' did not produce such a scale (see Figures 3.8 and 3.9 for voltage recordings).

Reducing L-type calcium channel density to 63 S/m^2 in the apical dendrite tuft stopped the appearance of calcium spikes in the tuft (Figures 3.11-3.13).

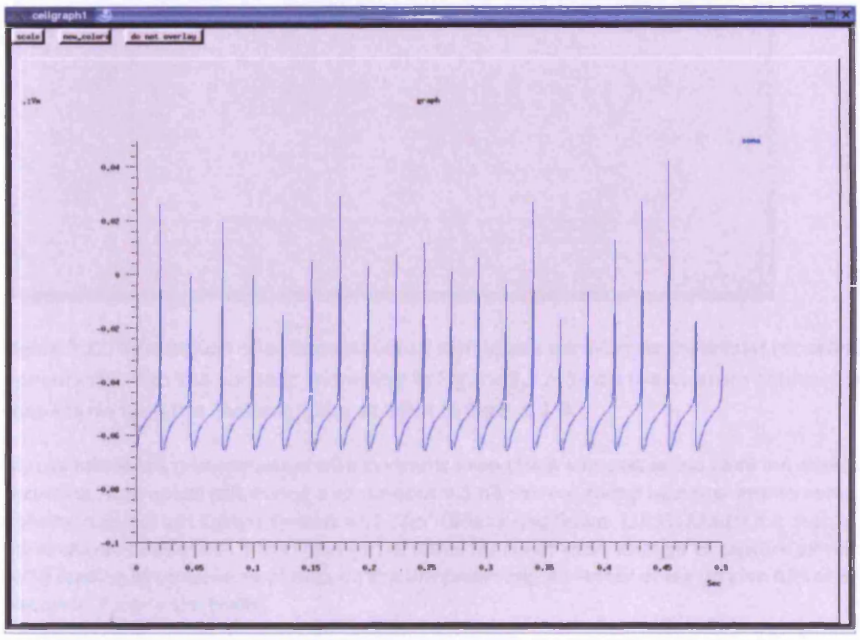

Figure 3.11: Simulation demonstrating regular firing in a reconstructed mitral cell soma. Reducing calcium channel density in the apical dendrite tuft prevents the calcium spike disruption seen in Figure 3.8.

Mouse mitral cell reconstruction with synthetic axon (1006 compartments 2646 ion channels) with membrane voltage recording from soma during a continuous 0.5 nA current clamp injection into to soma, L-type calcium channel density in apical tuft compartments = 63 S/m^2 (Bhalla and Bower (1993) Model ion channels used, see Table 3.1 for the other channel densities). If this recording is compared with Figure 3.8 it will be seen that here the spiking frequency is constant. In Figure 3.8 a calcium spike at 250 ms in the apical tuft provokes an out of phase sodium spike in the soma that causes a longer refractory period before the firing goes back to the same frequency as before. Time steps (dt) of 0.005 ms is not short enough to capture all the peaks of the action potentials (APs) leading to variable amplitude on the Vm recording. A shorter dt would give APs of equal height. X axis = Time (seconds, Y axis = Vm (volts).

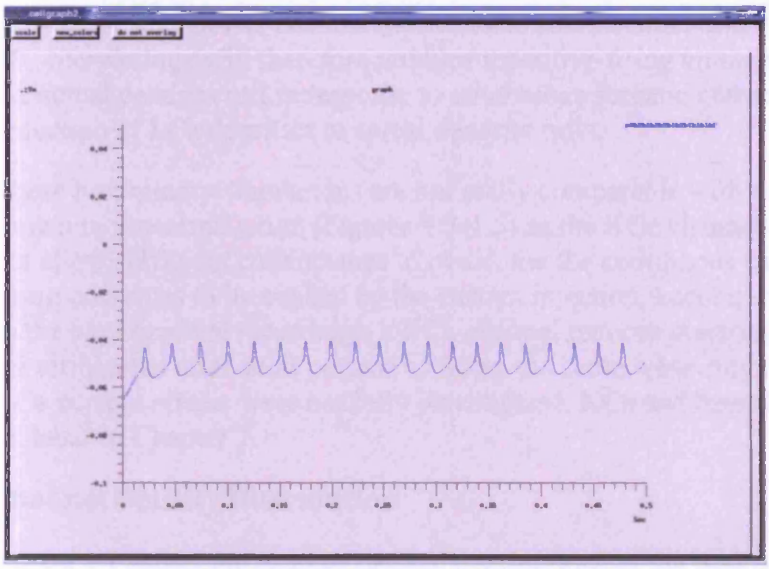

Figure 3.12: Simulation of a reconstructed mitral cell membrane potential recorded in the apical dendrite tuft concurrent with the somatic recording in Figure 3.11. Since the calcium channel density has been reduced there is no longer a calcium spike as seen in Figure 3.9.

Mouse mitral cell reconstruction with synthetic axon (1006 compartments 2646 ion channels) with membrane voltage recording from apical tuft during a continuous 0.5 nA current clamp injection into to soma, L-type calcium channel density in apical tuft compartments = 63 S/m^2 (Bhalla and Bower (1993) Model ion channels used, see Table 3.1 for the other channel densities). Time steps (dt) of 0.005 ms is not short enough to capture all the peaks of the action potentials (APs) leading to variable amplitude on the Vm recording. A shorter dt would give APs of equal height. X axis = Time (seconds, Y axis = Vm (volts).

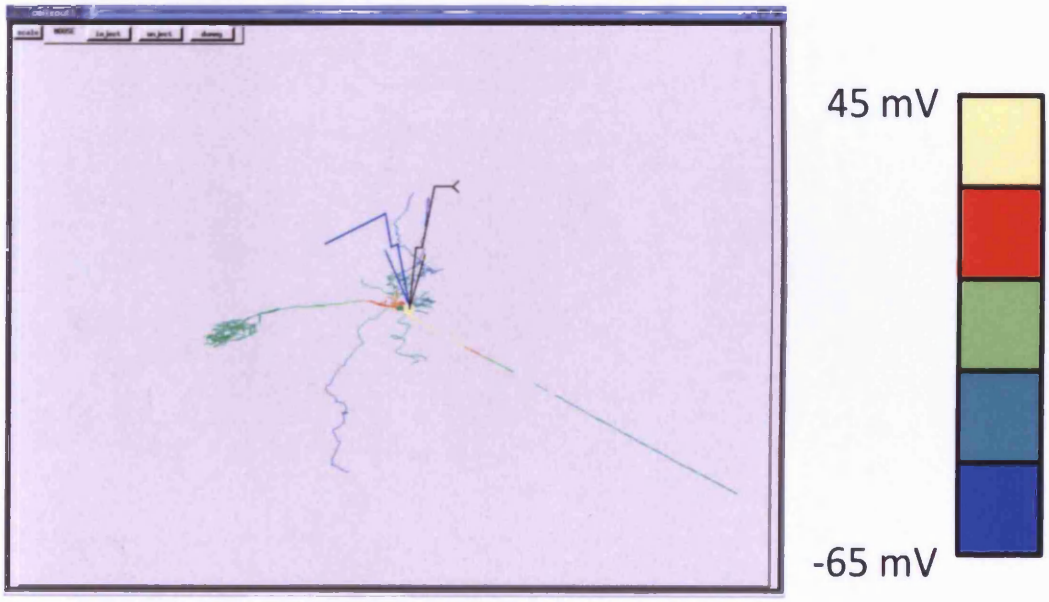

Figure 3.13: Graphic representation of the reconstructed mitral cell in Figures 3.11 and 3.12 using colours to represent the membrane voltage changes during an action potential.

Mouse mitral cell reconstruction with synthetic axon (1006 compartments 2646 ion channels) graphic of action potential (yellow colour of soma shows that it is depolarised in an action potential compared with the cooler colours of the rest of cell where the cell is still below the action potential threshold) during 0.5 nA current clamp injection into to soma, L-type calcium channel density in apical tuft compartments = 63 S/m^2 (Bhalla and Bower (1993) Model ion channels used, see Table 3.1 for the other channel densities). Colour scale is approximate because 'Genesis Neurokit' did not produce such a scale (see Figures 3.11 and 3.12 for voltage recordings).

The Bhalla and Bower channel mechanisms and densities when combined with reconstructed MC morphology will therefore produce repetitive firing uninterrupted by calcium spikes in the apical dendrite tuft in response to continuous somatic current injection with moderate reduction of LCa densities in apical dendrite tufts.

These preliminary simulations are not really comparable with the experimental recordings shown in the introduction (Figures 1.3-1.5) as the KCa channels included in the model did not allow sufficient conductance to overcome the continuous current injection. The repetitive firing continues to be evoked by the current injection, keeping the cell above firing threshold. In the experimental recordings, a KCa channel reduces membrane potential so bursts of firing are terminated after short periods of firing. As these were only preliminary experiments, the KCa current effects were not fully investigated. KCa and burst firing termination is examined in detail in Chapter 7.

Channel Density Distribution

Tables 3.1 shows the channel density distributions of the Bhalla and Bower model and Migliore model respectively.

Hodgkin and Huxley (Hodgkin and Huxley 1952d) used a leak conductance G_{Leak} to cover conductances in other channels (such as chloride channels) that were not modelled by the sodium and potassium channels. In all simulators that are used in this thesis this conductance is modelled as $G_{Leak} = 1/R_m$. This conductance has no net current flow at the resting membrane potential which in *Genesis* is called *EREST_ACT* (Volts) and in Neuron *e_pas* (mV). In *Genesis*, R_m is set directly while Neuron uses g_pas = $G_{Leak} = 1/R_m$.

Topology	Geometry			Passive				Active (S/m^2)					
Section/compartment	Compartments	L (μm)	Dia (μm)	R_m	R_i	C_m	*EREST_ACT*	LCa	K	K_A	KCa	Na	K2
Apical Tuft	94	Polar	3.5-0.5	10	2.0	0.01	-0.065	95	28	-	-	-	-
Primary Dendrite	6	570	7.9-4.7	10	2.0	0.01	-0.065	22	17.4	-	-	13.4	12.3
Proximal Lateral Dendrite	32 20	Polar	5.8-2.7 2.7-1.5	10	2.0	0.01	-0.065	4	8.5	-	-	330	226
Distal Lateral Dendrite	120	Polar	2.2-0.9	10	2.0	0.01	-0.065	-	-	-	-	122	128
Soma	1	32	32	10	2.0	0.01	-0.065	40	28	58.7	142	1532	1956
Axon [0]	1	10	10	10	2.0	0.01	-0.065	20	15.5	51.5	88.7	4681	1541
Axon [1]	1	10	7	10	2.0	0.01	-0.065	20	15.5	51.5	88.7	4681	1541
Axon [2]	1	10	5	10	2.0	0.01	-0.065	20	15.5	51.5	88.7	4681	1156
Axon [3]	1	10	3	10	2.0	0.01	-0.065	20	15.5	51.5	88.7	4681	1156
Axon [4]	1	10	2	10	2.0	0.01	-0.065	20	15.5	51.5	88.7	4681	1156
Axon [5]	1	10	1.5	10	2.0	0.01	-0.065	-	-	-	-	3511	771
Axon [6]	1	20	1.5	10	2.0	0.01	-0.065	-	-	-	-	3511	771
Axon [7]	1	50	1.5	10	2.0	0.01	-0.065	-	-	-	-	2340	771
Axon [8]	1	50	1.0	10	2.0	0.01	-0.065	-	-	-	-	1170	771
Axon [9]	1	90	0.9	10	2.0	0.01	-0.065	-	-	-	-	586	385
Axon [10]	1	90	0.9	10	2.0	0.01	-0.065	-	-	-	-	234	77
Axon [11]	1	90	0.9	10	2.0	0.01	-0.065	-	-	-	-	117	77
Axon [12]	1	90	0.9	10	2.0	0.01	-0.065	-	-	-	-	117	77

Table 3.1: Channel Distributions for the Bhalla and Bower model: the model is divided up into sections or compartments (column 1) for which there are set variables. The number of compartments, length of compartments and diameter of compartments that make up these sections is given in the next 3 columns. Where polar coordinates are used it is not possible to easily give length estimates. The passive parameters for each compartment are given in the next 4 columns, R_i (Ω.m), C_m (F/m^2), R_m ($Ω.m^2$), *EREST_ACT* (V) is the resting potential at which there is no net current across the membrane resistance. The channel mechanisms included are a L-type calcium current; a fast delayed rectifier potassium current (K); a transient outward potassium current (K_A); a voltage and calcium dependent potassium current (KCa); a fast sodium current (Na); and a slow delayed rectifier potassium current (τ is slower (larger) by a factor of 4; K2).

Na, K_{dr} and K_A Channel Mechanism Kinetics

		α	β	∞	τ
Na^6	m^3	$\frac{0.32(V+42)}{1-e^{-\frac{V+42}{4}}}$	$\frac{0.28(V+15)}{e^{(\frac{V+15}{5})-1}}$	$\frac{\alpha}{\alpha+\beta}$	$\frac{1}{\alpha+\beta}$
	h	$\frac{0.128}{e^{\frac{V-38}{18}}}$	$\frac{4}{1+e^{-\frac{V+15}{5}}}$	$\frac{\alpha}{\alpha+\beta}$	$\frac{1}{\alpha+\beta}$
K_{dr}^7	n^2	These channels are (there are fast and slow versions of the delayed rectifier potassium currents in this model) modelled as a table of values rather than equations.		$\frac{\alpha}{\alpha+\beta}$	$\frac{1}{\alpha+\beta}$
K_A^8	p			$\frac{1}{1+e^{-\frac{v+42}{13}}}$	1.38
	q			$\frac{1}{1+e^{\frac{v+110}{18}}}$	150

Table 3.2: Bhalla and Bower model conductance equations: Columns give the equations for the rate constants α(V) and β(V), the steady state value ∞(V), and the time constant τ(V). The second column gives the gating variables and powers for the channel mechanisms in the first column. In this case the K_A mechanism is described only in terms of the steady state value and time constant.

The kinetics for the Na, K_{dr} and K_A channels in the Bhalla and Bower are given in Tables 3.2.

Having established that the channel mechanisms and densities from the Bhalla and Bower (1993) model are compatible with reconstructed MC morphology, I next started fitting the individual MC passive parameters. This fitting process is described in Chapter 4.

[6] Slightly modified from Traub 1982.

[7] Both modified from Adams et al. 1980 and Aldrich et al. 1979.

[8] Yamada et al. 1989.

Chapter 4 : Constructing Passive Mitral Cell Models

In the previous chapter I referred to some empirical simulations that were not fully constrained by experimental measurements to get an idea of how well the Migliore (Migliore et al. 2005) and Bhalla and Bower (Bhalla and Bower 1993) model active properties work with detailed MC reconstructions. From this chapter onwards, I change to a systematic development of a detailed biophysical model. Here I use experimental recordings to provide the constraint for fitting the passive parameters R_i[9], C_m, and R_m. These fittings are carried out on detailed reconstructions of the MCs the recordings were made in.

Estimation of passive parameters from somatic recordings has had a long history (including Rall, 1959; Barrett and Crill, 1974; Clements and Redman, 1989; Major et al., 1994; Thurbon et al., 1998; Perreault and Raastad, 2006). The use of two site electrophysiology with an accurate morphological reconstruction to fit passive parameters is more recent and has been applied to neocortical pyramidal neurons (Stuart and Spruston, 1998; Golding et al., 2005) and Purkinje cells (Roth and Häusser, 2001). Here I apply the same method to the mitral cells of the rat olfactory bulb. Shen and colleagues (Shen et al, 1999) carried out direct fitting of seven passive parameters to the first 4 ms after the onset of a current injection in a two site injection/recording protocol. These passive parameters include dendritic diameters in a simple canonical model. Here I use the experimental recordings of Kamilla Angelo[10] (MC recordings using a two site recording protocol) for direct fitting of 3 passive parameters to current injection transients using accurate 3D reconstructions of the actual cell from which the transients were recorded. With neuromorphic rendering of electrotonic transformations (see Methods in this chapter) using our passive model, I demonstrate that the efficacy with which voltage transfers in the somatopetal direction is mainly determined by the branching structure of the tuft with very little attenuation occurring in the large diameter trunk of the apical dendrite. In contrast, the outgoing (somatofugal) voltage control of dendritic branches in the tuft from the soma is largely determined by the dimensions of the trunk of the apical dendrite providing a low attenuation link between soma and tuft. Using sinusoidal current injection waveforms the transfer of voltage in the passive MC is largely unaffected by the frequency (0-100 Hz) with which the voltage arises at the synapse.

---

[9] In the literature there appears to be inconsistent use of R_i and R_a, both Neuron and Genesis use R_a. Neuron calls R_a, cytoplasmic resistivity with units of Ω-Cm, while Genesis call R_a specific axial resistance (units Ω.m they also give R_a = ri.l). In Johnston and Wu (1995) R_i is used: ri = axial resistance (Ohm/cm) while talking about infinite cylinders, R_i = specific intracellular resistivity (Ω-cm). These references taken together suggest that R_i and R_a can be used interchangeably. In this thesis I will refer to intracellular resistance as R_i.

[10] Institute of Neuroscience and Pharmacology, Panum institute, Copenhagen. At the time the recordings were made Kamilla was working for Troy Margrie at UCL.

Methods

Electrophysiology

Sprague-Dawley rats (P21-P28) were anaesthetized with isoflurane and decapitated. Acute olfactory bulb slices (300 μm) were cut in ice-cold slice solution in the horizontal plane (MICROM-HM650V, Zeiss) and incubated for 45-60 min at 34 °C prior to recording. Mitral cell (MC) soma and apical dendrites were visualised by infrared differential interference contrast (IR-DIC) video microscopy and recorded from with low resistance (7-12 MΩ) glass pipette electrodes in the whole-cell patch-clamp configuration. Gigaseal cell-attached configuration was obtained first and subsequently the membrane-patch was removed to obtain a whole-cell recording. The voltage signal (filtered/sampled 6 kHz/50 kHz) was amplified with a Multiclamp 700A (Molecular devices) connected to a Macintosh computer through an ITC-18 board (Instrutech). Data acquisition and current injection was done with the Nclamp/NeuroMatics electrophysiological software (J. Rothman, www.thinkrandom.com/) built to run under the IGOR Pro scientific graphing and data analysis software (www.wavemetrics.com/). Bridge balancing and pipette capacitance compensation were done on the current injecting electrode by visual inspection on an oscilloscope of the charging of the membrane in response to -200 pA (100 Hz) square pulse injection. Only experiments with an access resistance below 40 MΩ were used. All recordings were done at physiological temperature, 33-35°C. The internal pipette solution contained (mM): 130 methanesulphonic acid, 10 Hepes, 7 KCl, 0.05 EGTA, 2 Na_2ATP, 2 MgATP, 0.5 Na_2GTP, 0.4% biocytin and was titrated to pH 7.2 with KOH. The slice solution was composed of (mM): 125 NaCl, 2.5 KCl, 2 $CaCl_2$, 1 $MgCl_2$, 25 $NaHCO_3$, 1.25 NaH_2PO_4, 25 D-glucose and was perfused with 95%/5% O_2/CO_2. The external recording solution included (mM): 105 NaCl, 12.5 KCl, 26[11] $NaHCO_3$, 1 $MgCl_2$, 1 $CoCl_2$, 0.001 TTX, 0.05 PicroToxin, 0.01 NBQX, 0.01 D-APV, 25 D-glucose, titrated to pH 7.4 with 95%/5% O_2/CO_2. This solution was designed to block all active currents. However Figures 2.2 and 2.3 show receptor types that have not been blocked by substances included in the slice solution. Therefore it has been assumed that the MCs are passive when reciprocity is demonstrated by an exact overlap of recordings for different injection conditions (Figure 4.1C). All chemicals were from Sigma and Tocris.

Voltage responses for use in the passive parameter fitting procedure were obtained by performing simultaneous patch-clamp injection/recording from two sites; one pipette in the soma the other in the apical dendrite. Depolarising or hyperpolarizing current injection pulses were applied to one of the pipettes for 0.5 ms after 50 ms baseline recording. The recording was continued until 200 ms and repeated 10 - 20 times. The combination of depolarising or hyperpolarizing injection current pulses and the two locations for injection or recording gives four separate groups of traces with which to constrain the parameter fits. Recordings were scaled to give superimposed baselines for the four recordings. Only transfer voltage responses (i.e. voltage recordings made from an electrode at a distance from the electrode used to inject the current pulse) were fitted while determining the passive parameters, thus the local voltage response derived from the current injecting electrode was not used in order to minimise possible errors originating from pipette artefacts.

[11] The NaH_2PO_4 is not included in the recording solution to avoid precipitation, thus an extra 1 mM $NaHCO_3$ buffer was added.

Histology

The structure of each MC recorded from was obtained by filling the cell with biocytin through the whole-cell pipette and subsequently processing the slices histologically. Immediately after ending the recording, the patch pipettes were carefully withdrawn from the dendrite/soma and the slice was fixed for a minimum of 24 hours in a 4 % paraformaldehyde phosphate buffered solution (PBS) at 4°C. The membranes were permeabilised with pre-cooled 100% methanol at -20°C for 10 mins. Endogenous peroxidase activity was blocked with 1 % H_2O_2/10% methanol and the signal was amplified by incubation for 18-24 hours in the ABC kit solution (Vectastain). The slices were washed thoroughly with PBS between each step. After a DAB (3,3-diaminobenzidine hydrochloride) amplification (1 mg/ml, 15 mins at room temperature) the stain was developed by adding H_2O_2. The progress of the staining was followed under the microscope to ensure a dark brown, not completely black, colouration of the dendrites, which was found to be optimal for digital tracing of the full morphology. The slices were mounted under coverslips with Mowiol 4-88 medium (Calbiochem).

Morphological reconstruction

Neurolucida (MicroBrightField, Colchester, VT, USA) reconstructions were produced using a light microscope (BX-61, Olympus) with 100x oil immersion objective. The axon and dendrites are represented by diameters located by 3D coordinates and the soma by a 2D outline.

The inter pipette distances were estimated from DIC images obtained during experimentation.

The amount of shrinkage produced by the histological methodology used for fixing the slice has not been estimated. Therefore as a worst case scenario a modified version of the reconstruction was produced for comparison in which 50% shrinkage was simulated by doubling the z-plane within Neurolucida.

Compartmental modelling

Simulations were carried out using the 'Neuron' simulator (Hines and Carnevale, 1997, 2000). Neurolucida reconstructions were converted to 'Neuron' parameter files using Neurons' built in Import3d tool. The spatial segmentation was handled by the d-lambda rule setting a value for d-lambda of 0.1 (Hines and Carnevale, 2001).

Later compartmental models in Neuron where mostly created with the help of neuroConstructs (Gleeson et al., 2007) 3D. This tool automates some of the aspects of model specification which allows a degree of randomisation in synapse location. Its 3D visualisation allows rotation of cells for inspection of their morphology.

Fitting passive parameters

In compartmental models each compartment is modelled as an equivalent circuit which includes values for C_m, R_m and up and downstream R_i. Normally this equivalent circuit would also include values for active conductances, but these are not used for a passive model. So a differential equation for each compartment can be given as:

$$C_m \frac{dV_m}{dt} = \frac{(E_m - V_m)}{R_m} + \frac{(V'_m - V_m)}{R'_i} + \frac{(V''_m - V_m)}{R_i} + I_{inject}$$

The apostrophies are used to indicate up and down stream membrane voltages or axial resistance (for fully labelled equivalent circuit see Bower and Beeman 1998). The simulator will numerically solve the linked equations in parallel at the time interval set as "dt". When a current injection is made in one compartment the changes in another compartment can be recorded. The model is set-up to mimic the dual electrode experimental set-up. The simulation recording is then compared with the experimental recording using a least squares comparison. A fitting algorithm is used to vary the passive parameters in a way that finds the smallest error value on the least squares test.

Here the parameter fitting was carried out using the principle axis method (Brent, 1973; a development of the 'conjugate gradient' method of Press et al., 1992). The implementation of this algorithm in the 'Neuron' simulator is known as 'PRAXIS' (for a tutorial on the use of this algorithm in parameter fitting see http://www.neuron.yale.edu/neuron/docs/optimiz/model/outline.html).

Some early attempts were made at fitting using an alternative simulated annealing algorithm (Kirkpatrick et al., 1983; Press et al. 1992) using an implementation for 'Neuron' (Weaver and Wearne, 2006). However although this method has the advantage that the whole parameter field is systematically assessed reducing the likelihood of being stuck in a local minimum, it proved to be too cumbersome in practice. Some 40,000 iterations were required to find a best-fit using simulated annealing versus 100-200 using PRAXIS. Similar results were achieved in both cases suggesting that local minima where not a big problem using PRAXIS. However as I were concentrating on the use of PRAXIS I used multiple starting points to promote the likelihood of finding of the global minimum.

I have chosen to fit C_m, R_m, and R_i, as Kamilla Angelo was using whole cell patch-clamp recordings I am assuming that there is no need for somatic shunt resistance R_{sh} (Clements and Redman, 1989; Major et al., 1994). Also I have made no attempt to fix R_i to assumed values (Clements and Redman, 1989; Major et al., 1994).

These passive values were directly fitted to current injection pulse transients within the 3D rat mitral cell morphological reconstructions. To enable the concurrent fitting to four separate recordings (depolarising or hyperpolarising current injection into the soma and recorded in the apical dendrite or the other way round as detailed under electrophysiology) two Neuron *point process managers* were used in the simulation to mimic the input conditions at the soma and the nearest point to the distance between pipettes that the *point process manager* would allow (Table 4.3). Insufficient pipette properties where measured for the pipettes in the experimental work to be able to model the electrodes. Recording was simply carried out by sampling the membrane voltage at the location of the *point process manager* and current injection was handled by the *point process manager* without giving the pipettes any compartments of their own. The passive parameters generated from the fits, like the experimental recordings, produce simulations for current injection into the soma and recorded in the apical dendrite that can be superimposed on a recording made in the soma from similar injections in same location in the apical dendrite. Under passive conditions these recordings superimpose, a phenomenon known as reciprocity. A further confirmation of passivity is linear scaling. To test this, simulations were carried out with current injections of 0.5 and 1.0 nA to determine whether the 0.5 nA current response superimposes on that in response to the 1.0 nA injection.

No allowance has been made to add increased surface area to the morphology to compensate for the surface area of spines as there is no evidence for the presence of spines in mitral cells (Price and Powell, 1970b; Nagata, 1989).

Electrotonic Dimensions

Neuromorphic renderings of electrotonic transformations were produced using Neuron's Impedance Shape tool that allows a functional contribution of impedance at a range of frequencies to be assessed (http://www.neuron.yale.edu/course/zclass/zclass.htm, Carnevale et al. 1995, 1997). These are images of the neuron morphology in which the length of individual fibres are scaled by natural log of attenuation (Carnevale et al., 1995). The greater the attenuation the longer the fibre becomes. Two versions are available V_{in} and V_{out}: the V_{in} version shows the attenuation from all points on the rest of the cell into the selected point and conversely V_{out} shows the attenuation out from the selected point to all other points on the cell.

	Cell 1	Cell 2	Cell 3	Cell 4	Cell 5	Cell 6
Inter electrode distance (μm)	116	125	100	133	206	137
Sections	53	117	131	49	71	37
Segments	839	2417	1740	1072	2018	1161
Total surface area (μm^2)	12703	15499	13823	10493	25427	14754
Tuft surface area (μm^2)	1934	2858	4898	1560	888	1145
Soma surface area (μm^2)	1309	799	887	749	2331	1019

Table 4.1: Morphological dimensions of the six olfactory bulb mitral cells used in the study.

Results

	Cell 1	Cell 2	Cell 3	Cell 4	Cell 5	Cell 6	Mean
R_i (Ω cm)	323	153	83	169	249	62	173 ± 99
C_m (μF cm^{-2})	2.03	1.93	1.77	1.97	1.60	2.16	1.91 ± 0.2
R_m (Ω cm^2)	1276	4100	2301	3915	6867	2823	3547 ± 1934

Table 4.2: Mitral cell passive parameters fitted to reconstructed cell morphology and dual current clamp pulse recordings.

Six mitral cells were selected for parameter fitting based on the quality of electrophysiological recordings and the proximity of resting potential to -60 mV. Detailed reconstructions using Neurolucida were made for the six cells (The range of morphological dimensions is summarised in Table 4.1). Direct fitting to dual current clamp pulse recordings (Figure 4.1A) of passive parameters (intracellular restivity (R_i), specific membrane capacitance (C_m) and the specific membrane resistance (R_m)) were made using the PRAXIS fitting algorithm in Neuron (see Methods). The parameter values were always determined by fitting to experimental recordings using digital reconstructions from the same cell.

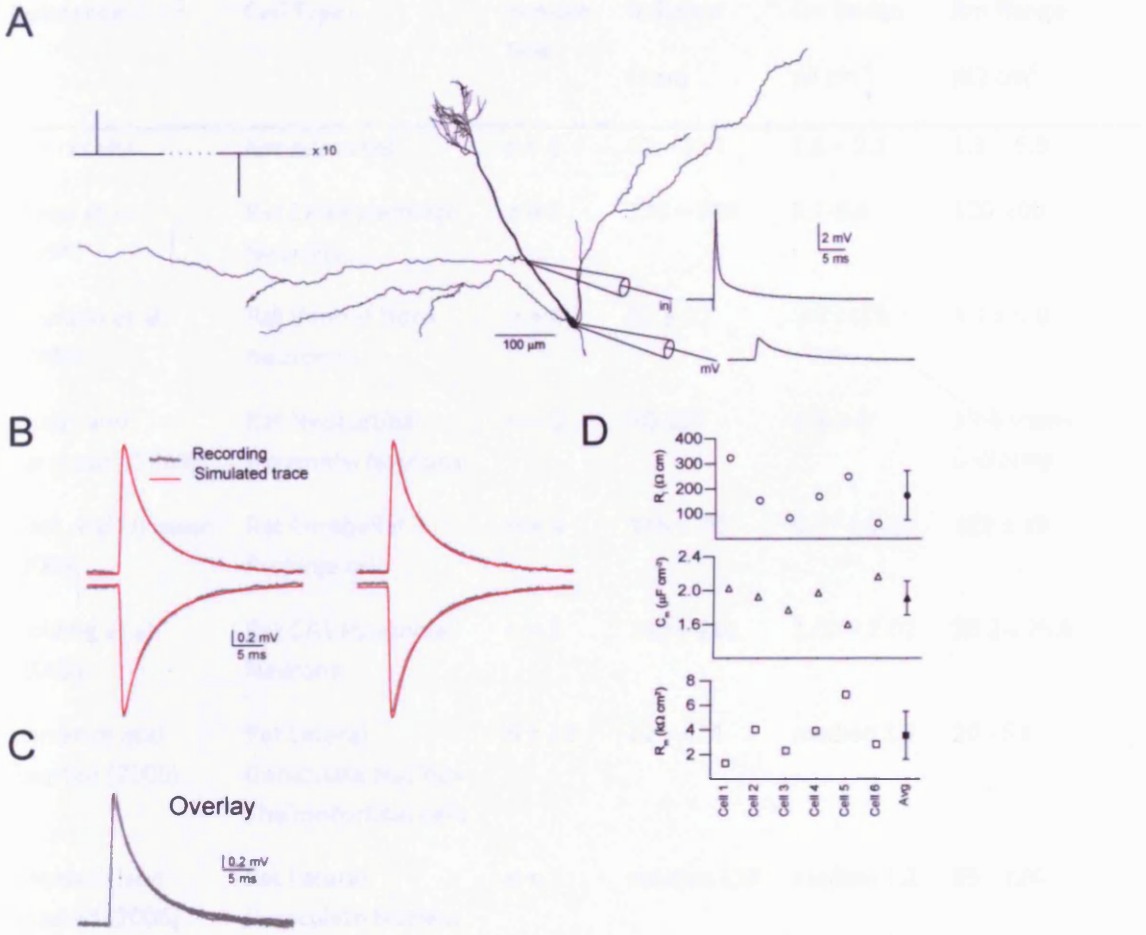

Figure 4.1 Direct fitting of passive parameters for rat olfactory bulb mitral cells using short current clamp injections and Neurolucida reconstructions in a dual recording site protocol. (A) Shows one of the mitral cells with the positions of the patch-clamp electrodes and experimental recordings. (B) Shows experimental recordings (black trace) from distal apical dendrite (right) and soma (left) recording sites for depolarising (top) and hyperpolarising (bottom) current injections at the electrode at the alternate end of the electrode compared to the simulation for the best fit passive parameters (red trace). Superimposed are the fitted curves produced with the best fit parameters found by the PRAXIS algorithm using the Neuron simulator, showing that the model gives a good fit to the experimental recordings. (C) Shows all four experimental recordings in B) superimposed as a test of reciprocity to show that the blocking conditions used had resulted in the cell exhibiting passive behaviour. (D) The fitted passive parameters R_i, C_m, and R_m for each of the 6 cells are all of the same order of magnitude (Figure courtesy of Kamilla Angelo).

Prior to the recordings synaptic and ionic activity were blocked by adding specific blocker to the bath solution (see Methods). Also, whether the cells expressed the hyperpolarisation-activated cation current (Ih) was tested by injecting hyperpolarising steady state pulses (1 sec) to 20-25 mV below the resting potential. None of the six cells chosen for parameter fitting exihibited the rebound sag characteristic of the I_h current. Under these conditions the membrane acted in a highly linear and reciprocal manner, where the transfer voltage responses of the dendrite and the soma from current injection in either location and at different amplitudes showed almost perfect superimosition when scaled by 1/current (Figure 4.1C), implying that the membrane was passive. Accurate fits to the voltage responses were achieved (Figure 4.1B) giving passive parameter values for all six cells which were of the same order of magnitude (Figure 4.1D, Table 4.2). In comparison with published figures for other brain regions C_m is high and R_m is low (Table 4.3). The fitting of passive parameters to steady state recordings with current injections of 50 ms gave values in the same range (R_i 98-251 Ω, C_m 1.9-2.6 µF cm^{-2}, R_m 1.4-7.9 kΩ cm^2).

Reference	Cell Type	Sample Size	Ri Range Ω cm	Cm Range μF cm^{-2}	Rm Range KΩ cm^2
Our results	Rat mitral cell	n = 6	62 – 323	1.6 – 2.1	1.3 – 6.9
Major et al. (1994)	Rat CA3 Pyramidal Neurons	n = 4	170 – 340	0.7-0.8	120-200
Thurbon et al. (1998)	Rat Ventral Horn Neurones	n = 4	87 ± 22	2.4 ± 0.5	5.3 ± 0.9
Stuart and Spruston (1998)	Rat Neocortical Pyramidal Neurons	n = 3	70-100	1.1-1.5	35-5 (non-uniform)
Roth and Häusser (2001)	Rat Cerebellar Purkinje cells	n = 4	115 ± 20	0.77 ± 0.17	122 ± 18
Golding et al. (2005)	Rat CA1 Pyramidal Neurons	n = 3	139 – 261	1.02 – 2.02	10.2-125.6
Perreault and Raastad (2006)	Rat Lateral Geniculate Nucleus Thalmocortical cells	n = 15	22 – 424	median 1.2	20 - 53
Perreault and Raastad (2006)	Rat Lateral Geniculate Nucleus Interneurons	n = 3	median 113	median 1.2	83 - 124

Table 4.3: Comparison of published passive parameters produced using direct fitting protocols in several different regions of the brain.

To estimate the confidence limits imposed on the results by various sources of error I carried out a detailed assessment of potential sources that will be presented over the next few paragraphs. In the discussion section some further sources of error will be covered that I felt had been successfully dealt with by other authors.

Algorithm and Individual Cell Reconstructions

To be sure that the PRAXIS fitting algorithm, combined with our cell reconstructions, are capable of consistent and accurate fitting, even at extreme parameter combinations, I used a series of target parameters to produce simulations using the individual mitral cell reconstructions. In these simulations I mimicked the experimental conditions by using injected current pulses for depolarising and hyperpolarising current injections of 0.45 nA at the apical dendrite while recording at the soma or visa-versa. The groups of simulated recordings were then used to test the PRAXIS passive parameter fitting and the resulting fits were compared with the target figures. All six reconstructions produced perfect fits (typical error values for least square comparisons between target curve and simulation were 2.5×10^{-9}) to the curves and a precise match of the target parameters, showing that there is no error stemming directly from the algorithm or artefacts induced by the use of the cell

reconstructions. This was true for target parameter values chosen to cover R_m and C_m values found in the other studies.

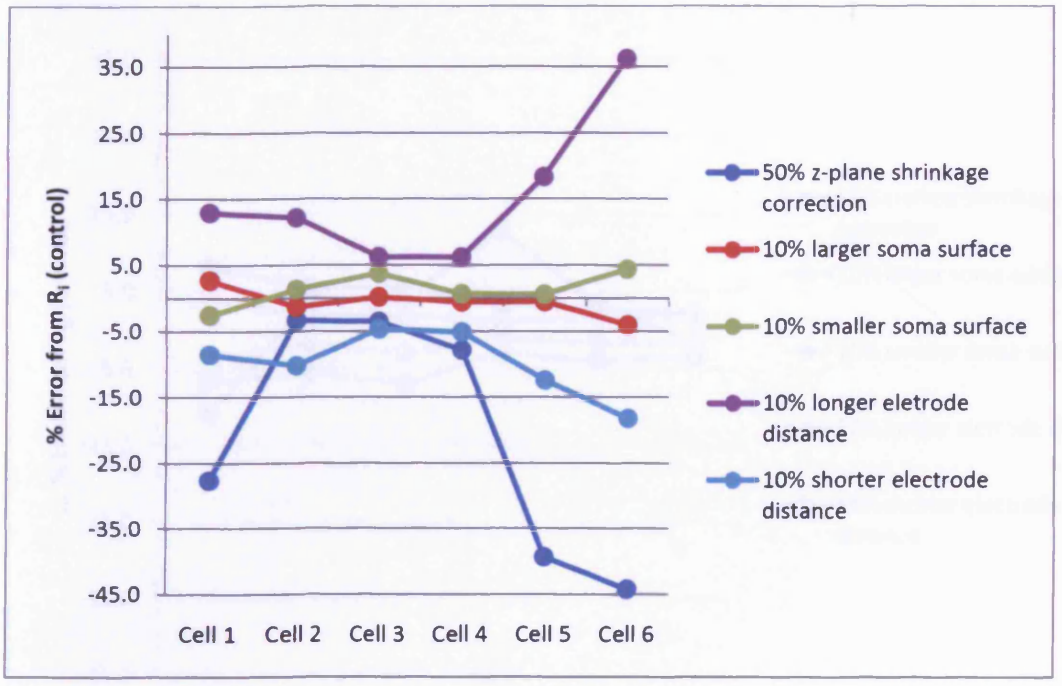

Figure 4.2: Percentage error was calculated for R_i for comparisons between the control R_i for the standard conditions for fitting the passive parameters and modified conditions as follows: (a) a doubling of z-plane dimensions to simulate a 50% shrinkage correction (dark blue line). (b) 10% larger soma surface area (red line). (c) 10% smaller soma surface area (green line). (d) 10% greater inter electrode distance (purple line). (e) 10% smaller inter electrode distance (light blue line).

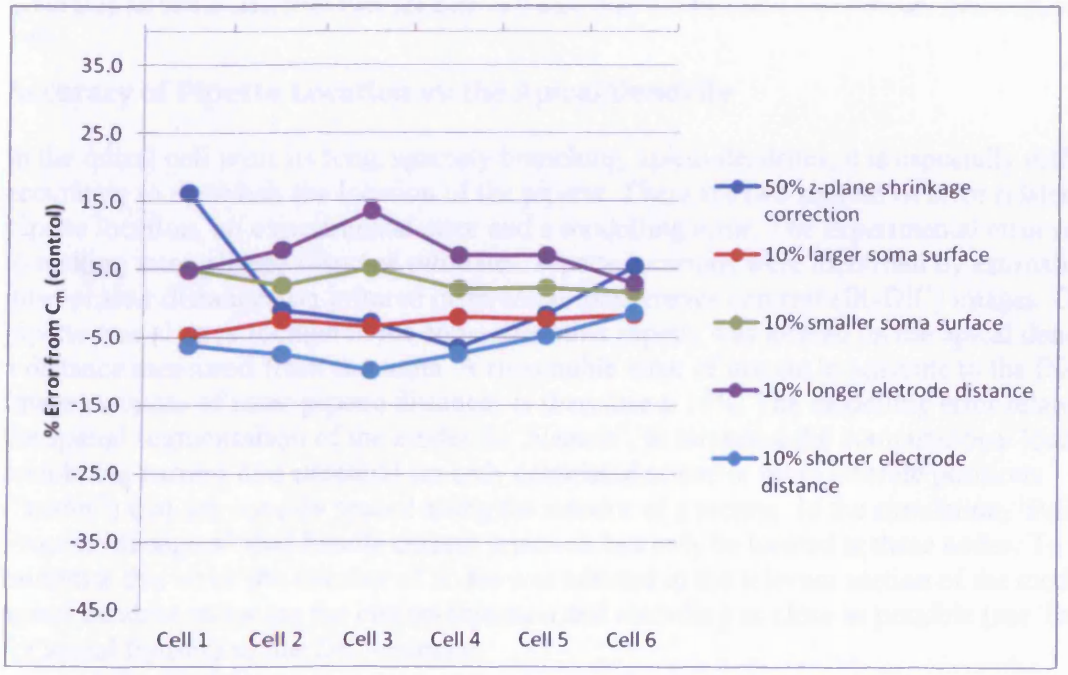

Figure 4.3: Percentage error was calculated for C_m for comparisons between the control C_m for the standard conditions for fitting the passive parameters and modified conditions as follows: (a) a doubling of z-plane dimensions to simulate a 50% shrinkage correction (dark blue line). (b) 10% larger soma surface area (red line). (c) 10% smaller soma surface area

(green line). (d) 10% greater inter electrode distance (purple line). (e) 10% smaller inter electrode distance (light blue line).

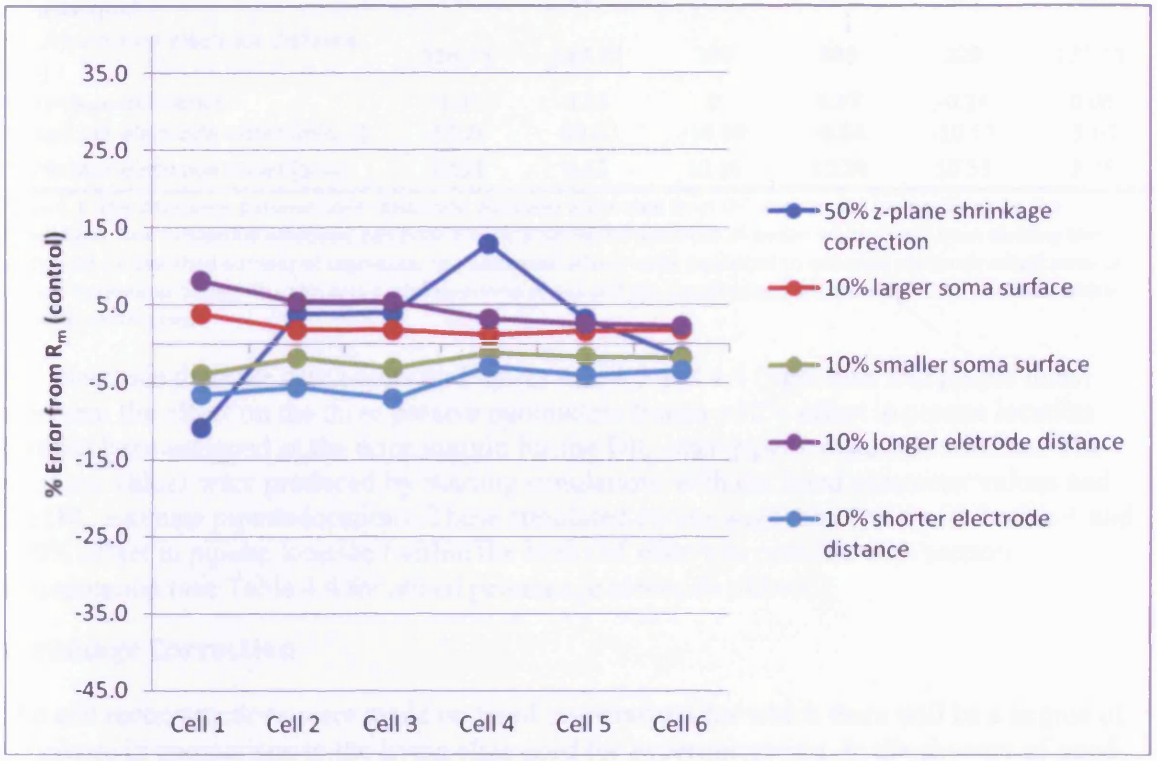

Figure 4.4: Percentage error was calculated for R_m for comparisons between the control R_m for the standard conditions for fitting the passive parameters and modified conditions as follows: (a) a doubling of z-plane dimensions to simulate a 50% shrinkage correction (dark blue line). (b) 10% larger soma surface area (red line). (c) 10% smaller soma surface area (green line). (d) 10% greater inter electrode distance (purple line). (e) 10% smaller inter electrode distance (light blue line).

Accuracy of Pipette Location on the Apical Dendrite

In the mitral cell with its long, sparsely branching, apical dendrites, it is especially difficult accurately to establish the location of the pipette. There are two sources of error related to the pipette location, an experimental error and a modelling error. The experimental error relates to making inter pipette distance estimates. Pipette locations were identified by estimating inter-pipette distances on infrared differential interference contrast (IR-DIC) images. One pipette was always located in the soma, the other pipette was located on the apical dendrite at a distance measured from the soma. A reasonable error of margin to attribute to the DIC image estimate of inter-pipette distances is therefore ± 10%. The modelling error relates to the spatial segmentation of the model. In 'Neuron', to minimise the computational load, the membrane current and potential are only calculated at one or more discrete positions ("nodes") that are equally spaced along the interior of a section. In the simulation, 'Point Process Managers' that handle current injection can only be located at these nodes. To minimise this error the number of nodes was adusted in the relevant section of the model's apical dendrite to locate the current injection and recording as close as possible (see Table 4.3 for actual figures) to the DIC estimate.

	Cell 1	Cell 2	Cell 3	Cell 4	Cell 5	Cell 6
Experimental inter electrode distance (μm)	116	125	100	133	206	137
Simulation inter electrode distance (μm)	114.43	128.89	100	139	205	137.11
Percentage difference	-1.35	3.11	0	4.97	-0.24	0.08
Percentage electrode offset (minus)	-10.26	-10.63	-10.36	-9.88	-10.53	-9.69
Percentage electrode offset (plus)	10.53	9.65	10.36	10.28	10.53	9.75

Table 4.4: The difference between inter-electrode distances estimated from DIC images and the positions on the simulations. The simulation electrode positions are dictated by the positions of nodes which result from dividing the section into a specified number of segments. The electrode offsets were produced to estimate electrode offset error in passive parameter fitting. The aim was a 10% electrode offset and the actual values are what could be achieved within the node restrictions.

The electrode distance data points on Figures 4.2, 4.3 and 4.4 (light blue and purple lines) represent the effect on the three passive parameters from a ±10% offset in pipette location that has been assigned as the error margin for the DIC inter-pipette distance estimates. The error bar values were produced by running simulations with the fitted parameter values and the DIC estimate pipette locations. These simulated curves were then fitted with both a + and - 10% offset in pipette location (within the limits of what was possible with section segmentation (see Table 4.4 for actual percentage electrode offsets)).

Shrinkage Correction

The cell reconstructions were made on fixed preparations for which there will be a degree of shrinkage in comparison to the living slice used for experimentation. In the absence of good estimates of the degree of shrinkage produced by the fixation methodology used, I looked at the effect of 50% shrinkage. A doubling of the z-plane values in the reconstruction was used to simulate the 50% shrinkage (shrinkage correction data points dark blue line on Figures 4.2, 4.3, 4.4). It is unlikely that shrinkage was as severe as this but a large figure gives us a chance to observe the impact of shrinkage with a high safety margin. Please note, that during electrical recordings the maintainace of the slice under a platinum grid brings about a preferential shrinkage in the z-plane.

The noticeably larger errors are found to affect R_i, for cells 1, 5 and 6. There do not appear to be obvious differences between the morphology of cells 1, 5, and 6 and cells 2, 3, and 4 that would explain the first group having larger R_i for shrinkage correction. Table 4.5 shows some morphological measurements; the inter electrode distance, apical dendrite diameters at the proximal end and at the electrode positions seem to be the measurements most likely to affect fitting errors.

	Cell 1	Cell 2	Cell 3	Cell 4	Cell 5	Cell 6
Experimental inter electrode distance (μm)	116	125	100	133	206	137
Total Surface Area (μm^2)	12703.11	15499.31	13823.46	10493.86	25427.41	14753.79
Tuft Surface Area (μm^2)	1933.67	2857.93	4897.56	1559.59	888.34	1145.05
Soma Surface Area (μm^2)	1309.98	798.93	886.97	748.84	2331.426	1019
Diameter of Proximal end of apical dendrite (μm)	2.995	3.215	2.475	1.81	2.55	1.81
Diameter at apical dendrite electrode (μm)	1.44	1.295	1.11	1.07	1.295	1.295

Table 4.5: Morphological measurements of the reconstructed mitral cells used in the parameter fitting simulations.

It is also difficult to spot any differences in the experimental recording used for fitting (Figure 4.5) that might explain the observed increased magnitude of Ri error for Cells 1, 5 and 6 with shrinkage correction. Cell 5 exhibits a slower depolarisation time course than the

other recordings. But this is not the case for cells 1 and 6. It can therefore only be concluded that for Ri fitting with shrinkage correction there is a complex relationship that will increase the observed error for a subset of cells.

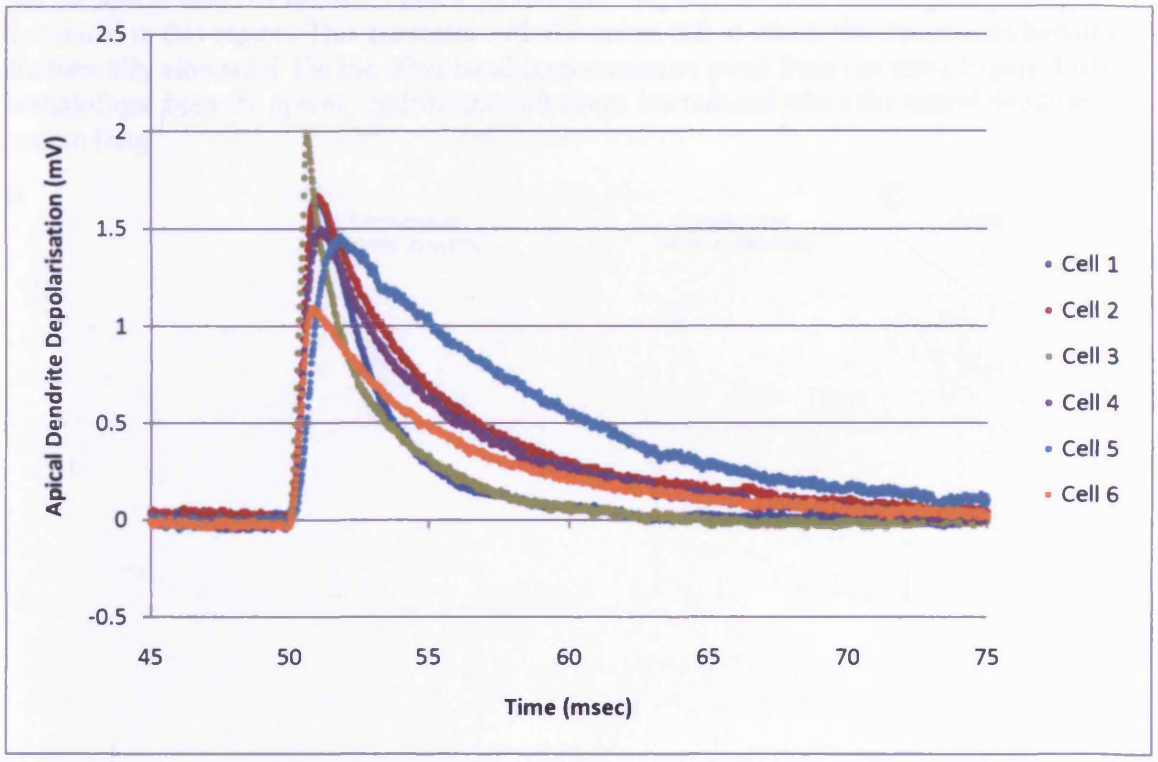

Figure 4.5: Experimental recordings in the soma from depolarising current injections into the distal apical dendrite. This is one of the four conditions that is used for fitting the passive parameters.

Soma Surface Area

Reconstruction of the soma in Neurolucida is restricted to putting a 2D outline round a single (shifting) plane of focus. When this outline is imported into Neuron using the Import3d tool, a series of diameters perpendicular to an axis are used to create a 3D interpretation of the 2D outline. This approach produces a soma comprising about 20 segments that the simulator can handle, but cannot be claimed to be an accurate estimation of the soma surface area. To assess the importance of soma surface area in fitting accuracy, I increased and decreased all the diameters in segments forming the soma polygon by 10% and performed fits with the new dimensions (soma surface area data points are the red and green lines on Figure 4.2, 4.3, 4.4).

The error plots in Figure 4.2 show that the the intracellular resisitivity (left chart) is the passive parameter which, out of the three, was most sensitive to experimental and simulation inaccuracies. Logically the R_i values in particular are very prone to be influenced by changes in the interelectrode distance error and shrinkage correction.

Electrotonic Dimensions of the Mitral Cell

Once the passive parameters of a cell have been established the relative dimensions of cell in terms of space constants (λ) can be calculated. To compensate for the deviation of the morphology from infinite cylinders and allow the cell to be visualised in terms of flow of charge I have used Neuron's Impedance Shape tool (see Methods).

The Neuromorphic renderings of the electronic transformations can be compared with the unmodified reconstructions in Figure 4.6A. For attenuation towards the soma, Figure 4.6B Somatopetal the axon and lateral dendrites are relatively unmodified by the transformations. But the apical dendrite becomes much shorter showing that the flow of charge is greatly facilitated in this region. This contrasts with the apical tuft in which the dimensions become dramatically elongated. On the other hand for attenuation away from the soma Figure 4.6B Somatofugal both the apical dendrite and tuft fibres are reduced while the lateral dendrites remain long.

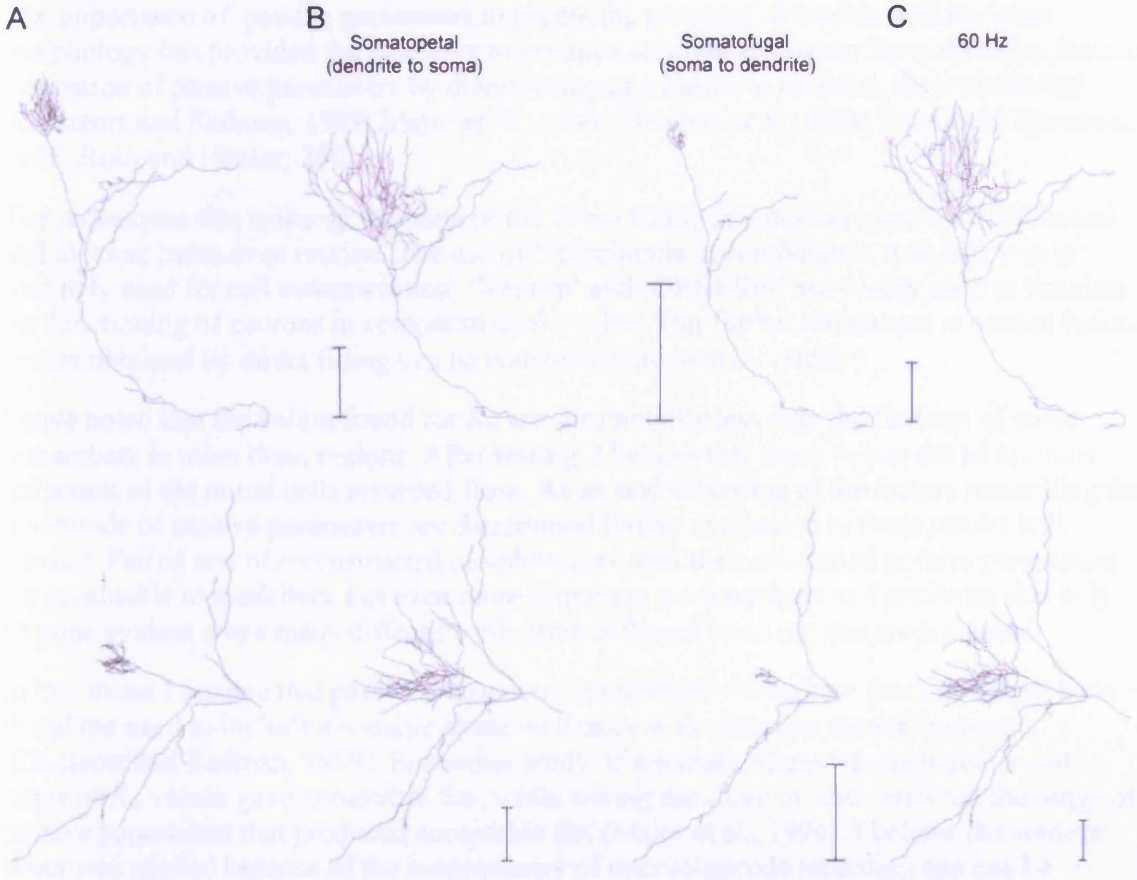

Figure 4.6 A: Actual dimensions of reconstructions of two of the rat olfactory mitral cells used in the study. B: Neuromorphic renderings of attenuation for the same two olfactory bulb mitral cells produced using Neuron's Impedance Shape tool (see Methods). The effect of attenuation towards the soma (somatopetal) and away from the soma (somatofugal) are shown for a constant voltage input. The calibration bars represents attenuation of one $\log_e$ unit decay in voltage. Somatopetal attenuation has little effect on the dimensions of the axon and lateral dendrites, but attenuation is low in the apical trunk so its length is reduced. The attenuation in the apical tuft is high so its dimensions become elongated. For the somatofugal direction the attenuations are quite different, attenuation is low into the apical tuft so it becomes reduced like the apical trunk while the lateral dendrites show little effect remaining long. C: Neuromorphic renderings of the same two mitral cells for attenuation towards from the soma for a voltage input at 60 Hz. The calibration bars represent attenuation of one $\log_e$ unit decay in voltage.

The use of impedance measurements for attenuation calculation in Neuron's Impedance Shape tool, allows attenuation assessments to be made at a range of different frequencies. Input to the mitral cells apical dendrite tufts, from sensory afferents outside the OB and feedback mechanisms within the OB, are known to occur at a wide range of frequencies (e.g. Schoppa and Westbrook, 2001; Friedman and Strowbridge, 2003). I therefore compared attenuation across theta, alpha and gamma frequencies in the range 0-100 Hz without any noticeable differences (compare Figure 4.6B at 0 Hz to Fig. 4.6C at 60 Hz).

Discussion

Detailed models of neurons require reconstructions of cell morphology in combination with accurate estimates of the passive parameters. The electrotonic dimensions of the cell are a product of the passive parameters. Without a good estimate of these parameters the interactions between the active conductances that allow neurons to process input data in a controlled manner can only be guessed at. Detailed morphological reconstructions are rendered meaningless without the associated passive parameters.

The importance of passive parameters in producing meaningful models with accurate morphology has provided the incentive to produce accurate estimates. Several studies feature estimation of passive parameters by direct fitting as a means to establish their credibility (Clements and Redman, 1989; Major et al., 1994; Thurbon et al., 1998; Stuart and Spruston, 1998; Roth and Häuser, 2001).

The techniques that make up the parts of the direct fitting process have become established and in some cases even routine. The use of Neurolucida in combination with biocytin is routinely used for cell reconstruction. 'Neuron' and 'GENESIS' are widely used to simulate the functioning of neurons in compartmental models. But further refinement is needed before results obtained by direct fitting can be considered universally credible.

I have noted that the values found for R_m are substantially less than the findings of some researchers in other brain regions. After testing, I believe that these values are an accurate reflection of the mitral cells recorded from. As an understanding of the factors controlling the magnitude of passive parameters are determined further evaluation of these results will emerge. Paired sets of reconstructed morphologies with their associated passive parameters are invaluable to modellers, but even more important are the patterns of attributes that only become evident when many different cells from different brain regions are compared.

In this thesis I assume that passive parameters are uniform throughout the cell. Others have found the need to include a somatic shunt resistance to fit recorded current transients (Clements and Redman, 1989). In another study, if a somatic shunt was included, a wide range of R_m values gave acceptable fits, while setting the shunt to zero restricted the range of passive parameters that produced acceptable fits (Major et al., 1994). I believe the somatic shunt was needed because of the inadequacies of microelectrode recording and can be discarded when using patch clamp recording (Roth and Häuser, 2001).

Next, the problem of non-uniqueness in which a range of possible combinations of parameters give equally good fits was considered (Roth and Häuser, 2001). This was examined with the two recording pipette protocol (Stuart and Spruston, 1998; Roth and Häuser, 2001) by producing simulated recordings for target parameters and checking how accurately the algorithm coped with the fitting. This produced a perfect fit for all cell reconstructions, which suggests that it would not be unreasonable to assume a high degree of confidence in the direct fitting algorithm. Multiple starting points were used when fitting experimental recordings to avoid the risk of identifying local minima in the optimisation process.

However, there are still sources of error in other parts of the protocol that need accounting for. Fixation shrinkage, pipette location as measured by inter-pipette distance and soma morphology are spatial accuracy problems that result from difficulty in precise measurement. It is possible to improve on the scalar accuracy of the model by for example increasing "nseg" (number of nodes in a section). However until we have the ability to improve the

accuracy of the experimental estimated measurements this would assume a precision that is not justified. A refinement to the experimental method would be achieved by marking the exact location of the pipette for identification in the reconstruction process. Also, if the conversion of the Neurolucida reconstruction to a Neuron compatible morphology file could place the identified pipette locations at positions 0.5 along a section then as long as "nseg" remains an odd number the electrode would always be in precisely the right position. These two amendments would effectively remove electrode location as a source of error. In addition, reconstruction from the unfixed tissue slices would remove the effects of fixation that currently distort the reconstruction.

Extensive discussion of the error resulting from lower frequency recorded noise has been made elsewhere (Major et al., 1994;Thurbon et al., 1998; Roth and Häuser, 2001). For the recordings used to constrain the passive parameters in the MC models for this thesis, noise was filtered above 6 kHz and the cells were pharmacologically isolated to minimise spontaneous synaptic inputs. While Major and colleagues (1994) considered this to be an important source of error, analysis by Thurbon and colleagues (Thurbon et al., 1998) found no significant effect, even when the noise was magnified by a factor of 10, after inserting sampled noise into simulated curves for target parameters. Roth and Häuser (2001) also came to the conclusion that signal noise was not a significant source of error when they carried out balanced resampling of the experimental recordings using a bootstrap method.

Once the passive parameters have been established and incorporated into a passive model, the model can be used to establish the electrotonic dimensions of the mitral cell. Traditionally these dimensions are assessed in terms of electrotonic length but I have chosen to use neuromorphic renderings of electrotonic transformation (see Methods) which allow a more intuitive representation of the electrotonic dimensions. Using Neuron's Impedance Shape tool allows the functional measurement of impedance to correct for deviations from calculated electrotonic length (L) due to non infinite cylinders and branching structures (Zador et al., 1995). The use of impedance also allows an assessment of frequency effects. Comparisons of the electronic transformations with unmodified reconstructions show that the apical dendrite allows for greater ease of current flow than the lateral dendrites and axon. The apical tuft, with its complex branching structure, becomes much more elongated, reducing the synaptic stimulation that it receives. This is likely to increase the required summation of multiple synaptic stimuli needed to provoke spiking in the soma. This is true across the wide range of frequencies for which input is known to activate mitral cells. The lateral dendrites are also seen to remain electrotonically elongated in response to output from the soma in the passive cell. The length of lateral dendrites is a consideration when looking at the ability of back propagating spikes to provoke lateral inhibition.

To summarise, the passive parameters R_i, C_m and R_m for rat olfactory bulb mitral cells have been fitted to dual pipette short pulse current injection recordings using the PRAXIS fitting algorithm in Neuron with detailed morphological reconstructions of the same cells from which the recordings were made. The mean values and standard deviation for the parameters were: $R_i = 173 \pm 99\ \Omega$ cm, $C_m = 1.91 \pm 0.20\ \mu F\ cm^{-2}$ and $R_m = 3547 \pm 1934\ \Omega\ cm^2$. Compared to published figures for cells in other brain regions, the R_m values are very low and C_m values are rather high. Experiments to assess sources of error such as fixation shrinkage, inaccurate estimation of pipette location and estimation of soma surface area from 2D outline of the fixed cell, have proved the parameter values to be both credible and accurate. The model was used to assess the electrotonic dimensions of a mitral cell, which suggested that the apical dendrite allows a greater ease of current flow than the lateral dendrites and axon.

Chapter 5 Strategies and parameters in OB model Development

Now that I have fitted passive models to reconstructions of six MCs, I need to see what active properties can be used from earlier MC models. From a modelling perspective, where comparisons are to be made with published data it increases validity if as many parameters as possible are the same between the models compared. For this purpose it was necessary to investigate the components of other models to see what should be reused to render comparisons as significant as possible. There are two sources that I considered for this purpose, the models of Bhalla and Bower (1993) and Migliore et al. (2005). Some of the ion channels from the Bhalla and Bower (1993) model have already been considered in Chapter 3. In this chapter a more systematic comparison of the active properties of the two models when incorporated in my MC passive model will be undertaken. As mentioned in Chapter 3 in the simulators section, this will require the conversion of the computer code from both models to XML. Bhalla and Bower (1993) is a *Genesis* model while Migliore et al. (2005) is a *Neuron* model. Once the conversion of scripts to XML is completed, components taken from either model can be compared in either simulator (*Genesis* or *Neuron* see Chapter 3) from scripts generated by neuroConstruct (see Chapter 3). However most of my simulations were carried out in *Neuron*.

The ion channel densities for the Bhalla and Bower (1993) model are given in Table 3.1 in Chapter 3 and for Migliore et al. (2005) model in Table 5.1 in this chapter.

Topology		Geometry			Passive				Na channel			K^+ channels		
Section	connect	nseg	L (µm)	Dia (µm)	R_i	C_m	g_pas	e_pas	gbar_na	sh_na	Ena	gbar_ka	gbar_kdr	ek
Tuftden(x20)	priden[1] 1:0	30	300	0.4	150	1.8	8.33×10^{-0512}	-65	0.04	10	50	0.004	0.0001	-90
Priden	soma 1:0	5	300	3.0	150	1.8	8.33×10^{-05}	-65	0.04	10	50	0.004	0.0001	-90
secden[0]	soma 0.5:0	4	100	2.0	150	1.8	8.33×10^{-05}	-65	0.04	10	50	0.004	0.0001	-90
secden[1]	soma 0.5:0	5	100	2.0	150	1.8	8.33×10^{-05}	-65	0.04	10	50	0.004	0.0001	-90
Soma	(root segment)	1	25	20	150	1.8	8.33×10^{-05}	-65	0.04	10	50	0.004	0.0001	-90
Hillock	soma 0:0	3	5	16.15	150	1.8	8.33×10^{-05}	-65	0.4	10	50	0.004	0.0001	-90
Initialseg	hillock 1:0	3	30	1.5	150	1.8	0.001	-65	0.4	0	50	0.04	0.0001	-90

Table 5.1: Channel Distribution for the Migliore model: the model is divided into sections (column 1) which are connected to each other as detailed in column 2. The number of nodes per section (places were calculations are made when the simulation is run and connection or mechanisms can be placed) length of section and diameter of section are detailed in the geometry columns. This is followed by the passive parameters, R_i (Ω.cm), C_m (µF/cm^2), g_pas = $1/R_m = G_{Leak}$ and has units of mho/cm^2, e_pas (mV) is the resting potential at which there is no net current across the membrane resistance. The channel mechanisms included are a fast sodium current (Na); a delayed rectifier potassium current (K); a transient outward potassium current (K_A); gbar units for these mechanisms is S/cm^2, the equilibrium potentials for the ion species is in mV.

[12] This passive conductance is equal to a R_m of 12,000 Ω.cm^2.

		α	β	∞	τ
Na^{13} q10 = 2	m^3	$\frac{0.4(V+30)}{1-e^{\frac{V+30}{7.2}}}$	$\frac{0.124(V+30)}{e^{\frac{V+30}{7.2}}-1}$	$\frac{\alpha}{\alpha+\beta}$	$\frac{1}{\frac{\alpha+\beta}{qt}}$
	h	$\frac{0.03(V+45)}{1-e^{\frac{V+45}{1.5}}}$	$\frac{0.01(V+45)}{e^{\frac{V+45}{1.5}}-1}$	$\frac{1}{1+e^{\frac{V+50-sh_2}{4}}}$	$\frac{1}{\frac{\alpha+\beta}{qt}}$
K_{dr}^{14} q10 = 2	n	$e^{0.055(V+50)}$	$e^{0.5\times0.055(V+50)}$	$\frac{1}{1+e^{\frac{V-21}{10}}}$	$\frac{\beta}{qt\times0.0035(1+\alpha)}$
K_A^{15} q10 = 3	m	$e^{0.1(V+45)}$	$e^{0.75\times0.1(V+45)}$	$\frac{1}{1+e^{\frac{V-9.9-7.6}{14}}}$	$\frac{\beta}{qt\times0.04(1+\alpha)}$
	h	$e^{0.2(V+70)}$	$e^{0.99\times0.2(V+70)}$	$\frac{1}{1+e^{\frac{V-5.7+47.4}{6}}}$	$\frac{\beta}{qt\times0.018(1+\alpha)}$

Table 5.2: Migliore model conductance equations: Columns give the equations for the rate constants α(V) and β(V), the steady state value ∞(V), and the time constant τ(V). The second column gives the gating variables and powers for the channel mechanisms in the first column. The time constant in this model is subject to a temperature adjustment (q10).

The kinetics for the Na, K_{dr} and K_A channels in the Bhalla and Bower, and Migliore models are given in Tables 3.2 and 5.2. When the XML versions of these equations were set up, the ChannelML (this is the http://www.neuroml.org/ standard XML description for channel mechanisms that are used in neuroConstruct, see simulators above) standard did not allow the use of tables of values. Modelling channel mechanisms using look up tables rather than equations is likely to be supported by ChannelML in the future as it supported by both *Neuron* and *Genesis*. Using equations fitted to the experimental values has been the usual way to model channel mechanisms since Hodgkin and Huxley's model. The look up table method is used for the delayed rectifier potassium channels in the Bhalla and Bower model. It is therefore easier to construct the model for this research using the Migliore implementation of the potassium channels. This choice also makes sense because the equations K_{dr} and K_A channels for the Migliore model are based on experimental measurements made in MCs (Wang et al. 1996). In the case of the sodium channels it is possible to make a direct comparison between the examples in the Bhalla and Bower model and the example in the Migliore model (Figure 5.1). The main difference is in the extent of the recovery after the AP. The sodium channel reaches an equilibrium after a partial recovery from the AP at which the effect of a partial activated Na channel is in opposition to the leak conductance (in neuroConstruct the value of R_m is set as a leak resistance which has a set reversal potential (usually -65 mV), this will be covered in more detail later in the chapter). The membrane potential for this equilibrium for the Bhalla and Bower Na channel is 0 mV while for the Migliore Na channel it is about -18 mV. For these reasons I used the channel kinetics from the Migliore model as the basis for the Na, K_{dr} and K_A channels in my model.

[13] Migliore et al. 1999.

[14] Wang et al. 1996.

[15] Wang et al. 1996.

In a second set of simulations I used a reconstructed rat mitral cell from which the passive parameters had been determined from fits to experimental recordings (see Chapter 4, cell 2). The model was setup in neuroConstruct using XML versions of the Migliore model Na, K_{dr} and K_A channels at the densities given in Table 3.2.

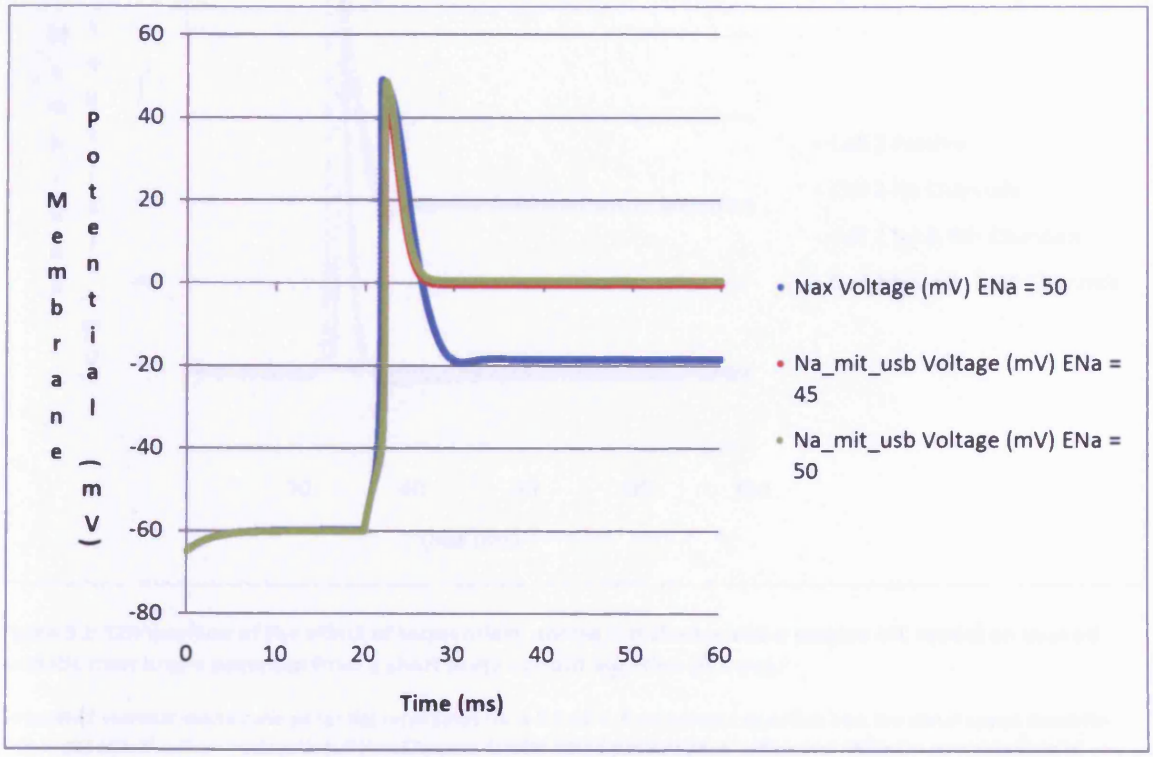

Figure 5.1: Comparison of differences in MC somatic membrane potential responses evoked by a short pulse current injections (0.5 ms) when the only active property present is either the Bhalla and Bower (1993) sodium channel or the Migliore et al. (2005) sodium channel.

Simulated somatic membrane potential recordings for a 0.1 nA 0.5 ms current injection into the distal apical dendrite tuft of rat mitral cell reconstruction 2 (see Chapter 4) with fitted passive parameters and different combinations of conductances from the Migliore model. Comparison between Bhalla and Bower Sodium channel (Na_mit_usb) and Migliore sodium channel (Nax).

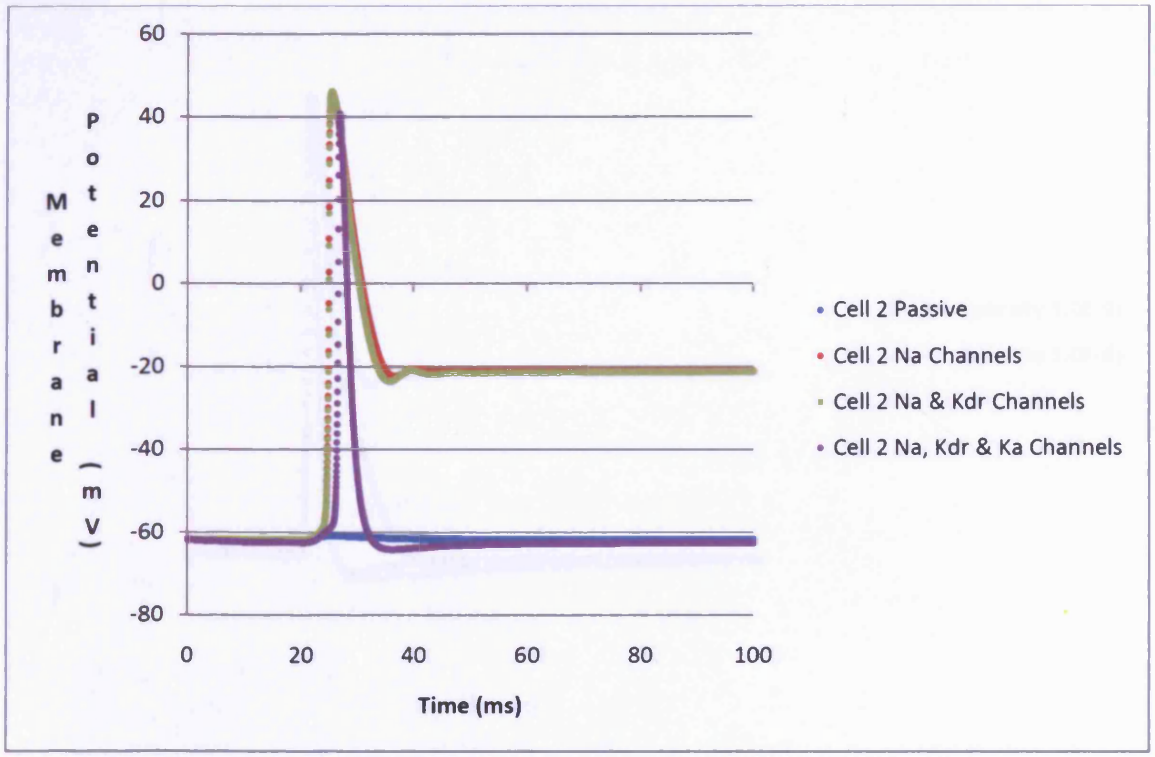

Figure 5.2: Comparison of the effect of sequentially adding ion channels to a passive MC model on evoked somatic membrane potential from a short pulse current injection (0.5 ms).

Simulated somatic membrane potential recordings for a 0.1 nA 0.5 ms current injection into the distal apical dendrite tuft of rat mitral cell reconstruction 2 (see Chapter 4) with fitted passive parameters and different combinations of conductances from the Migliore model.

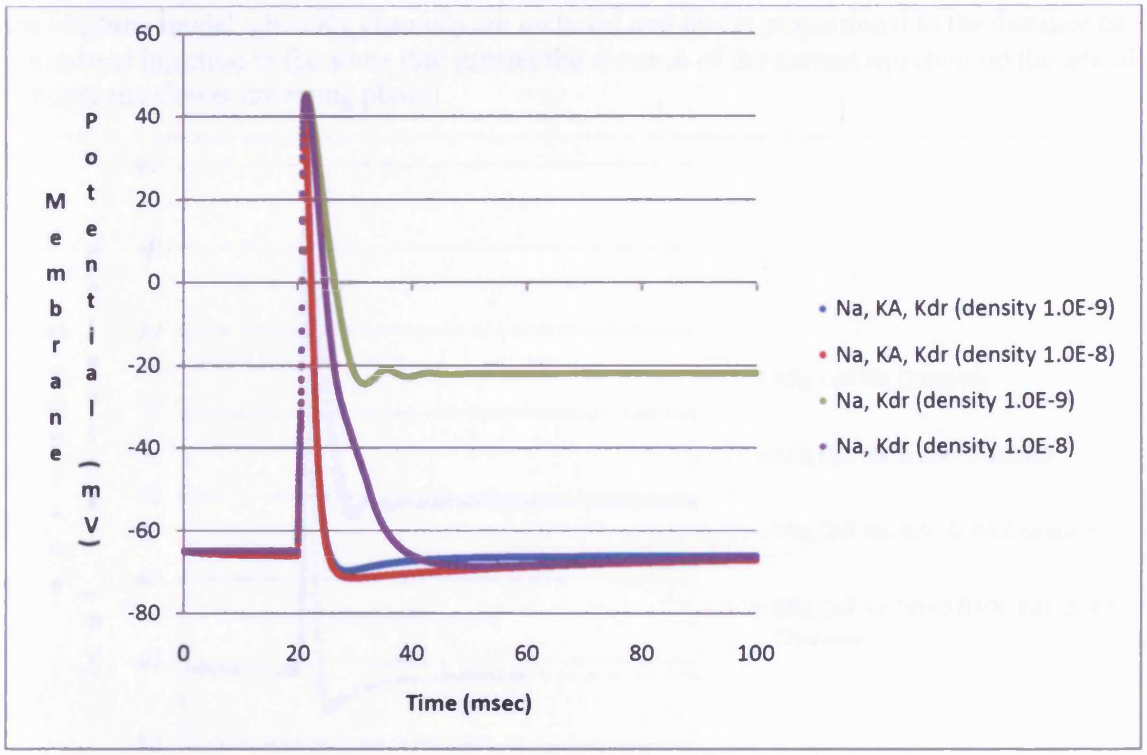

Figure 5.3: Increasing the density of K_{dr} channels has a large effect on the recovery of the membrane potential after the depolarisation of an AP until K_A channels are also present.

Simulated somatic membrane potential recordings for a 3.0 nA 0.5 ms current injection into the soma of rat mitral cell reconstruction 2 (see Chapter 4) with fitted passive parameters and different combinations of conductances from the Migliore model to test the effect of K_{dr} channel density.

Figure 5.2 shows that the K_A channel mechanism is needed for a full recovery of the MC to resting potential after an action potential. However adding the K_A channel also slows time course of the rising phase of the AP. This slowing of the AP rising phase by the K_A channel was not evident when the original Migliore morphology was used (Figure 5.4).

The addition of the K_{dr} channel is seen to have little effect on the recovery of the membrane potential at the density used in Migliore et al. (2005) in Figure 5.2. However increasing the density by one order of magnitude from 1.0×10^{-9} µS µm^{-2} to 1.0×10^{-8} µS µm^{-2} produces a slow recovery to the resting potential (purple trace, Figure 5.3). However, this increase in K_{dr} density is largely masked by the presence of the K_A channels (compare blue and red traces, Figure 5.3).

Investigating this slowing of the time course a bit further to make sure that it is both a function of morphology and the K_A channel, the location of the current injection was moved (Figure 5.5). When the current injection moves out of the small fibres of the apical dendrite tuft 0.1 nA is sub-threshold for action potential initiation. But the slowness of AP rising phase time course is clearly proportional to increased distance from the soma.

In summary, in view of the above it was decided to proceed with the Migliore model Na, K_{dr} and K_A channels with our reconstructed morphology and fitted passive parameters. With this setup a 0.1 nA current injection into apical tuft is sufficient to produce an action potential in the soma, but in the larger apical dendrite a larger current injection is need for AP initiation. With the reconstructed morphology the AP has a slower time course in the rising phase than

the Migliore model when K_A channels are included and this is proportional to the distance of the current injection to the soma (the greater the distance of the current injection up the apical dendrite the slower the rising phase).

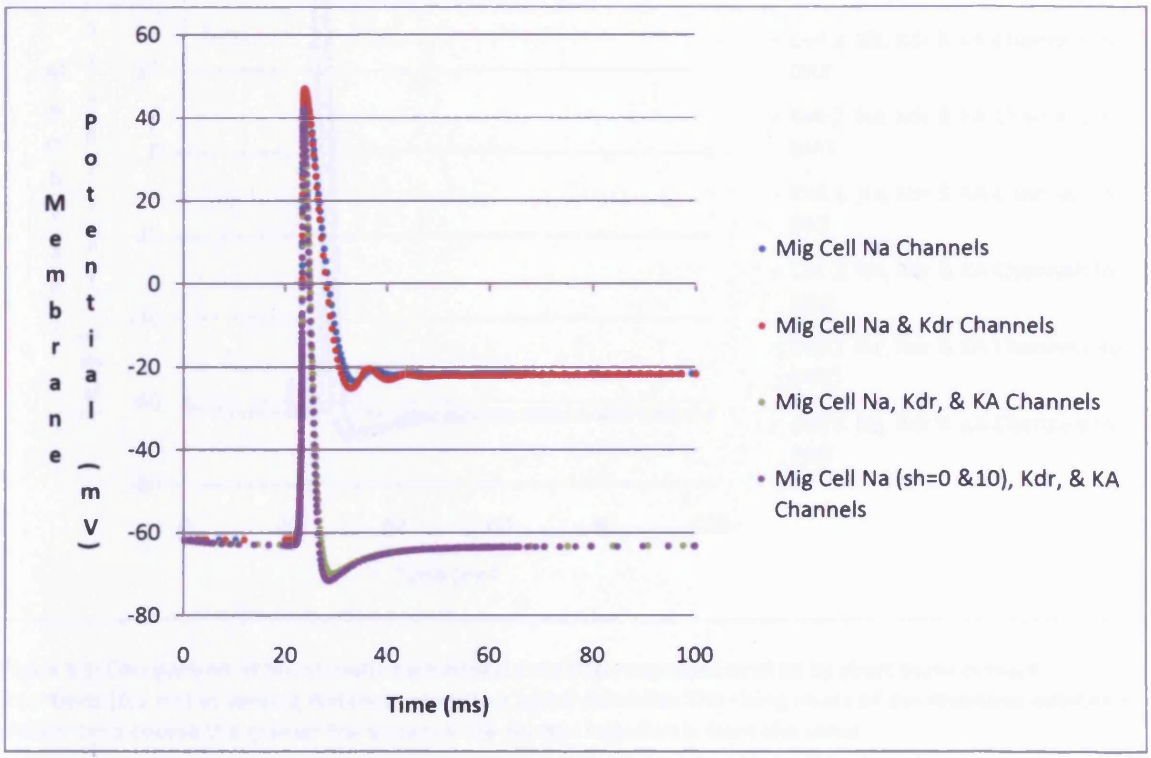

Figure 5.4: The comparison of sequentially adding ion channel types on mitral cell somatic membrane potential evoked responses as shown in Figure 5.2 with the reconstructed MC morphology changed to the simpler Migliore et al. (2005) morphology. Note that the slowing of the rising phase of the AP produced by the K_A channel in Figure 5.2 is no longer observed here.

Simulated somatic membrane potential recordings for a 0.1 nA 0.5 ms current injection into the distal apical dendrite tuft of Migliore model simple morphology with fitted passive parameters for cell 2 (see Chapter 4) and different combinations of conductances from the Migliore model.

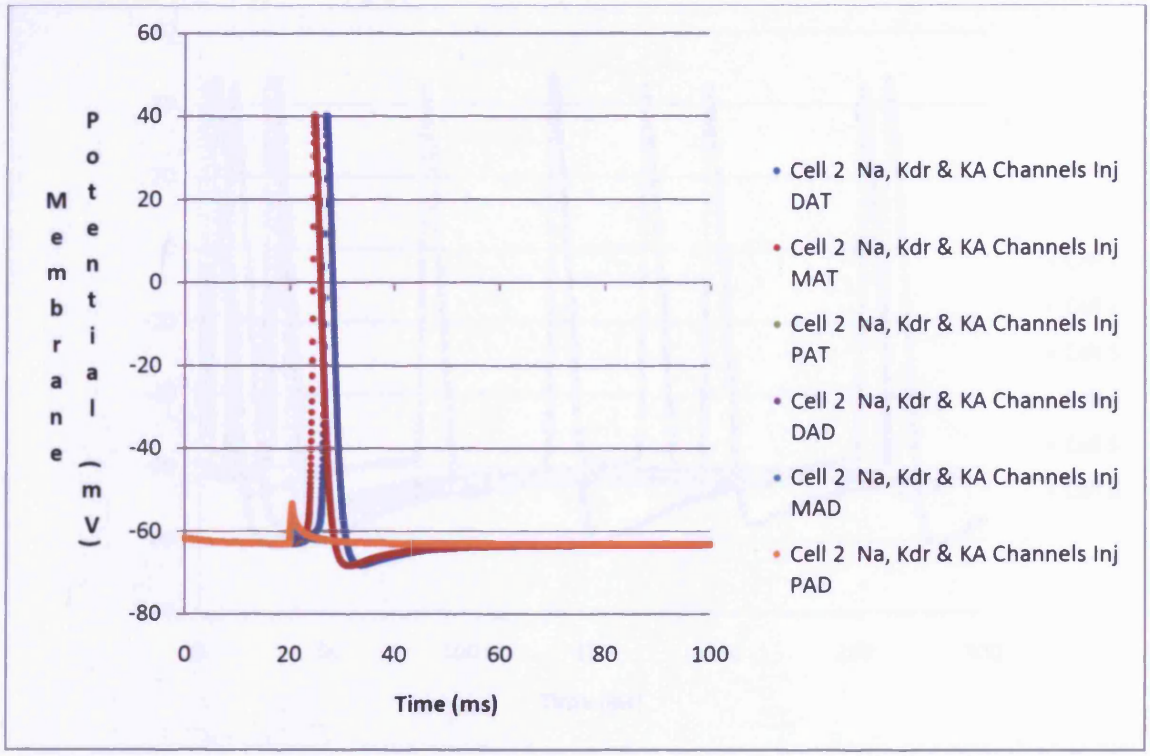

Figure 5.5: Comparison of MC somatic membrane potential responses evoked by short pulse current injections (0.5 ms) at varying distances along the apical dendrite. The rising phase of the response exhibits a slower time course the greater the distance the current injection is from the soma.

Somatic membrane potential recordings for a 0.1 nA 0.5 ms current injection into various locations in rat mitral cell reconstruction 2 (see Chapter 4) with fitted passive parameters and different combinations of conductances from the Migliore model. Distal Apical Dendrite Tuft (DAT); Medial Apical Dendrite Tuft (MAT); Proximal Apical Dendrite Tuft (PAT); Distal Apical Dendrite (DAD); Medial Apical Dendrite (MAD); Proximal Apical Dendrite (PAD).

Simulation Initiation Potential and Leak Reversal Potential

Having decided to proceed with the Migliore model Na, K_{dr} and K_A channels with the reconstructed morphology and fitted passive parameters the next step is to look at variation across six MC reconstructions. Initially all the cells with the simulation initiation potential and leak reversal potential were set to the experimental mean resting potentials for the fitting recordings (see Chapter 4 for derivation of the mean resting potential, and this Chapter, Figure 5.6 for results). Some of the cells fire spontaneously as they are continuously above the firing threshold potential.

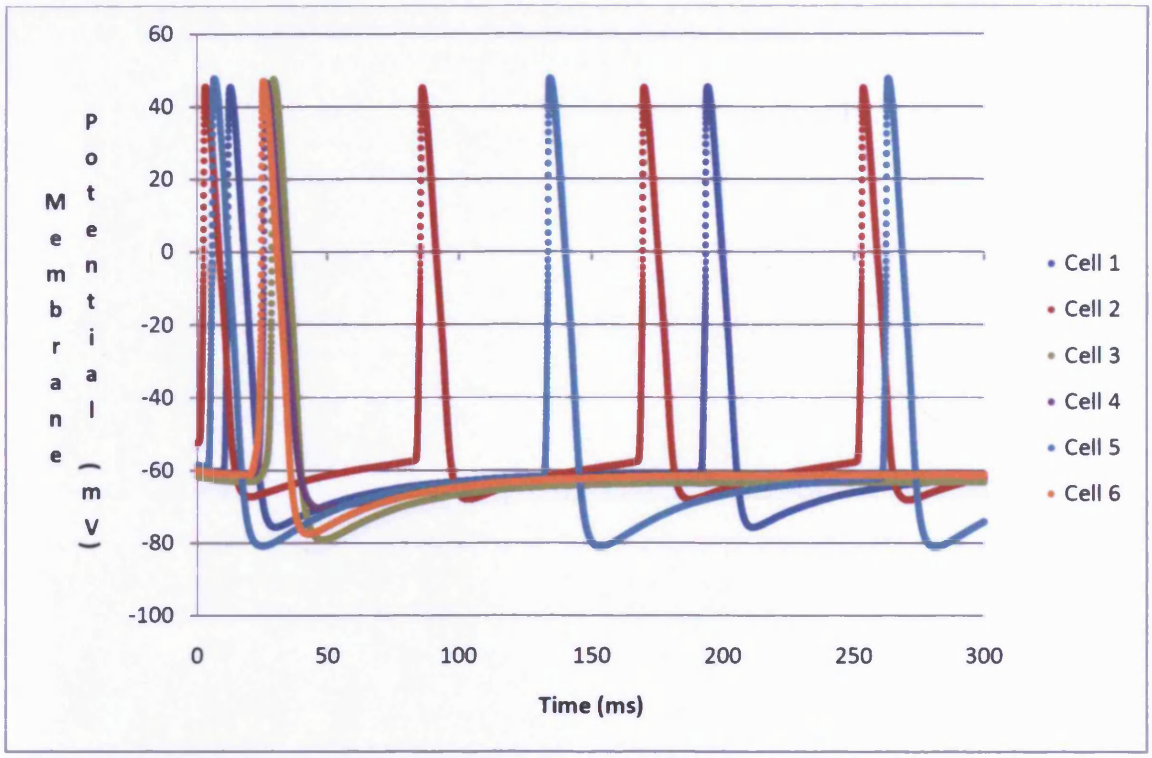

Figure 5.6: MCs with leak reversal potentials set higher than firing threshold fire repetitively.

6 different MCs all with simulation initiation potential and the reversal potential for the leak potential set to the mean experimental values for the respective cells (Cell 1 -52.57 mV; Cell2 -61.73 mV; Cell 3 -59.63 mV; Cell 4 -60.11 mV; Cell 5 -58.55 mV; Cell 6 -60.01 mV). A 0.5 millisecond 1.0 nA current clamp pulse was applied at the distal tuft of each cell after a delay of 20 ms (current initiated at T = 20 ms coincident with the rising phase of the action potential for Cell 6 which is the orange trace). The firing is clearly spontaneous and repetitive in 3 of the cells rather than being provoked by the current clamp pulse.

If instead the simulation initiation potentials and leak reversal potentials of all 6 cells are set to -65 mV, APs are only initiated by current injection (Figure 5.7). The relationship between the set potential of an MC and spontaneous firing is illustrated further when the setting is changed over 5 mV intervals (Figure 5.8).

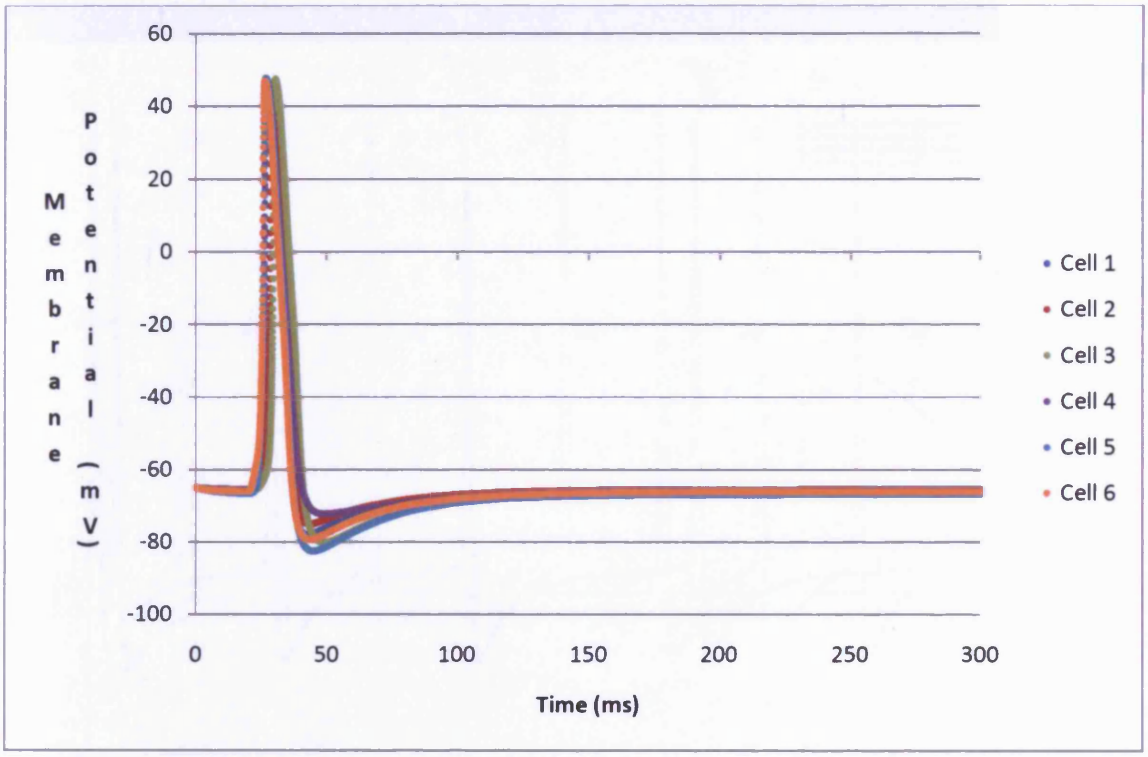

Figure 5.7: MCs with the leak reversal potential set to -65 mV fire once in response to a single short pulse current injection (0.5 ms).

6 different MCs all with simulation initiation potential and the reversal potential for the leak potential set to -65 mV. A 0.5 millisecond 1.0 nA current clamp pulse was applied at the distal tuft after a delay of 20 msec. The firing is now only initiated by current clamp pulses.

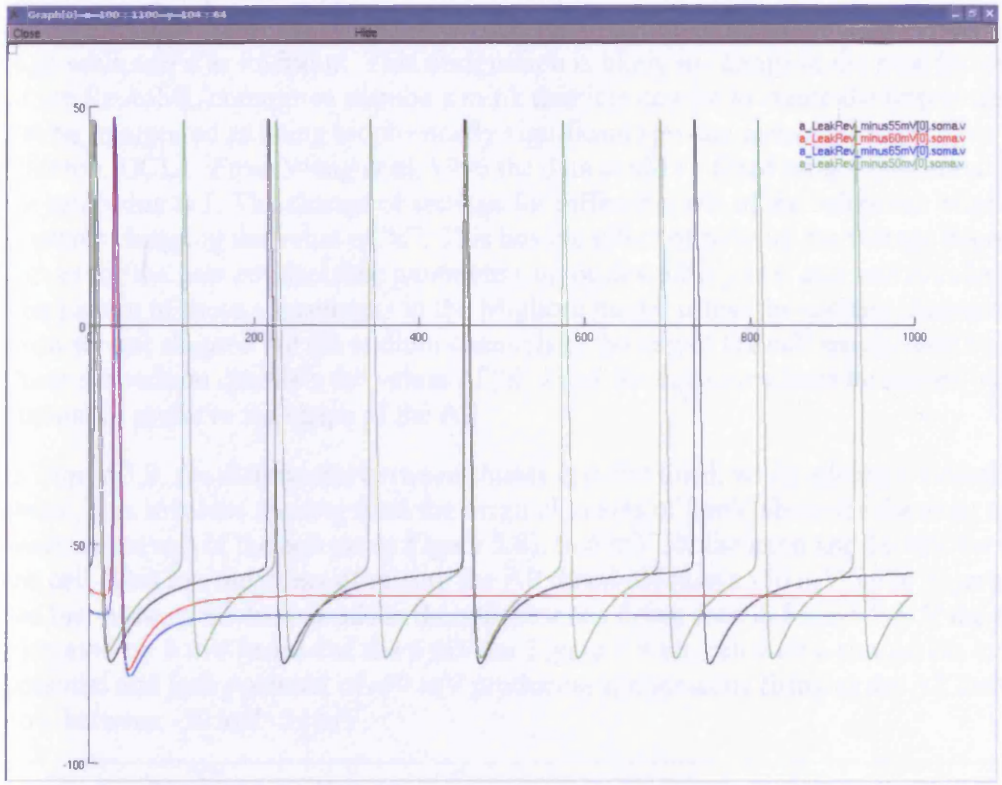

Figure 5.8: Increasing the leak reversal potentials of a MC increases AP frequency.

Both the reversal potential of the leak current and initiation potential of the simulation were varied at 5 mV intervals from -65 mV to -50 mV in a simulation of a rat olfactory bulb mitral cell to produce input evoked action potential at -65 (blue trace) and -60 mV (red trace) which is replaced by spontaneous tonic firing at -55 mV (black trace) of almost 5 Hz this rises to 9 Hz at - 50 mV (green trace). The simulation has Na, K_{dr} and K_A channel mechanisms converted from Migliore et al (2005). Input is a current clamp pulse into the distal apical tuft of 1.0 nA for 0.5 ms after a 20 ms delay (x-axis Time (ms), y-axis somatic membrane potential (mV)).

Migliore Sodium Channel Shunt

The implementation of the sodium channel for the MC model in Migliore et al. (2005) uses two different settings of the equations for different parts of the cell. This setup gives the back propagation properties of APs that has been described in Shen et al. (1999) and Chen et al. (1997). In the XML conversion of this channel which is needed to work within neuroConstruct (for original equations see Table 5.2 above), the equations for m (α and β) and h (α and β) are of the linoid[16] form:

$$\frac{A * (K * (v - d))}{1 - exp^{(-(K*(v-d)))}}$$

The equation for h inf (the steady state variable) is of the similar sigmoid form which still has the variables A = rate (ms^{-1}), K = slope (mV^{-1}) and d = half maximal activation (or inactivation, mV). These equations result from curve fitting to experimental recordings (Migliore et al. 2005, Wang et al. 1996) it is therefore prudent to be careful about assuming

[16] Linoid is a term that was used by the NeuronML standards committee to describe a linear exponential equation. It has recently been changed to exp_linear and describes equations that are exponential for values of V much below the midpoint (d) and linear for values of V much greater than d. This is a private communication from Padraig Gleeson, UCL who is a member of the NeuronML standards committee.

any biophysical significance. However the latest NeuroML standard has referred to A as rate, K as scale and d as midpoint. This designation is likely to change in the near future as some of the NeuroML committee members think that it is unwise to create the impression that they can be interpreted as being biophysically significant (private communication from Padraig Gleeson, UCL). From Wang et al. 1996 the data could be fitted monoexponential hence A the rate value is 1. The change of settings for different parts of the cell in the Migliore model involves changing the value of "d". This has the effect of moving the voltage dependence curves for the gate conductance parameters up or down the y mV axis and is called a shunt. The pattern of these adjustments in the Migliore model is that the sodium channels in the axon are not shunted but the sodium channels in the rest of the cell are shunted by 10 mV. To shunt the sodium channels the values of "d" in all the equations must be moved by the same amount to preserve the shape of the AP.

In Figure 5.9, the differential between shunts is maintained, while adding a further 6 mV shunt. This involves moving from the original values of 0 mV shunt for the axon and 10 mV shunt in the rest of the cell (as in Figure 5.8), to 6 mV for the axon and 16 mV for the rest of the cell. This has the effect of raising the AP threshold above -50 mV, so in Figure 5.9 we can see that none of the cells produce the spontaneous firing seen in Figure 5.8. If the shunts are increased by 5 mV instead of the 6 mV for Figure 5.9 the cell with a simulation initiation potential and leak potential of -50 mV producing spontaneous firing as the AP threshold is now between -50 and -55 mV.

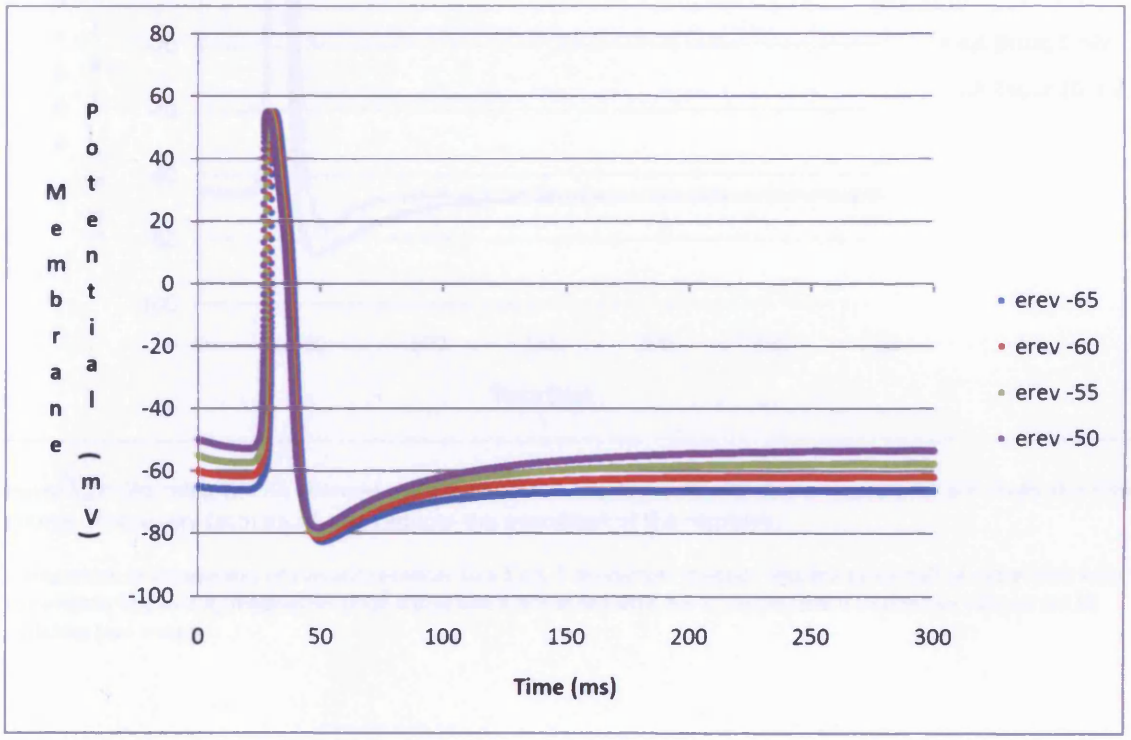

Figure 5.9: Increasing the shunt (increasing the midpoint d for the kinetic equation see text above) on MC sodium channels increases firing threshold.

Varying the reversal potential of the leak current and initiation potential at 5 mV intervals from -65 mV (blue trace) to -50 mV (purple trace) in a simulation of a rat olfactory bulb mitral cell. The simulation has Na, K_{dr} and K_A channel mechanisms converted from Migliore et al (2005). Input is a current clamp pulse into the distal apical tuft of 1.0 nA for 0.5 ms after a 20 ms delay. The sodium channel has a 6 mV shunt for the axon, and a 16 mV shunt for the rest of the cell giving an AP threshold above -50 mV. Compare with Figure 5.8 where axon shunt is zero and rest of the cell has a 10 mV shunt.

Shunting the K_A Channel Mechanism

To get an understanding of how the K_A mechanism gate variables influence AP form in the Migliore model I carried out some shunting (the term shunt is explained in the previous section on sodium channel shunt) of this channel mechanism. K_A, mα, mβ, hα and hβ are all exponentials of the form A*exp(k*(v-d)) where A is 1 so the variables are limited to k and d (see Table 5.2 for original equations). Shunting "d" in the equations for all the gate variables by 20 mV will raise the curves for gate activation and gate inactivation by 20 mV. This slows the recovery time course from the depolarisation produced by the sodium channel and reduces the overshoot below the resting membrane potential (Figure 5.20). Increasing the shunt to 50 mV increase spike height, further slows recovery after AP depolarisation and prevents recovery overshoot (Figure 5.11).

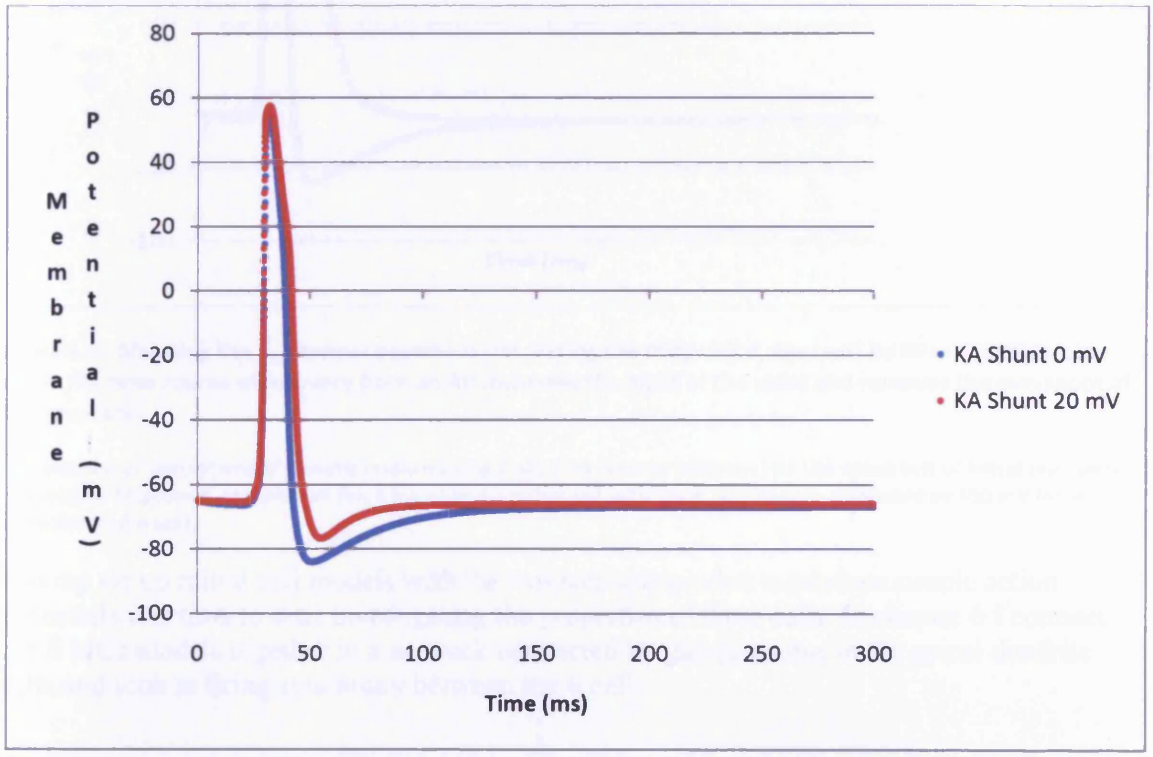

Figure 5.10: Shunting the KA channel equations (increasing the midpoint d, see text) by 20 mV slows the time course of recovery from an AP and reduces the overshoot of the recovery.

comparison of simulations of somatic response to a 1 nA, 5 ms current injection into the apical tuft of mitral cells with the original Migliore K_A mechanism (blue trace) and a mitral cell with the K_A mechanism d shunted by +20 mV for all variables (red trace).

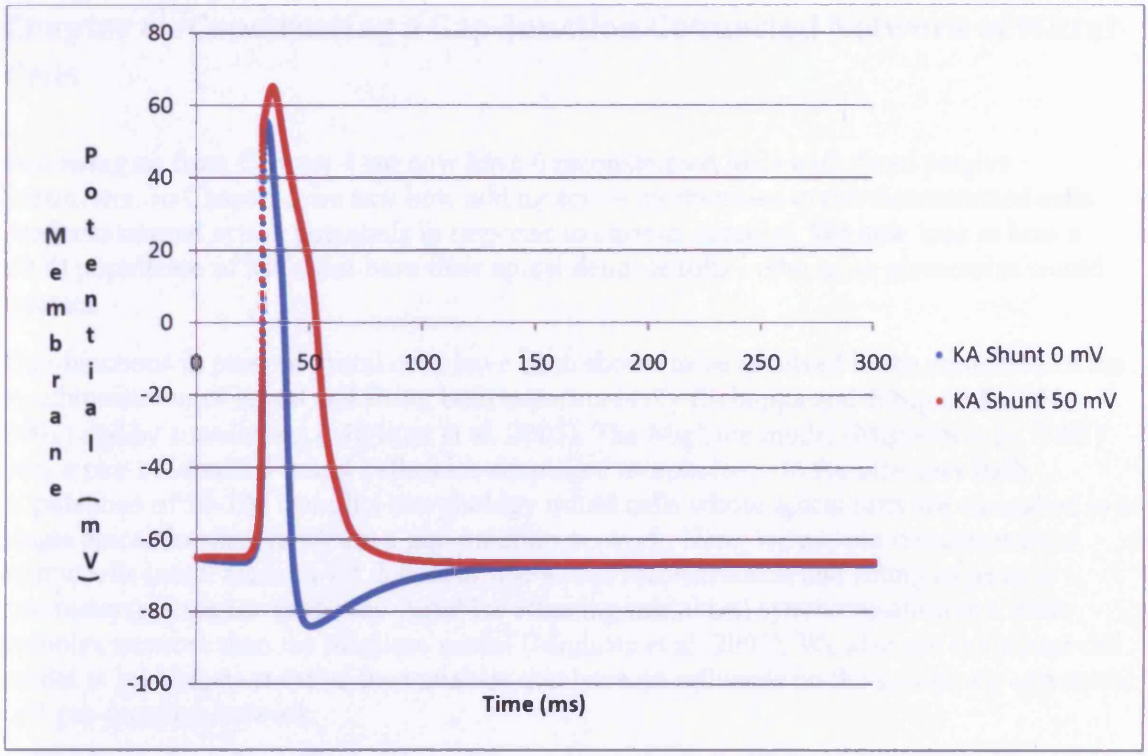

Figure 5.11: Shunting the K_A channel equations (increasing the midpoint d, see text) by 50 mV considerably slows the time course of recovery from an AP increases the hight of the spike and removes the overshoot of the recovery.

comparison of simulations of somatic response to a 1 nA, 5 ms current injection into the apical tuft of mitral cells with the original Migliore K_A mechanism (blue trace) and a mitral cell with the K_A mechanism d shunted by +50 mV for all variables (red trace).

Having set up mitral cell models with the mechanisms needed to produce simple action potentials it is time to start investigating the properties of these cells. In chapter 6 I connect the 6 MCs models together in a network connected by gap-junctions in the apical dendrite tufts and look at firing synchrony between the 6 cells.

Chapter 6 : Constructing a Gap-Junction Connected Network of Mitral Cells

Following on from Chapter 4 we now have 6 reconstructed MCs with fitted passive parameters. In Chapter 5 we saw how adding active mechanisms to the reconstructed cells produces normal action potentials in response to current injection. We now look at how a small population of MCs that have their apical dendrite tufts in the same glomerulus would interact.

Gap-junctions in pairs of mitral cells have been shown to be involved in the mediation of the synchronisation of mitral cell firing both experimentally (Schoppa and Westbrook 2001, 2002) and by simulations (Migliore et al. 2005). The Migliore model (Migliore et al. 2005) uses a pair of identical mitral cells with simplified morphology. In the olfactory bulb, populations of 50-100 complex morphology mitral cells whose apical tufts are enmeshed in a single apical dendrite tuft form a gap-junction network. Here, we use our 6 reconstructed mitral cells (see Chapter 4 for details of mitral cell reconstruction and fitting of passive parameters) to start to probe the variables effecting mitral cell synchronisation in a more complex network than the Migliore model (Migliore et al. 2005). We also use our mitral cell model to investigate some of the variables that have an influence on the synchrony of a mitral cell gap-junction network.

Active Properties

The Migliore model (Migliore et al. 2005) Na, K_{dr} and K_A *Neuron* channel mechanism scripts were converted to XML versions (ChannelML). This is to enable the use of combinations of mechanisms from Genesis channel scripts particularly those from the Bhalla and Bower (1993) model as the model develops. It is possible using neuroConstruct to produce code in either the Neuron or Genesis script languages (http://www.neuroml.org/). To validate these conversions, as being true copies that impart the exactly the same properties as the originals, direct comparisons of the original Neuron and Genesis versions of the mechanisms and *xml* versions were made in neuroConstruct comparing voltage response and internal variables in a single segment cell (Gleeson et al. 2007). Chapter 5 gives details of testing that was carried out on these cell mechanisms with the reconstructed cells to make sure the model performs as expected with the modifications that have been made to the Migliore model.

Network Connections and Firing Synchronisation Test

Network connections were created using gap-junctions between mitral cell apical tufts. The morphologically reconstructed cells are from different animals and therefore the apical dendrites are not orientated in the same way, as would be the case if they had all come from the same glomerulus in the same animal. However using neuroConstruct to spatially re-position the mitral cells it was possible to partially enmesh the apical tufts (Figure 6.1).

The gap-junctions (parameters from Migliore et al., 2005) were incorporated into the apical tuft segments with 100 network connections established between pairs of mitral cells using a networking facility built into neuroConstruct. Immunocytochemistry studies of OB glomeruli have succeeded in detecting gap-junctions between MC intraglomerular dendrites in mice (Kosaka and Kosaka 2004, Christie et al. 2005, Rash et al. 2005) but as yet these studies are limited qualitative studies. For this reason I experimented with 1, 10 and 100 gap-junctions. With the lower numbers of gap-junctions using coupling ratios of around 0.04 did not

produce synchronisation of firing, so I settled on the higher figure of 100 gap-junctions. The efficient synchronisation with 100 gap-junctions is likely due to the conductance being distributed evenly across the apical dendrite tuft so it will be in closer proximity to the input. The distribution across the apical dendrite tufts with 100 gap-junctions per pair giving a total of 1600 gap-junctions in a 6 cell network (Figure 6.2) can be seen in Figure 6.3. Gap-junction conductance was adjusted to give coupling ratios measured experimentally between 0.01 and 0.08 (Schoppa and Westbrook 2002). To measure coupling ratio a -0.3 nA hyperpolarising current injection with a 50 ms delay and 150 ms duration was injected into the soma of the pre-mitral cell and the somatic voltage displacement for the pre- and post-gap-junction mitral cells were compared.

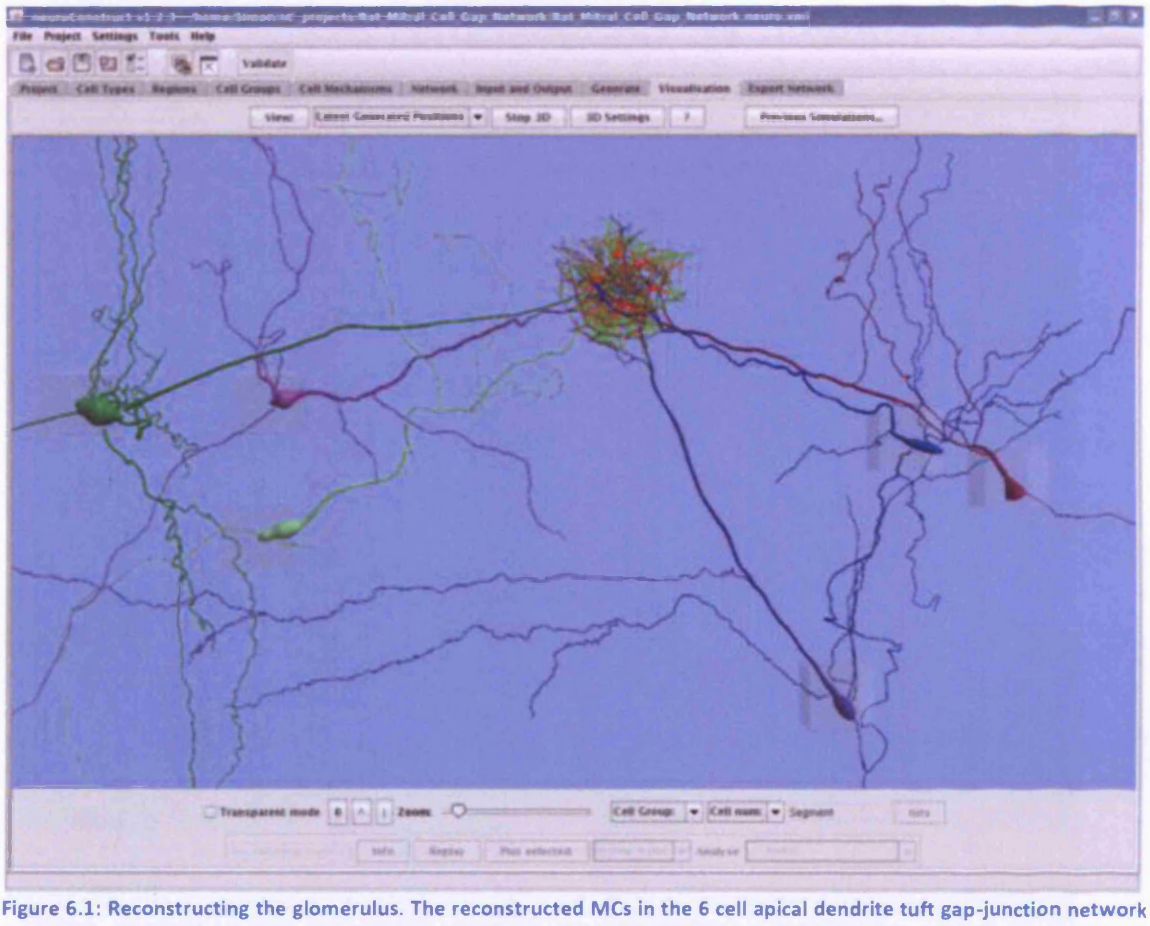

Figure 6.1: Reconstructing the glomerulus. The reconstructed MCs in the 6 cell apical dendrite tuft gap-junction network model come from different animals so to enmesh the apical dendrite tufts the apical dendrites end up in many different orientations when they would naturally be almost parallel.

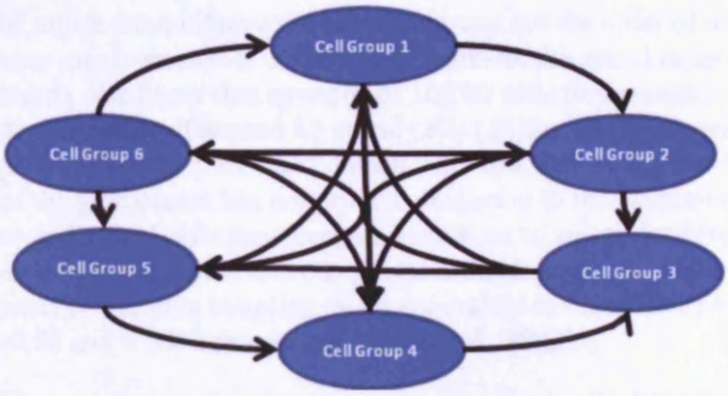

Figure 6.2: Connection pattern for the 6 mitral cell network, all cells are linked to all other cells by 100 gap-junctions on the apical tufts (16 sets of 100).

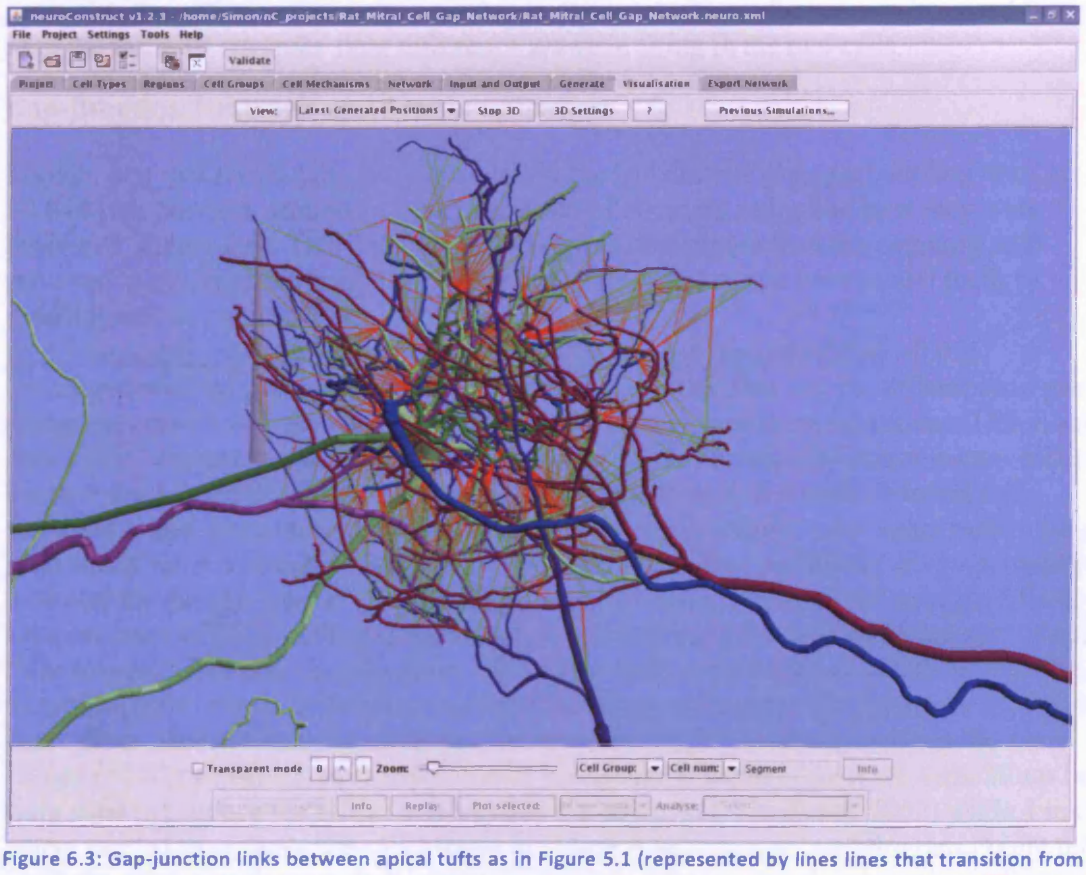

Figure 6.3: Gap-junction links between apical tufts as in Figure 5.1 (represented by lines lines that transition from red at one end of the connection to green at the other end of the connection). Because the cells are from different animals, they do not interlock in the same way as a normal glomerulus. This means that the connections are not intimate but are remote by up to 50 µm. However since in the simulation they are electrical connections, there is no spatial separation between the connections, so they will behave like normal gap-junctions.

Testing for the synchronisation of firing between mitral cells by gap-junctions was carried out using the Migliore protocol (Migliore et al., 2005). Current injections were made at 20 randomly placed locations in the apical tufts of two connected mitral cells. These continuous depolarising current injections were just above threshold and produced tonic firing in the mitral cells. Using 20 locations for current injection allows lower current to be applied to the individual locations so the limit of individual gap-junctions' current transmission does not limit the total transmission between the cells. This mimics to a small degree the large number

of inputs from olfactory receptor neurons but the order of magnitude of individual inputs is very much greater. It is difficult to estimate the actual order of magnitude of number of inputs. We know that upwards of 10,000 olfactory receptor neurons converge on the apical dendrite tufts of around 80 mitral cells (Alison and Warwick 1949). However the densely packed and complex (see Chapter 2 for discussion of juxta- and intra-glomerular cells) nature of the glomerulus has not proved conducive to the estimation of the number of synapses from an individual olfactory receptor neuron on to apical dendrite tufts of mitral cells. But with 20 inputs the current is low enough on individual inputs to allow sufficient flow across the gap-junctions to give coupling ratios equivalent to those found by experimental measurement (0.01 and 0.08; Schoppa and Westbrook, 2002).

The current injection is applied to both mitral cells, but the start of the current injection was delayed by 10 ms (time delay comes from the Migliore et al. (2005) protocol) for one of the mitral cells. If the mitral cells were not connected, or only weakly connected, by gap-junctions, this offset in the start of current injection would produce desynchronised firing, with the same 10 ms spike time difference between firing in the two cells.

Gap-Junction Network and Synchronisation

Initially just two mitral cells were included in the simulations giving a coupling ratio of ~0.044 (see previous section for an explanation of coupling ratios and how they were measured; Figure 6.4). This coupling ratio is somewhat higher than the coupling ratio achieved in the Migliore model (Migliore et al., 2005; measured from model forfig6-modeldb.hoc as published at http://senselab.med.yale.edu/modeldb/ShowModel.asp?model=43039 ~0.031). Synchronisation of spiking in the 2 cell simulation is immediate but the difference in passive parameters means that the sub-threshold depolarisation remains asynchronous. This is not the case in the Migliore model (Migliore et al., 2005) where complete synchronisation occurs because the passive parameters of the two cells are identical. But aside from the sub-threshold asynchrony comparison between a simulation using the same setup minus the gap-junctions (Figure 6.5) and with the gap-junctions reveals that the degree of synchronisation mediated by the gap-junction is substantial. Experimental assessment of correlated firing between pairs of MCs (Schoppa and Westbrook 2002) used the ratio of probability of spikes from two cells in a cross correlogram fall within 10 ms versus between 30 to 40 ms. This type of probabilistic criteria is suited to experimental work on neurons but cannot be applied to simulations, that produce the same result every time, while parameters remain the same. However for comparison purposes it can be noted that in the experimental work 20 ms bins were used to produce the cross correlograms (Schoppa and Westbrook 2002) while 1 ms bins where needed to separate the spike trains in Figure 6.4a (see cross correlogram Figure 6.4c). From the cross correlogram the mean absolute lag[17] for the pair of spike trains in Figure 6.4a was 0.44 ± 0.75 ms which is an order of magnitude better synchrony than the experimental method was looking for. For comparison the cross correlogram (Figure 6.5b) performed on the pair of MCs minus the gap-junctions in Figure 6.5a, has a mean absolute lag of 4.29 ± 0.83 ms.

[17] Lag is used in cross correlograms to denote the shift along the time axis (ms) needed for a spike to line up with a spike in the other pair. The y axis in the cross correlogram is the number of examples of spike pairs that line up for a particular unit of lag.

At about 2-3 ms in duration the APs have a slower than normal time course compared to experimental durations of about 0.8-1 ms (e.g. Chen et al. 1997, Christie and Westbrook 2003). This extended duration is a function of the gate kinetic equations for the Na, K_{dr} and K_A ion channels in the Migliore et al. (2005) model that are used in the simulations. In Figure 6.6 a comparison is made by superimposing simulations using my reconstructed morphology and the simple morphology used by Migliore et al. (2005). The distance between the apical tuft and the soma is shorter in the Migliore et al. (2005) morphology than my reconstructed morphology. This produces a faster time course in the rising phase of the AP for the Migliore et al. (2005) morphology. This relationship between the distance of the current injection and soma and speed of the AP rising phase had already been noted in Figure 5.5. However, the overall duration of APs is unaffected by morphology (Figure 6.6). It would be desirable in the future to have more experimental measurements of channel gating kinetics to be able to have more realistic AP time course properties.

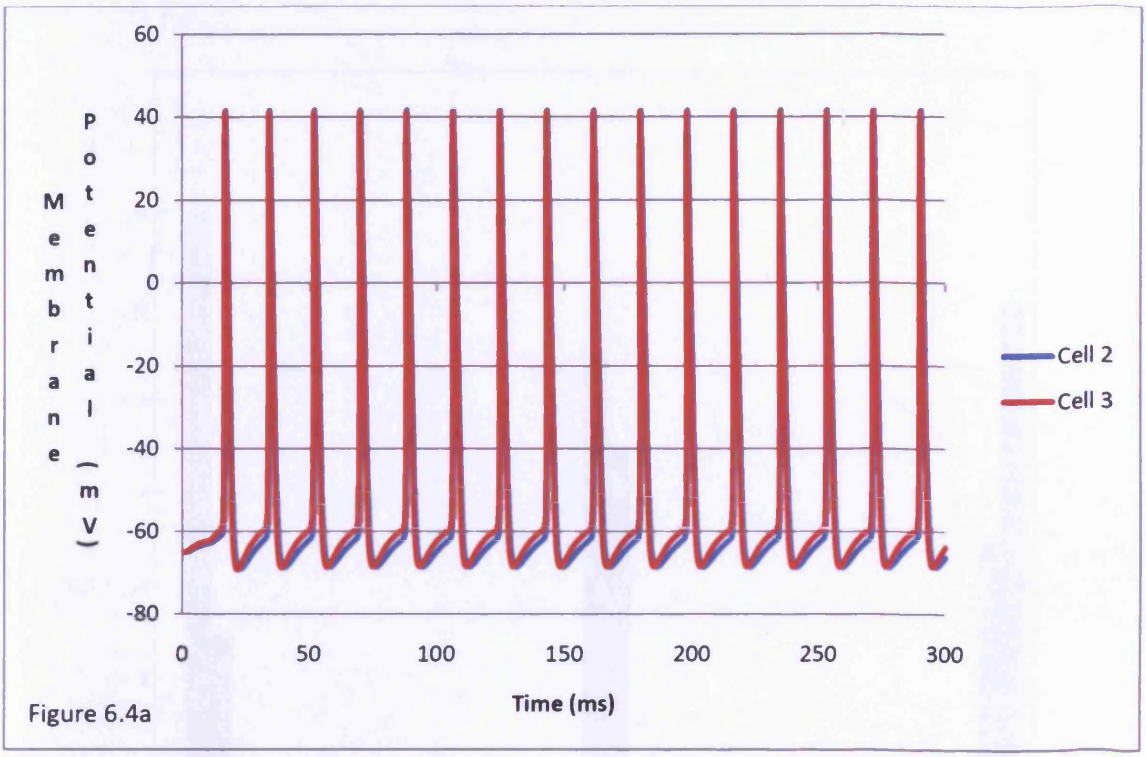

Figure 6.4a

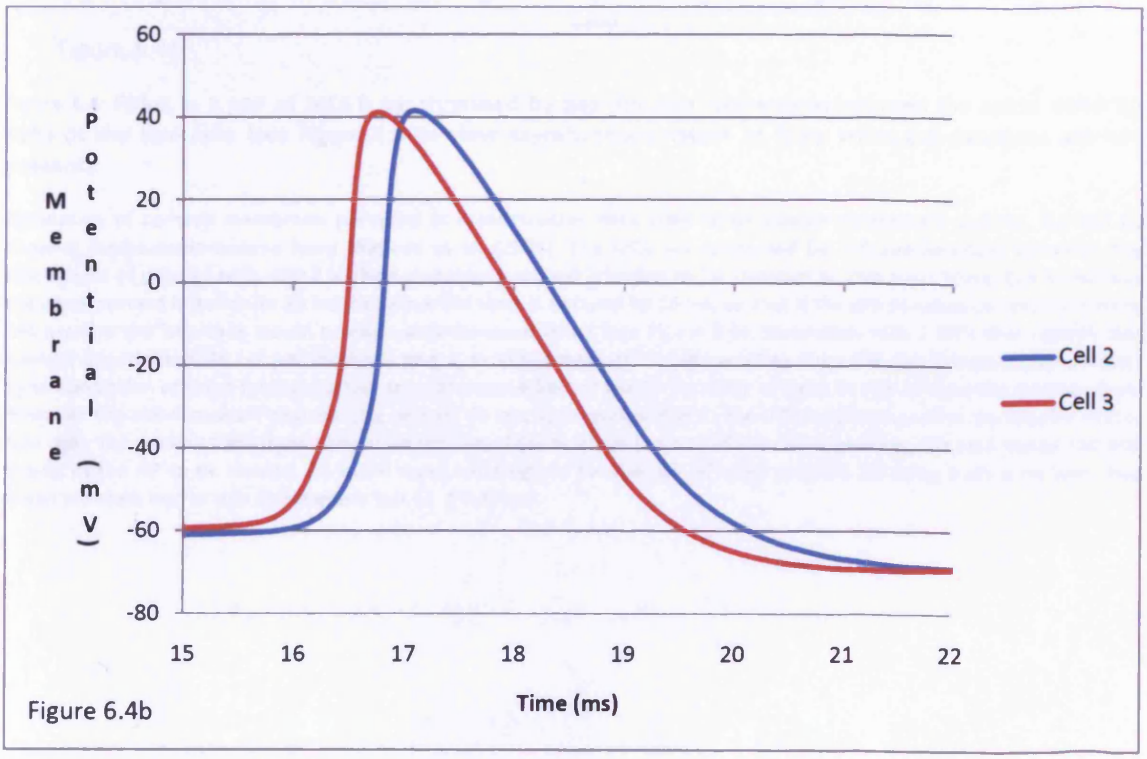

Figure 6.4b

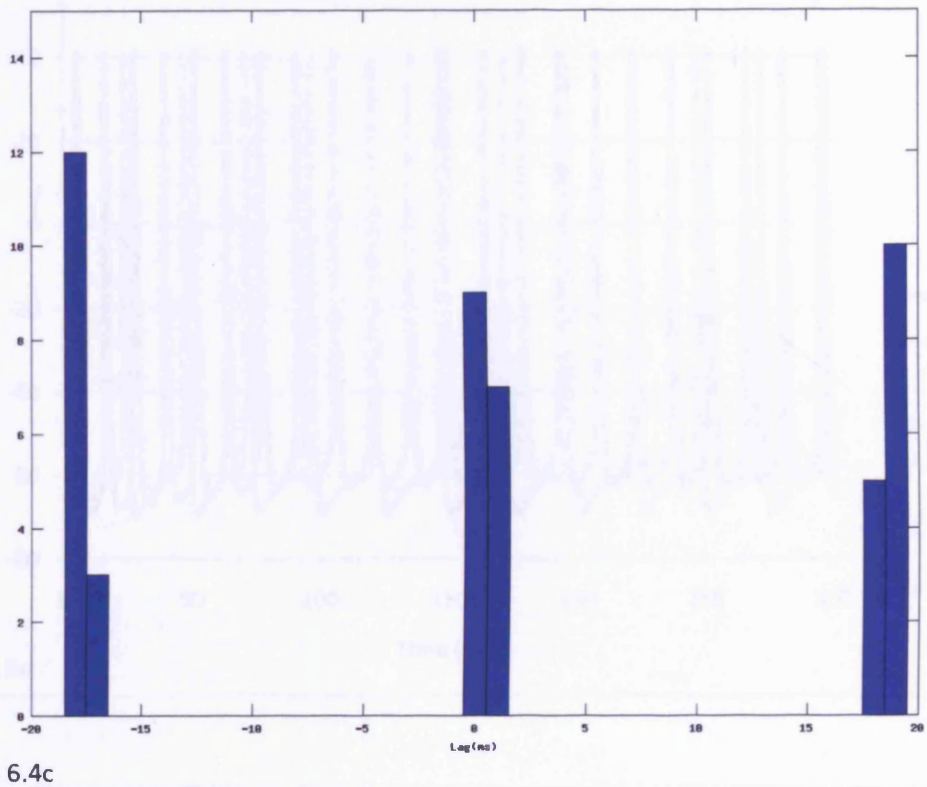

Figure 6.4c

Figure 6.4: Firing in a pair of MCs is synchronised by gap-junction connections between the apical dendrite tufts of the two cells (see Figure 6.5 to view asynchronous nature of firing when gap-junctions are not present).

Simulation of somatic membrane potential in reconstructed MCs with fitted passive parameters and Na, K_{dr} and K_A channel mechanisms derived from Migliore et al. (2005). The MCs are connected by 100 gap-junctions between the apical tufts of pairs of cells. Cell 2 is given a constant current injection to 20 locations to give tonic firing. Cell 3 receives the same current injection to 20 locations but the start is delayed by 10 ms, so that if the gap-junction connections were not present the two cells would produce asynchronous firing (see Figure 6.5). Simulation with 2 MCs that receive the current injections (0.03 nA per location) and a coupling ratio of ~0.044 resulting from the gap-junction connections. Synchronisation of firing (absorbing the asynchronous effect of the 10 ms delay of input to one of the cells) is immediate however the sub-threshold depolarising phases do not synchronise due to the differences in passive parameter of the two cells (b) shows an enlarged time scale version of (a) to allow the size of the offset between the two traces and the timing of the AP to be viewed. (c) is the cross correlogram for the pair of spike trains in (a) using 1 ms time bins. The mean absolute lag for this correlogram is 0.44 ± 0.75 ms.

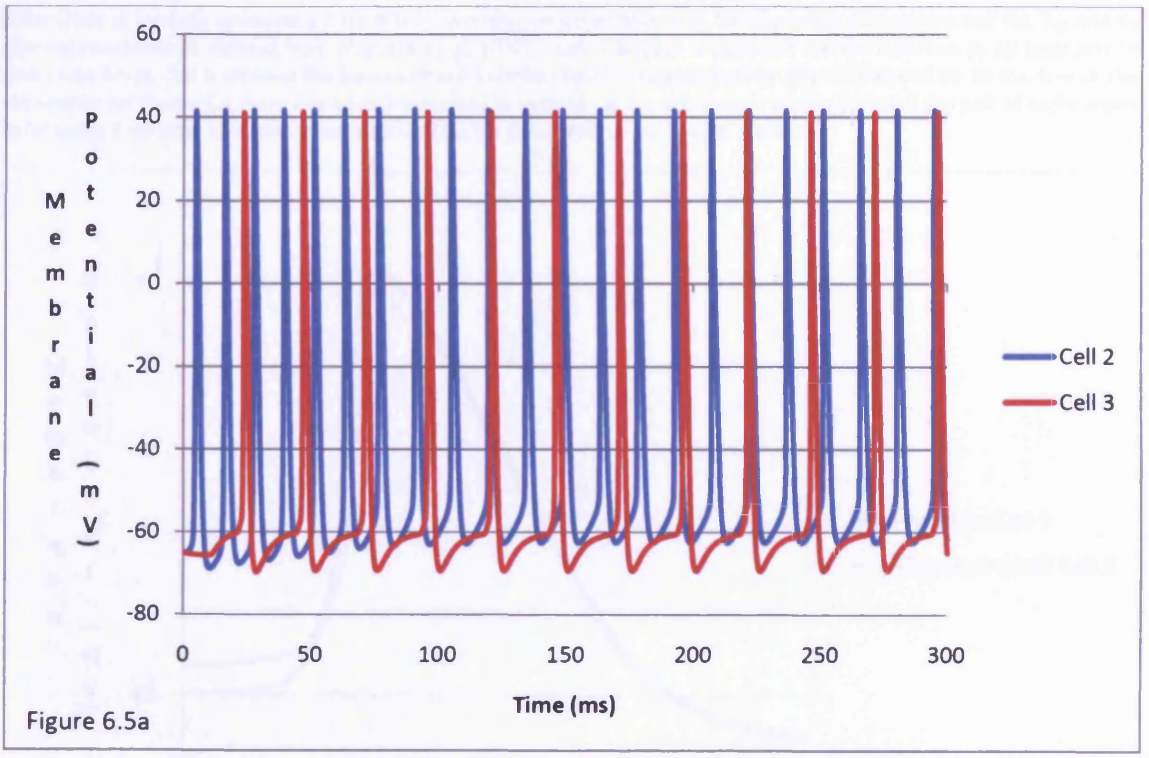

Figure 6.5a

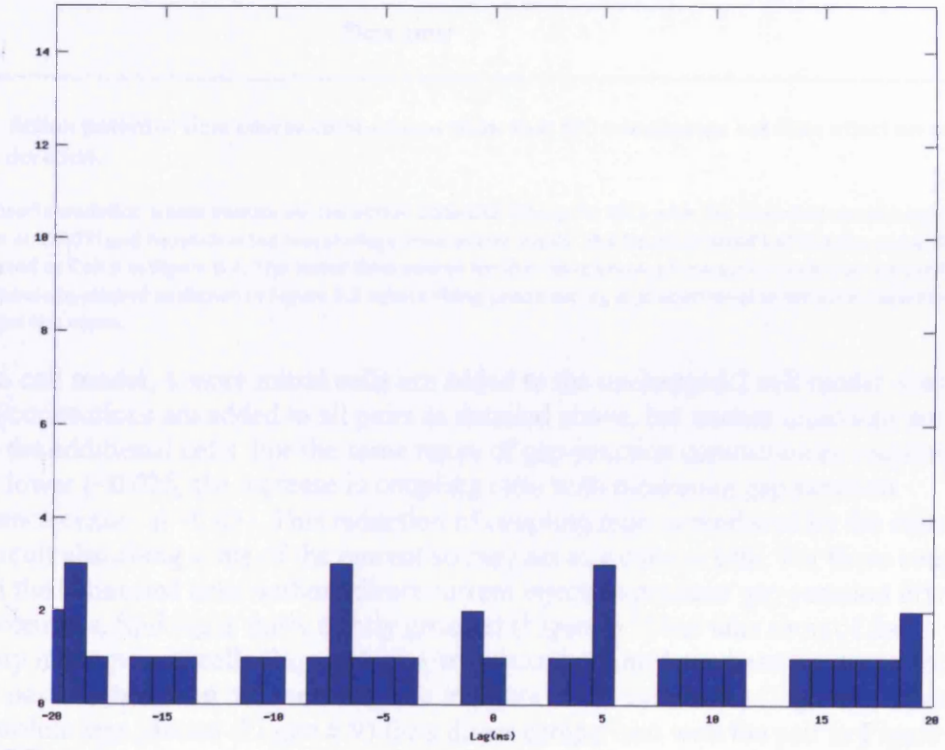

Figure 6.5b

Figure 6.5: Asynchronous firing in a pair of MCs with same set up as Figure 6.4a minus the gap-junction connections.

Simulation of somatic membrane potential in two reconstructed MCs with fitted passive parameters and Na, K_{dr} and K_A channel mechanisms derived from Migliore et al. (2005). Cell 2 is given a constant current injection to 20 locations to give tonic firing. Cell 3 receives the same current injection to 20 locations but the start is delayed by 10 ms. Unlike the simulation for Figure 6.4 there are no gap-junctions in this set-up. (b) is the cross correlogram for the pair of spike trains in (a) using 1 ms time bins. The mean absolute lag for this correlogram is 4.29 ± 0.83 ms.

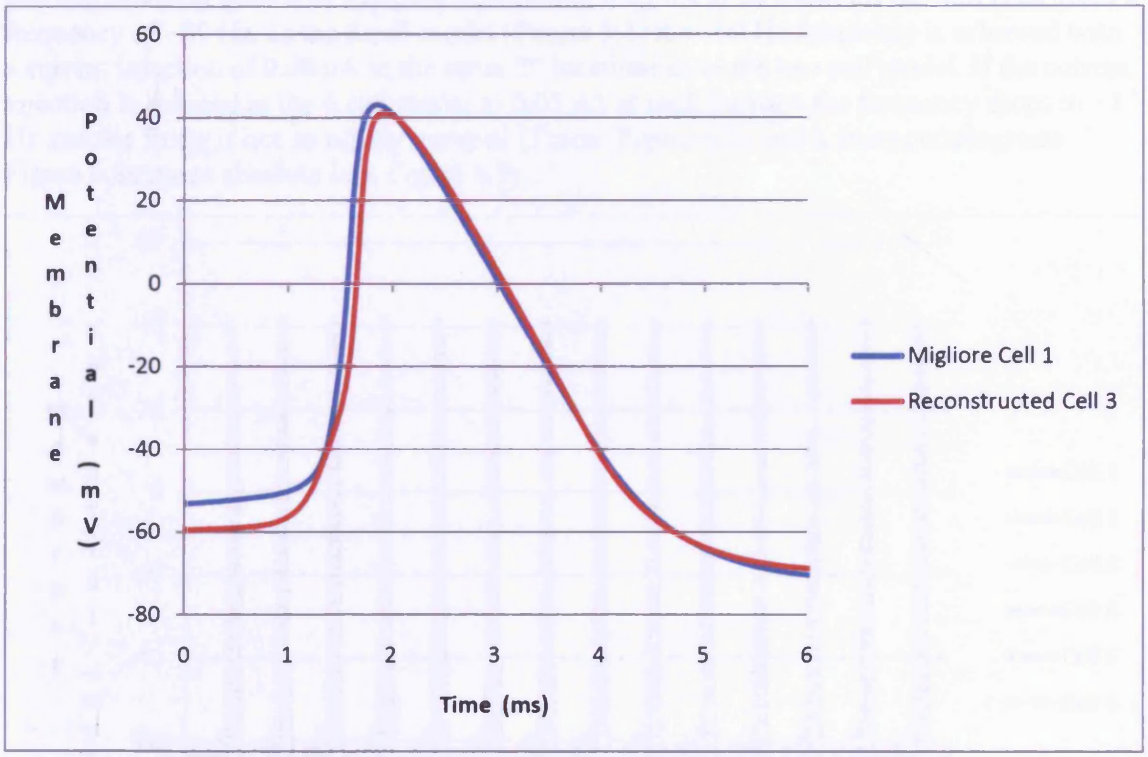

Figure 6.6: Action potential time course comparisons show that MC morphology has little effect on action potential duration.

Superimposed simulation traces comparing the action potential timing for MCs with the canonical morphology used in Migliore et al. (2005) and reconstructed morphology used in this thesis. The Reconstructed Cell 3 is the same simulation trace depicted as Cell 3 in Figure 6.4. The faster time course for the rising phase of the action potential for the Migliore cell is morphology related as shown in Figure 5.5 where rising phase timing is proportional to distance between current injection and the soma.

For the 6 cell model, 4 more mitral cells are added to the unchanged 2 cell model. Gap-junction connections are added to all pairs as detailed above, but current injections are not made to the additional cells. For the same range of gap-junction conductances coupling ratios are now lower (~0.025, the increase in coupling ratio with increasing gap-junction conductance ceases at ~0.03). This reduction of coupling ratio is produced by the extra 4 cells in the circuit absorbing some of the current so they act as a current sink. For these coupling ratios all the connected cells without direct current injection produce gap-junction driven action potentials. Spiking is fairly tightly grouped (Figure 6.7) but falls short of the synchrony in the pair of cells (Figure 6.4). Cross correlograms have been produced for all possible pairs within the 6 MC network as a measure of the synchrony (Figure 6.7c) and the mean absolute lags plotted (Figure 6.9) for a direct comparison with the pair in Figure 6.4. The differences in the sub-threshold depolarising phase reflect the range of passive parameters across the 6 mitral cells. The firing rate is proportional to the amplitude of current injection and proportionally lower than in the two cell model. The explanation for this is the rate that the input current can depolarise the cell. The current injection depolarises the cells until the threshold of the sodium channel is reached which sets off the action potential

sequence of channel mechanism activation and deactivation. After an action potential has occurred the current injection will again start depolarising the cell. Higher current amplitude depolarises the cells fast and in a 6 cell setup the current sink effect of the extra 4 cells absorbs some of the current amplitude and reduces the rate of the cell depolarisation. In the two cell model (Figure 6.4) a current injection of 0.03 nA at 20 locations on both cells gives a frequency of ~50 Hz. In the 6 cell model (Figure 5.1) the ~50 Hz frequency is achieved with a current injection of 0.06 nA to the same 20 locations as in the two cell model. If the current injection is reduced in the 6 cell model to 0.05 nA at each location the frequency drops to ~17 Hz and the firing is not so tightly grouped (Traces Figure 6.8a and b cross correlograms Figure 6.8c mean absolute lags Figure 6.9).

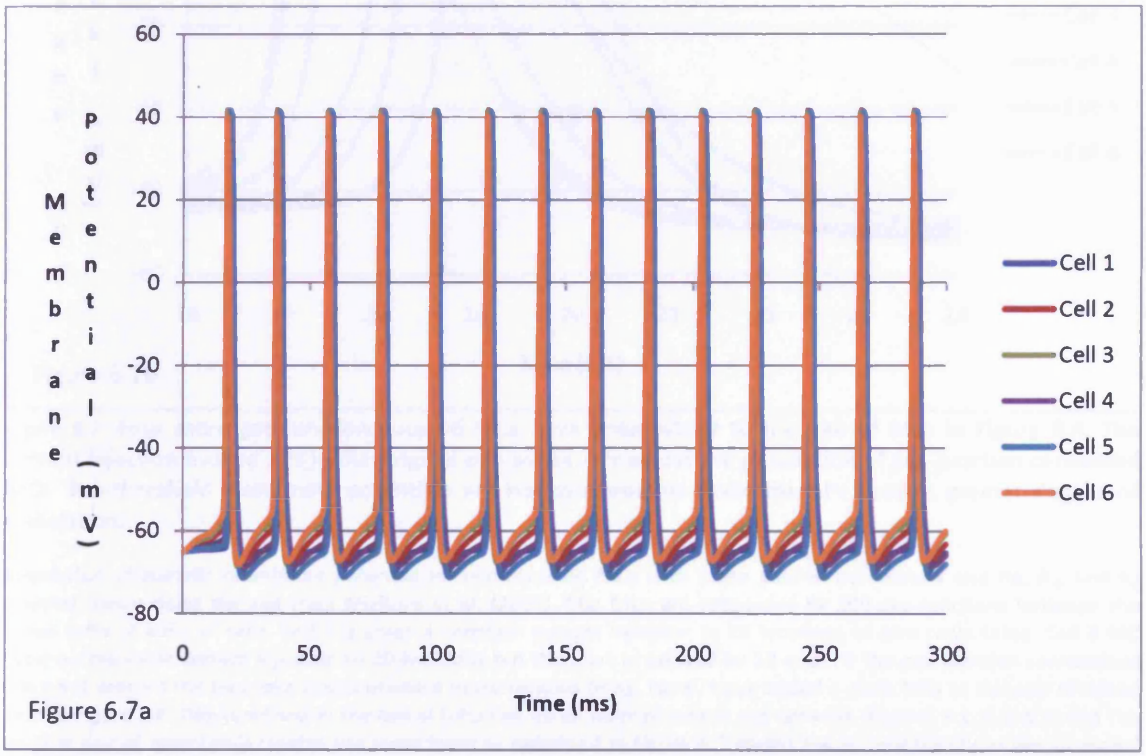

Figure 6.7a

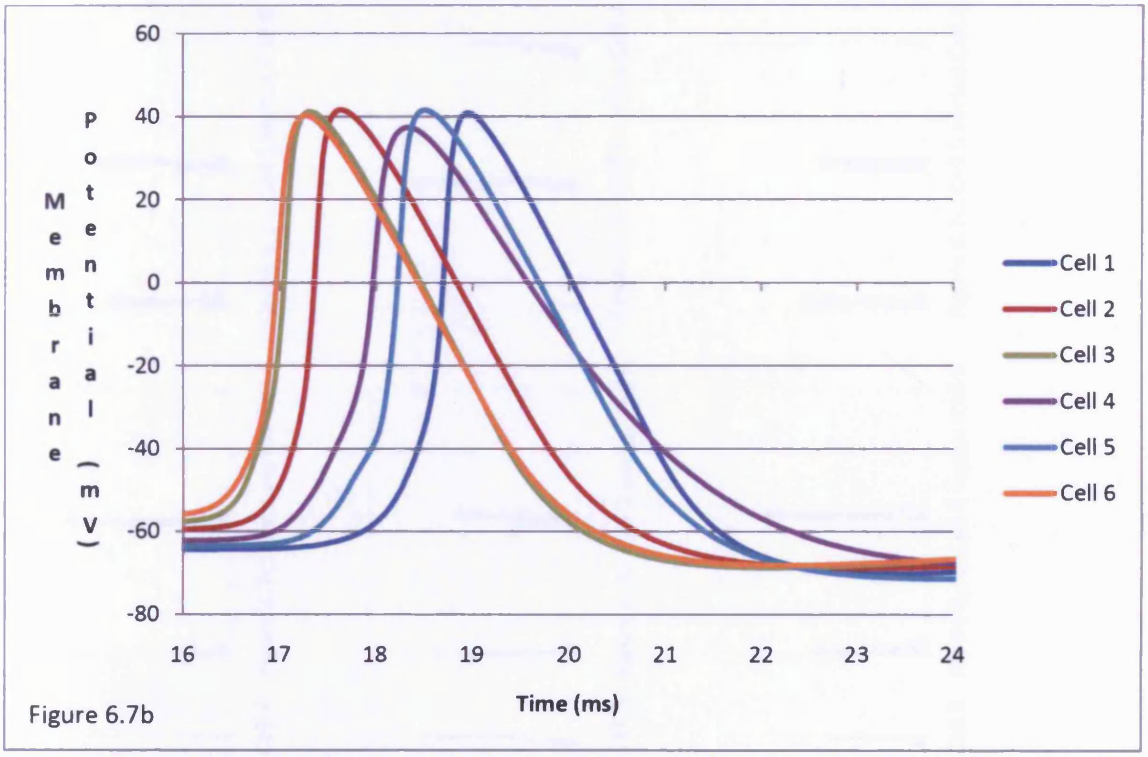

Figure 6.7: Four more gap-junction coupled MCs have been added to the pair of MCs in Figure 6.4. The current injection evoked APs in the original pair evoke APs across the population of gap-junction connected MCs. Sub-threshold membrane potentials are not synchronous while the APs show a greater degree of correlation.

Simulation of somatic membrane potential in reconstructed MCs with fitted passive parameters and Na, K_{dr} and K_A channel mechanisms derived from Migliore et al. (2005). The MCs are connected by 100 gap-junctions between the apical tufts of pairs of cells. Cell 2 is given a constant current injection to 20 locations to give tonic firing. Cell 3 MC receives the same current injection to 20 locations but the start is delayed by 10 msec. If the gap-junction connections were not present the two cells would produce asynchronous firing. Here I have added 4 more MCs to the pair of mitral cells in Figure 6.4. Gap-junctions in the apical tufts link up all pairs of cells in the network (Figures 6.1, 6.2, 6.3) and the original pair of mitral cells receive the same input as described in Figure 6.2 except the current injections are increased to 0.06 nA per location. In the model configured in this way the coupling ratio drops to ~0.025, but gap-junction driven firing is observed in all the cells. Firing of all cells is tightly grouped but full synchronisation is not achieved cells (b) shows an enlarged time scale version of (a) to allow the size of the offset between the two traces and the timing of the AP to be viewed. (c) are the cross correlograms for all pair combinations for the spike trains in (a) using 1 ms time bins. The mean absolute lag for these correlogram are shown in Figure 6.9.

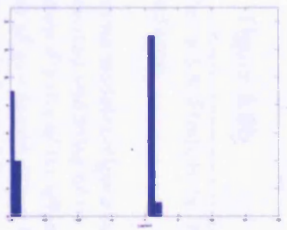

Figure 6.7c: Cell 1 versus Cell 2

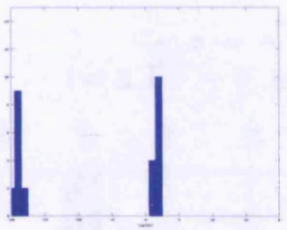

Figure 6.7c: Cell 1 versus Cell 3

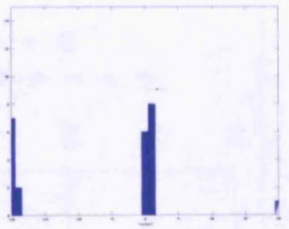

Figure 6.7c: Cell 1 versus Cell 4

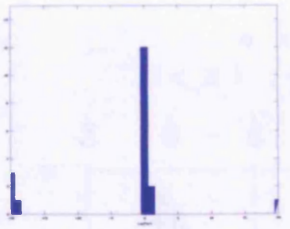

Figure 6.7c: Cell 1 versus Cell 5

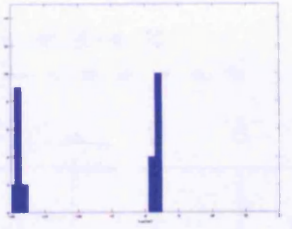

Figure 6.7c: Cell 1 versus Cell 6

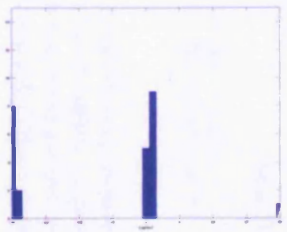

Figure 6.7c: Cell 2 versus Cell 3

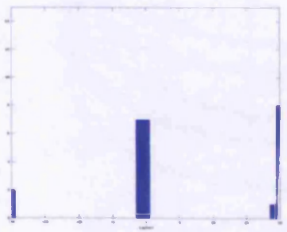

Figure 6.7c: Cell 2 versus Cell 4

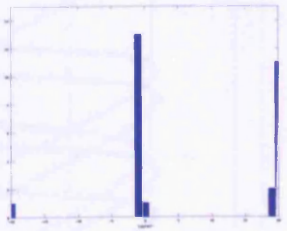

Figure 6.7c: Cell 2 versus Cell 5

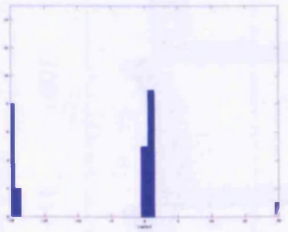

Figure 6.7c: Cell 2 versus Cell 6

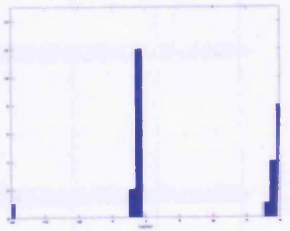

Figure 6.7c: Cell 3 versus Cell 4

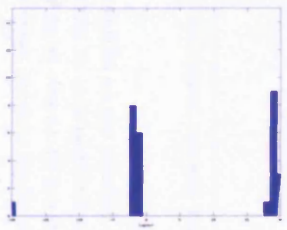

Figure 6.7c: Cell 3 versus Cell 5

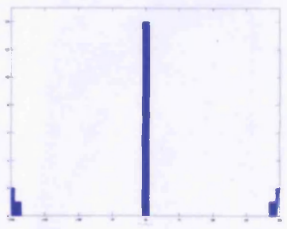

Figure 6.7c: Cell 3 versus Cell 6

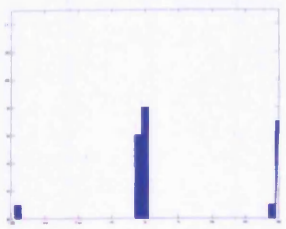

Figure 6.7c: Cell 4 versus Cell 5

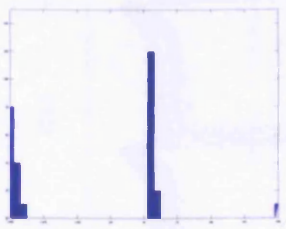

Figure 6.7c: Cell 4 versus Cell 6

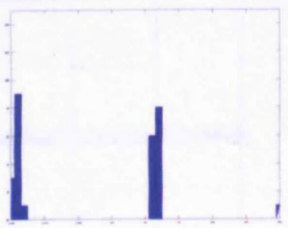

Figure 6.7c: Cell 5 versus Cell 6

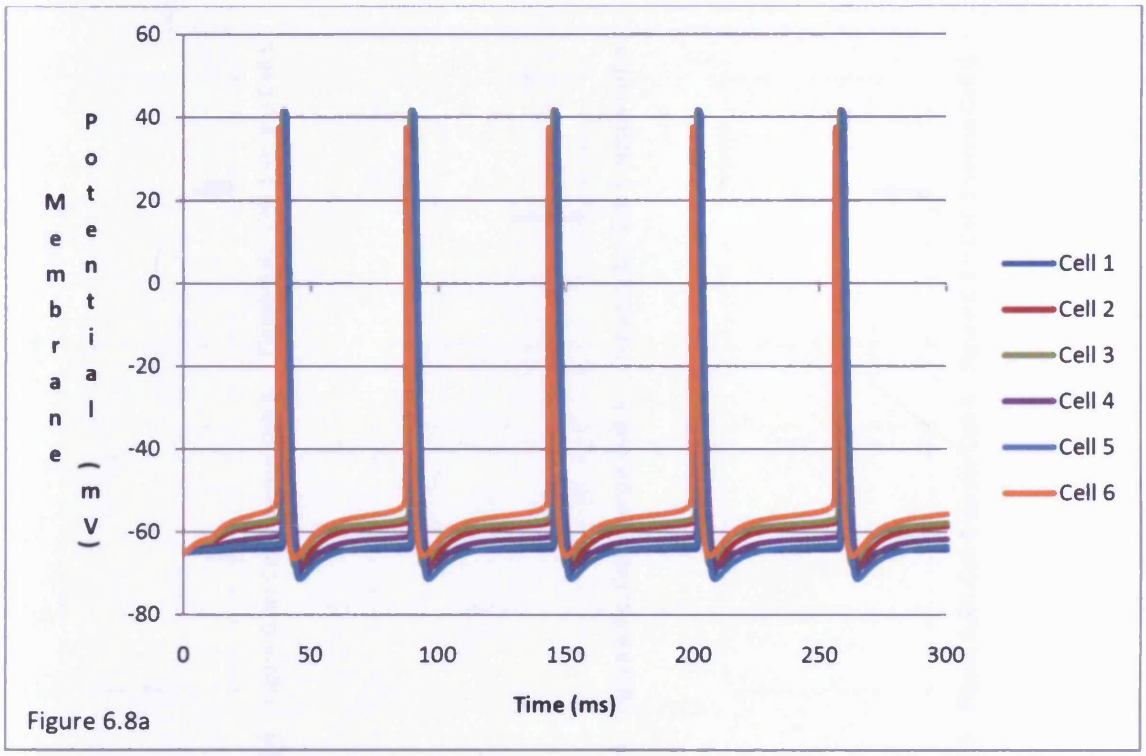

Figure 6.8a

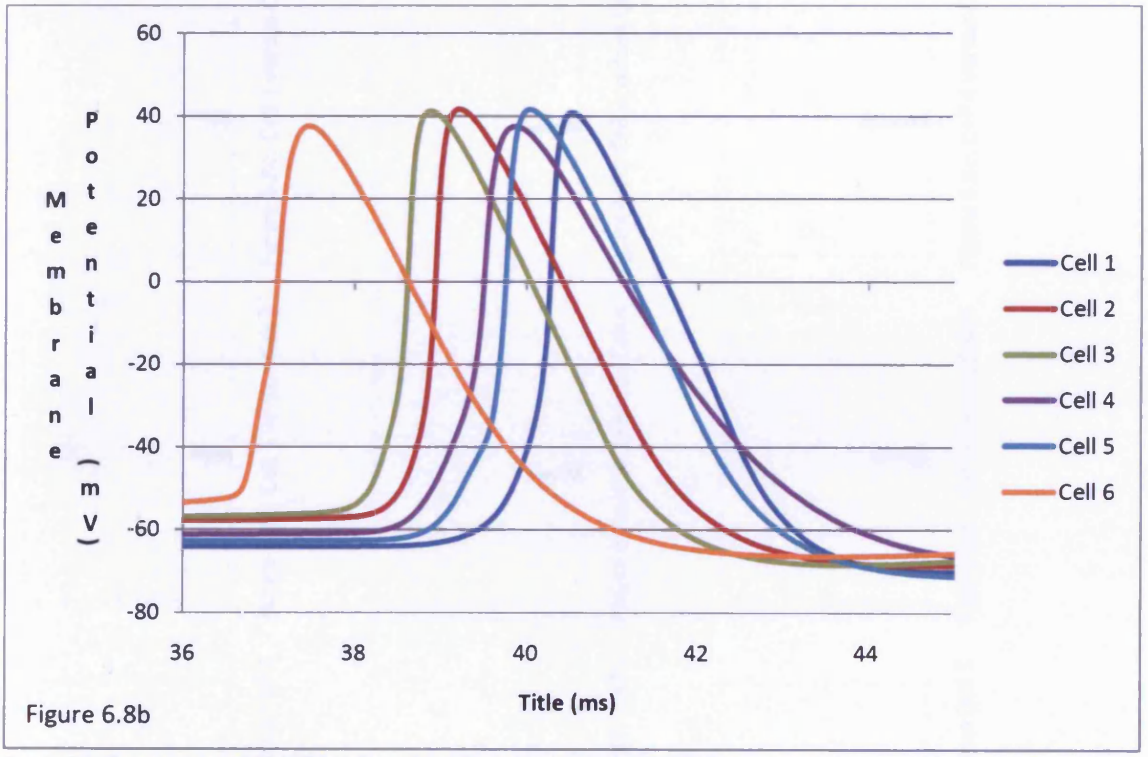

Figure 6.8b

Figure 6.8: Frequency of MC firing is reduced when the size of the continuous current injection to 2 MCs is reduced.

Same model configuration as Figure 6.7, but current injections are reduced to 0.05 nA per location. Frequency of firing is reduced and firing of the mitral cells is not so tightly grouped cells (b) shows an enlarged time scale version of (a) to allow the size of the offset between the two traces and the timing of the AP to be viewed. (c) are the cross correlograms for all pair combinations for the spike trains in (a) using 1 ms time bins. The mean absolute lag for these correlogram are shown in Figure 6.9.

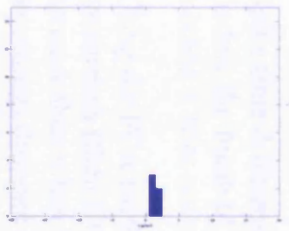

Figure 6.8c: Cell 1 versus Cell 2

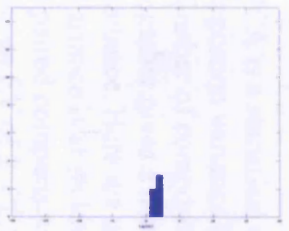

Figure 6.8c: Cell 1 versus Cell 3

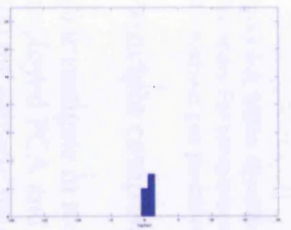

Figure 6.8c: Cell 1 versus Cell 4

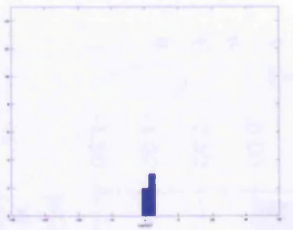

Figure 6.8c: Cell 1 versus Cell 5

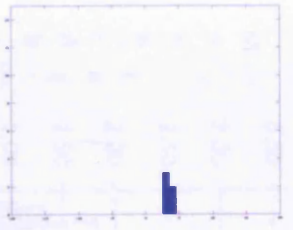

Figure 6.8c: Cell 1 versus Cell 6

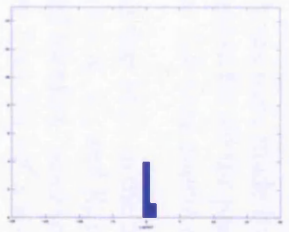

Figure 6.8c: Cell 2 versus Cell 3

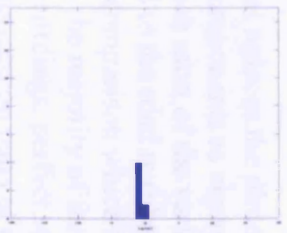

Figure 6.8c: Cell 2 versus Cell 4

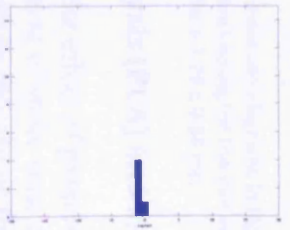

Figure 6.8c: Cell 2 versus Cell 5

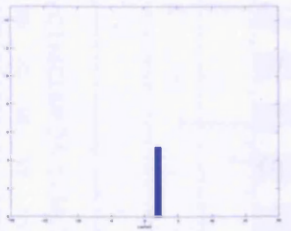

Figure 6.8c: Cell 2 versus Cell 6

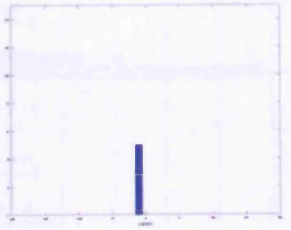

Figure 6.8c: Cell 3 versus Cell 4

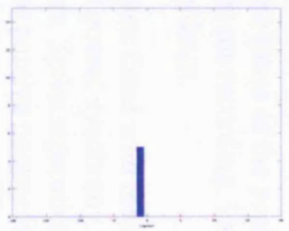

Figure 6.8c: Cell 3 versus Cell 5

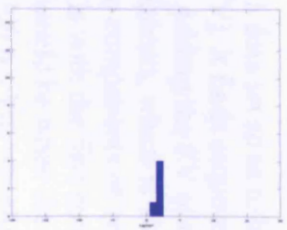

Figure 6.8c: Cell 3 versus Cell 6

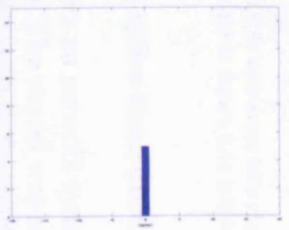

Figure 6.8c: Cell 4 versus Cell 5

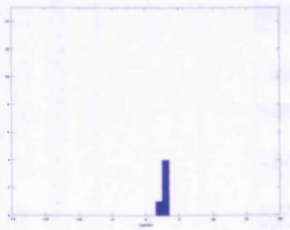

Figure 6.8c: Cell 4 versus Cell 6

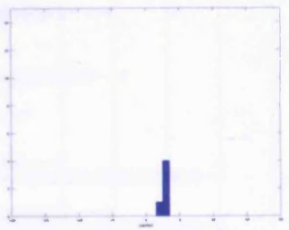

Figure 6.8c: Cell 5 versus Cell 6

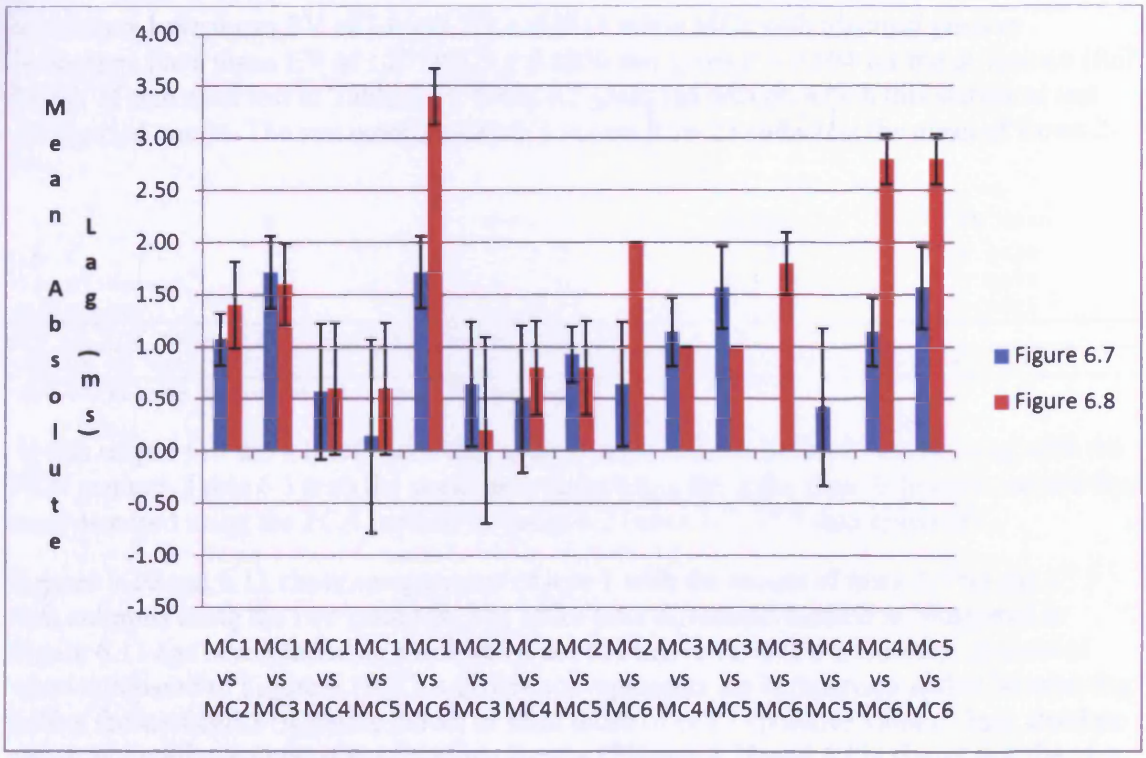

Figure 6.9: Mean absolute lags for the cross correlograms in Figures 6.7c and 6.8c with error bars showing standard deviation. For comparison the mean absolute lag for the pair with gap-junctions in Figure 6.4a is 0.44 ± 0.75 ms and the pair without gap-junctions in Figure 6.5a is 4.29 ± 0.83 ms.

Principle component analysis (PCA) and measuring spike-time differences

To investigate in more detail the effect of passive parameters on network synchrony I employed PCA and measurement of spike-time differences. The model was set to produce 300 ms somatic membrane voltage recordings for each of the cells in the model. These simulations were compared for synchrony using two different methods.

PCA is a statistical method that reduces the dimensions in a data set so as to be able to apportion variance between components as eigenvalues (EV). It finds sequentially a specified number of components in which most of the variance lies. Adding the EV of the components together gives a number equal to the total number of components, which is 100% of the variance. Here we use paired comparison which allows two components of variance. Variance is at its lowest when the majority of the variance is with the first component. So for a paired comparison of two recordings, perfect synchrony would be when the first component has an EV of 2. PCA was performed on pairs of complete 300 ms Vm waveforms (Table 6.2) and in some cases EV approach 2 indicating high degree of synchronisation.

Spike time difference comparisons were made by finding the times of the peak voltage and finding the mean of the differences for all the peaks in a 300 ms recording. Unlike the PCA method it does not compare the full time course of the recordings.

Using the PCA method I found that MCs in the network when fitted with their own passive parameters (their fitted values for R_i, C_m and R_m) generated poorer synchrony across the network than when MCs shared identical passive parameters. Spike separation for pairs recordings dropped from above 1 ms for MCs with different passive parameters to below 0.5 ms. This difference is confirmed with PCA where MCs with their own (different) passive

parameters have mean EV of 1.6600 SD ± 0.2511 while MCs with identical passive parameters have mean EV of 1.8779 SD ± 0.1050 this gives P = 0.004 for the difference (full details of statistical test in Table 6.1). Table 6.2 gives the data on which this statistical test was carried out on. The test compares Row 1 versus Row 23 (which is the mean of Rows 2-22).

	N	Mean	StDev	SE Mean
Row 1	15	1.6600	0.2511	0.0648
Row 23 (mean)	15	1.8779	0.1050	0.0271
Difference	15	-0.2179	0.2420	0.0625

99% CI for mean difference: (-0.4040, -0.0319)

T-Test of mean difference = 0 (vs not = 0): T-Value = -3.49 P-Value = 0.004

Table 6.1: Paired T for Row 1 - Row 23 (mean)

At this stage I just did a brief check that spike time difference method was agreeing with the PCA method. Table 6.3 tests the same recordings using the spike time difference method that were assessed using the PCA method in Table 6.2 (rows 1-7, 1st 5 data columns).

Figures 6.10 and 6.11 show comparisons of row 1 with the means of rows 2-7 for the 1st 5 data columns using the two methods. The spike time difference method as illustrated in Figure 6.11 has been plotted as absolute values to remove the extra orientation dimension when compared to Figure 6.10. This difference represents the comparison spikes happpening before those of cell 1 (negative value) or after those of cell 1 (positive value). Once absolute values are used, a comparison of the two figures (Figures 6.10 and 6.11) shows that the two methods give qualitatively similar results.

			Cell 1 /Cell 2	Cell 1 /Cell 3	Cell 1 /Cell 4	Cell 1 /Cell 5	Cell 1 /Cell 6	Cell 2 /Cell 3	Cell 2 /Cell 4	Cell 2 /Cell 5	Cell 2 /Cell 6	Cell 3 /Cell 4	Cell 3 /Cell 5	Cell 3 /Cell 6	Cell 4 /Cell 5	Cell 4 /Cell 6	Cell 5 /Cell 6	Row
All cells have fitted passive parameters			1.4718	1.2578	1.8157	1.9131	1.2572	1.8991	1.7908	1.6662	1.8772	1.5712	1.4427	1.9955	1.9501	1.5571	1.4340	1
R_i (Ω cm)	C_m (μF cm^{-2})	R_m (Ω cm^2)	All Cells have Identical passive parameters															
322.92	2.026	1275.8	1.9353	1.9964	1.8813	1.6327	1.9208	1.9398	1.7658	1.5038	1.9977	1.8988	1.6613	1.9274	1.8742	1.7461	1.4826	2
153.23	1.9267	4099.9	1.9402	1.9669	1.9372	1.8397	1.9218	1.9936	1.8522	1.7249	1.9968	1.8873	1.7680	1.9844	1.9546	1.8222	1.6910	3
83.051	1.7722	2301.3	1.9349	1.9475	1.9414	1.8688	1.9348	1.9985	1.8555	1.7535	1.9988	1.8662	1.7667	1.9983	1.9715	1.8427	1.7401	4
168.94	1.9744	3914.7	1.9395	1.9677	1.9307	1.8185	1.9173	1.9928	1.8412	1.6999	1.9958	1.8803	1.7476	1.9812	1.9473	1.8067	1.6611	5
248.95	1.599	6867.1	1.9525	1.9855	1.9345	1.7953	1.9201	1.9862	1.8540	1.6896	1.9919	1.9068	1.7563	1.9641	1.9293	1.8087	1.6373	6
62.258	2.1649	2823.1	1.9351	1.9397	1.9218	1.8450	1.9377	1.9981	1.8415	1.7393	1.9974	1.8365	1.7347	1.9993	1.9732	1.8224	1.7198	7
83.051	1.9267	4099.9	1.9407	1.9503	1.9318	1.8535	1.9372	1.9990	1.8537	1.7489	1.9982	1.8599	1.7570	1.9980	1.9691	1.8330	1.7269	8
322.92	1.9267	4099.9	1.9542	1.9966	1.9164	1.7137	1.9135	1.9658	1.8322	1.6110	1.9882	1.9209	1.7228	1.9305	1.8925	1.7774	1.5500	9
168.94	1.9267	4099.9	1.9412	1.9710	1.9363	1.8323	1.9197	1.9918	1.8511	1.7177	1.9960	1.8916	1.7676	1.9800	1.9508	1.8182	1.6805	10
248.95	1.9267	4099.9	1.9478	1.9881	1.9276	1.7727	1.9122	1.9801	1.8418	1.6622	1.9909	1.9076	1.7446	1.9538	1.9217	1.7939	1.6079	11
62.258	1.9267	4099.9	1.9396	1.9479	1.9311	1.8569	1.9392	1.9989	1.8539	1.7560	1.9976	1.8543	1.7573	1.9988	1.9737	1.8336	1.7343	12
153.23	1.7722	4099.9	1.9438	1.9685	1.9425	1.8502	1.9262	1.9942	1.8622	1.7403	1.9970	1.8945	1.7803	1.9856	1.9567	1.8335	1.7077	13
153.23	2.026	4099.9	1.9386	1.9662	1.9341	1.8349	1.9200	1.9933	1.8478	1.7189	1.9967	1.8842	1.7633	1.9839	1.9540	1.8172	1.6846	14
153.23	1.9744	4099.9	1.9390	1.9663	1.9371	1.8374	1.9205	1.9935	1.8511	1.7126	1.9968	1.8866	1.7651	1.9842	1.9535	1.8212	1.6879	15
153.23	1.599	4099.9	1.9475	1.9700	1.9482	1.8607	1.9308	1.9949	1.8723	1.7556	1.9972	1.9015	1.7922	1.9870	1.9586	1.8452	1.7244	16
153.23	2.1649	4099.9	1.9356	1.9647	1.9293	1.8259	1.9164	1.9929	1.8395	1.7062	1.9966	1.8779	1.7529	1.9830	1.9524	1.8078	1.6711	17
153.23	1.9267	2301.3	1.9338	1.9640	1.9378	1.8385	1.9156	1.9925	1.8444	1.7131	1.9970	1.8833	1.7606	1.9835	1.9546	1.8159	1.6809	18
153.23	1.9267	1275.8	1.9200	1.9585	1.9365	1.8348	1.9076	1.9895	1.8264	1.6893	1.9984	1.8738	1.7465	1.9835	1.9557	1.8068	1.6670	19
153.23	1.9267	3914.7	1.9402	1.9671	1.9381	1.8421	1.9221	1.9935	1.8538	1.7279	1.9968	1.8890	1.7712	1.9844	1.9553	1.8242	1.6945	20
153.23	1.9267	6867.1	1.9429	1.9657	1.9313	1.8264	1.9230	1.9952	1.8474	1.7147	1.9963	1.8782	1.7524	1.9858	1.9516	1.8141	1.6773	21
153.23	1.9267	2823.1	1.9360	1.9659	1.9386	1.8415	1.9180	1.9924	1.8484	1.7199	1.9970	1.8871	1.7673	1.9833	1.9551	1.8198	1.6876	22
Mean			1.9399	1.9674	1.9316	1.8201	1.9226	1.9894	1.8446	1.7050	1.9961	1.8841	1.7541	1.9790	1.9479	1.8148	1.6721	23
Standard Deviation			0.00724	0.0149	0.0135	0.0547	0.00874	0.0135	0.0206	0.0571	0.00261	0.0192	0.0261	0.0197	0.0249	0.0221	0.0615	
Maximum			1.9542	1.9966	1.9482	1.8688	1.9392	1.9990	1.8723	1.7560	1.9988	1.9209	1.7922	1.9993	1.9737	1.8452	1.7401	
Minimum			1.9200	1.9397	1.8813	1.6327	1.9076	1.9398	1.7658	1.5038	1.9882	1.8365	1.6613	1.9274	1.8742	1.7461	1.4826	
N			21	21	21	21	21	21	21	21	21	21	21	21	21	21	21	

Table 6.2: Table showing PCA tests for pairs of MCs. All the pairs on the first row have their own fitted passive parameters, while the rest of the rows are from pairs of MCs with identical passive parameters.

PCA comparisons of somatic recordings from MCs in the 6 cell apical dendrite tuft gap-junction connected network shown in Figure 6.1. Figure 6.7a shows the somatic recordings that were used for row 1 in which all the passive parameters are fitted values. Rows 2-23 show comparisons where the passive parameters are identical for all the cells. Over these rows the passive parameters are varied to understand their influence, values were chosen from amongst the fitted values for the six MCs but used in different combinations.

		Cell 1 Mean inter spike interval		Cell 2 mean difference from cell 1		Cell 3 mean difference from cell 1		Cell 4 mean difference from cell 1		Cell 5 mean difference from cell 1		Cell 6 mean difference from cell 1	
	n	Mean	SD	Mean	SD	Mean	SD	Mean	SD	Mean	SD	Mean	SD
Row 1	14	20.605	0.636	-1.2804	0.0106	-1.6429	0.0117	-0.59643	0.01336	-0.36071	0.02724	-1.6893	0.0128
Row 2	20	14.945	0.375622	-0.28625	0.0127604	0.01375	0.0206394	0.43625	0.0127604	0.95	0.0140488	-0.29875	0.0171583
Row 3	15	19.68	0.690445	-0.27	0.0103510	-0.183333	0.0121988	0.281667	0.0148404	0.545	0.0140153	-0.3	0
Row 4	16	17.6172	0.546254	-0.254688	0.0100778	-0.214063	0.0128087	0.3	0	0.457812	0.0119678	-0.240625	0.0125
Row 5	18	16.2167	0.392953	-0.269444	0.0137080	-0.177778	0.0117851	0.304167	0.0128624	0.590278	0.0194386	-0.306944	0.0115222
Row 6	21	14.22143	0.262474	-0.22143	0.008964	-0.10238	0.00752	0.284524	0.0185	0.616667	0.022822	-0.2869	0.012794
Row 7	17	17.44412	0.518677	-0.26765	0.014697	-0.24706	0.008303	0.382353	0.014697	0.539706	0.015459	-0.25	0

Table 6.3: Spike time differences in this table are used as a check on a subset of the PCA in Table 6.2.

Mean Spike time comparisons of somatic recordings from MCs in the 6 cell apical dendrite tuft gap-junction connected network shown in Figure 6.1. Figure 6.7a shows the somatic recordings that were used for row 1 in which all the passive parameters are fitted values. Rows 2-6 show comparisons where the passive parameters are identical for all the cells. The actual passive parameters can be seen in Table 6.1 (these are comparisons are the same as the first 5 data columns for the first 7 rows in Table 6.2).

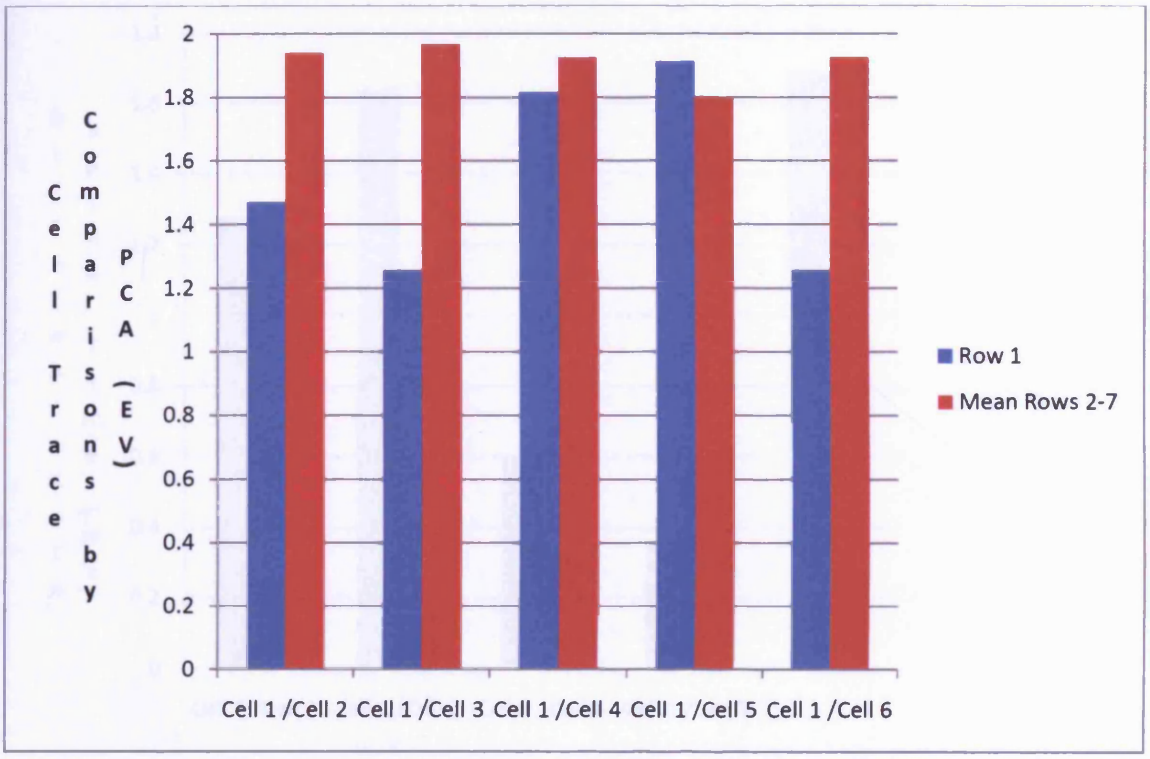

Figure 6.10: Taking a subset of the data from Table 6.2, which shows PCA for simulated somatic membrane potentials for pairs of MCs, it can be seen where individual MCs have different passive parameters the degree of synchrony is poorer (Row 1 blue columns) than where individual passive parameters are identical (Mean Rows 2-7 red columns).

The values are for principle component analysis for 300 ms samples of simulated somatic membrane potential from pairs of gap-junction connected MCs within a 6 cell network the Eigenvalues are taken from the first 5 data columns of Table 6.2. As the values approach EV of 2, the lower the variance between the MC traces and the better the synchrony.

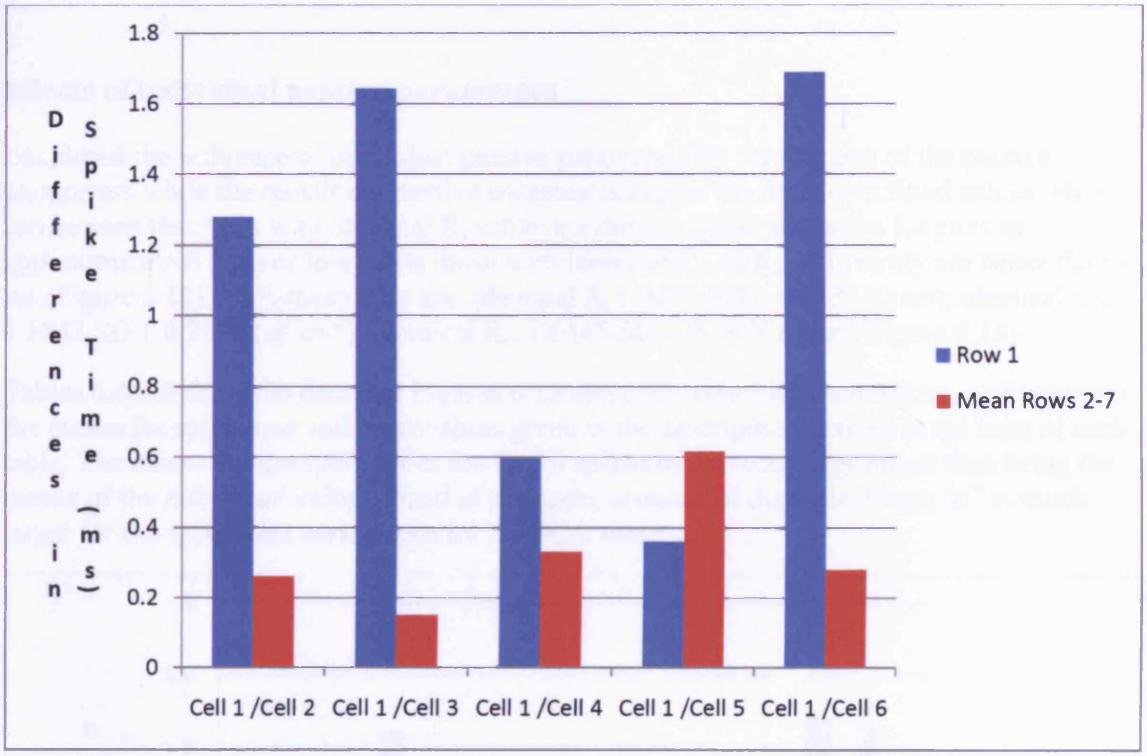

Figure 6.11: For comparison with Figure 6.10 now taking a subset of the data from Table 6.3 which gives spike differences for pairs of MCs, it can again be seen where individual MCs have different passive parameters the degree of synchrony is poorer (Row 1 blue columns) than where individual passive parameters are identical (Mean Rows 2-7 red columns).

Absolute (differences are both positive and negative in the orginal data) mean spike time differences for 300 ms samples of simulated somatic membrane potential from pairs of gap-junction connected MCs within a 6 cell network the Spike time differences are taken from the first 5 data columns of Table 6.3. Smaller spike time differences are indicative of better synchrony.

Effects of Individual passive parameters

I explored the influence of individual passive parameters by varying one of the passive parameters while the remaining passive parameters kept at the MCs own fitted values. Here it can be seen that MCs with identical R_i achieve a drop in spike separation for pairs to approximately 0.5 ms or less while those with identical C_m or R_m only rarely are better than 1 ms (Figure 6.12). PCA mean EVs are: identical R_i 1.9073 SD ± 0.0632 (Ω cm); identical C_m 1.5833 SD ± 0.2836 (μF cm^{-2}); identical R_m 1.6148 SD ± 0.2898 (Ω cm^2; Figure 6.13).

Tables 6.4-6.6 show the data that Figures 6.12 and 6.13 were constructed from, and represent the means for spike time and eigenvalues given in the descriptive sections at the base of each table. The means for the spike times are for all spikes in the recordings rather than being the means of the individual values found in the upper sections of the table, hence "n" is much larger for the spike time means than for the PCA means.

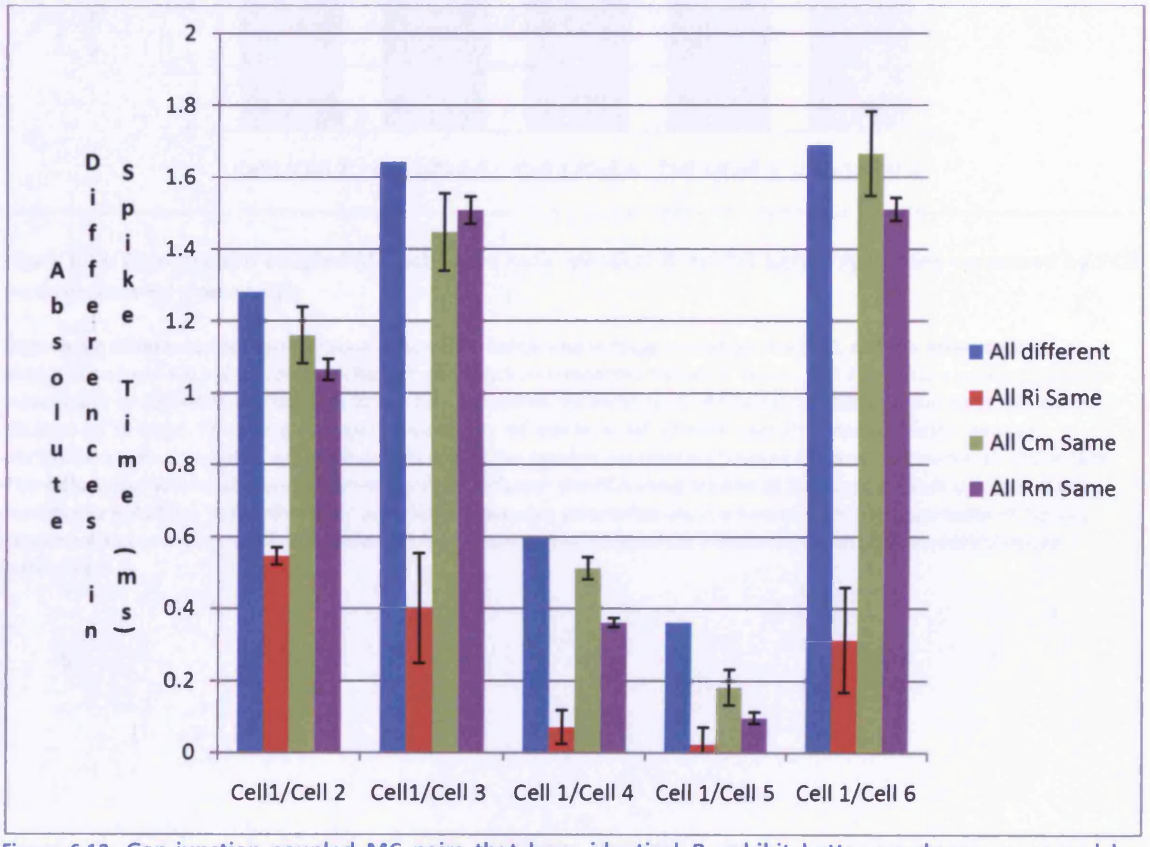

Figure 6.12: Gap-junction coupled MC pairs that have identical R_i exhibit better synchrony measured by reduction in spike time differences.

Spike time differences for comparisons of somatic membrane voltage recordings for cell1 and the other cells in simulations from a 6 MC apical dendrite tuft gap-junction connected network model. Cell 2 is given a constant current injection to 20 locations to give tonic firing. Cell 3 receives the same current injection to 20 locations but the start is delayed by 10 msec. The groups compare simulation set-ups in which all MCs have their own different passive parameters with simulation set-ups in which one of the passive parameters is set to identical values for all of the cells. The differences where all passive parameters are different are the means of all peaks for a single simulation. While those for one identical passive parameter are the means of all peaks from 6 simulations each with a different setting for the fixed passive parameter.

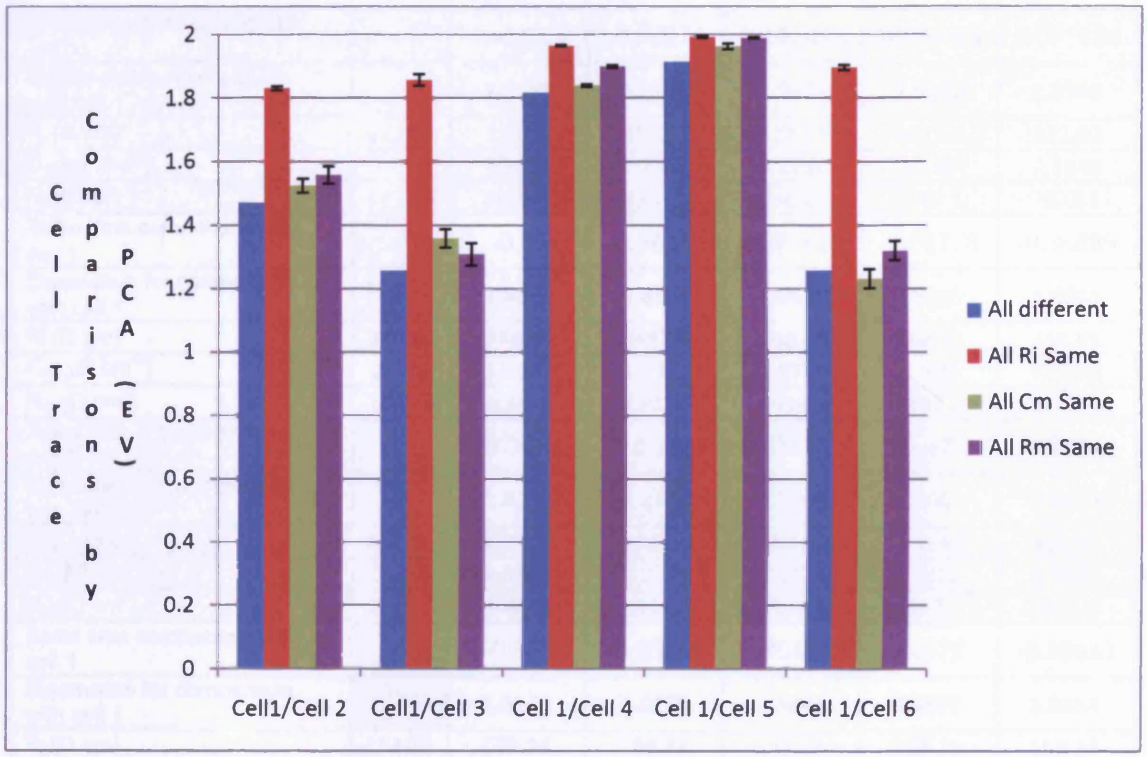

Figure 6.13: Gap-junction coupled MC pairs that have identical R_i exhibit better synchrony measured by PCA (red columns EV closer to 2).

Eigenvalue differences for comparisons of somatic membrane voltage recordings for cell1 and the other cells in simulations from a 6 MC apical dendrite tuft gap-junction connected network model. Cell 2 is given a constant current injection to 20 locations to give tonic firing. Cell 3 receives the same current injection to 20 locations but the start is delayed by 10 msec. The groups compare simulation set-ups in which all MCs have their own different passive parameters with simulation set-ups in which one of the passive parameters is set to identical values for all of the cells. The differences where all passive parameters are different are PCA comparisons of 300 msec simulations of somatic membrane potential. While those for one identical passive parameter are the means of PCA comparisons of 300 ms simulations of somatic membrane potential from 6 simulations each with a different setting for the fixed passive parameter.

	Cell 1	Cell 2	Cell 3	Cell4	Cell 5	Cell 6
Spike time comparison with cell 1		-0.55	-0.41974	0.102632	0.023684	0.023684
Eigenvalue for comparison with cell 1		1.8352	1.8875	1.9612	1.9932	1.8999
R_i (Ω cm)	322.92	322.92	322.92	322.92	322.92	322.92
C_m (μF cm^{-2})	2.026	1.9267	1.7722	1.9744	1.599	2.1649
R_m (Ω cm^2)	1275.8	4099.9	2301.3	3914.7	6867.1	2823.1
Spike time comparison with cell 1		-0.55	-0.46111	0.073611	-0.02778	-0.38889
Eigenvalue for comparison with cell 1		1.8322	1.8672	1.9633	1.9929	1.8905
R_i (Ω cm)	248.95	248.95	248.95	248.95	248.95	248.95
C_m (μF cm^{-2})	2.026	1.9267	1.7722	1.9744	1.599	2.1649
R_m (Ω cm^2)	1275.8	4099.9	2301.3	3914.7	6867.1	2823.1
Spike time comparison with cell 1		-0.5625	-0.50469	0.053125	-0.075	-0.39844
Eigenvalue for comparison with cell 1		1.8254	1.8458	1.9641	1.9883	1.8853
R_i (Ω cm)	168.94	168.94	168.94	168.94	168.94	168.94
C_m (μF cm^{-2})	2.026	1.9267	1.7722	1.9744	1.599	2.1649
R_m (Ω cm^2)	1275.8	4099.9	2301.3	3914.7	6867.1	2823.1
Spike time comparison with cell 1		-0.565	-0.50833	0.053333	-0.075	-0.39833
Eigenvalue for comparison with cell 1		1.8243	1.8427	1.9644	1.9872	1.8854
R_i (Ω cm)	153.23	153.23	153.23	153.23	153.23	153.23
C_m (μF cm^{-2})	2.026	1.9267	1.7722	1.9744	1.599	2.1649
R_m (Ω cm^2)	1275.8	4099.9	2301.3	3914.7	6867.1	2823.1
Spike time comparison with cell 1		-0.50882	-0.49118	0.125	-0.00588	-0.34412
Eigenvalue for comparison with cell 1		1.8406	1.8405	1.9637	1.9927	1.9014
R_i (Ω cm)	83.051	83.051	83.051	83.051	83.051	83.051
C_m (μF cm^{-2})	2.026	1.9267	1.7722	1.9744	1.599	2.1649
R_m (Ω cm^2)	1275.8	4099.9	2301.3	3914.7	6867.1	2823.1
Spike time comparison with cell 1		-0.53929	-0.46071	0.144643	0.005357	-0.32857
Eigenvalue for comparison with cell 1		1.8278	1.8507	1.9668	1.9936	1.9052
R_i (Ω cm)	62.258	62.258	62.258	62.258	62.258	62.258
C_m (μF cm^{-2})	2.026	1.9267	1.7722	1.9744	1.599	2.1649
R_m (Ω cm^2)	1275.8	4099.9	2301.3	3914.7	6867.1	2823.1
Spike time descriptive statistics		Cell1/Cell2	Cell1/Cell3	Cell1/Cell4	Cell1/Cell5	Cell1/Cell6
Mean for all Rm Same		-0.54545	-0.40101	0.070202	-0.02323	-0.31212
Standard Deviation		0.023518	0.152902	0.046521	0.046737	0.145044
Count		99	99	99	99	99
Confidence Level(99.0%)		0.006209	0.040369	0.012282	0.012339	0.038294
Eigenvalue descriptive statistics		Cell1/Cell2	Cell1/Cell3	Cell1/Cell4	Cell1/Cell5	Cell1/Cell6
Mean for all Rm Same		1.830917	1.855733	1.963917	1.991317	1.894617
Standard Deviation		0.006288	0.018257	0.00181	0.002801	0.008656
Count		6	6	6	6	6
Confidence Level(99.0%)		0.010351	0.030053	0.00298	0.004611	0.014249

Table 6.4: Details of simulations and results carried out to produce "All R_i same" columns in Figures 6.12 and 6.13.

Key	Cell 1	Cell 2	Cell 3	Cell4	Cell 5	Cell 6
Spike time comparison with cell 1		-1.275	-1.59531	-0.55469	0.20625	-1.83281
Eigenvalue for comparison with cell 1		1.4967	1.3257	1.8330	1.9562	1.1964
R_i (Ω cm)	322.92	153.23	83.051	168.94	248.95	62.258
C_m (μF cm^{-2})	2.1649	2.1649	2.1649	2.1649	2.1649	2.1649
R_m (Ω cm^2)	1275.8	4099.9	2301.3	3914.7	6867.1	2823.1
Spike time comparison with cell 1		-1.20441	-1.51176	-0.52647	0.205882	-1.73676
Eigenvalue for comparison with cell 1		1.5105	1.3399	1.8375	1.9564	1.2113
R_i (Ω cm)	322.92	153.23	83.051	168.94	248.95	62.258
C_m (μF cm^{-2})	2.026	2.026	2.026	2.026	2.026	2.026
R_m (Ω cm^2)	1275.8	4099.9	2301.3	3914.7	6867.1	2823.1
Spike time comparison with cell 1		-1.18676	-1.48676	-0.51765	0.201471	-1.70147
Eigenvalue for comparison with cell 1		1.5178	1.3480	1.8398	1.9568	1.2201
R_i (Ω cm)	322.92	153.23	83.051	168.94	248.95	62.258
C_m (μF cm^{-2})	1.9744	1.9744	1.9744	1.9744	1.9744	1.9744
R_m (Ω cm^2)	1275.8	4099.9	2301.3	3914.7	6867.1	2823.1
Spike time comparison with cell 1		-1.16029	-1.45	-0.50147	0.2	-1.66765
Eigenvalue for comparison with cell 1		1.5241	1.3552	1.8418	1.9572	1.2277
R_i (Ω cm)	322.92	153.23	83.051	168.94	248.95	62.258
C_m (μF cm^{-2})	1.9267	1.9267	1.9267	1.9267	1.9267	1.9267
R_m (Ω cm^2)	1275.8	4099.9	2301.3	3914.7	6867.1	2823.1
Spike time comparison with cell 1		-1.10667	-1.365	-0.505	0.135	-1.58
Eigenvalue for comparison with cell 1		1.5379	1.3809	1.8384	1.9723	1.2515
R_i (Ω cm)	322.92	153.23	83.051	168.94	248.95	62.258
C_m (μF cm^{-2})	1.7722	1.7722	1.7722	1.7722	1.7722	1.7722
R_m (Ω cm^2)	1275.8	4099.9	2301.3	3914.7	6867.1	2823.1
Spike time comparison with cell 1		-1.025	-1.26094	-0.46406	0.129688	-1.46094
Eigenvalue for comparison with cell 1		1.5588	1.4060	1.8450	1.9756	1.2800
R_i (Ω cm)	322.92	153.23	83.051	168.94	248.95	62.258
C_m (μF cm^{-2})	1.599	1.599	1.599	1.599	1.599	1.599
R_m (Ω cm^2)	1275.8	4099.9	2301.3	3914.7	6867.1	2823.1
Spike time descriptive statistics		Cell1/Cell2	Cell1/Cell3	Cell1/Cell4	Cell1/Cell5	Cell1/Cell6
Mean for all Rm Same		-1.16097	-1.44694	-0.51173	0.180867	-1.66531
Standard Deviation		0.079144	0.10741	0.030504	0.049064	0.117843
Count		98	98	98	98	98
Confidence Level(99.0%)		0.021006	0.028508	0.008096	0.013022	0.031277
Eigenvalue descriptive statistics		Cell1/Cell2	Cell1/Cell3	Cell1/Cell4	Cell1/Cell5	Cell1/Cell6
Mean for all Rm Same		1.5243	1.35928333	1.83925	1.96241667	1.23116667
Standard Deviation		0.02177016	0.02931644	0.00406731	0.00900098	0.03011987
Count		6	6	6	6	6
Confidence Level(99.0%)		0.0358362	0.04825825	0.00669526	0.01481665	0.04958079

Table 6.5: Details of simulations and results carried out to produce "All C_m same" columns in Figures 6.12 and 6.13.

Key	Cell 1	Cell 2	Cell 3	Cell4	Cell 5	Cell 6
Spike time comparison with cell 1		-1.05789	-1.50921	-0.35	-0.07763	-1.50395
Eigenvalue for comparison with cell 1		1.5702	1.3179	1.9018	1.9919	1.3286
R_i (Ω cm)	322.92	153.23	83.051	168.94	248.95	62.258
C_m (μF cm^{-2})	2.026	1.9267	1.7722	1.9744	1.599	2.1649
R_m (Ω cm^2)	6867.1	6867.1	6867.1	6867.1	6867.1	6867.1
Spike time comparison with cell 1		-1.04853	-1.48382	-0.35294	-0.09412	-1.48971
Eigenvalue for comparison with cell 1		1.5741	1.3291	1.9009	1.9882	1.3369
R_i (Ω cm)	322.92	153.23	83.051	168.94	248.95	62.258
C_m (μF cm^{-2})	2.026	1.9267	1.7722	1.9744	1.599	2.1649
R_m (Ω cm^2)	4099.9	4099.9	4099.9	4099.9	4099.9	4099.9
Spike time comparison with cell 1		-1.04853	-1.48382	-0.35588	-0.1	-1.49265
Eigenvalue for comparison with cell 1		1.5734	1.3289	1.9005	1.9879	1.3363
R_i (Ω cm)	322.92	153.23	83.051	168.94	248.95	62.258
C_m (μF cm^{-2})	2.026	1.9267	1.7722	1.9744	1.599	2.1649
R_m (Ω cm^2)	3914.7	3914.7	3914.7	3914.7	3914.7	3914.7
Spike time comparison with cell 1		-1.05	-1.48833	-0.36667	-0.11	-1.49333
Eigenvalue for comparison with cell 1		1.5727	1.3313	1.8987	1.9869	1.3366
R_i (Ω cm)	322.92	153.23	83.051	168.94	248.95	62.258
C_m (μF cm^{-2})	2.026	1.9267	1.7722	1.9744	1.599	2.1649
R_m (Ω cm^2)	2823.1	2823.1	2823.1	2823.1	2823.1	2823.1
Spike time comparison with cell 1		-1.06471	-1.50147	-0.36912	-0.10294	-1.50882
Eigenvalue for comparison with cell 1		1.5569	1.3074	1.8959	1.9866	1.3165
R_i (Ω cm)	322.92	153.23	83.051	168.94	248.95	62.258
C_m (μF cm^{-2})	2.026	1.9267	1.7722	1.9744	1.599	2.1649
R_m (Ω cm^2)	2301.3	2301.3	2301.3	2301.3	2301.3	2301.3
Spike time comparison with cell 1		-1.12083	-1.57639	-0.36944	-0.09444	-1.56944
Eigenvalue for comparison with cell 1		1.5056	1.2409	1.8918	1.9881	1.2604
R_i (Ω cm)	322.92	153.23	83.051	168.94	248.95	62.258
C_m (μF cm^{-2})	2.026	1.9267	1.7722	1.9744	1.599	2.1649
R_m (Ω cm^2)	1275.8	1275.8	1275.8	1275.8	1275.8	1275.8
Spike time descriptive statistics		Cell1/Cell2	Cell1/Cell3	Cell1/Cell4	Cell1/Cell5	Cell1/Cell6
Mean for all Rm Same		-1.0657767	-1.5082524	-0.3604369	-0.0958738	-1.5104369
Standard Deviation		0.02865239	0.03760416	0.01238885	0.01569356	0.03199346
Count		103	103	103	103	103
Confidence Level(99.0%)		0.0074106	0.00972587	0.00320423	0.00405895	0.00827473
Eigenvalue descriptive statistics		Cell1/Cell2	Cell1/Cell3	Cell1/Cell4	Cell1/Cell5	Cell1/Cell6
Mean for all Rm Same		1.55881667	1.30925	1.89826667	1.98826667	1.31921667
Standard Deviation		0.02684872	0.03468808	0.00379508	0.00189807	0.02987155
Count		6	6	6	6	6
Confidence Level(99.0%)		0.04419609	0.05710059	0.00624715	0.00312444	0.04917203

Table 6.6: Details of simulations and results carried out to produce "All R_m same" columns in Figures 6.12 and 6.13.

Discussion

In the Migliore model (Migliore et al., 2005) asynchronous firing mitral cells rapidly synchronise across gap-junctions. Using the same set up as the Migliore model (Migliore et al., 2005) the spiking of two mitral cells becomes synchronised even more efficiently when using the reconstructed cells with the fitted passive parameters. This is because the coupling ratios achieved with 100 gap-junctions in the reconstructed cell model is ~42% higher than the Migliore model (Migliore et al., 2005). Differences between the passive parameters of the two mitral cells do not affect the ability of the gap-junctions to mediate synchronisation. However, these differences in passive parameters are visible in the sub threshold depolarisations.

When four further mitral cells are added to the gap-junction network the coupling ratio between the two test mitral cells is substantially reduced (~-23%). The extra four cells and extra gap-junctions required for networking produce a current sink that reduces coupling ratios between individual pairs. The requirement for a higher current injection to maintain firing frequency is further evidence of the current sink effect of the mitral cell network. The net result over and above the requirement for higher input is that synchronisation is no longer so efficient. Tight clumping of spikes is achieved rather than complete synchronisation.

One of the reasons for the lack of synchrony across the network is the difference in PPs between individual cells. The MCs in the model are from different animals and different locations within the OB. By carrying out a range of different simulations in which one of the individual passive parameters is fixed to a single value for all the cells it is possible to show that differences in R_i between the cells of the model has a greater influence on synchronisation than the other passive parameters. There are a number of factors that are now coming together to construct a consistent story about how synchronisation of a intraglomerular population of MCs might be achieved:

1. For the same MC coupling ratio (see section above "Network Connections and Firing Synchronisation Test"), synchronisation is better with a greater number of lower conductance apical dendrite tuft gap-junctions (100 gap-junctions per pair MCs was better than 1 or 10 with the conductance in all cases adjusted to achieve the same coupling ratio). This suggests that proximity of the gap-junctions to the current injection improves the degree of synchronisation.

2. For the same total current input amplitude, synchronisation is better with a larger number of lower value current injections. This fits with point 1 in that if the input has close proximity to gap-junctions of relatively low individual conductance a large number of relatively low current inputs will not be restricted so much by the gap-junction conductance threshold and the total current flow across all the gap-junctions will be greater.

3. The final piece in this gap-junction circuit is intracellular resistance. If R_i for all the cells is the same the current flows most easily in all directions. Otherwise current will tend to flow in the direction of least resistance which will not aid synchrony. This raises the question of whether R_i might be tuned across intraglomerular populations of MCs? It is feasible that channel conductances might vary to achieve a certain value of R_i, but it would need experimental measurements to verify if this happens in practice. Since the reconstructed MCs in this study were from different populations, their R_is naturally vary. However, it could also be the case that the integration of output from

the population of MCs by the next level of neurons is such that a tighter synchronisation would be of no benefit. In this case tuning of all the passive parameters or just that of R_i would not be needed. But this analysis has identified one of the causes of variance even if the degree of variance subsequently proves to have no systems significance because of the integrative abilities of downstream neurons.

The Migliore model uses a basic set of active properties that just includes those channel mechanisms required to produce action potentials (Na, K_{dr} and K_A). Mitral cells however are endowed with a greater diversity of channel mechanisms and also display glutamate self excitation from AMPA receptors. It is possible that some of these mechanisms compensate for the current sink properties of the network, enhancing the coupling ratio and improving synchronisation. In Chapter 6 these mechanisms are added and I investigate their effects on coupling ratios and synchronisation.

Chapter 7 : Extending the Scope of the model to include calcium mechanisms

In the previous chapter we looked at synchronisation of a small population of MCs across apical dendrite tuft gap-junctions. For this I used the Migliore model (Migliore et al. 2005) Na, K_{dr} and K_A channel mechanisms. Migliore and co-workers in their paired MC synchronisation tests deliberately stuck to this simple set of channel mechanisms and evoked tonic firing by a continuous injection current. This was to avoid complicating sources of periodicity that might influence the synchronisation of the paired MCs. Now that I have explored the simple Migliore case in a small network it is time to start looking at the range of modulatory mechanisms. I have chosen to start with calcium modulation.

As we have seen in Chapter 2, MCs are known to have a range of other channel mechanisms and the Bhalla and Bower model (Bhalla and Bower 1993) made use of implementations for L-type calcium, and KCa channel mechanisms and a sub membrane calcium ion pool. Bhalla and Bower (1993) used "brute force[18]" fitting techniques to plot the parameter space for the densities of the calcium mechanisms. Their parameters were fitted to current-clamp recordings in the presence of current blocking agents (Jahr and Nicoll 1982b, Mori et al. 1981a).

The channel parameters in the Bhalla and Bower model (1993) were[19]:

MC calcium channel (modified from De Schutter and Bower 1991 and Hirano and Hagiwara 1989)

Equation 7.1

$$g_K = \bar{g}_{Ca} . s . r^{20}$$

Equation 7.2

$$\alpha_s = 7.5/(1 + \exp\left(\frac{13 - v}{7}\right))$$

Equation 7.3

$$\beta_s = 1.65/(1 + \exp\left(\frac{v - 14}{4}\right))$$

[18] Brute force fitting techniques involve mapping out the whole parameter space so the regions of best fit can be studied. This differs from the fitting methods used in Chapter 5 for the fitting of the passive parameters that used an algorithm to search the parameter space to find an optimum fit.

[19] These are the equations published in Bhalla and Bower (1993) the implementations of the equations that were used in carrying out the work in Bhalla and Bower (1993) in Genesis script language were published at http://senselab.med.yale.edu/modeldb/ShowModel.asp?model=2733, the differences are discussed in the text of this chapter. Also see note on Hodgkin-Huxley notation below equations that explains gating variables and how they are derived from the α and β equations.

[20] The Hodgkin Huxley notation used in these equations is explained at the end of this group of equations. The values 's' and 'r' are gating variables that conform to the HH notation.

Equation 7.4

$$\alpha_r = 6.8 * 10^{-3}/(1 + \exp\left(\frac{v + 30}{12}\right))$$

Equation 7.5

$$\beta_r = 0.06/(1 + \exp\left(-\frac{v}{11}\right))$$

MC KCa Channel (x represents calcium ion concentration, modified from Traub 1982)

Equation 7.6

$$g_{KCa} = \bar{g}_{KCa} \cdot y^{21}$$

Equation 7.7

$$\alpha_y = \exp\left(\frac{v - 65}{27}\right) * (500(0.015 - x)/(\exp\left(\frac{0.015 - x}{0.0013}\right) - 1)$$

Equation 7.8

$$\beta_y = 0.05$$

The notation for these equations follow the Hodgkin-Huxley formalism i.e. an ion conductance (g_{ion}) is equal to the product of its maximum conductance ($gbar_{ion}$[22]) and identified gating variables. These gating variables are described by a differential equation of the format:

$$\frac{d_{gating\ variable}}{dt} = \alpha_{gating\ variable}(v)(1 - gating\ variable) - \beta_{gating\ variable}(v) gating\ variable$$

v = membrane potential (volts), x = [Ca^{2+}] in the local compartment calcium pool.

I implemented the Bhalla and Bower channel mechanisms in ChannelML (with the help of Padraig Gleason, UCL). This was to allow the use of the Bhalla and Bower channel mechanisms with the Migliore channel mechanisms using neuroConstruct. The originals were implemented in an early version of the Genesis script language. The L-type calcium channel was a straight forward conversion, but the KCa channel proved more problematic. It was originally created using an obsolete Genesis object called a vdep channel. The vdep channel

[21] The Hodgkin Huxley notation used in these equations is explained at the end of this group of equations. The value 'y' is a gating variable that conform to the HH notation.

[22] The value, gbar here, is a longhand version of the symbol after the = sign in equation 6.1, which is used as the symbol does not exist in Microsoft font libraries. For modelling purposes, the value gbar is the maximum conductance possible through the total examples of particular type of ion channel represented at a particular compartment. In the model, this value is specified for the compartments (where required either individually or in groups e.g. all compartments of the apical dendrite tuft) and somewhat confusingly is referred to as a channel density as it denotes the total maximum conductance for examples of that channel on the compartment. This value is also often referred to as gmax instead of the original Hodgkin-Huxley notation of gbar.

was incompatible with integrator routines that speed up the running of calculations during simulations so was replaced by tabchannel and tab2Dchannel mechanisms.

Unfortunately the implementation of a set of equations in a script can have an effect on the behaviour of a mechanism. Modelling of neurons, like any other branch of science, requires comparability of experiments within the corpus of published literature. For mitral cells the two key works that need to be referenced for experimental comparisons are Bhalla and Bower (1993) and Migliore et al (2005). In Chapter 6, I only proceeded with my own network synchronisation tests once I had managed to replicate the synchronisation findings of Migliore et al (2005) on a two cell setup. In this chapter establishing the comparisons of implementations of ion channels is needed to ensure that my model conforms to the optimised parameter space of Bhalla and Bower (1993). Their brute force fitting revealed a robust distinct parameter space in MCs which produced stable burst firing. So where I find differences in channel mechanism implementation I need to quantify those differences. Then establish if by adjustment, the model can be made to conform to the Bhalla and Bower (1993) parameter space to produce stable burst firing.

I will go through the details of the scripts in due course and the differences observed, but first will give details of the comparison process. So as to minimise any differences between implementations and ensure the accuracy of the a translation of an original implementation and ChannelML implementation side by side simulations are carried out in a simple cell with all other parameters identical (Figure 7.1).

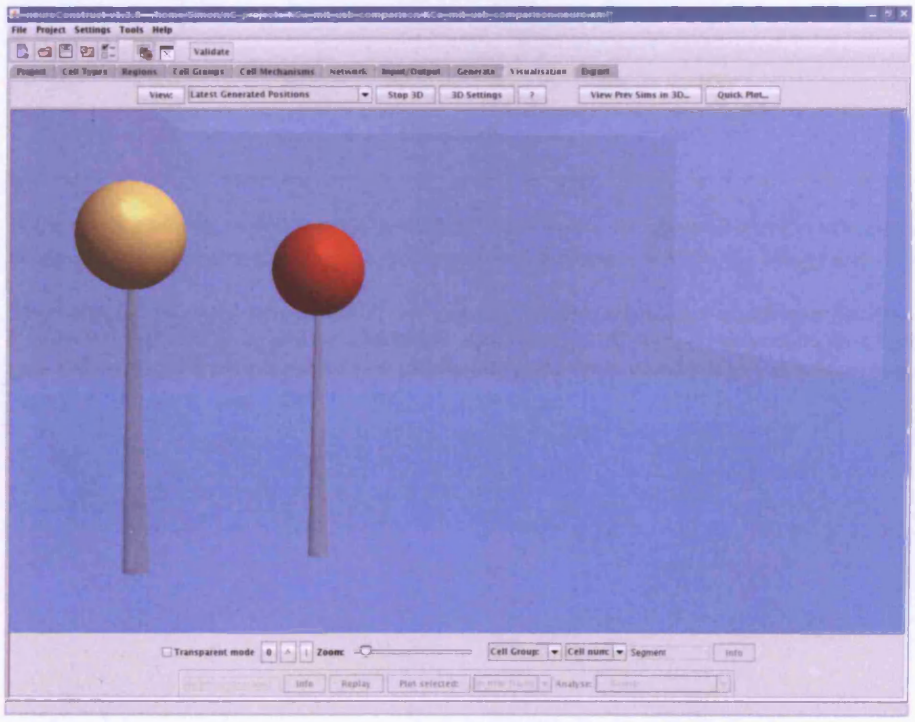

Figure 7.1: Simple neuron set up used for perfecting XML translations of ion channel implementation code.

Comparison simulations are used to assess the accuracy of translation for channel mechanisms from the original Genesis script file to a ChannelML version for use in neuroConstruct. For these simulations two identical cells are set up consisting of a single segment soma with a total surface area of 1671 μm^2 (radius of spherical cell fitted to i/o response for the passive reconstructed cell). The passive parameters were set at values from one of the fitted cells at C_m 2.03 x 10^{-8} $\mu F\ \mu m^{-2}$; R_i 3229.2 $k\Omega\ \mu m$ and R_m 7.84 x 10^{-9} $mS\ \mu m^{-2}$ as a leak potential with a reversal potential -65 mV. The membrane potential is initialised at -65 mV and current injections of 0.2 nA are applied after 20 msec for a duration of 60 msec.

The comparison simulations are set up with original Genesis versions and ChannelML versions of the L-type calcium channel at a density of 4.0×10^{-8} mS μm^{-2}; KCa channel at a density of 1.42×10^{-7} mS μm^{-2}; Ca pool with a resting $[Ca^{2+}]$ of 5.2×10^{-6} mM a sub membrane shell thickness 10^{-6} metres and a decay constant of 0.01 seconds (Figures 7.2 and 7.3).

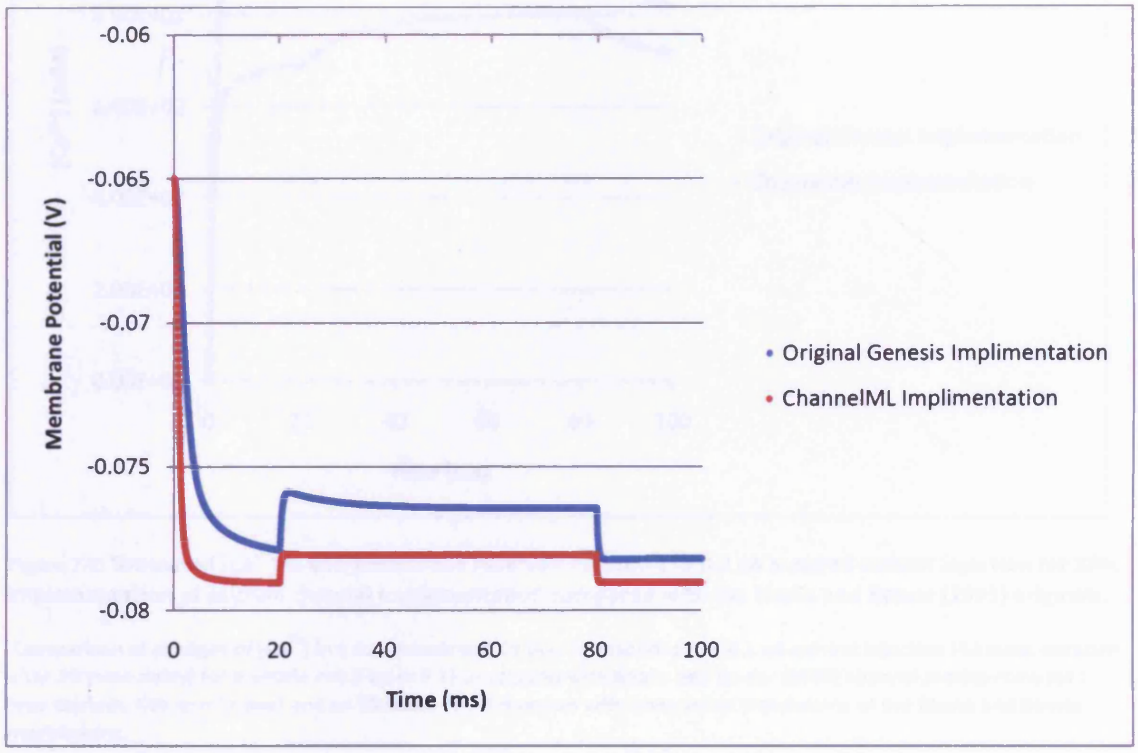

Figure 7.2: Simulated membrane potential response to 0,2 nA stepped current injection for XML implementation of calcium channel implementation compared with the Bhalla and Bower (1993) originals.

Comparison of the membrane potential response to a 0.2 nA current injection (60 msec duration after 20 msec delay) for a simple cell (Figure 7.1) simulation with Bhalla and Bower (1993) channel mechanisms for L-type calcium, KCa and Ca pool and an identical cell simulation with ChannelML translations of the Bhalla and Bower mechanisms.

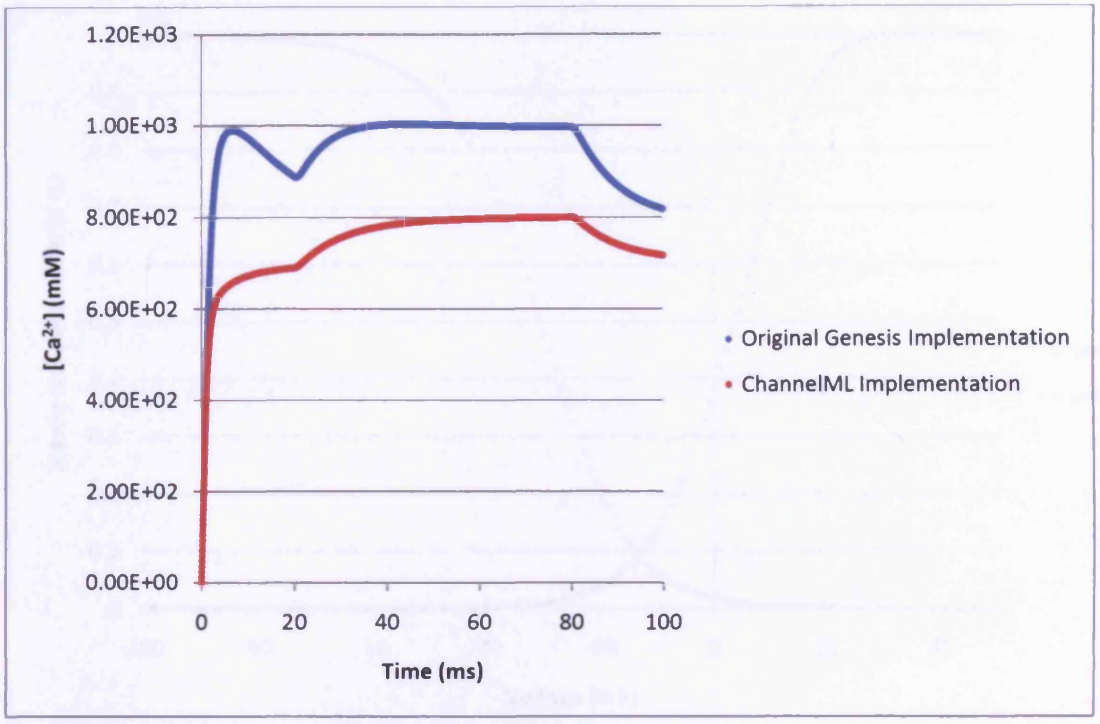

Figure 7.3: Simulated $[Ca^{2+}]$ in sub-membrane reservoir response to 0.2 nA stepped current injection for XML implementation of calcium channel implementation compared with the Bhalla and Bower (1993) originals.

Comparison of changes of $[Ca^{2+}]$ in a sub membrane Ca pool in response to a 0.2 nA current injection (60 msec duration after 20 msec delay) for a simple cell (Figure 7.1) simulation with Bhalla and Bower (1993) channel mechanisms for L-type calcium, KCa and Ca pool and an identical cell simulation with ChannelML translations of the Bhalla and Bower mechanisms.

In the simulated membrane potential recording (Figure 7.2) the membrane potential initial drops rapidly from the initiation potential of -65 mV until it approaches E_K the reversal potential for potassium ions for the KCa channel of -80 mV. This is possible because the L-type calcium channel allows the flow of calcium ions into the calcium pool. This would at first appear unlikely considering the steady state activation variables of the L-type calcium channel (Figure 7.4). However the value for 's' in Equation 1is not actually zero, at t = 0, s = 6.58 x 10^{-5} and r = 0.975 and when multiplied by gbar (gmax) for the L-type calcium channel of 4.0 x 10^{-8} produces a value for conductance of 2.57 x 10^{-12}. This is sufficient to produce the calcium influx depicted in Figure 6.3.

Equation 7.9

$$g_K = \bar{g}_{Ca}.s.r$$

In Figure 7.3, the decay in $[Ca^{2+}]$ that is observed towards the end of both simulated recordings and at the lead up to the current injection for the original Genesis version is a function of the calcium pool object. In the living cell a calcium pump would be responsible for such a decay, but as a simple method of modelling this, a decay is given with a decay constant (tau) of 0.01 seconds. The fact that the decay in $[Ca^{2+}]$ at this point is able to overcome the rate of calcium coming into the cell is due to the KCa channel hyperpolarising the cell to a point where the decay is greater than influx through the L-type calcium channel. So the KCa channel provides a part of a feedback mechanism that reduces L-type calcium channel conductance in response to rising $[Ca^{2+}]$ levels in the calcium pool.

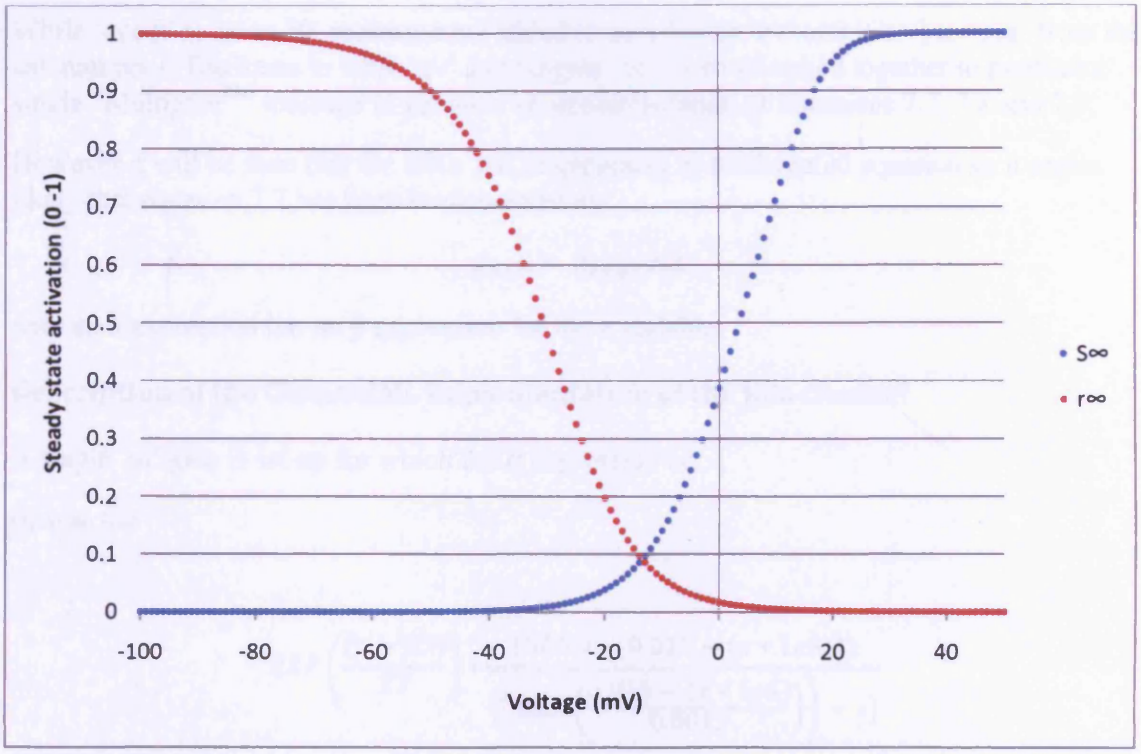

Figure 7.4: Steady state activation variables responses for the Bhalla and Bower L-type calcium channel plotted against membrane potential.

Now that I have explained some of the characteristics of the simulated recordings in Figures 7.2 and 7.3 I can look at the main purpose of the figures, which is to compare the ChannelML implementations with the original Genesis implementation. Clearly there is some discrepancy between the implementation as depicted in Figures 7.2 and 7.3. The ChannelML implementation follows the equations precisely. Therefore we need to look at the script for the original KCa vdep channel in comparison to the ChannelML version to understand what the differences are.

Description of the 'vdep' implementation of the KCa channel

In the vdep version (see Appendix for script listing) we see that a table called 'qv' is filled with:

Equation 7.10

$y = (\exp\left(\frac{v-(-0.065)}{0.027}\right))$ where v = voltage

and a tabgate called 'qca' is set-up with an α equation:

Equation 7.11

$y(x) = ((5.0e^5 * 0.015) + (-5.0e^5) * x)/(-1 + \exp\left(\frac{x+(-0.015)}{-0.0013}\right))$, where x = $[Ca^{2+}]$.

While 'qca β' is set to 50, messages are added to pass Vm to 'qv' and [Ca^{2+}] to 'qca' from the calcium pool. The items in table 'qv' and tabgate 'qca' are multiplied together to produce a single "Multigate[23]" message to generate an implementation of Equations 7.7, 7.8 and 7.9.

However it will be seen that the table 'qv' is generated as a diferential equation so it seems likely that equation 7.7 has been implemented as:

$$g_{KCa} = \bar{g}_{KCa} \cdot y \cdot z$$

with an α expression but no β expression for the z variable.

Description of the ChannelML implementation of the KCa channel

A single 'm' gate is set-up for which the α expression is:

Equation 7.12

$$EXP\left(\frac{(v-65)}{27}\right) * \frac{(500.0 * (0.015 - (x * 1e6)))}{(\left(EXP\left(\frac{0.015 - (x * 1e6)}{0.0013}\right)\right) - 1)}$$

where v = membrane voltage and x = [Ca^{2+}] (mM)

while β_m is set to 0.05.

Comparisons

The vdep implementation has its voltage dependency in SI Units (volts) rather than physiological units (millivolts) so the top half of Equation 6.10 has been multiplied by 1000 to compensate. Also the missing bracket in the published equation at the end of the top line of Ca dependant part has been replaced.

The channelML implementation of the KCa channel is almost precisely the same as the published equations, except that the [Ca^{2+}] is multiplied by a factor of 10^6 (this corrects a neuroConstruct internal correction that is not needed in this case so for the purpose of the equations, this value can be ignored as the two corrections cancel each other out). Again the top half of the Ca-dependent part of the equation has a bracket replaced closing that expression.

A number of strategies were tried to adjust the ChanneML implementation to give a closer approximation to the original Genesis implementation. Adjusting the SI unit correction factor

---

[23] Notes from Genesis reference manual: A vdep_channel calculates Gk by multiplying gbar by any number of factors of the form (gate_state)^(power). These are typically received with the MULTGATE message from a tabgate element. For example, Gk = gbar*h*m^3 could be implemented with:

```
addmsg Na_squid/m Na_squid MULTGATE m 3
addmsg Na_squid/h Na_squid MULTGATE m 1
```

Here, m and h are vdep_gate or tabgate elements, and Na_squid is a vdep_channel. Note that the field for the gate variable is called 'm', regardless of the name of the gate element.

up from 1000 to 10,000 gave some improvement, but a close fit could only be achieved by a ChannelML implementation if a two gate approach is taken. The justification for this is that in the original Genesis implementation, the voltage dependent part of the equation is handled as a separate differential equation to fill the qv table as if it was a separate gate, but with just an α value. The problem with this is that in channelML implementations both gates must have a β value. I tried many different values and found that I could fit the curve using values for m β and z β. The optimal values that I found were m β = 0.008 and z β = 0.0021 (Figure 7.5 and 7.6, ChannelML Implementation 2 gate Mod 1 gives an almost perfect fit to the original Genesis implementation).

```
//=============================================================================
// ChannelML 2 gate implementation of KCa_mit_usb
//=============================================================================

<current_voltage_relation cond_law="ohmic" ion="k" default_gmax="3.6" default_erev="-80">
      <conc_dependence name="Calcium" ion="ca" charge="2" variable_name="ca_conc"
min_conc="0" max_conc="1e-8"/>
    <gate name="m" instances="1">
      <closed_state id="m0"/>
      <open_state id="m" fraction="1"/>
      <transition name="alpha" from="m0" to="m" expr_form="generic" expr="(exp ((v-65)/27))"/>
          <transition name="beta" from="m" to="m0" expr_form="generic" expr="0.008"/>
    </gate>
    <gate name="z" instances="1">
                  <closed_state id="z0"/>
                  <open_state id="z" fraction="1"/>
        <transition name="alpha" from="z0" to="z" expr_form="generic" expr="(500.0*(0.015 -
(ca_conc*1e6)))/( (exp ((0.015 - (ca_conc*1e6))/0.0013)) -1)"/>
                  <transition name="beta" from="z" to="z0" expr_form="generic" expr="0.0021"/>
    </gate>
 </current_voltage_relation>
```

It is now clear that vdep object and tab2D object implemented via ChannelML perform differently. When Bhalla and Bower carried out their brute force fitting they found that the optimal parameter space was broad. As in my MC model I am using the Migliore et al. (2005) Neuron based Na, K_{dr} and K_A channels it makes sense to use ChannelML implementations so as to be able to use the Genesis implementations in Neuron via neuroConstruct. I will therefore start by trying two different implementations of the MC model. One will use the standard ChannelML implementation of the KCa channel, while the other will use the 2 gate modification with the fitted β values that I used to get as close as possible to the original Genesis vdep implementation. This will enable me to assess the relative effect of the difference between the vdep and ChannelML implementation in a complete cell model. If there is little difference between them or the difference can be overcome by some tuning of the model it will be better to continue with the less complicated ChannelML implementation rather than the two gate version.

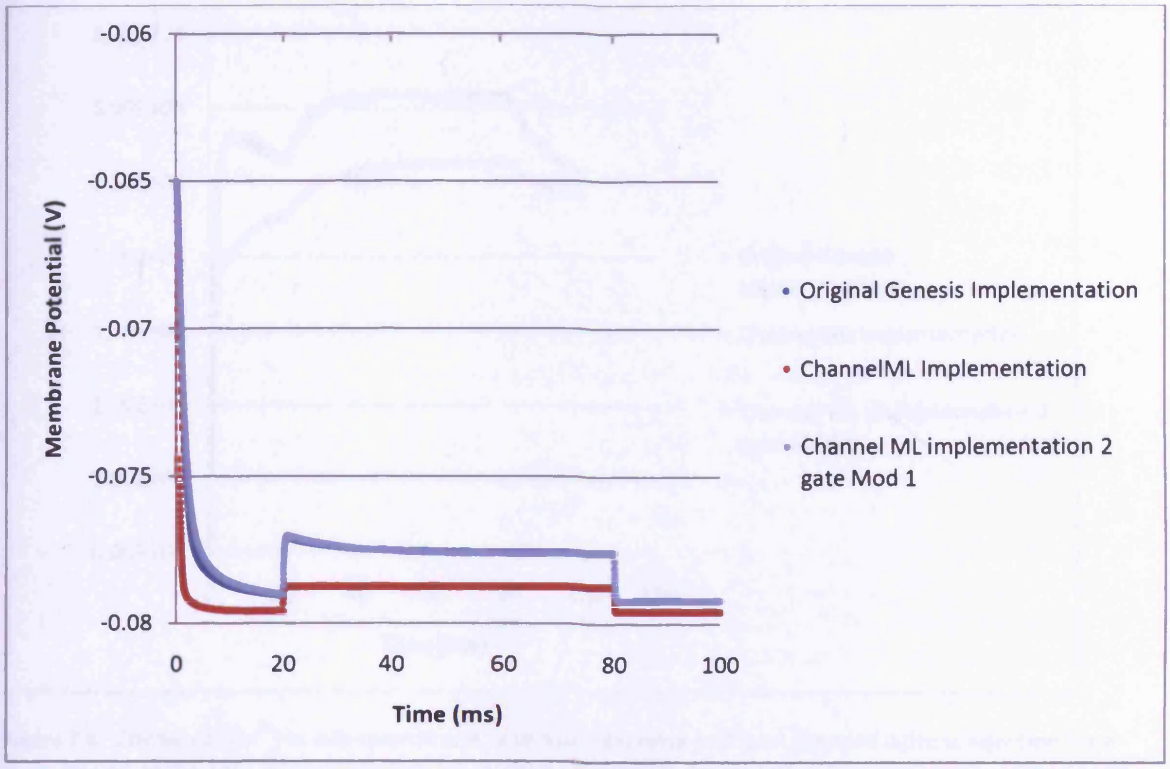

Figure 7.5: Simulated membrane potential response to 0,2 nA stepped current injection for a new version of the XML implementation of calcium channel implementation that has been modified to fit the Bhalla and Bower (1993) originals.

Comparison of the membrane potential response to a 0.2 nA current injection (60 msec duration after 20 msec delay) for a simple cell (Figure 7.1) simulation with Bhalla and Bower (1993) channel mechanisms for L-type calcium, KCa and Ca pool and an identical cell simulation with ChannelML translations of the Bhalla and Bower mechanisms. In an attempt at getting the response closer to that of the original Bhalla and Bower Genesis vdep channel, a two gate implementation was used in which the β variables are adjusted to fit to the vdep response.

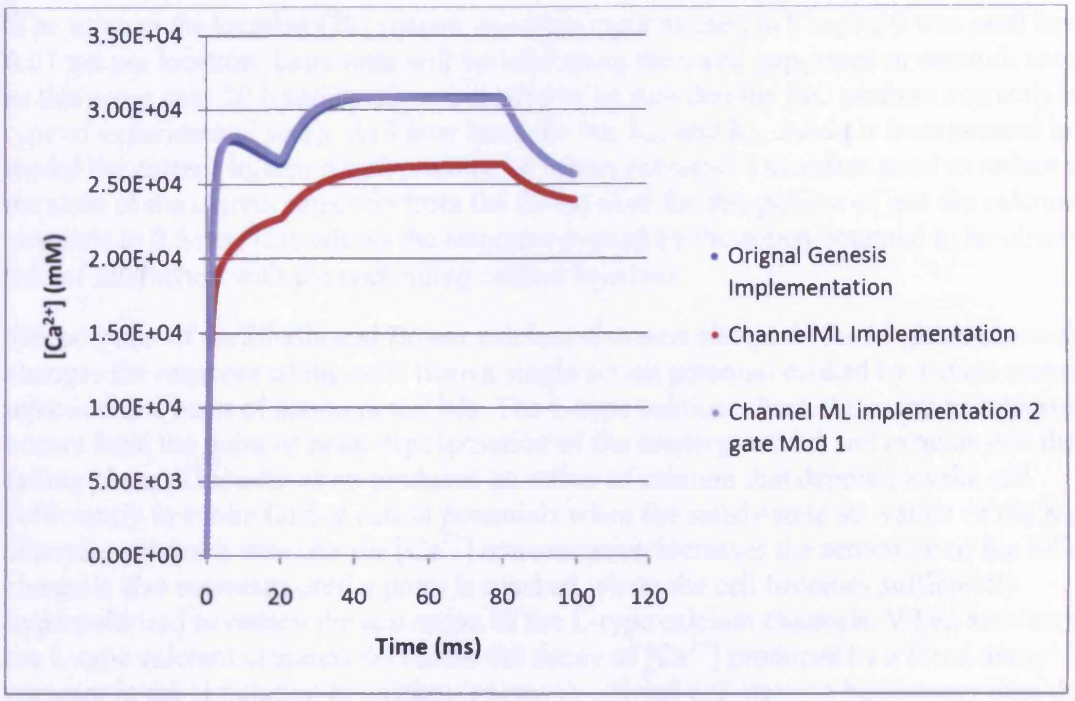

Figure 7.6: Simulated $[Ca^{2+}]$ in sub-membrane reservoir response to 0.2 nA stepped current injection for a new version of the XML implementation of calcium channel implementation that has been modified to fit the Bhalla and Bower (1993) originals.

Comparison of changes of $[Ca^{2+}]$ in a sub membrane Ca pool in response to a 0.2 nA current injection (60 msec duration after 20 msec delay) for a simple cell (Figure 7.1) simulation with Bhalla and Bower (1993) channel mechanisms for L-type calcium, KCa and Ca pool and an identical cell simulation with ChannelML translations of the Bhalla and Bower mechanisms. In an attempt at getting the response closer to that of the original Bhalla and Bower Genesis vdep channel, a two gate implementation was used in which the β variables are adjusted to fit to the vdep response.

Full Mitral Cell Test

Following the analysis of the Bhalla and Bower calcium translations on a simple spherical cell I now test the translations in a full MC with Migliore et al. (2005) Na, K_{dr} and K_A channels. I run two comparison cells as with the simple test (Figure 7.7). One cell is reserved for the ChannelML version of the KCa channel that is fitted to the vdep properties that I will call KCa_cml_vdep. The other cell is reserved for the ChannelML version of KCa channel that is based on the published equations, that I will call KCa_cml.

I use MC 2 from Chapter 5 with the passive parameters that were fitted to experimental recordings. The densities of the channels that are now added are listed in Table 7.1.

	L-type calcium	KCa	Ca Pool
Soma	4.0×10^{-8} μS μm^{-2}	1.4×10^{-7} μS μm^{-2}	5.2×10^{-6} μS μm^{-2}
Axon	2.0×10^{-8} μS μm^{-2}	8.9×10^{-8} μS μm^{-2}	5.2×10^{-6} μS μm^{-2}
Apical Dendrite Tuft	9.5×10^{-8} μS μm^{-2}	None	None
Apical Dendrite	2.2×10^{-8} μS μm^{-2}	None	None
Proximal Lateral Dendrite	4.0×10^{-9} μS μm^{-2}	None	None

Table 7.1: Channel densities of calcium mechanisms used in the Bhalla and Bower (1993) model that are used as a starting point for my MC tests. The Ca Pool values are set as densities, but are really used to set the resting $[Ca^{2+}]$ in mM.

The same multi-location (20) current injection input as used in Chapter 6 was used here with 0.07 nA per location. Later tests will involve using the 6 cell gap-junction network set up and as this setup uses 20 location input, I wanted to be sure that the MC perform correctly in this type of experimental setup. As I now have the Na, K_{dr} and K_A channels incorporated into the model the current injection will produce an action potential. I therefore need to reduce the duration of the current injection from the 60 ms used for comparison of just the calcium channels to 0.5 ms. This allows the response evoked by the action potential to be observed free of interaction with the continuing current injection.

The addition of the Bhalla and Bower calcium channels alongside the Migliore channels changes the response of the cells from a single action potential evoked by a short current injection to a burst of action potentials. The L-type calcium channel maximum activation occurs from the point of peak depolarisation of the action potential and extends into the falling phase. This activation produces an influx of calcium that depolarises the cell sufficiently to evoke further action potentials when the steady state activation of the K_{dr} channels approach zero. As the $[Ca^{2+}]$ concentration increases the activation of the KCa channels also increases until a point is reached where the cell becomes sufficiently hyperpolarised to reduce the activation of the L-type calcium channels. When activation of the L-type calcium channels decreases the decay of $[Ca^{2+}]$ produced by a fixed decay constant in the simulation or calcium pumps in a living cell starts to be stronger than the influx and $[Ca^{2+}]$ and a point is reached where the burst firing is quenched.

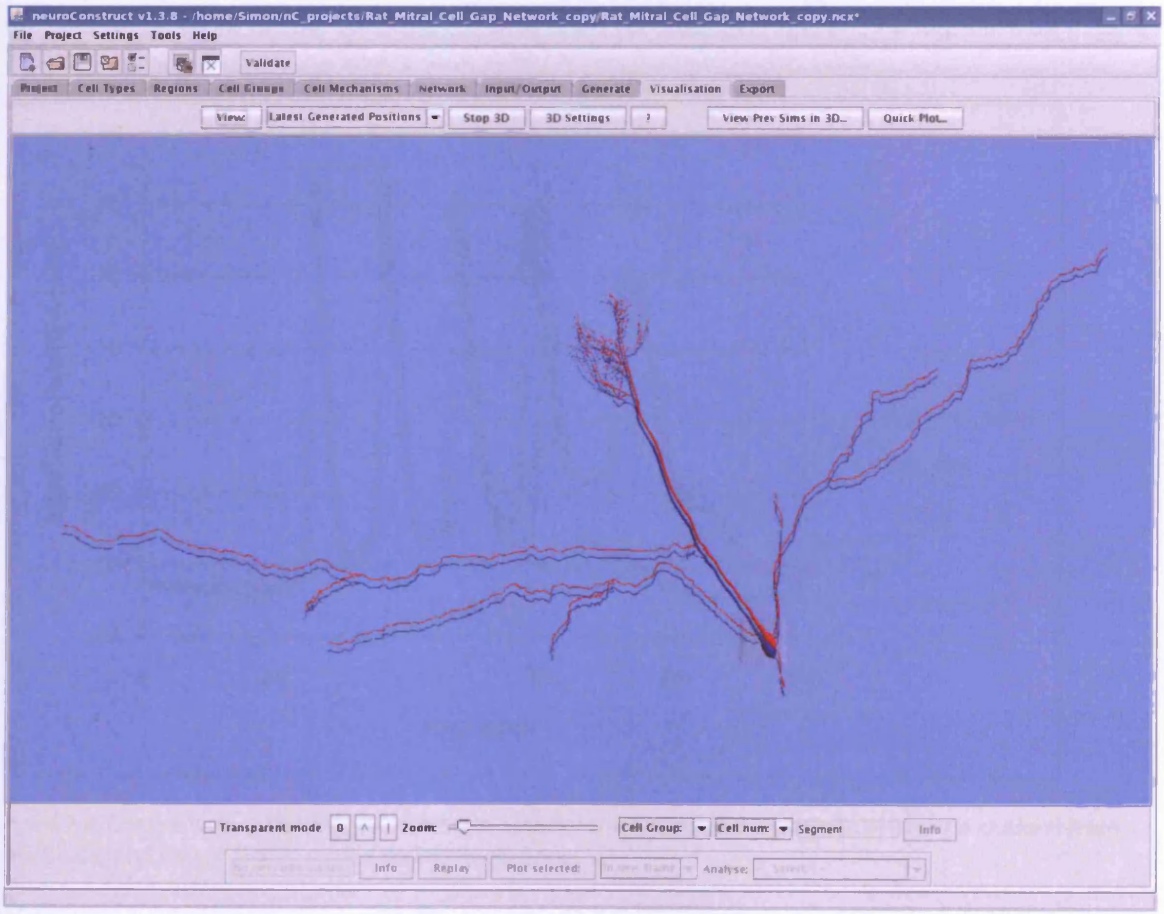

Figure 7.7: Two identical mitral cell models are used for testing variations of ChannelML translations of the Bhalla and Bower (1993) KCa channel.

Figure 7.8 shows the differences between KCa_cml_vdep and KCa_cml in a standard Mitral Cell 2 setup using the Bhalla and Bower (1993) channel densities for the calcium mechanisms as listed in Table 7.1.

The densities of the KCa_cml channels were now systematically adjusted to see if the cell could be tuned to give a similar response to that of KCa_cml_vdep. It was found that a two orders of magnitude increase of densities from the values given in Table 1 to 1.4×10^{-5} μS μm^{-2} and 8.9×10^{-6} μS μm^{-2} was needed to give a similar membrane potential response to a current injection (20 x 0.07 nA 0.5ms, Figure 7.9). The next phase of gap-junction testing can now use either the KCa_cml channels at the higher densities or KCa_cml_vdep at the Bhalla and Bower model densities.

With Figure 7.8 it is now possible to start making comparisons with the experimental recordings in Chapter 1 (Figures 1.3-1.5). We have a single short pulse (0.5 ms) current injection so the setup for the simulation is not strictly comparable. But there are comparisons that can be made. As mentioned in Chapter 6 the length of the action potentials are longer in the simulations that points to the kinetic equations for the Na, K_{dr} and K_A channels being insufficiently close to their real counterparts. Also the experimental recordings show a strong overshoot in the recovery phase of the APs suggesting that the total K_{dr} and K_A conductance maximum is greater. The variability of influences on the burst firing in experimental recordings cannot be replicated in simulations but in the experimental recordings the firing is seen not to fade away so the the KCa_cml_vdep eample or the highest densities of KCa_cml are seen to be more in line with the experimental recordings (Figure 7.9 compare with Figure 1.5).

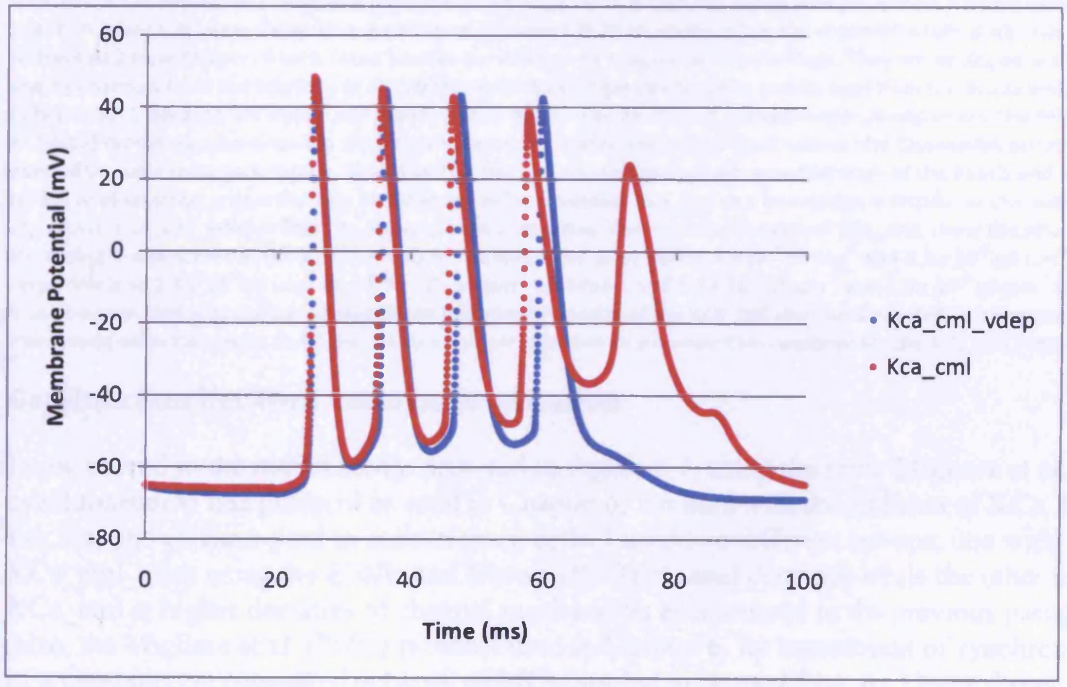

Figure 7.8: Comparison of the simulated effects of different XML implementations of the KCa channel from the Bhalla and Bower (1993) model on MC burst firing.

Comparison of simulated membrane potential recordings for two identical mitral cells receiving a 0.07 nA current injection (after a 20 msec delay for a duration of 0.5 msec) at 20 locations in the apical dendrite tuft. Both cells are Mitral Cell 2 from Chapter 4 with fitted passive parameters to experimental recordings. They are equipped with Na, K_{dr} and K_A channels from the Migliore et al. (2005) model and L-type calcium, KCa and Ca pool from the Bhalla and Bower (1993) model. Because the Bhalla and Bower (1993) model was developed in the Genesis simulator and the Migliore et

al. (2005) model was developed in the Neuron simulator, translation of the mechanisms into ChannelML scripts was needed to make them compatible. Since the KCa channel translations are not a perfect copy of the Bhalla and Bower (1993) original script properties two versions are being assessed. KCa_cml as a translation is faithful to the published equations, KCa_cml_vdep is fitted to the response properties.

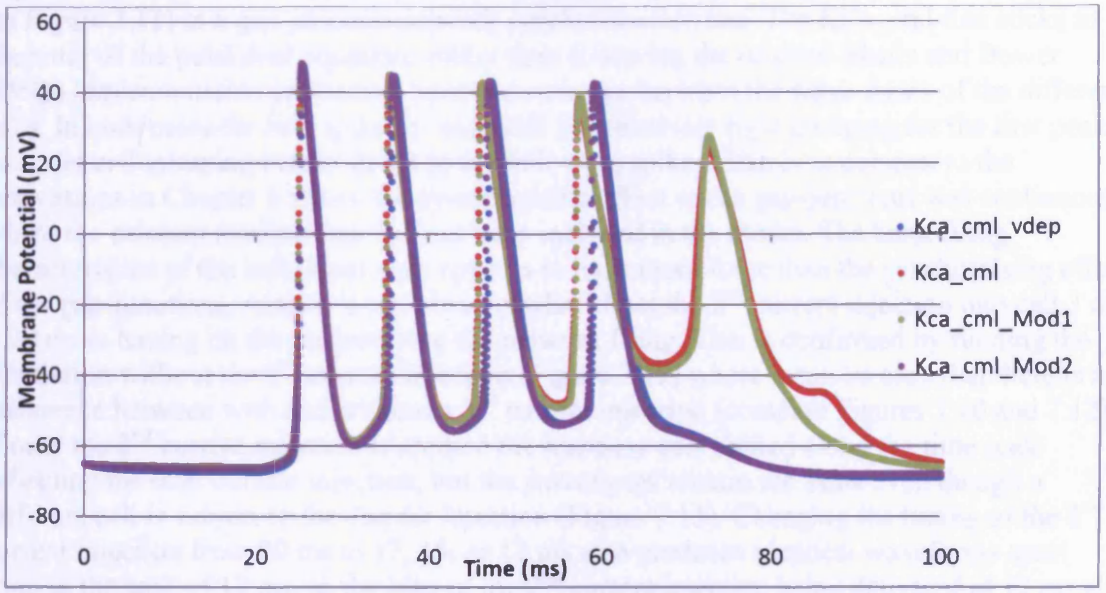

Figure 7.9: Increasing the density of one of XML implementation of a KCa channel from Figure 7.8 brings the MC burst firing response in line with that of the other XML implementation of a KCa channel.

Comparison of simulated membrane potential recordings for two identical mitral cells receiving a 0.07 nA current injection (after a 20 msec delay for a duration of 0.5 msec) at 20 locations in the apical dendrite tuft. Both cells are Mitral Cell 2 from Chapter 4 with fitted passive parameters to experimental recordings. They are equipped with Na, K_{dr} and K_A channels from the Migliore et al. (2005) model and L-type calcium, KCa and Ca pool from the Bhalla and Bower (1993) model. Because the Bhalla and Bower (1993) model was developed in the Genesis simulator and the Migliore et al. (2005) model was developed in the Neuron simulator, translation of the mechanisms into ChannelML scripts was needed to make them compatible. Since the KCa channel translations are not a perfect copy of the Bhalla and Bower (1993) original script properties two versions are being assessed. KCa_cml as a translation is faithful to the published equations, KCa_cml_vdep is fitted to the response properties. The two modification of KCa_cml, show the effect of increasing the densities of the KCa channels in the soma and axon from 1.4×10^{-7} μS μm^{-2} and 8.9×10^{-8} μS μm^{-2} respectively to 1.4×10^{-6} μS μm^{-2} and 8.9×10^{-7} μS μm^{-2} for Mod 1 and 1.4×10^{-5} μS μm^{-2} and 8.9×10^{-6} μS μm^{-2} for Mod 2. It can be seen that a two order of magnitude increase of density of the KCa_cml channel is needed to bring the membrane potential response of the cell to a current injection to a comparable response for the KCa_cml_vdep channel.

Gap-Junction Network and Synchronisation

I now moved to the model set-up depicted in Figure 6.1, using the same Migliore et al. (2005) synchronisation test protocol as used in Chapter 6, but here with the addition of KCa, L-type calcium and calcium-pool to each of the 6 cells. I used two different set-ups, one with KCa_cml_vdep using the Bhalla and Bower (1993) channel densities while the other used KCa_cml at higher densities of channel mechanisms as discussed in the previous paragraph. Also, the Migliore et al. (2005) protocol used in Chapter 6, for assessment of synchronisation of a gap-junction connected network of MCs, needed to be modified. As I have shown in Figures 7.8 and 7.9 the addition of calcium channels to the model causes the MCs to exhibit burst firing. For this reason I do not need a continuous current injection to induce repetitive firing. I have therefore changed the inputs to cells 2 and 3 to duration of 0.5 ms. I still use the majority of the parameter settings that were described in Chapter 6. The current injections are delivered after a delay of 10 ms to cell 2 and 20 ms to cell 3 all at 20 locations in the apical

tuft. I continue to use the 1600 gap-junctions with conductance adjusted to give coupling ratios in line with those mentioned in Chapter 6.

Figures 7.10 and 7.11 compare the effects of KCa_cml_vdep (in Figure 7.10) and KCa_cml (in Figure 7.11) in a gap-junction network synchronisation test. The KCa_cml that sticks to the letter of the published equations rather than following the original Bhalla and Bower (1993) implementation produces a bit more variation between the wave forms of the different cells. In both cases the first spike for each cell has relatively tight grouping for the first peak but inter cell grouping breaks down in the following spikes. This is in contrast to the simulations in Chapter 6 where the synchronising effect of the gap-junctions was continuous where the calcium mechanisms had not been included in the model. The burst firing characteristics of the individual cells appears to have more force than the synchronising effect of the gap-junctions. Also, it is not obvious what effect the 2nd current injection into cell 3 at t = 20 ms is having on desynchronising the network firing. This is confirmed by running the simulation without the 2nd current injection (Figure 7.12) where it can be seen that there is no difference between with and without a 2nd current injection (compare Figures 7.10 and 7.12). If only the 2nd current injection is applied the response gets shifted along the time scale reflecting the later current injection, but the waveforms remain the same even though a different cell is subject to the current injection (Figure 7.13). Changing the timing of the 2nd current injection from 20 ms to 17, 15, or 12 ms also produces identical waveforms apart from in the case of 12 ms. In the case of the 2nd current injection being delivered at 12 ms all the APs in the waveforms are shifted to about 0.6 ms earlier but the overall patterns remain the same. This suggests that the two current injections are integrated together allowing threshold potential be achieved 0.6 ms earlier (Figure 7.14. It therefore appears that once a MC simulation using the Bhalla and Bower (1993) calcium mechanisms receives a stimulus that is above firing potential that the waveform of its response is robust to influence by further stimuli be they direct or via gap-junctions.

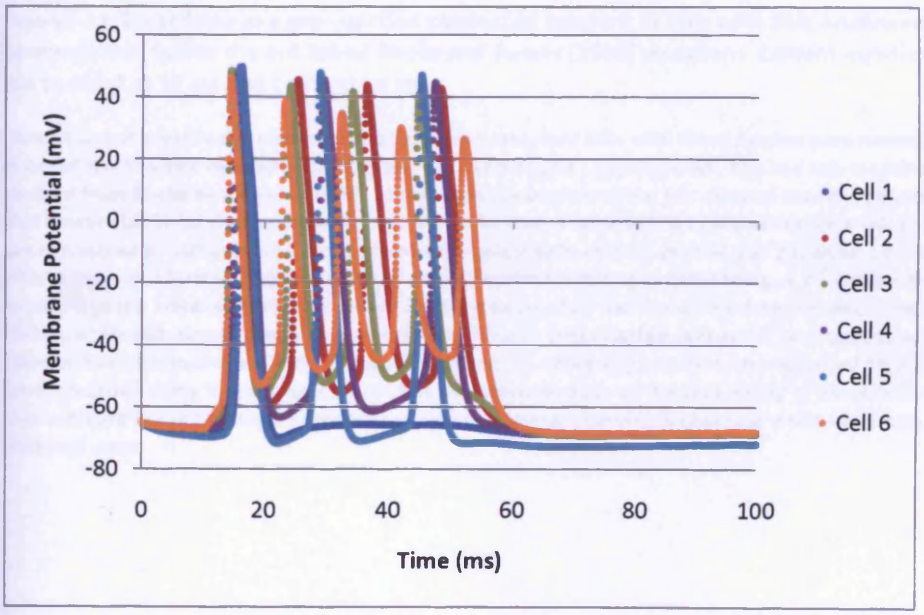

Figure 7.10: Burst firing in a gap-junction connected network of MCs with XML implementation of the KCA channels that mimics the Bhalla and Bower (1993) implementation. Current injections of 20x0.5 nA 0.5 ms to Cell 2 at 10 ms and Cell 3 at 20 ms.

Simulation of somatic membrane potential in reconstructed MCs with fitted passive parameters and Na, K_{dr} and K_A channel mechanisms derived from Migliore et al. (2005) and L-type calcium, KCa and sub-membrane calcium pool

derived from Bhalla and Bower (1993). In this case the version of the KCa channel is fitted to the response of the original Genesis Bhalla and Bower implementation of the channel, that I refer to as KCa_cml_Vdep in the text. The MCs are connected by 100 gap-junctions between the apical tufts of pairs of cells. Cell 2 is given a current injection of 0.5 nA after a delay of 10 ms to 20 locations in its apical dendrite tuft to give burst firing. A 2nd current injection of 0.5 nA to 20 locations in the apical dendrite tuft of cell 3 after a delay of 20 ms. The 10 ms delay between two current injections to two separate cells would produce asynchronous firing in unconnected cells and is here used to test the ability of the gap-junction to synchronise firing in a small network. The coupling ratio has been adjusted ~0.025 , a level at which gap-junction driven firing is observed in some but not consistently in all the cells. Firing of the cells is not tightly grouped as was achieved in the chapter 5 experiments. However some clumping is observed while some cells are seen to behave in different ways.

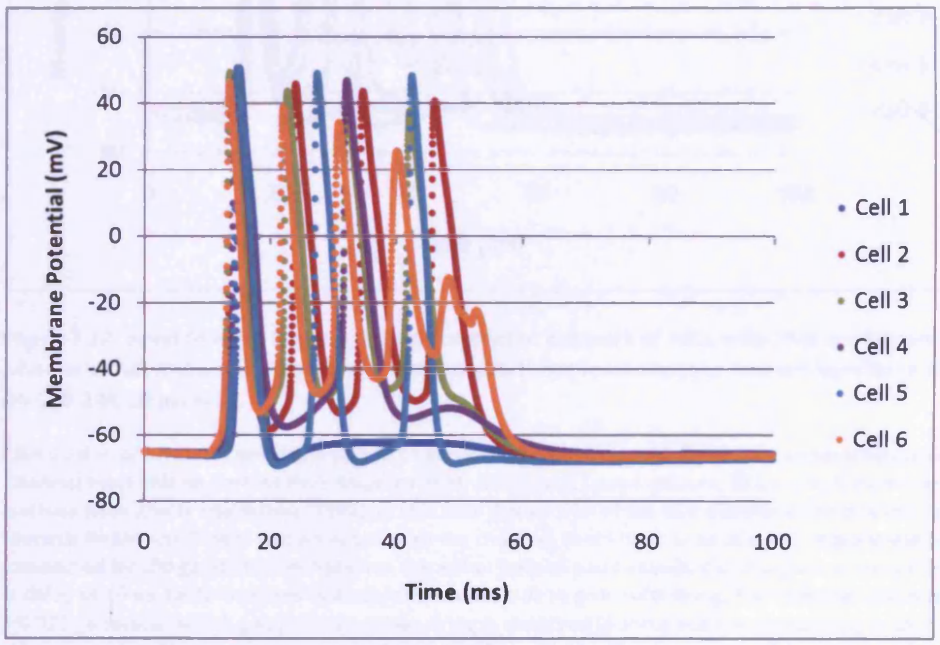

Figure 7.11: Burst firing in a gap-junction connected network of MCs with XML implementation of the KCa channels that follow the published Bhalla and Bower (1993) equations. Current injections of 20x0.5 nA 0.5 ms to Cell 2 at 10 ms and Cell 3 at 20 ms.

Simulation of somatic membrane potential in reconstructed MCs with fitted passive parameters and Na, K_{dr} and K_A channel mechanisms derived from Migliore et al. (2005) and L-type calcium, KCa and sub-membrane calcium pool derived from Bhalla and Bower (1993). In this case the version of the KCa channel uses the equations published in Bhalla and Bower (1993) for the implementation of the channel. I refer to this implementation as KCa_cml in the text. The MCs are connected by 100 gap-junctions between the apical tufts of pairs of cells. Cell 2 is given a current injection of 0.5 nA after a delay of 10 ms to 20 locations in its apical dendrite tuft to give burst firing. A 2nd current injection of 0.5 nA to 20 locations in the apical dendrite tuft of cell 3 after a delay of 20 ms. The 10 ms delay between two current injections to two separate cells would produce asynchronous firing in unconnected cells and is here used to test the ability of the gap-junction to synchronise firing in a small network. The coupling ratio has been adjusted ~0.025 , a level at which gap-junction driven firing is observed in some but not consistently in all the cells. Firing of the cells is not tightly grouped as was achieved in the chapter 5 experiments. However some clumping is observed while some cells are seen to behave in different ways.

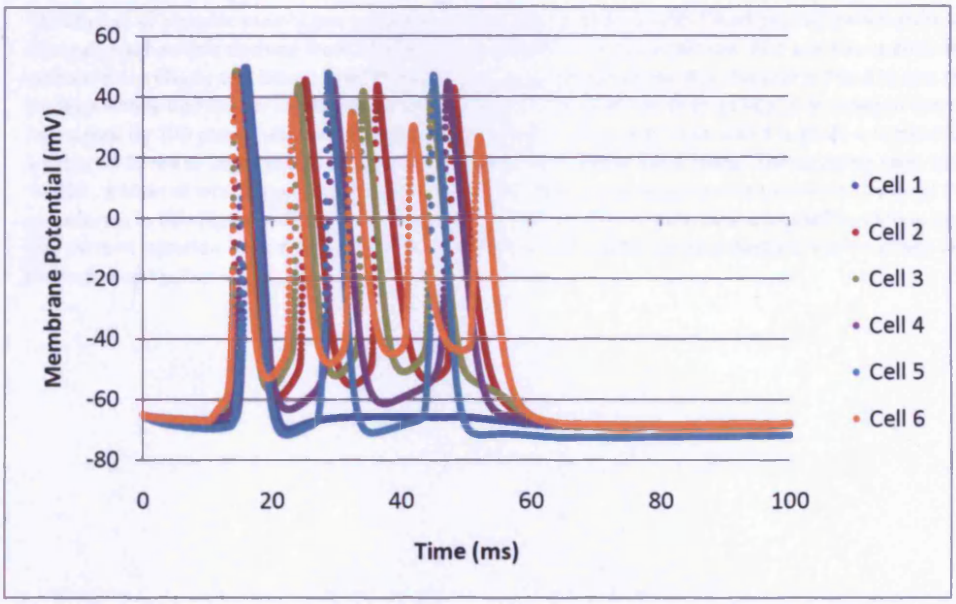

Figure 7.12: Burst firing in a gap-junction connected network of MCs with XML implementation of the KCa channels that mimics the Bhalla and Bower (1993) implementation. Current injections of 20x0.5 nA 0.5 ms to Cell 2 at 10 ms only.

Simulation of somatic membrane potential in reconstructed MCs with fitted passive parameters and Na, K_{dr} and K_A channel mechanisms derived from Migliore et al. (2005) and L-type calcium, KCa and sub-membrane calcium pool derived from Bhalla and Bower (1993). In this case the version of the KCa channel is fitted to the response of the original Genesis Bhalla and Bower implementation of the channel, that I refer to as KCa_cml_Vdep in the text. The MCs are connected by 100 gap-junctions between the apical tufts of pairs of cells. Cell 2 is given a current injection of 0.5 nA after a delay of 10 ms to 20 locations in its apical dendrite tuft to give burst firing. The coupling ratio has been adjusted ~0.025 , a level at which gap-junction driven firing is observed in some but not consistently in all the cells. There is no obvious visible difference between this figure and figure 6.11 which receives a 2nd input at t = 20 ms into cell 3.

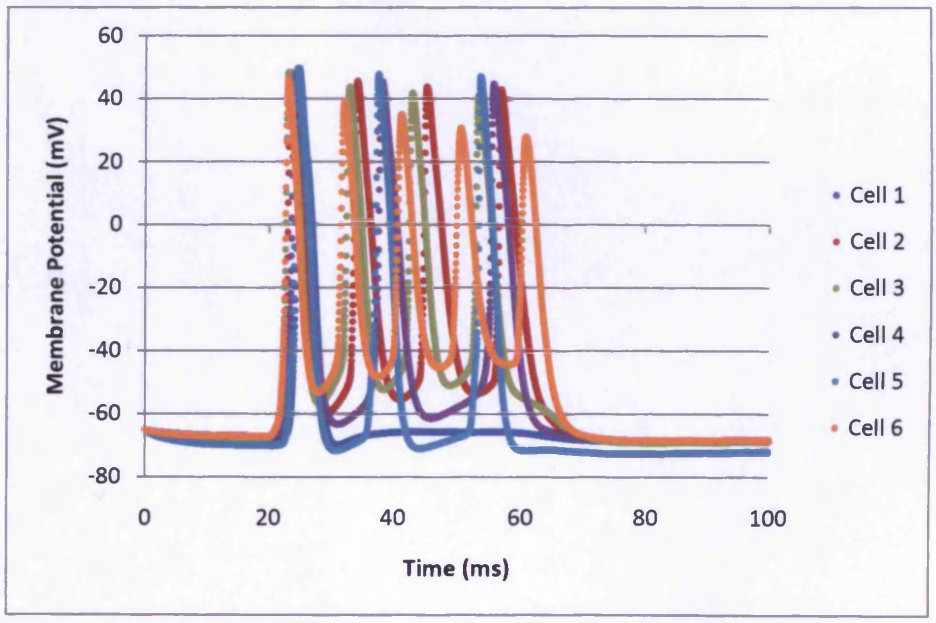

Figure 7.13: Burst firing in a gap-junction connected network of MCs with XML implementation of the KCa channels that mimics the Bhalla and Bower (1993) implementation. Current injections of 20x0.5 nA 0.5 ms to Cell 3 at 20 ms only.

Simulation of somatic membrane potential in reconstructed MCs with fitted passive parameters and Na, K_{dr} and K_A channel mechanisms derived from Migliore et al. (2005) and L-type calcium, KCa and sub-membrane calcium pool derived from Bhalla and Bower (1993). In this case the version of the KCa channel is fitted to the response of the original Genesis Bhalla and Bower implementation of the channel, that I refer to as KCa_cml_Vdep in the text. The MCs are connected by 100 gap-junctions between the apical tufts of pairs of cells. Cell 3 is given a current injection of 0.5 nA after a delay of 20 ms to 20 locations in its apical dendrite tuft to give burst firing. The coupling ratio has been adjusted ~0.025 , a level at which gap-junction driven firing is observed in some but not consistently in all the cells. Comparing the waveforms in this figure with those of figure 6.13 it can be seen that they are just shifted along by the extra 10 ms delay. The current injection occurring on a different cell does not appear to have had any visible effect on the waveforms of the individual cells.

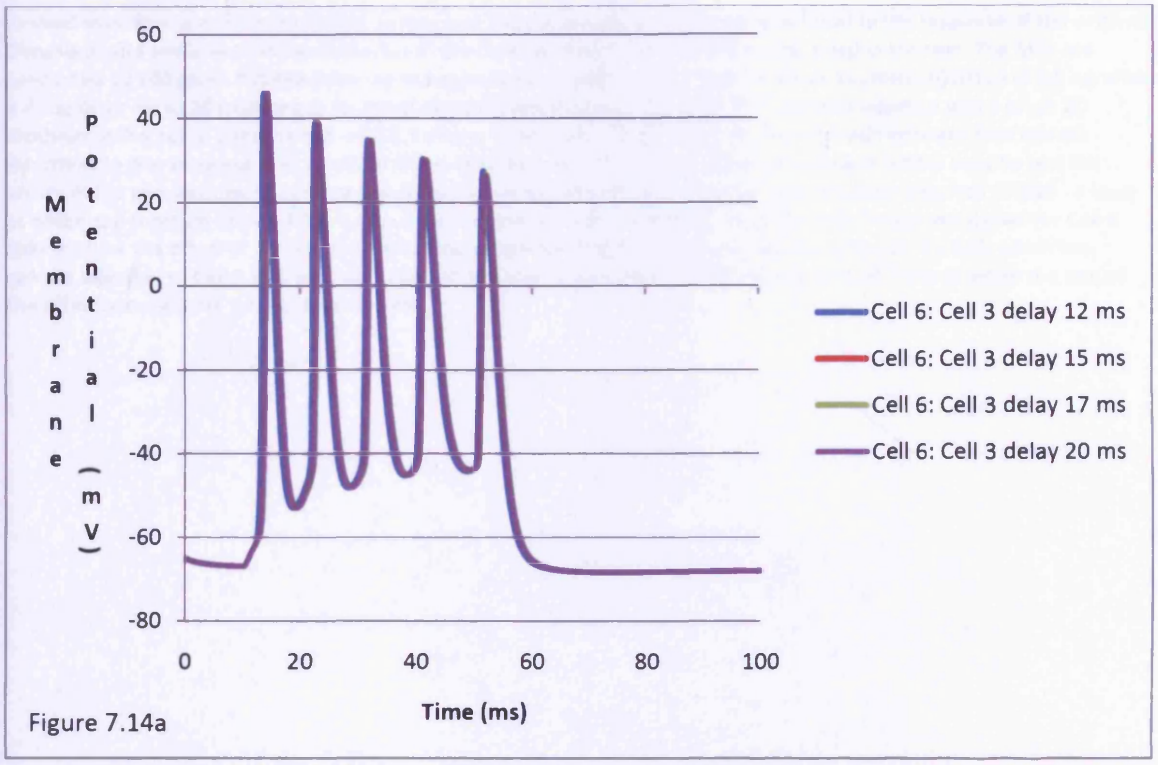

Figure 7.14a

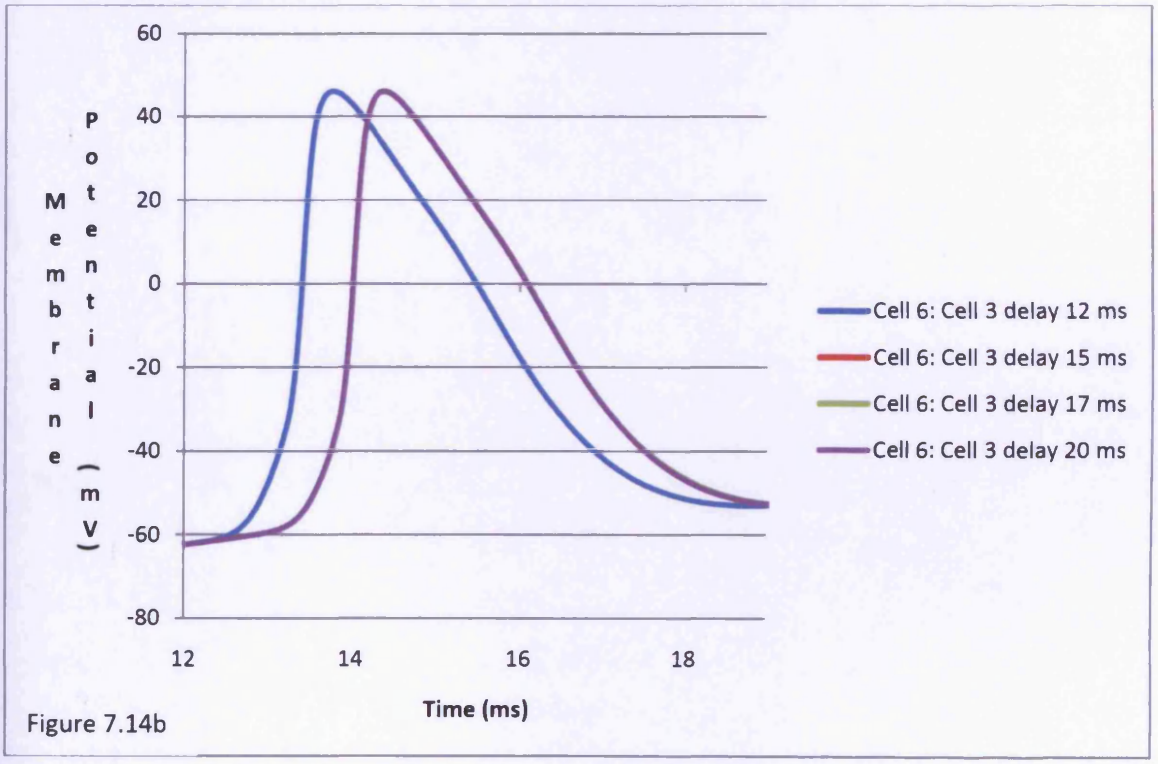

Figure 7.14b

Figure 7.14: Burst firing in a gap-junction connected network of MCs with XML implementation of the KCa channels that mimics the Bhalla and Bower (1993) implementation. This time just the traces for Cell 6 are shown so the effects of varying the interval between current injections can be shown. Current injections of 20x0.5 nA 0.5 ms to Cell 2 at 10 ms and Cell 3 at 12, 15, 17 or 20 ms.

Simulation of somatic membrane potential in reconstructed MCs with fitted passive parameters and Na, K_{dr} and K_A channel mechanisms derived from Migliore et al. (2005) and L-type calcium, KCa and sub-membrane calcium pool

derived from Bhalla and Bower (1993). In this case the version of the KCa channel is fitted to the response of the original Genesis Bhalla and Bower implementation of the channel, that I refer to as KCa_cml_Vdep in the text. The MCs are connected by 100 gap-junctions between the apical tufts of pairs of cells. Cell 2 is given a current injection of 0.5 nA after a delay of 10 ms to 20 locations in its apical dendrite tuft to give burst firing. A 2nd current injection of 0.5 nA to 20 locations in the apical dendrite tuft of cell 3 after a delay of 12, 15, 17 or 20 ms. The intervals between two current injections to two separate cells would produce asynchronous firing in unconnected cells and is here used to test the ability of the gap-junction to synchronise firing in a small network. The coupling ratio has been adjusted ~0.025 , a level at which gap-junction driven firing is observed in some but not consistently in all the cells. Traces are shown for Cell 6 only to show the effect of varying the interstimulus interval (Figure 7.10 shows the traces for all the cells when the current injection to Cell 3 is at t=20 ms). Figure7.14b shows an enlarged time scale version of 7.14a to allow the size of the offset between the traces to be viewed.

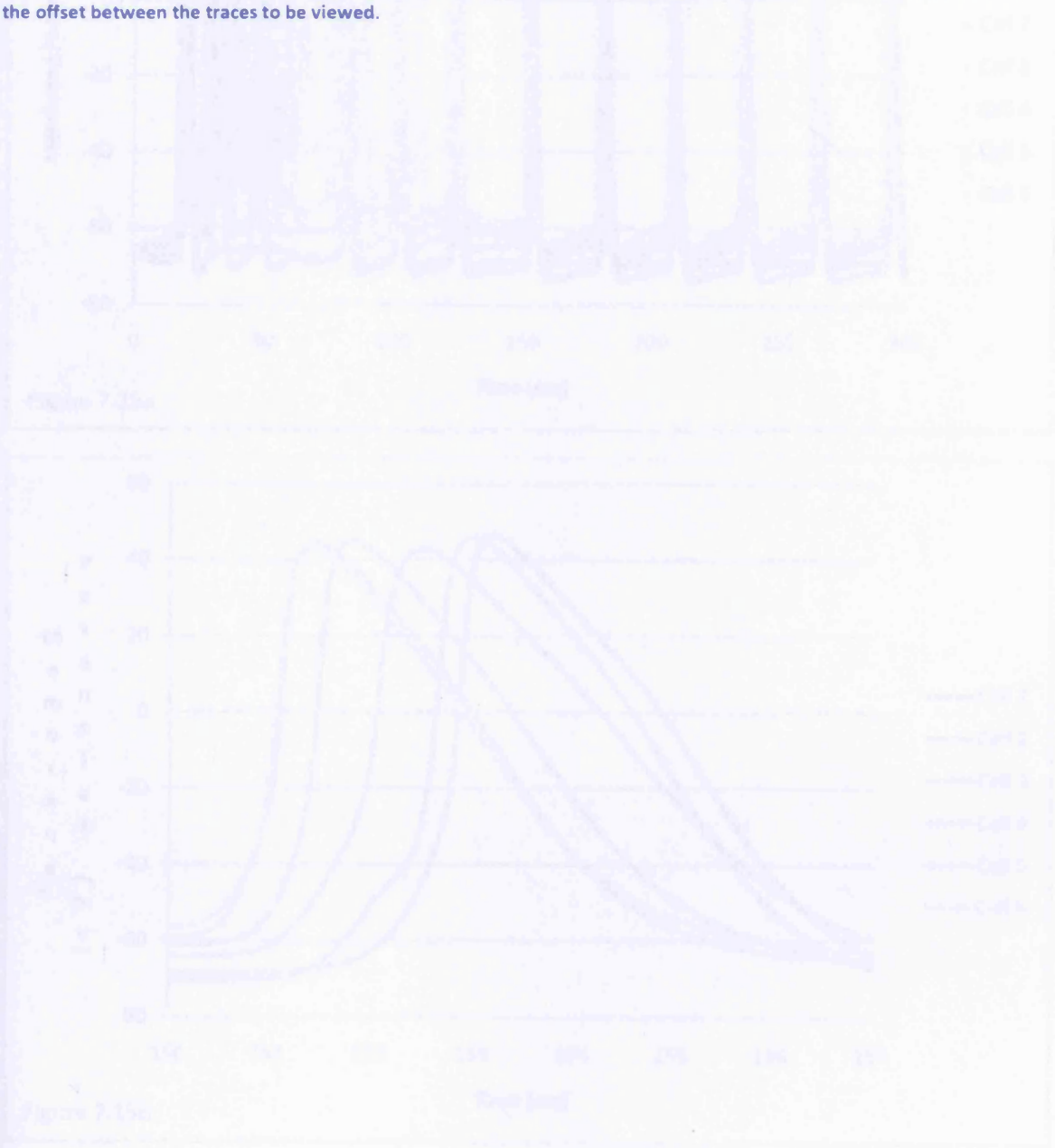

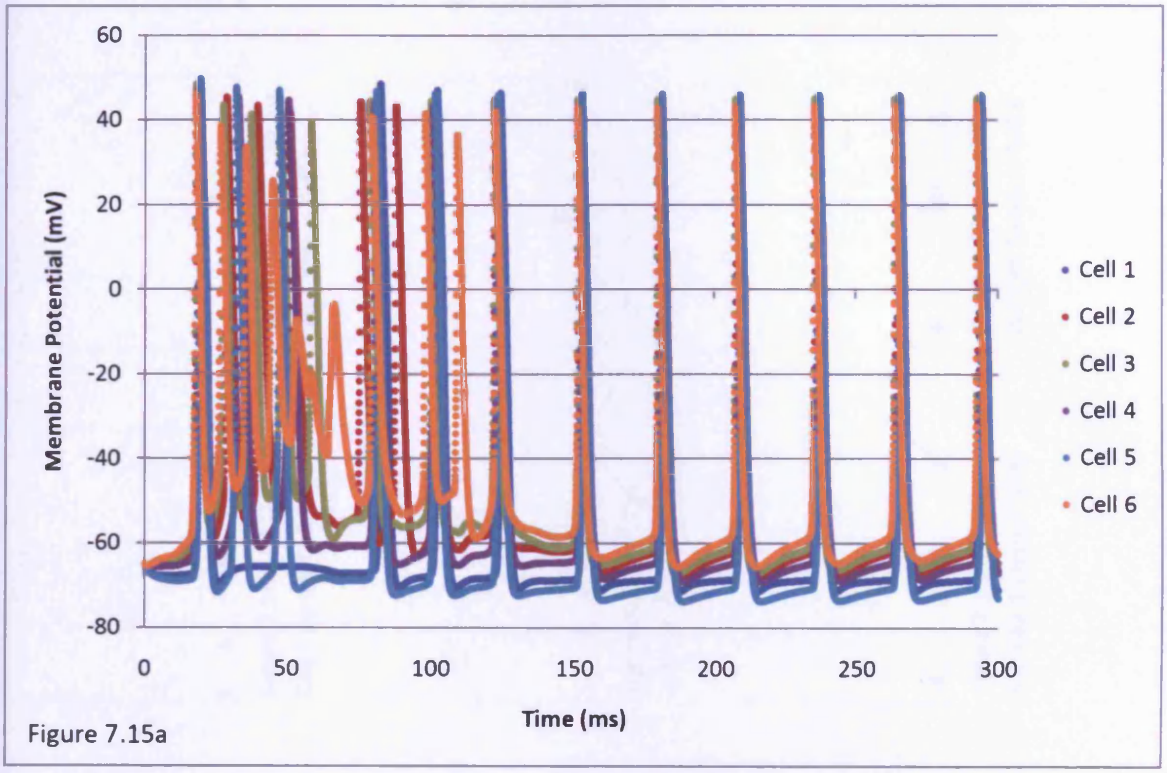

Figure 7.15a

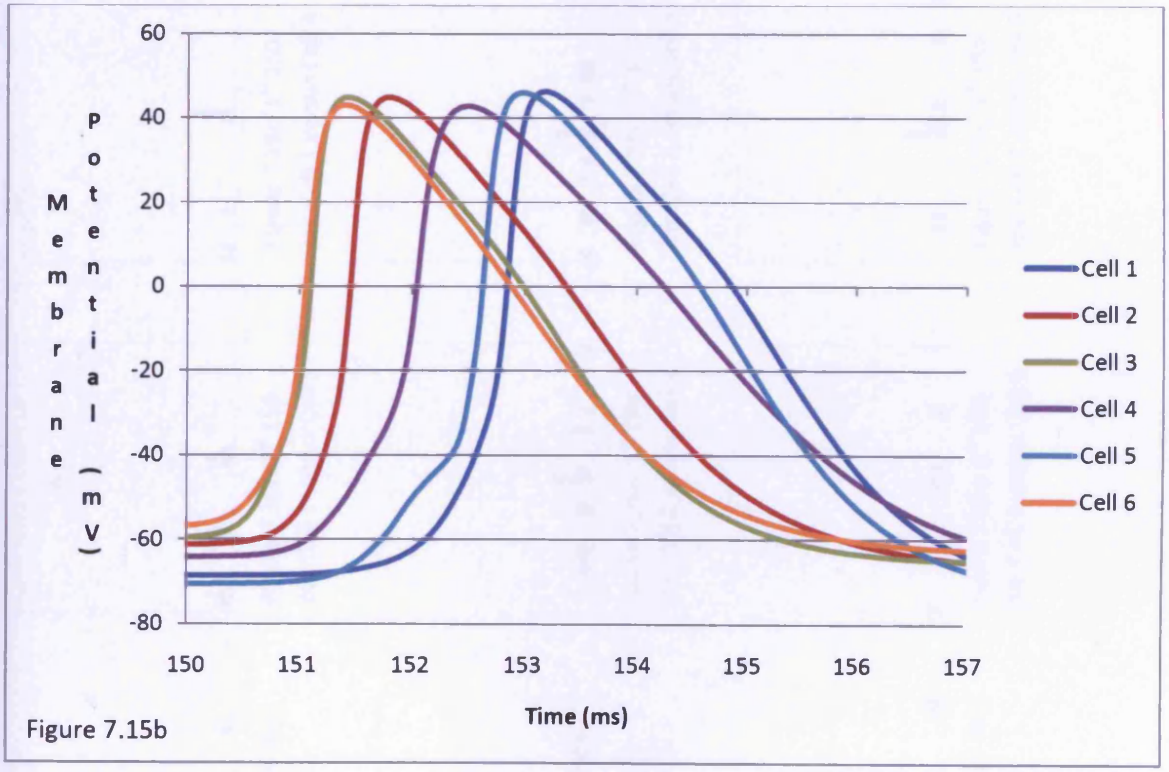

Figure 7.15b

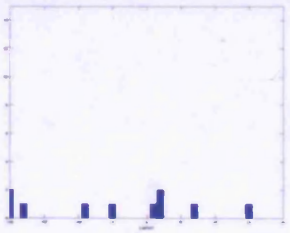

Figure 7.15c: 1st 150 ms: Cell 1 versus Cell 2

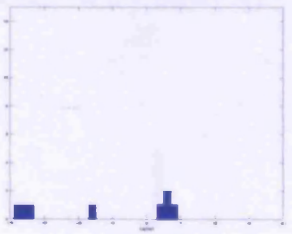

Figure 7.15c: 1st 150 ms: Cell 1 versus Cell 3

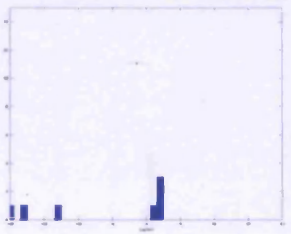

Figure 7.15c: 1st 150 ms: Cell 1 versus Cell 4

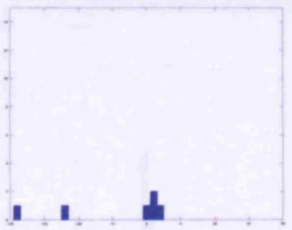

Figure 7.15c: 1st 150 ms: Cell 1 versus Cell 5

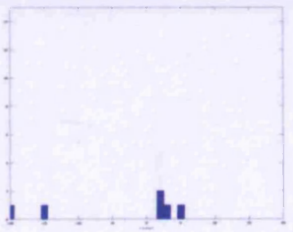

Figure 7.15c: 1st 150 ms: Cell 1 versus Cell 6

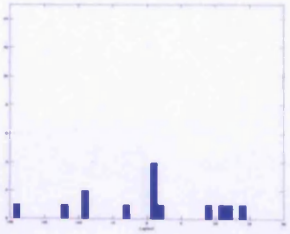

Figure 7.15c: 1st 150 ms: Cell 2 versus Cell 3

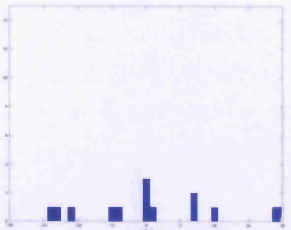

Figure 7.15c: 1st 150 ms: Cell 2 versus Cell 4

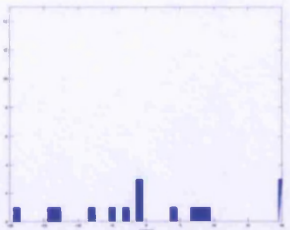

Figure 7.15c: 1st 150 ms: Cell 2 versus Cell 5

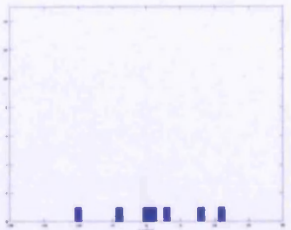

Figure 7.15c: 1st 150 ms: Cell 2 versus Cell 6

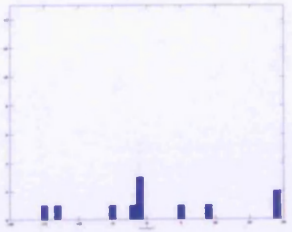

Figure 7.15c: 1st 150 ms: Cell 3 versus Cell 4

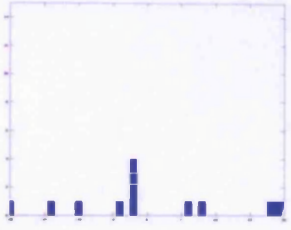

Figure 7.15c: 1st 150 ms: Cell 3 versus Cell 5

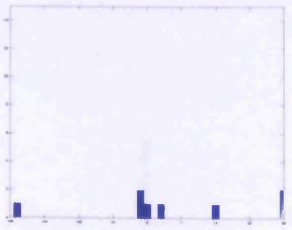

Figure 7.15c: 1st 150 ms: Cell 3 versus Cell 6

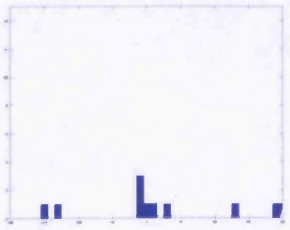

Figure 7.15c: 1st 150 ms: Cell 4 versus Cell 5

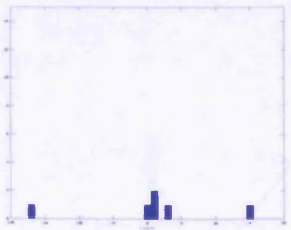

Figure 7.15c: 1st 150 ms: Cell 4 versus Cell 6

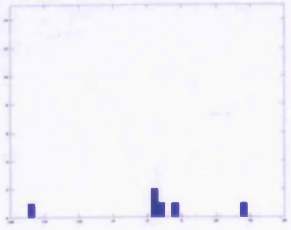

Figure 7.15c: 1st 150 ms: Cell 5 versus Cell 6

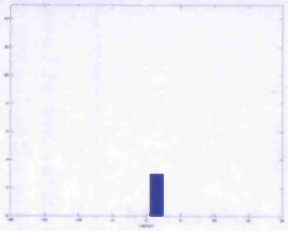

Figure 7.15c: 2st 150 ms: Cell 1 versus Cell 2

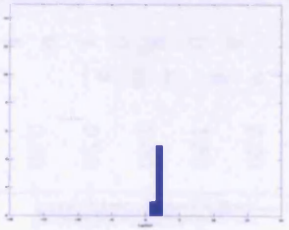

Figure 7.15c: 2st 150 ms: Cell 1 versus Cell 3

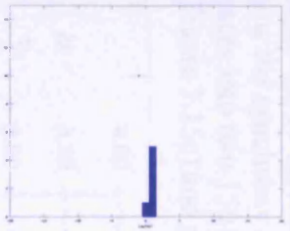

Figure 7.15c: 2st 150 ms: Cell 1 versus Cell 4

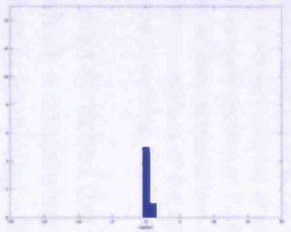

Figure 7.15c: 2st 150 ms: Cell 1 versus Cell 5

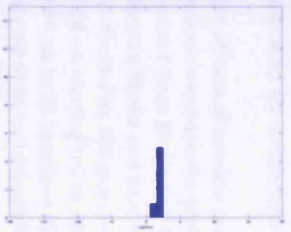

Figure 7.15c: 2st 150 ms: Cell 1 versus Cell 6

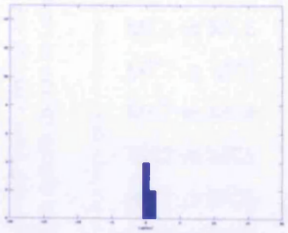

Figure 7.15c: 2st 150 ms: Cell 2 versus Cell 3

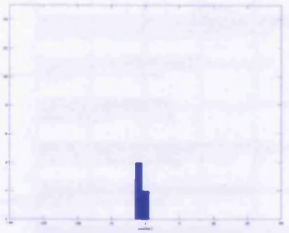

Figure 7.15c: 2st 150 ms: Cell 2 versus Cell 4

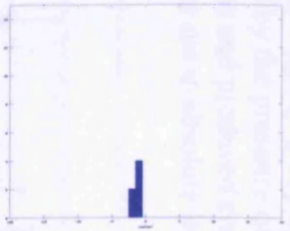

Figure 7.15c: 2st 150 ms: Cell 2 versus Cell 5

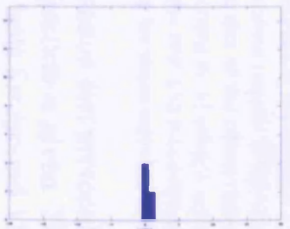

Figure 7.15c: 2st 150 ms: Cell 2 versus Cell 6

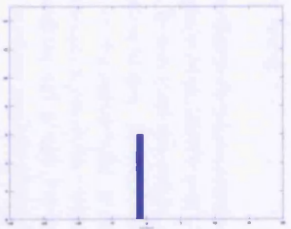

Figure 7.15c: 2st 150 ms: Cell 3 versus Cell 4

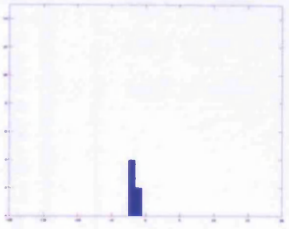

Figure 7.15c: 2st 150 ms: Cell 3 versus Cell 5

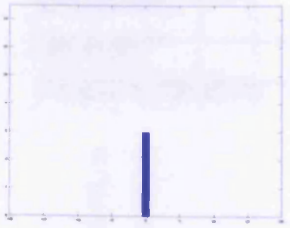

Figure 7.15c: 2st 150 ms: Cell 3 versus Cell 6

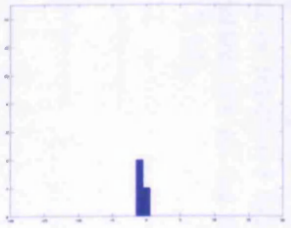

Figure 7.15c: 2st 150 ms: Cell 4 versus Cell 5

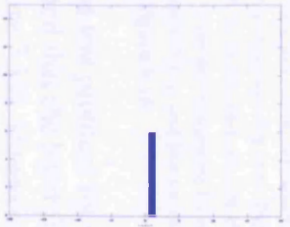

Figure 7.15c: 2st 150 ms: Cell 4 versus Cell 6

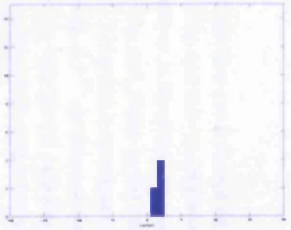

Figure 7.15c: 2st 150 ms: Cell 5 versus Cell 6

Figure 7.15: The current injection into Cells 2 and 3 is now changed to a continuous current injection with the start of the current injection into Cell 3 delayed by 10 ms. An initial period of asynchronous burst firing is followed by synchronous repetitive firing.

Simulation of somatic membrane potential in reconstructed MCs with fitted passive parameters and Na, K_{dr} and K_A channel mechanisms derived from Migliore et al. (2005) and L-type calcium, KCa and sub-membrane calcium pool derived from Bhalla and Bower (1993). In this case the version of the KCa channel is fitted to the response of the original Genesis Bhalla and Bower implementation of the channel, that I refer to as KCa_cml_Vdep in the text. The MCs are connected by 100 gap-junctions between the apical tufts of pairs of cells. Cell 2 is given a continuous current injection of 0.06 nA starting t=0 to 20 locations in its apical dendrite tuft to give burst firing. A 2nd continuous current injection of 0.06 nA to 20 locations in the apical dendrite tuft of cell 3 after a delay of 10 ms. The 10 ms delay between two current injections to two separate cells would produce asynchronous firing in unconnected cells and is here used to test the ability of the gap-junction to synchronise firing in a small network. The coupling ratio has been adjusted ~0.025 , a level at which gap-junction driven firing is observed in some but not consistently in all the cells. Firing of the cells is not tightly grouped for the first 120 ms as was achieved in the Chapter 6 experiments. However after the burst firing phase is completed the firing of all the cells becomes regular in tight groups of action potentials. Figure7.15b shows an enlarged time scale version of 7.15a to allow the size of the offset between the traces to be viewed. (c) are the cross correlograms for all pair combinations for the spike trains in (a) using 1 ms time bins. The cross correlograms have been performed on 150 ms sections of the spike trains so the first 150 ms covers the period of burst firing and the second half of just the repetitive firing. The mean absolute lag for these correlogram are shown in Figure 7.16.

I next switched the synchronisation test protocol back to the test protocol for Chapter 6 in which a continuous current injection is given. This confirmed that the burst firing produces a desynchronising effect which lasts for around 120 ms (Figure 7.15). However after 120 ms (Figure 7.15) all the cells settle down to a rhythmic firing pattern for which the action potentials of each of the cells are tightly grouped as in Chapter 6 (Figure 6.7a). To compare how the synchrony is affected by the presence of burst firing or repetitive firing, I split the traces into two 150 ms sections and produced cross correlograms for all the pair combinations (Figure 7.15c) and plotted their mean absolute lags (Figure 7.16).

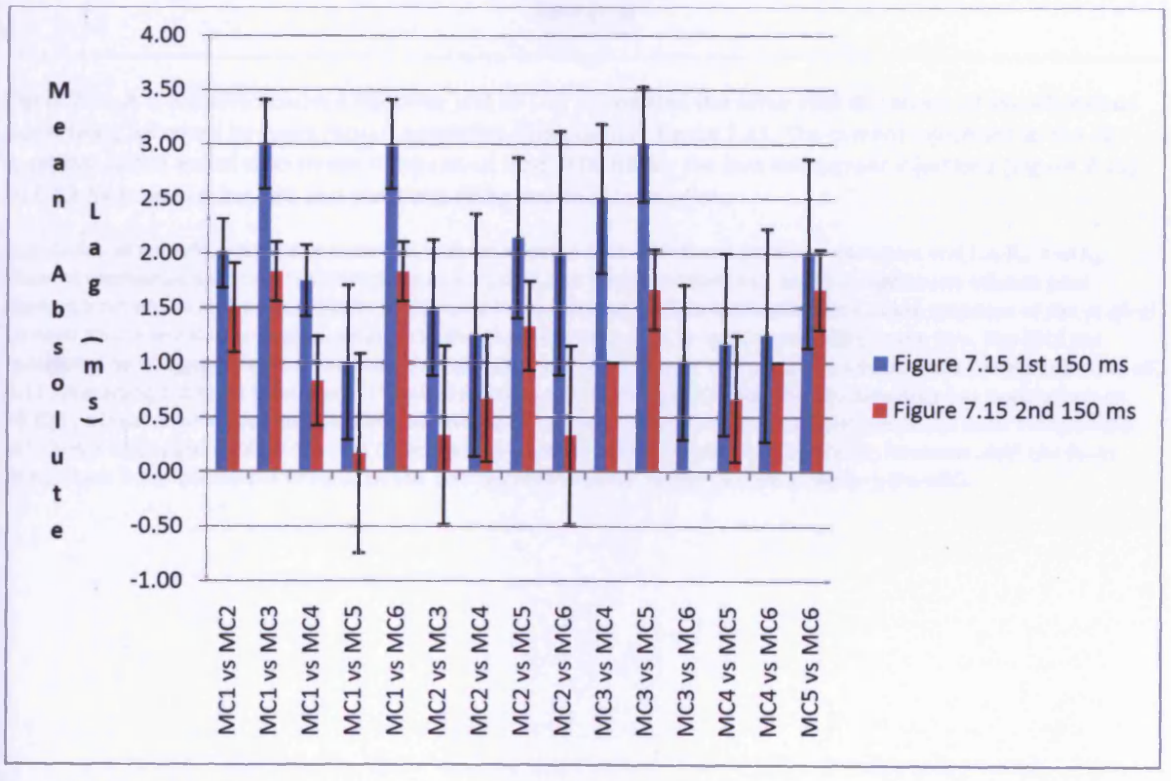

Figure 7.16: Mean absolute lags for the cross correlograms in Figures 7.15c with error bars showing standard deviation. For comparison the mean absolute lag for the pair with gap-junctions in Figure 6.4a is 0.44 ± 0.75 ms and the pair without gap-junctions in Figure 6.5a is 4.29 ± 0.83 ms.

Further tests with continuous current injections to a single cell in the network produced similar patterns with asynchronous burst firing followed by synchronous repetitive firing (Figure 7.17 for Cell 2 and Figure 7.18 for Cell 3. The overall timing varies depending on the cell receiving the current injection and the delay before the current injection starts and the current injection needs to be doubled up from 0.06 nA to 0.12 nA to evoke the APs.

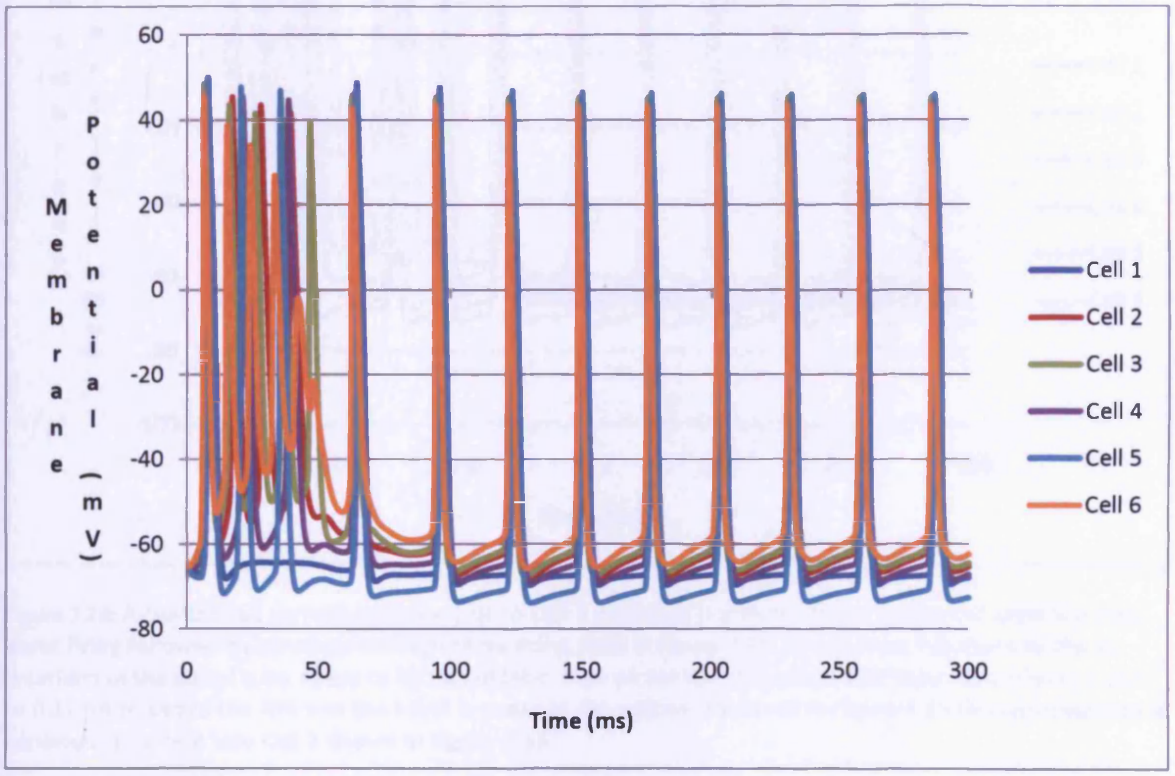

Figure 7.17: A continuous current injection just to Cell 2 produces the same kind of pattern of asynchronous burst firing followed by synchronous repetitive firing seen in Figure 7.15. The current injections to the 20 locations in the apical tufts needs to be raised from 0.06 nA for the two cell current injections (Figure 7.15) to 0.12 nA to evoke the APs and the burst firing commences earlier.

Simulation of somatic membrane potential in reconstructed MCs with fitted passive parameters and Na, K_{dr} and K_A channel mechanisms derived from Migliore et al. (2005) and L-type calcium, KCa and sub-membrane calcium pool derived from Bhalla and Bower (1993). In this case the version of the KCa channel is fitted to the response of the original Genesis Bhalla and Bower implementation of the channel, that I refer to as KCa_cml_Vdep in the text. The MCs are connected by 100 gap-junctions between the apical tufts of pairs of cells. Cell 2 is given a continuous current injection of 0.12 nA starting t=0 to 20 locations in its apical dendrite tuft to give burst firing. The coupling ratio has been adjusted ~0.025 , a level at which gap-junction driven firing is observed in some but not consistently in all the cells. Firing of the cells is not tightly grouped for the first 50 ms as was achieved in the Chapter 6 experiments. However after the burst firing phase is completed the firing of all the cells becomes regular in tight groups of action potentials.

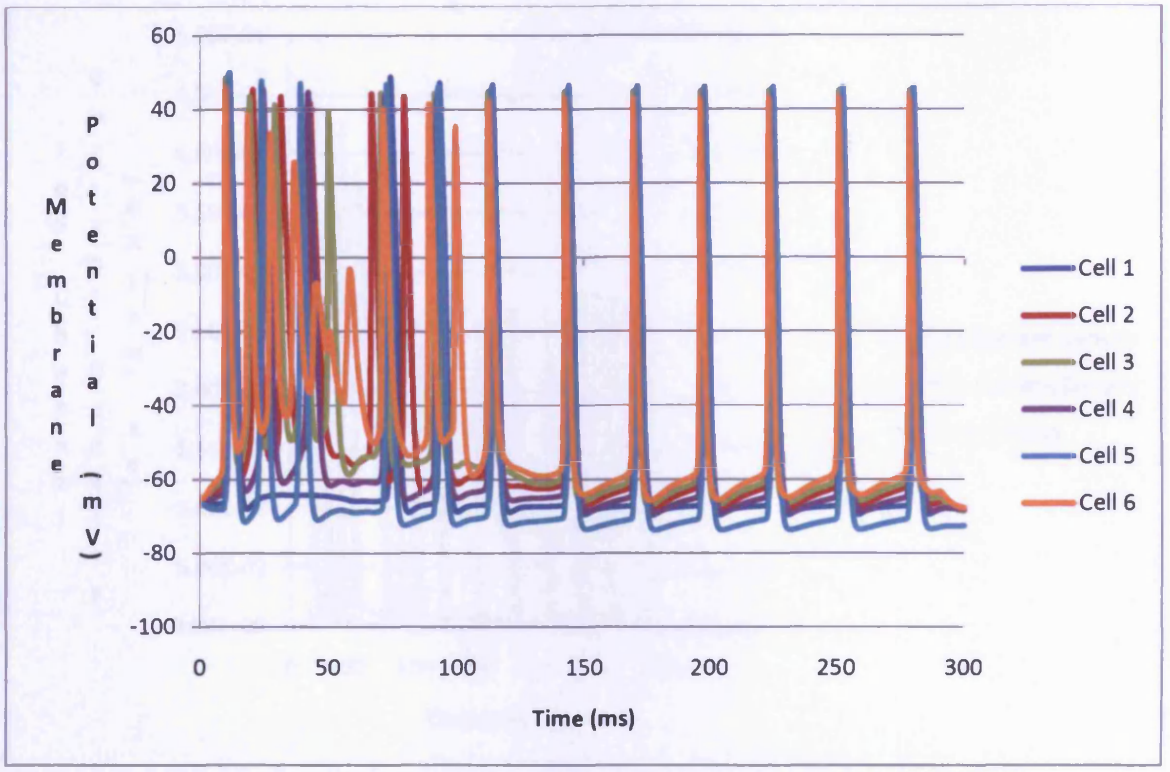

Figure 7.18: A continuous current injection just to Cell 3 produces the same kind of pattern of asynchronous burst firing followed by synchronous repetitive firing seen in Figure 7.15. The current injections to the 20 locations in the apical tufts needs to be raised from 0.06 nA for the two cell current injections (Figure 7.15) to 0.12 nA to evoke the APs and the burst is closer to the pattern observed in Figure 7.15 than produced by a continuous current into Cell 2 shown in Figure 7.16.

Simulation of somatic membrane potential in reconstructed MCs with fitted passive parameters and Na, K_{dr} and K_A channel mechanisms derived from Migliore et al. (2005) and L-type calcium, KCa and sub-membrane calcium pool derived from Bhalla and Bower (1993). In this case the version of the KCa channel is fitted to the response of the original Genesis Bhalla and Bower implementation of the channel, that I refer to as KCa_cml_Vdep in the text. The MCs are connected by 100 gap-junctions between the apical tufts of pairs of cells. Cell 3 is given a continuous current injection of 0.12 nA starting t=10 ms to 20 locations in its apical dendrite tuft. The coupling ratio has been adjusted ~0.025 , a level at which gap-junction driven firing is observed in some but not consistently in all the cells. Firing of the cells is not tightly grouped for the first 120 ms as was achieved in the Chapter 6 experiments. However after the burst firing phase is completed the firing of all the cells becomes regular in tight groups of action potentials

In an effort to understand why the continuous current injection simulation (Figure 7.15) produces a rhythmic firing pattern after 120 ms rather than further episodes of burst firing I plotted more variables for Cell 2 (Figure 7.19). It can be seen that there is a decay in the maximum current density through L-type calcium channels over time while KCa channel maximum current densities are maintained. This allows the KCa channels to terminate further APs after single appears for a recovery period when a further AP is evoked resulting in repetitive firing rather than burst firing. In Figure 7.20 I plot the 's' and 'r' gate variables (see equation 7.1) for the simulation shown in Figure 7.15. These plots show that the decay in the L-type channel current density maxima over time can be attributed to only partial activation of the 'r' gate variable. This cannot be attributed to the voltage dependency of the 'r' gate variable (see Figure 7.4) so plotting the time constants for the 's' and 'r' gate variables (Figure 7.21) reveals that the time constant (τ) for the 'r' variable is long (range above 150 ms to ~18 ms) so after the initial activation only partial activation is possible. Accurate measurement of the calcium channel parameters particular time constants are needed to improve the accuracy of this model.

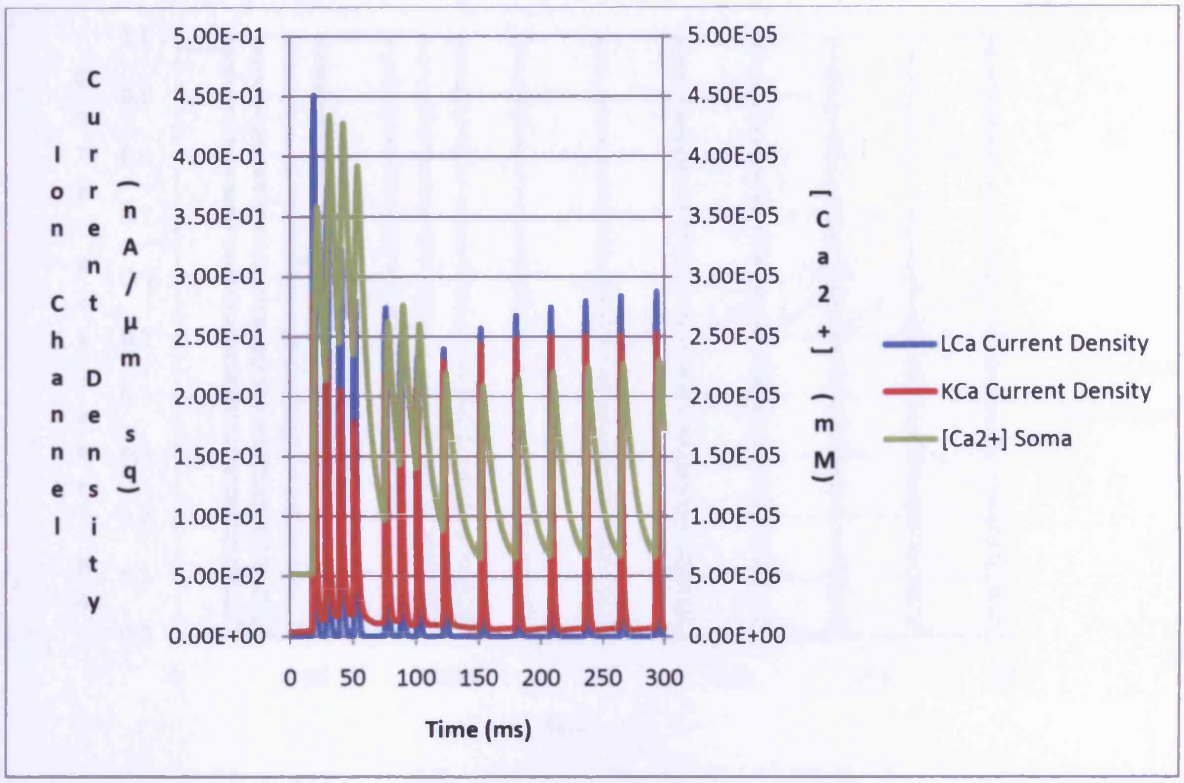

Figure 7.19: Plotting a range of variables for the simulation in Figure 7.15 shows that the change from burst firing to repetitive firing results from reduced current maxima of the L-type calcium channels so that KCa channel conductance is able to terminate the activity after a single AP.

Simulation of LCa and KCa channel current densities in the soma and $[Ca^{2+}]$ in a somatic sub-membrane Ca pool in reconstructed MCs with fitted passive parameters and Na, K_{dr} and K_A channel mechanisms derived from Migliore et al. (2005) and L-type calcium, KCa and sub-membrane calcium pool derived from Bhalla and Bower (1993). In this case the version of the KCa channel is fitted to the response of the original Genesis Bhalla and Bower implementation of the channel, that I refer to as KCa_cml_Vdep in the text. The MCs are connected by 100 gap-junctions between the apical tufts of pairs of cells. Cell 3 is given a continuous current injection of 0.12 nA starting t=10 ms to 20 locations in its apical dendrite tuft. The coupling ratio has been adjusted ~0.025 , a level at which gap-junction driven firing is observed in some but not consistently in all the cells. There is a decay in L-type calcium channe current that results in reduced $[Ca^{2+}]$ in the sub-membrane ca pool while KCa current continues to achieve normal levels. This combination causes a switch from burst firing to repetitive firing.

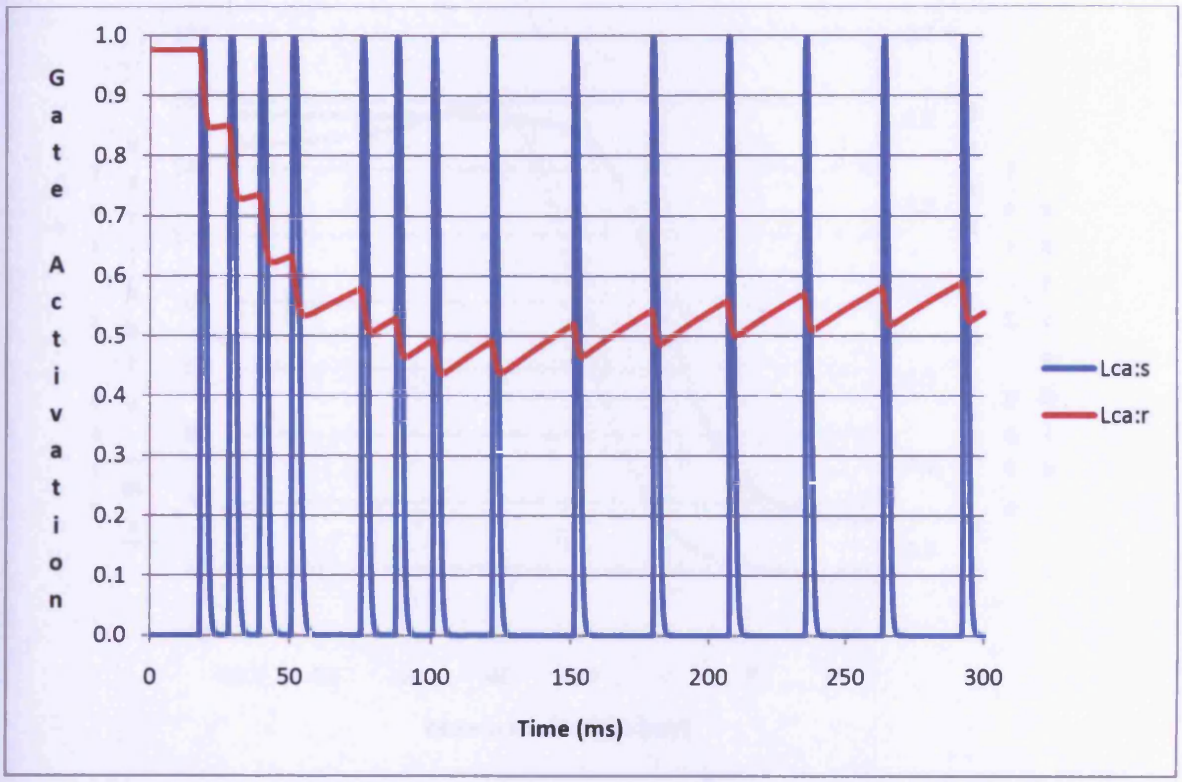

Figure 7.20: Plotting activation of the L-type calcium channel gate variables while the simulation in Figure 7.17is running shows that the 'r' gate activation decays to around 50% which explains the decay in L-type calcium channel current density maxima in Figure 7.19.

Simulation of LCa gate variable activation in reconstructed MCs with fitted passive parameters and Na, K_{dr} and K_A channel mechanisms derived from Migliore et al. (2005) and L-type calcium, KCa and sub-membrane calcium pool derived from Bhalla and Bower (1993). In this case the version of the KCa channel is fitted to the response of the original Genesis Bhalla and Bower implementation of the channel, that I refer to as KCa_cml_Vdep in the text. The MCs are connected by 100 gap-junctions between the apical tufts of pairs of cells. Cell 3 is given a continuous current injection of 0.12 nA starting t=10 ms to 20 locations in its apical dendrite tuft. The coupling ratio has been adjusted ~0.025 , a level at which gap-junction driven firing is observed in some but not consistently in all the cells. The decay in L-type calcium channel 'r' gate variable activation explains the decay in L-type calcium channel current density maxima shown in Figure 7.19.

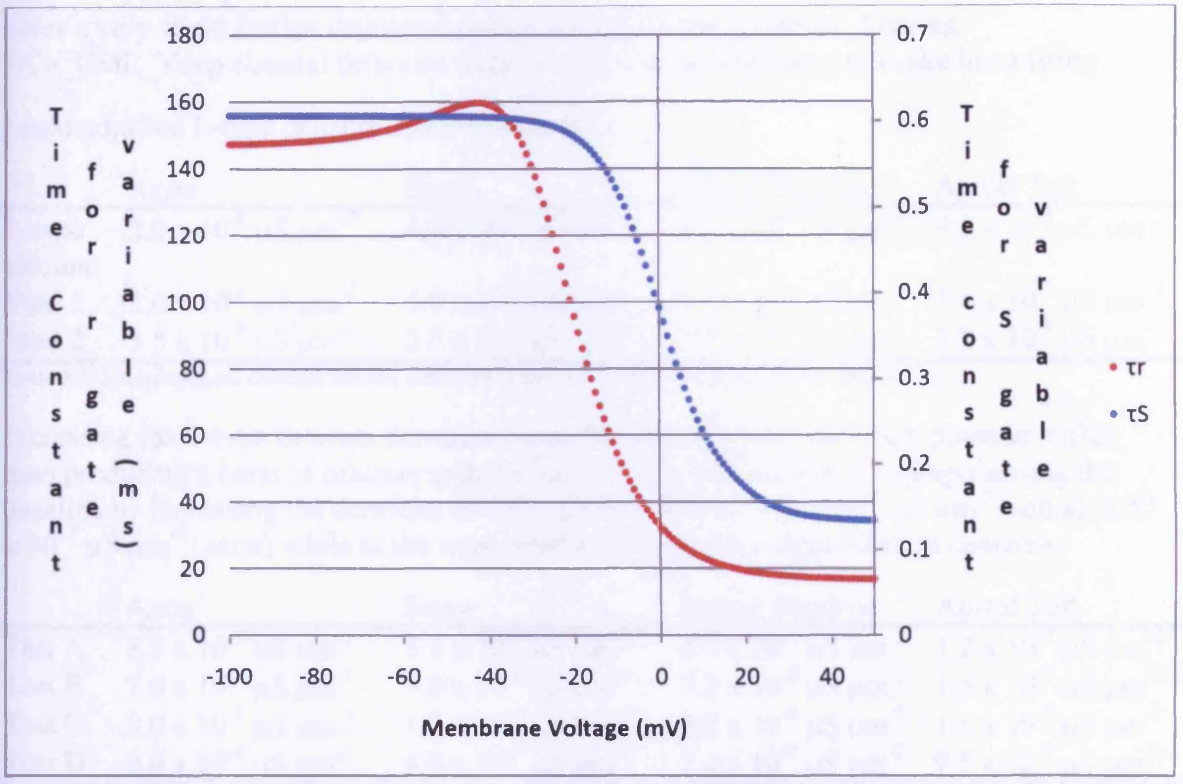

Figure 7.21: Plotting time constant against membrane voltage for the Bhalla and Bower (199) L-type calcium channel gate variables shows long time constants for th 'r' variable which stop the activation levels recovering in Figure 7.20.

The findings of the robust nature of burst firing wave-forms in the MC models presented here, raises questions about the role of gap-junctions in synchronising the responses (as suggested in Chapter 6). Should gap-junctions be regarded more as a trigger spreading stimulation across the population? Could there also be individual tuning of MCs to give more synchronised wave forms?

These questions are all difficult to answer because, as I have described in Chapter 2, there are many more layers of modulation than have been incorporated into this model. In addition the lack of experimental data limits the ability to constrain the models.

However it is possible to observe whether changing the densities of some of the channels renders the waveforms more similar to one another.

Influence of Calcium Mechanism Densities on Mitral Cell Wave Form

Looking at Figures 7.10-7.13, Cell 1 consistently fires once, but fails to produce burst firing in response to the current injection stimulus across the gap-junctions. Cell 1 is the cell whose response least similar to the waveforms of the other cells. I have therefore selected this cell to observe whether experimenting with calcium channel densities produces burst firing in line with the other cells. First of all, adjusting the densities of KCa_CML_Vdep in the soma and axon by several orders of magnitude fails to trip the cell into burst firing (Figure 7.21). An order of magnitude increase in channel densities has a strong hyperpolarising effect on the resting potential, but the current injection still induces the cell to fire. An order of magnitude decrease in channel densities depolarises the baseline resting potential and once the cell has fired a distinct after-depolarisation is seen. This after-depolarisation is not sufficient to induce a further action potential. Decreasing the channel densities a further order of magnitude only

calcium				
Mod 1	3.0×10^{-8} µS µm^{-2}	5.0×10^{-8} µS µm^{-2}	4.2×10^{-8} µS µm^{-2}	1.6×10^{-7} µS µm^{-2}
Mod 2	3.5×10^{-8} µS µm^{-2}	5.5×10^{-8} µS µm^{-2}	3.7×10^{-8} µS µm^{-2}	1.2×10^{-7} µS µm^{-2}

Table 7.2: L-type calcium channel density adjustment for cell 1 used for simulations in Figure 7.22.

Increasing the L-type calcium densities slows the recovery from an action potential rather than producing a burst of discrete spikes (Figure 7.22). So I looked at hyperpolarising the baseline by increasing the densities of KCa_CML_Vdep to 1.42×10^{-6} µS µm^{-2} (soma); 8.87×10^{-7} µS µm^{-2} (axon) while at the same time increasing the L-type calcium channels:

	Axon	Soma	Apical Dendrite	Apical Tuft
Test A	3.5×10^{-8} µS µm^{-2}	5.5×10^{-8} µS µm^{-2}	3.7×10^{-8} µS µm^{-2}	1.2×10^{-7} µS µm^{-2}
Test B	7.0×10^{-8} µS µm^{-2}	9.0×10^{-8} µS µm^{-2}	7.2×10^{-8} µS µm^{-2}	1.5×10^{-7} µS µm^{-2}
Test C	8.0×10^{-8} µS µm^{-2}	1.0×10^{-7} µS µm^{-2}	8.2×10^{-8} µS µm^{-2}	1.6×10^{-7} µS µm^{-2}
Test D	2.0×10^{-7} µS µm^{-2}	4.0×10^{-7} µS µm^{-2}	2.2×10^{-7} µS µm^{-2}	9.5×10^{-7} µS µm^{-2}

Table 7.3: Adjustments of L-type calcium channel densities made for cell 1 to produce the simulated membrane potentials in Figure 7.23.

Figure 7.23 again shows how increasing L-type calcium channel density slows the recovery from an action potential, but does not produce discrete spikes. Possibly a fitting algorithm would have a greater success at finding a set of channel density ratios that would produce discrete burst firing in Cell 1. However the relationships that would do this have not been revealed by simple manual fitting.

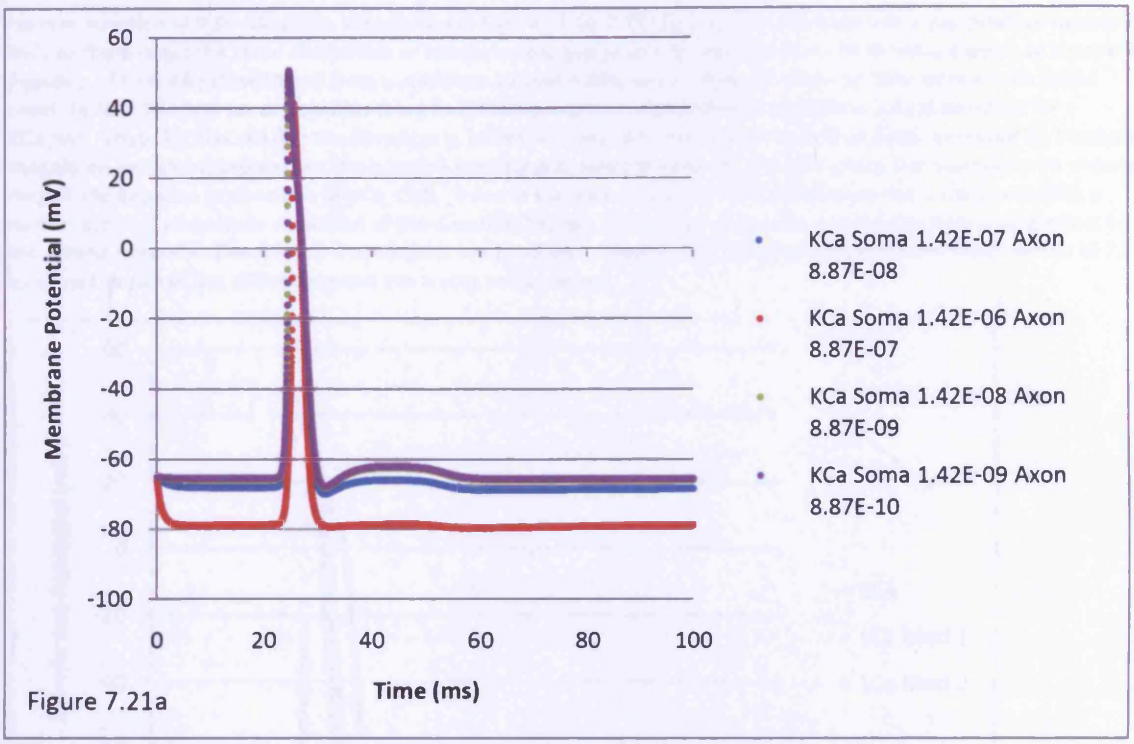

Figure 7.21a

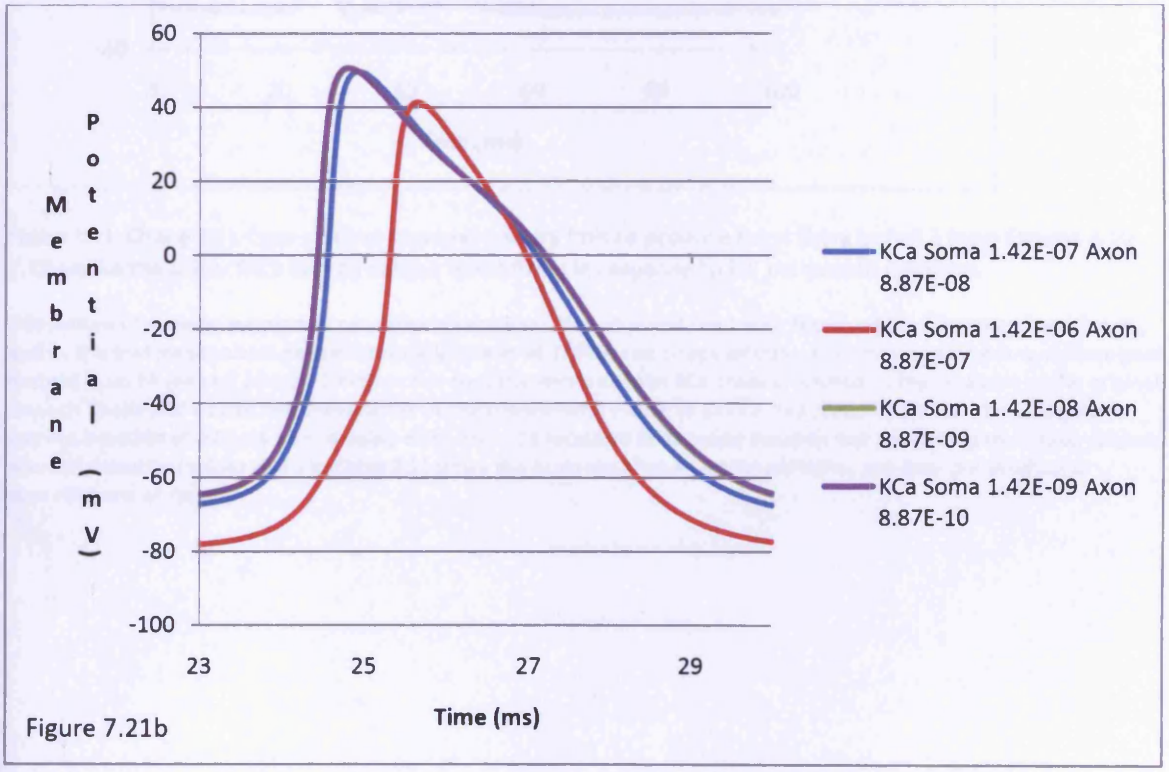

Figure 7.21b

Figure 7.22: Changing KCa channel density over several orders of magnitude fails to produce burst firing in Cell 1 from Figures 7.10-7.13 unlike the other MCs fails to exhibit burst firing in response to 0.5 ms current injection.

Simulation of somatic membrane potential in reconstruction of mitral cell 1 with fitted passive parameters and Na, K_{dr} and K_A channel mechanisms derived from Migliore et al. (2005) and L-type calcium, KCa and sub-membrane calcium pool derived from Bhalla and Bower (1993). In this case the version of the KCa channel is fitted to the response of the original Genesis Bhalla and Bower implementation of the channel that I refer to as KCa_cml_Vdep in the text. Cell 1 is given a

current injection of 0.09 nA(unlike simulations in Figures 7.10-7.13 cell 1 is not connected into a gap-junction network of MCs so there is not the same dissipation of charge across gap-junctions which reduces AP threshold down so a current injection of 0.09 nA rather than 0.5 nA is sufficient to evoke APs) after a delay of 20 ms to 20 locations in its apical dendrite tuft. The first set of densities (blue line) represents the original Bhalla and Bower (1993) densities for KCa_cml_Vdep. For the red line the densities in both the soma and axon membranes have been increased by 1 order of magnitude, which hyperpolarises the baseline (resting potential) to close -80 mV. The green line represents an order of magnitude decrease in densities of KCa_CML _Vdep in the axon and soma. This depolarises the resting potential, a further order of magnitude reduction of the densities (purple line) does not have an equivalent depolarising effect on the resting potential. Densities in chart legend are in μS μm^{-2}. Figure7.15b shows an enlarged time scale version of 7.15a to allow the size of the offset between the traces to be viewed.

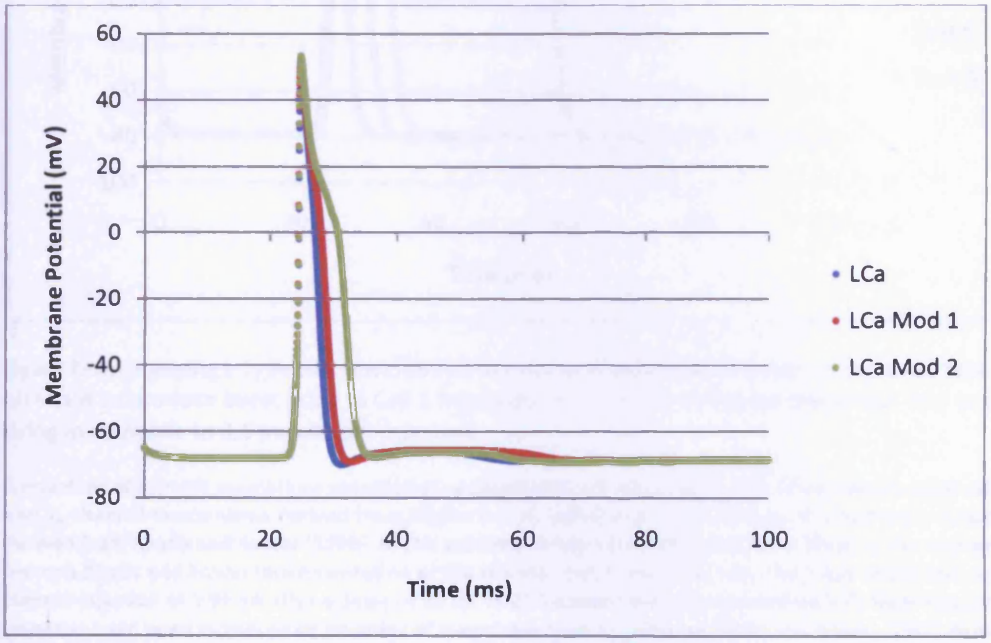

Figure 7.23: Changing L-type calcium channel density fails to produce burst firing in Cell 1 from Figures 7.10-7.13 unlike the other MCs fails to exhibit burst firing in response to 0.5 ms current injection.

Simulation of somatic membrane potential in reconstruction of mitral cell 1 with fitted passive parameters and Na, K_{dr} and K_A channel mechanisms derived from Migliore et al. (2005) and L-type calcium, KCa and sub-membrane calcium pool derived from Bhalla and Bower (1993). In this case the version of the KCa channel is fitted to the response of the original Genesis Bhalla and Bower implementation of the channel that I refer to as KCa_cml_Vdep in the text. Cell 1 is given a current injection of 0.09 nA after a delay of 20 ms to 20 locations in its apical dendrite tuft. Increasing the L-type calcium channel densities (values given in Table 7.2) slows the recovery after an action potential, but does not produce a discrete burst of spikes.

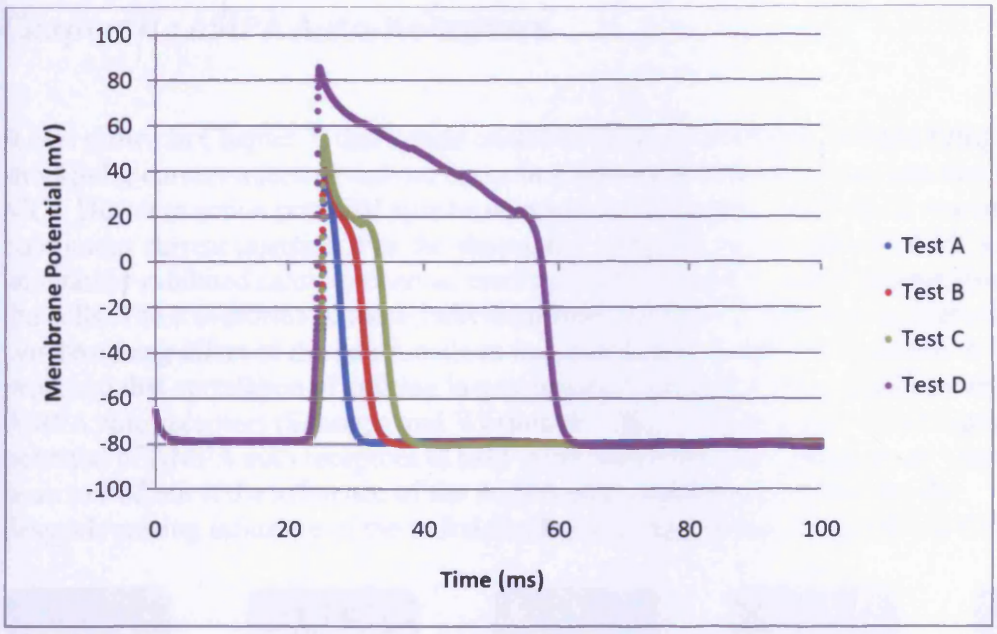

Figure 7.24: Changing L-type calcium channel density over over a wider range of densities than Figure 7.22 also fails to produce burst firing in Cell 1 from Figures 7.10-7.13 unlike the other MCs fails to exhibit burst firing in response to 0.5 ms current injection.

Simulation of somatic membrane potential in reconstruction of mitral cell 1 with fitted passive parameters and Na, K_{dr} and K_A channel mechanisms derived from Migliore et al. (2005) and L-type calcium, KCa and sub-membrane calcium pool derived from Bhalla and Bower (1993). In this case the version of the KCa channel is fitted to the response of the original Genesis Bhalla and Bower implementation of the channel that I refer to as KCa_cml_Vdep in the text. Cell 1 is given a current injection of 0.09 nA after a delay of 20 ms to 20 locations in its apical dendrite tuft. Here KCa_cml_Vdep densities have been increased by an order of magnitude from the original Bhalla and Bower (1993) densities to Soma 1.4 x 10^{-6} µS µm^{-2}; Axon 8.9 x 10^{-7} µS µm^{-2} . The L-type calcium channel densities are gradually increased (values given in Table 7.3). Like in Figure 7.23 increasing L-type calcium channel densities slows the recovery after an action potential, but does not produce a discrete burst of spikes.

In summary, a combination of the Bhalla and Bower (1993) L-type calcium, KCa and sub-membrane calcium-pool usually produces burst firing in MC simulations. Connecting together a network of the burst firing MCs by apical dendrite tuft gap-junctions does not promote synchronisation of the burst firing in my simulations. The wave form of individual MCs is characteristic for each cell and the gap-junction connections do not have a strong enough influence to modify the timing of spike trains sufficiently to have a synchronising effect. The most we can say is the gap-junctions will stimulate the connected cells into burst firing.

If a continuous current injection protocol is used for testing the synchronisation of a gap-junction connected network of MCs, burst firing does produce a desynchronising force for about 120 ms. However, the cells do settle down after this period into rhythmic synchronised firing.

Chapter 8 : AMPA Auto-Receptors

It was shown in Chapter 7, that synchronisation of action potentials in burst firing evoked by short pulse current injection did not occur in a simulated network of gap-junction connected MCs. However action potential synchronisation did occur after ~120 ms in response to continuous current injection. For the short pulse current injection individual MCs in the simulation exhibited calcium channel mediated burst firing that was characteristic for each of the cells. The waveforms of these individual burst firing MCs appeared to overcome the synchronising effect of the gap-junctions that was demonstrated in Chapters 6. It has been proposed that correlation of spiking in gap-junction connected MCs could be mediated by AMPA auto receptors (Schoppa and Westbrook 2002). In this chapter I investigate the potential of AMPA auto receptors to help synchronise MC burst firing in my simulations. I wish to find out if the influence of the AMPA auto receptors can overcome the desynchronising influence of the individual burst firing patterns of the MCs in Chapter 7.

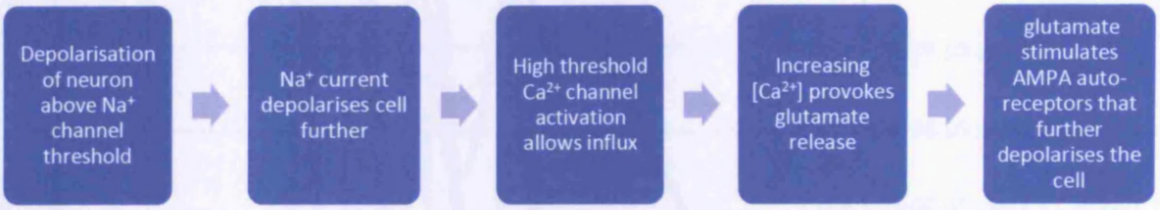

Figure 8.1 Trigger sequence for AMPA auto-receptors

To model AMPA auto-excitation a group of components need to be linked (see Figure 8.1). The auto-excitation is to be modelled in the apical dendrite tuft. The MCs already have ion channels that cover the first three steps in Figure 8.1.

Placing a calcium pool in the compartments of the apical dendrite tuft

The Bhalla and Bower (1993) MC setup that I have used so far, does not have a calcium pool in the apical dendrite tuft. I need a local increase in $[Ca^{2+}]$ to evoke the glutamate release so a calcium pool mechanism has to be added to all the compartments of the apical dendrite tuft. When the calcium pool was added, the L-type calcium channel density needed to be reduced from 9.5×10^{-8} μS μm^{-2} to 3.5×10^{-8} μS μm^{-2}. This was investigated in Mitral Cell 2 from Chapter 4 (see Figure 8.2). The $[Ca^{2+}]$ in each apical dendrite tuft compartment rises rapidly from the point of stimulation and decays rapidly towards the end of the burst firing as the calcium pool decay constant of 0.01 seconds reduces the $[Ca^{2+}]$ (Figure 8.3).

If an increase in $[Ca^{2+}]$ above a threshold is used as a trigger for glutamate release, the glutamate release will be triggered at the start of the burst and switched off at the end of the burst. Glutamate is released in vesicles which for modelling purposes can be considered as discrete quanta. The glutamate from these discrete quanta will rise rapidly and decay rapidly in the vicinity of the AMPA receptors. This would lead to multiple glutamate release events over the period of a firing burst. Fluctuations in $[Ca^{2+}]$ in the calcium pool at the soma (Figure 8.4) are observed in response to individual action potentials of the burst firing. However, the same kind of fluctuations of $[Ca^{2+}]$ in the calcium pool are not observed in the apical dendrite tuft (Figures 8.3 and 8.4). This is not caused by the APs failing to propagate into the apical dendrite tuft. It is rather the the depolarisation from the APs together with the activation of the L-type calcium channels in the narrow fibres of the tuft, which do not allow

charge to escape fast enough to allow membrane potential recovery towards resting potential in the time scales involved (Figure 8.5). Hence the L-type calcium channels remain activated and consequently the $[Ca^{2+}]$ remains elevated. But, if the $[Ca^{2+}]$ at the apical dendrite tuft were to fluctuate in response to individual action potentials, this would allow better control of the glutamate release. If AMPA auto receptors are to have a synchronising effect on action potentials across the network, it would seem logical that they would be evoked by the action potentials and not some arbitrary release of glutamate. Therefore I carried out some tests to see if I could promote these action potential driven $[Ca^{2+}]$ fluctuations by reducing the shell thickness of the calcium pool.

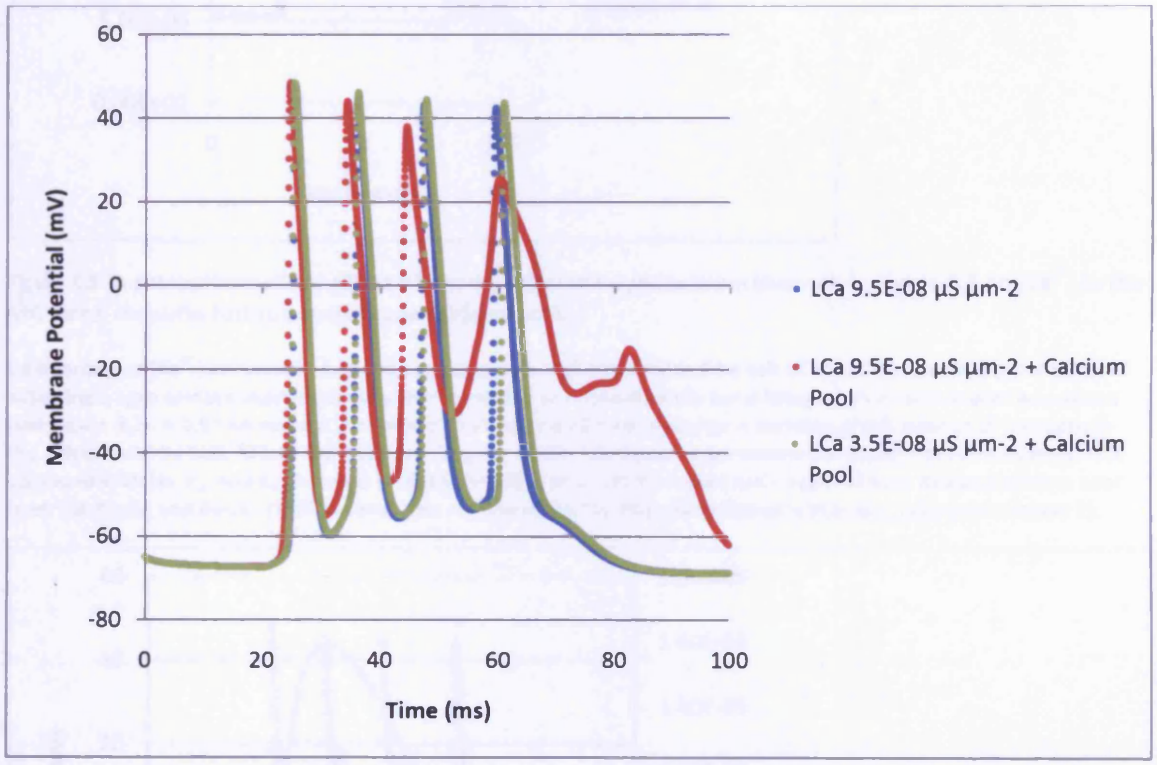

Figure 8.2: Adding a sub-membane calcium pool to the compartments of the apical dendrite tuft increases the effect of the L-type calcium channels which destabilises the burst firing in MCs (red trace) so the L-type calcium channel densities need to be reduced to compensate (green trace).

Comparison of simulated membrane potential recordings for Mitral Cell 2 showing the effect of adding a calcium pool to all the compartments of the apical dendrite tuft and the adjustment of L-type calcium channel density that is needed to re-stabilise the burst firing. A 0.07 nA current injection is given after a 20 msec delay for a duration of 0.5 msec at 20 locations in the apical dendrite tuft. Mitral Cell 2 is from Chapter 4 with fitted passive parameters to experimental recordings. It is equipped with Na, K_{dr} and K_A channels from the Migliore et al. (2005) model and L-type calcium, KCa and calcium pool from the Bhalla and Bower (1993) model. The version of the the KCa channel used is KCa_cml_vdep (see Chapter 7).

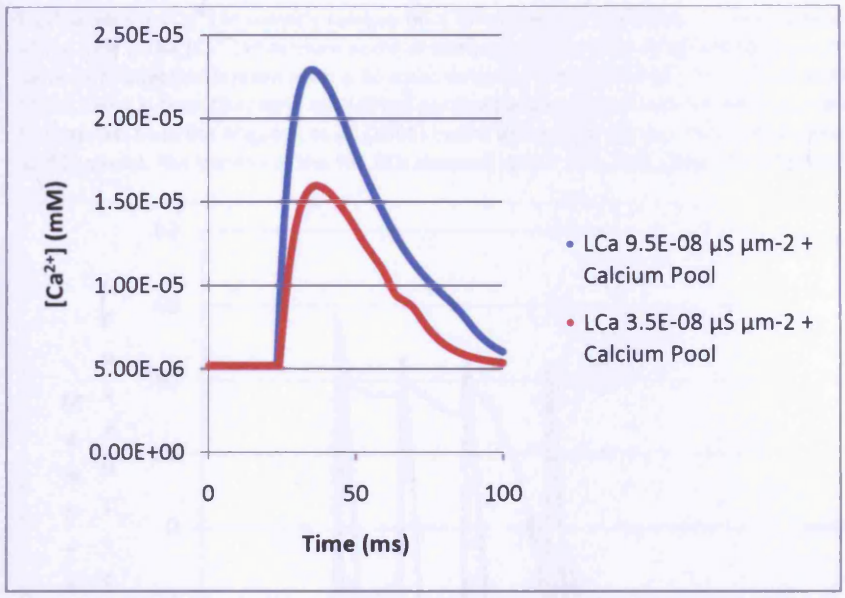

Figure 8.3: A comparison of the effect of the densities of L-type calcium channels in Figure 8.2 on [Ca^{2+}] in the MC apical dendrite tuft sub-membrane calcium pool.

Comparison of [Ca^{2+}] simulated plots in a compartment of the apical dendrite tuft of Mitral Cell 2 showing the effect of adjusting L-type calcium channel density that is needed to re-stabilise the burst firing when a calcium pool was added (see Figure 8.2). A 0.07 nA current injection is given after a 20 msec delay for a duration of 0.5 msec at 20 locations in the apical dendrite tuft. Mitral Cell 2 is from Chapter 4 with fitted passive parameters to experimental recordings. It is equipped with Na, K_{dr} and K_A channels from the Migliore et al. (2005) model and L-type calcium, KCa and calcium pool from the Bhalla and Bower (1993) model. The version of the the KCa channel used is KCa_cml_vdep (see Chapter 7).

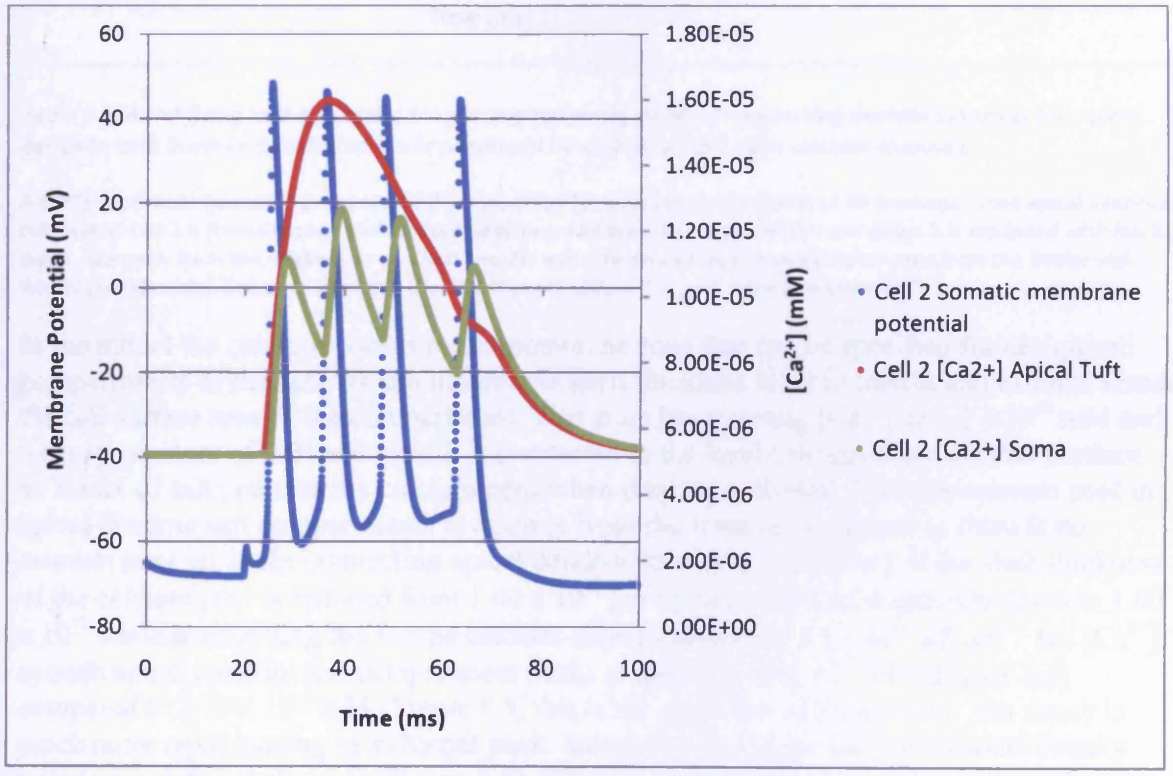

Figure 8.4: Burst firing in the somatic membrane potential is mirrored by fluctuations in [ca^{2+}] in the somatic sub-membrane calcium pool but [ca^{2+}] remains elevated for the entire period of burst firing in the sub-membrane calcium pool located in compartments of the apical dendrite tuft.

Fluctuations in $[Ca^{2+}]$ in somatic calcium pool in response to individual action potentials in a simulation of a burst firing Mitral Cell 2. The $[Ca^{2+}]$ in calcium pools of compartments of the apical tuft does not fluctuate in the same way. A 0.07 nA current injection is given after a 20 msec delay for a duration of 0.5 msec at 20 locations in the apical dendrite tuft. Mitral Cell 2 is from Chapter 4 with fitted passive parameters to experimental recordings. It is equipped with Na, K_{dr} and K_A channels from the Migliore et al. (2005) model and L-type calcium, KCa and calcium pool from the Bhalla and Bower (1993) model. The version of the the KCa channel used is KCa_cml_vdep (see Chapter 7).

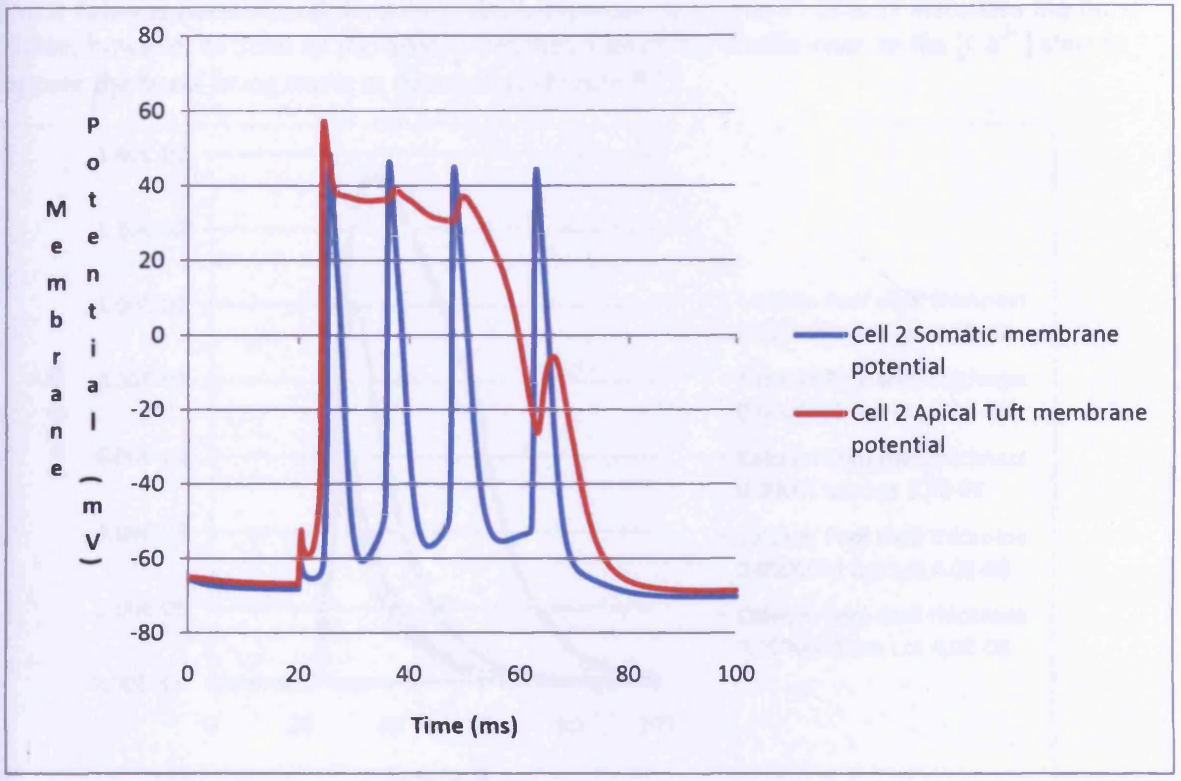

Figure 8.5: Burst firing in the somatic membrane potential evoke a long lasting depolarisation in the apical dendrite tuft. Further depolarisation is produced by activation of L-type calcium channels.

A 0.07 nA current injection is given after a 20 msec delay for a duration of 0.5 msec at 20 locations in the apical dendrite tuft. Mitral Cell 2 is from Chapter 4 with fitted passive parameters to experimental recordings. It is equipped with Na, K_{dr} and K_A channels from the Migliore et al. (2005) model and L-type calcium, KCa and calcium pool from the Bhalla and Bower (1993) model. The version of the the KCa channel used is KCa_cml_vdep (see Chapter 7).

In the model the calcium pool is a sub membrane zone that can be specified for designated compartments in the cell. Its sub membrane shell thickness is set in metres and extends across the full surface area of the compartment. This zone has a resting $[Ca^{2+}]$ of 5.2×10^{-6} mM and a decay constant of 0.01 seconds. It is connected to the local calcium channels that produce an influx of calcium into the calcium pool when they are activated. Here the calcium pool in apical dendrite tuft compartments is discrete from the soma calcium pool as there is no calcium pool set in the connecting apical dendrite (however see below). If the shell thickness of the calcium pool is reduced from 1.00×10^{-5} µm by two orders of magnitude down to 1.00×10^{-7} while maintaining the L-type calcium channel density at 3.5×10^{-8} µS µm^{-2}, the $[Ca^{2+}]$ in each apical dendrite tuft compartment peaks at around 5.00×10^{-3} mM (Figure 8.6) compared to 1.70×10^{-5} mM (Figure 8.3, this is the green line in Figure 8.6). The decay is much more rapid leading to a sharper peak. Increasing the L-type calcium channel density broadens out this peak again (Figure 8.6). This shows that $[Ca^{2+}]$ cannot be made to fluctuate in response to individual action potentials by altering the shell thickness.

In a further attempt to obtain fluctuating [Ca^{2+}] in the apical dendrite tuft in response to individual action potentials, I placed calcium pools in the compartments of the apical dendrite. This was to try and get some transmission of [Ca^{2+}] from the soma that does have the required fluctuations (Figure 8.4). With the L-type calcium channel density in each compartment of the apical dendrite set to the Bhalla and Bower (1993) value of 2.2 x 10^{-8} the burst firing is destabilised. Reducing the L-type calcium channel density stabilises the burst firing, however as soon as the density reaches a level that fluctuations in the [Ca^{2+}] start to appear the burst firing starts to destabilise (Figure 8.7).

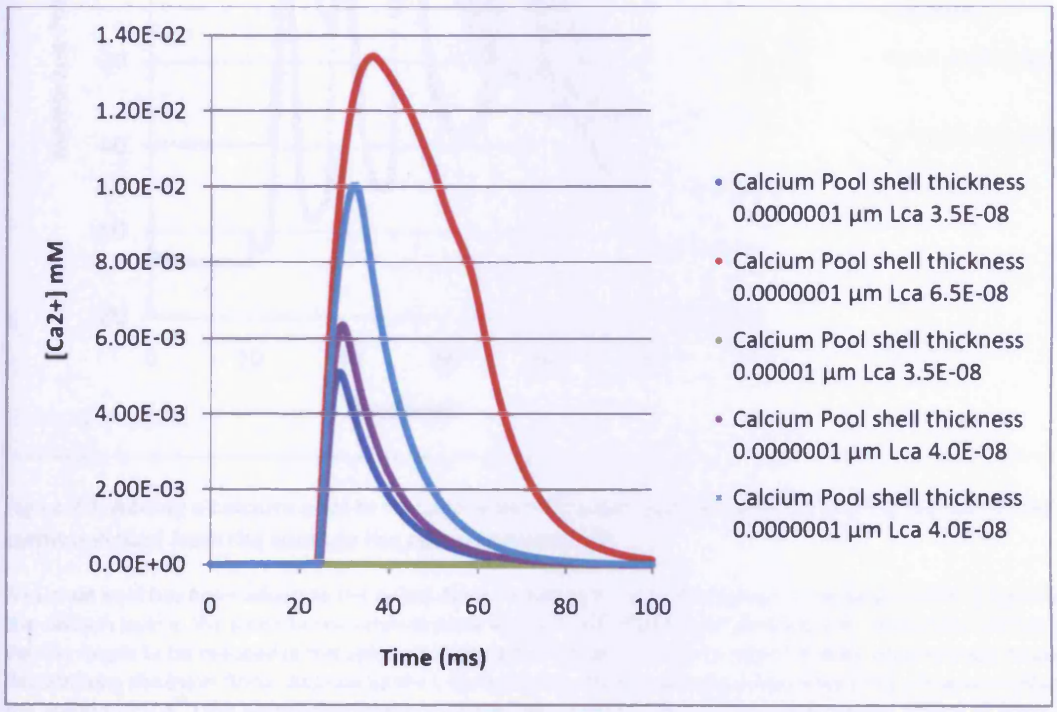

Figure 8.6: Adjusting the apical dendrite tuft sub-membrane calcium pool shell thickness and L-type calcium channel densities increases the size of the response in [Ca^{2+}] but cannot be used to promote fluctuations in [Ca^{2+}] apical dendrite tuft as is observed in calcium pool of the soma.

Comparison of [Ca^{2+}] recordings in a compartment of the apical dendrite tuft of Mitral Cell 2 showing the effect of adjusting calcium pool shell thickness and L-type calcium channel density. The green line is the same recording as the red line in Figure 7.3. A 0.07 nA current injection is given after a 20 msec delay for a duration of 0.5 msec at 20 locations in the apical dendrite tuft. Mitral Cell 2 is from Chapter 4 with fitted passive parameters to experimental recordings. It is equipped with Na, K_{dr} and K_A channels from the Migliore et al. (2005) model and L-type calcium, KCa and calcium pool from the Bhalla and Bower (1993) model. The version of the the KCa channel used is KCa_cml_vdep (see Chapter 7).

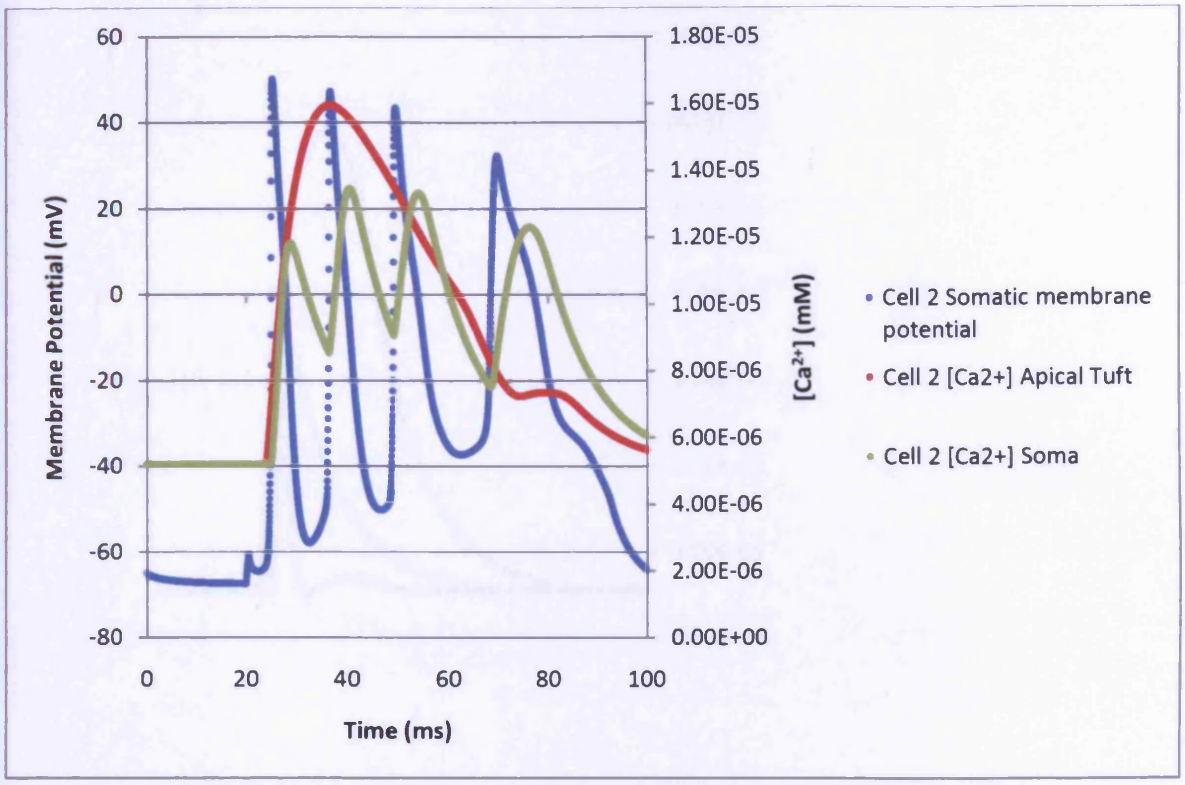

Figure 8.7: Adding a calcium pool to the apical dendrite tuft does not allow [Ca^{2+}] fluctuations to be communicated from the soma to the apical dendrite tuft.

A calcium pool has been added to the apical dendrite tuft to try to obtain some transmission of [Ca^{2+}] fluctuations from the calcium pool in the soma to the calcium pools in the compartments of the apical tuft. The L-type calcium channel density needs to be reduced in the apical dendrite once the calcium pool is added it to its compartment to avoid destabilising the burst firing. As soon as the L-type calcium channel density is high enough to allow some fluctuation in the apical tuft [Ca^{2+}] the burst firing starts to destabilise. A 0.07 nA current injection is given after a 20 msec delay for a duration of 0.5 msec at 20 locations in the apical dendrite tuft. Mitral Cell 2 is from Chapter 4 with fitted passive parameters to experimental recordings. It is equipped with Na, K_{dr} and K_A channels from the Migliore et al. (2005) model and L-type calcium, KCa and calcium pool from the Bhalla and Bower (1993) model. The version of the the KCa channel used is KCa_cml_vdep (see Chapter 7).

So far I have just considered the effects of adding the calcium pool to the apical dendrite tuft compartments of Mitral Cell 2. But as I have shown in Chapter 7 the burst firing characteristics of the different cells vary. I will again take the example of Mitral Cell 1 that does not produce burst firing in the simulations carried out for Chapter 7 (Figure 8.8).

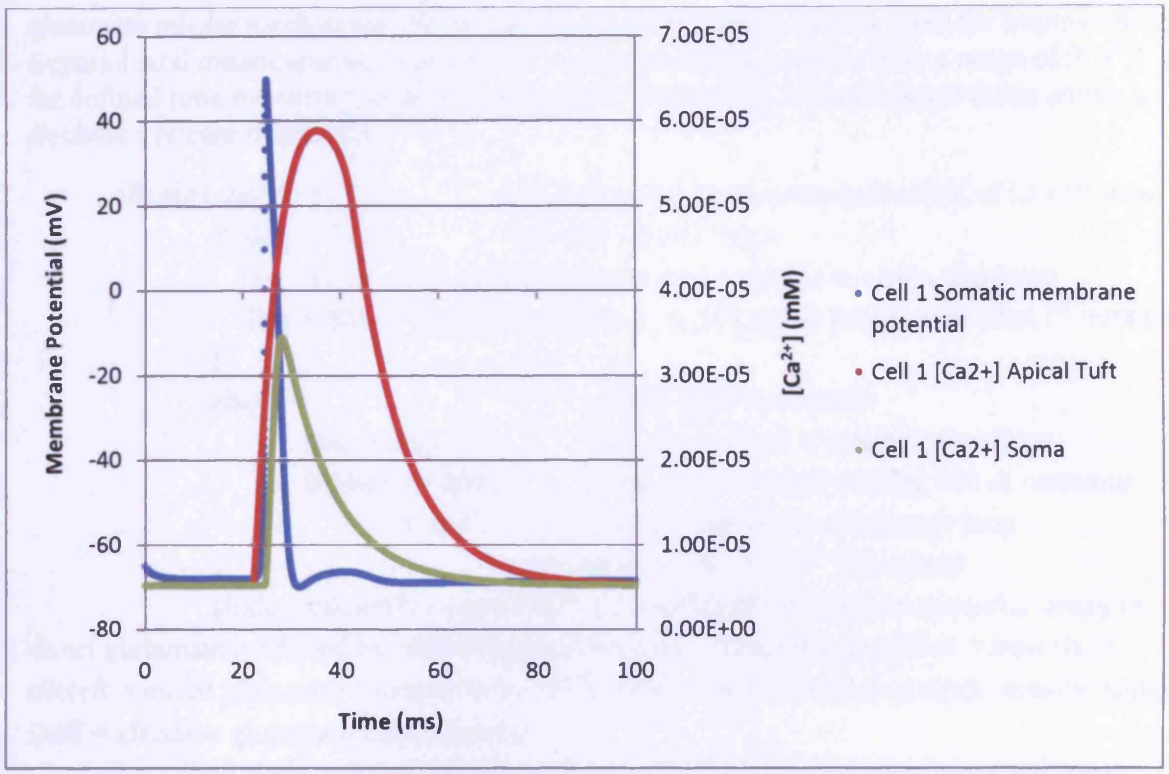

Figure 8.8: Mitral Cell 1 does not produce burst firing in simulations unlike the other 5 MCs that have been modelled. The absence of burst firing is accompanied by an absence of $[Ca^{2+}]$ fluctuations in the calcium pool of the MC soma.

In Mitral cell 1 the absence of burst firing is mirrored by the single $[Ca^{2+}]$ peak in the soma. Compare this with Figure 7.4 for Mitral Cell 2 in which burst firing does occur. A 0.07 nA current injection is given after a 20 msec delay for a duration of 0.5 msec at 20 locations in the apical dendrite tuft. Mitral Cell 2 is from Chapter 4 with fitted passive parameters to experimental recordings. It is equipped with Na, K_{dr} and K_A channels from the Migliore et al. (2005) model and L-type calcium, KCa and calcium pool from the Bhalla and Bower (1993) model. The version of the the KCa channel used is KCa_cml_vdep (see Chapter 7).

Controlling glutamate release in the apical dendrite tuft

I can use rising $[Ca^{2+}]$ in the calcium pool in apical dendrite tuft compartments to trigger a glutamate release mechanism situated locally in the same compartment of the apical dendrite tuft and use the decaying $[Ca^{2+}]$ at the end of the burst firing to switch off the glutamate release mechanism. But in between these two points, as I have shown, there are not fluctuations in $[Ca^{2+}]$ linked to individual action potentials. Therefore I need to use some other process to control glutamate release. As I have said earlier the glutamate release needs to be in discrete quanta corresponding to vesicles. I could use a random number generator to produce a time interval between release events, but have decided that for comparison purposes it is better to have a fixed time interval (multiples of dt, fitted to action potential intervals).

In the following script segment the $[Ca^{2+}]$ threshold is set to 1.2×10^{-5} mM and the time interval while the $[Ca^{2+}]$ continues above threshold is 400 x dt. The time interval was adjusted by trial and error to give glutamate release coincident with the action potential peaks, 400 x dt produced the best fit. A plot of the time intervals for glutamate release points in an identical simulation of Mitral Cell 2 as given in the green line of Figure 8.2 is given below Figure 8.9, tx1 plot (tx1 is the program clock that times vesicle release events). The

glutamate release mechanism is a part of the model for which there is room for improvement. Experimental measurements of glutamate vesicle release probability over a range of [Ca^{2+}] for defined time intervals could be used to produce gradients of time/release ratios within a stochastic release mechanism.

```
if(cai>1.2e-05) {              :when cai (the [Ca2+] is above the set threshold, of 1.2 x 10-5 then
        if (disc <= 0) {       :if pointer (disc) is zero
          tx1 = (t-1)   :zero the time difference (tx1) in gludir(-1 to avoid a singularity)
          disc = (disc + 1):add 1 to pointer i.e. pointer no longer zero after 1st iteration
        }
        else {                          :or if pointer is not zero
                disc = (disc + 1)        :add 1 to pointer to count dt iterations
                if (disc >= 400) {       :when pointer count reaches 400 dt iterations
                        disc = 0         :zero pointer and recommence loop
        }                       :every iteration above [Ca2+] threshold
        gludir= c0cleft*(1-exp(rPSD*rPSD/(4*Deff*(tx1-t)))):exponential decay in
```

direct glutamate produced by subtracting current time t from time at pointer = zero (tx1)
c0cleft = initial glutamate concentration (mM), rPSD = radius of post synaptic density (μm), Deff = effective glutamate concentration

```
        if(gludir>c0cleft){gludir=c0cleft}:stop [glutamate] exceeding initial release
```

concentration.

```
        pglu = gludir :[glutamate] pglu = direct glutamate diffusion (gludir)
        SOLVE states METHOD derivimplicit :use a particular method to calculate
        gampa = gbarampa *  O * RelProb :AMPA channel conductance (gampa) =
```

maximum AMPA channel conductance (gbarampa) x gate variable (O) x relative probability of glutamate residence on AMPA receptor (RelProb)

```
        iampa = (1e-6) * gampa * (v - Erev):AMPA current (iampa) = unit conversion
```

x AMPA channel conductance x difference of membrane potential from the reversal potential (Erev)

```
        }
}
```

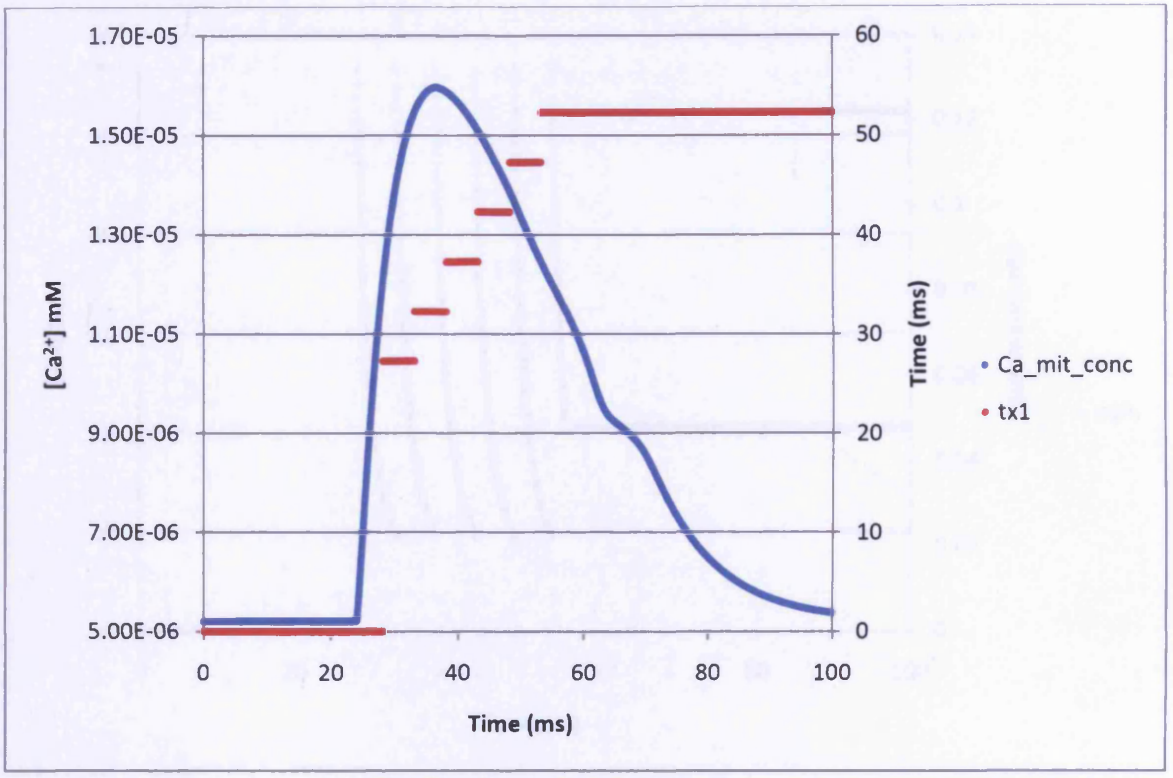

Figure 8.9: I have chosen to model the first stage of glutamate auto-excitation by using a [Ca^{2+}] threshold in calcium pools in compartments of the apical dendrite tuft to trigger a sequence of steps where quanta of glutamate are released.

The blue line is the [Ca^{2+}] recording in the calcium pool of a compartment of the apical dendrite tuft of Mitral Cell 2 (This is the same recording as the red line in Figure 7.3). The red line is a time interval for glutamate release given by the script above in response to the [Ca^{2+}] in the blue line. A 0.07 nA current injection is given after a 20 msec delay for a duration of 0.5 msec at 20 locations in the apical dendrite tuft. Mitral Cell 2 is from Chapter 4 with fitted passive parameters to experimental recordings. It is equipped with Na, K_{dr} and K_A channels from the Migliore et al. (2005) model and L-type calcium, KCa and calcium pool from the Bhalla and Bower (1993) model. The version of the the KCa channel used is KCa_cml_vdep (see Chapter 7).

The rest of the script is modified from Saftenku (2005). Both glutamate release and the AMPA receptor current are modelled in the same mechanism. For autoreceptors, this makes much more sense from a modelling perspective as both mechanisms are in close proximity. This means that I no longer have to setup link instructions between the two sets of mechanisms as they are handled locally within the script. Spill over of glutamate from adjacent cells (pglu=gludir + gluspill) was part of the original Saftenku (2005) script. However as spill over of glutamate is now thought unlikely to stimulate AMPA receptors of adjacent mitral cells (Christie and Westbrook 2006) I have removed this component. In my script glutamate is modelled by the equation:

$$pglu = 8.769mM \times (1 - EXP^{\frac{0.11\mu m \times 0.11\mu m}{4 \times 0.2\mu m^2 ms^{-1} \times (tx1 - t)ms}}), \quad \text{pglu} = [\text{glutamate}]$$

Equation 8.1

This equation gives fixed quanta release of glutamate with rapid decay. Returning to the simulation using Mitral Cell 2, the tx1 time steps give the pattern of glutamate release in Figure 8.10.

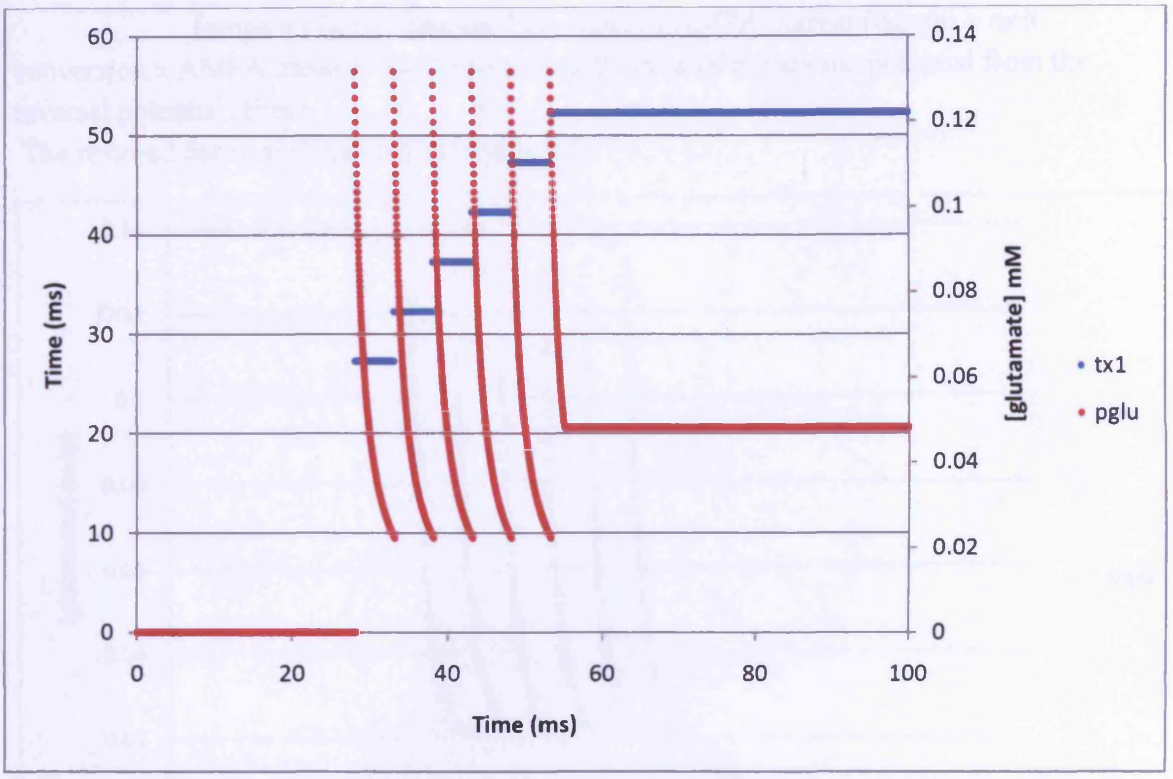

Figure 8.10: The stepped release points of the blue line represent the points when quanta of glutamate are released. The quanta of glutamate decay rapidly (Red line) according to equation 8.1.

The blue line is the time interval for glutamate release given by the [Ca^{2+}] threshold in the calcium pool of a compartment of the apical dendrite tuft of Mitral Cell 2 activating a time step of 400 x dt. The red line is the [glutamate] that results from the release of quanta of glutamate at the time steps and decays according to equation1. A 0.07 nA current injection is given after a 20 msec delay for a duration of 0.5 msec at 20 locations in the apical dendrite tuft. Mitral Cell 2 is from Chapter 4 with fitted passive parameters to experimental recordings. It is equipped with Na, K_{dr} and K_A channels from the Migliore et al. (2005) model and L-type calcium, KCa and calcium pool from the Bhalla and Bower (1993) model. The version of the the KCa channel used is KCa_cml_vdep (see Chapter 7).

The problem that is immediately obvious in Figure 8.10 is that pglu does not decay when [Ca^{2+}] drops below the set threshold. This can be rectified by pairing the if clause "if (cai>1.2e-05)" with an else clause:

```
else {   : allows pglu to decay once [Ca2+] drops below threshold
        if (pglu > 0) { :when [glutamate] not zero
        gludir= c0cleft*(1-exp(rPSD*rPSD/(4*Deff*(tx1-t)))) :exponential decay in
```

direct glutamate produced by subtracting current time t from time at pointer = zero (tx1) c0cleft = initial glutamate concentration (mM), rPSD = radius of post synaptic density (μm), Deff = effective glutamate concentration

```
        if(gludir>c0cleft){gludir=c0cleft}}:stop [glutamate] exceeding initial release
```

concentration.

```
        pglu = gludir :[glutamate] pglu = direct glutamate diffusion (gludir)
        SOLVE states METHOD derivimplicit  :use a particular method to calculate
        gampa = gbarampa *  O * RelProb :AMPA channel conductance (gampa) =
```

maximum AMPA channel conductance (gbarampa) x gate variable (O) x relative probability of glutamate residence on AMPA receptor (RelProb)

iampa = (1e-6) * gampa * (v - Erev)):AMPA current (iampa) = unit conversion x AMPA channel conductance x difference of membrane potential from the reversal potential (Erev) }

The restored decay is illustrated in Figure 8.11.

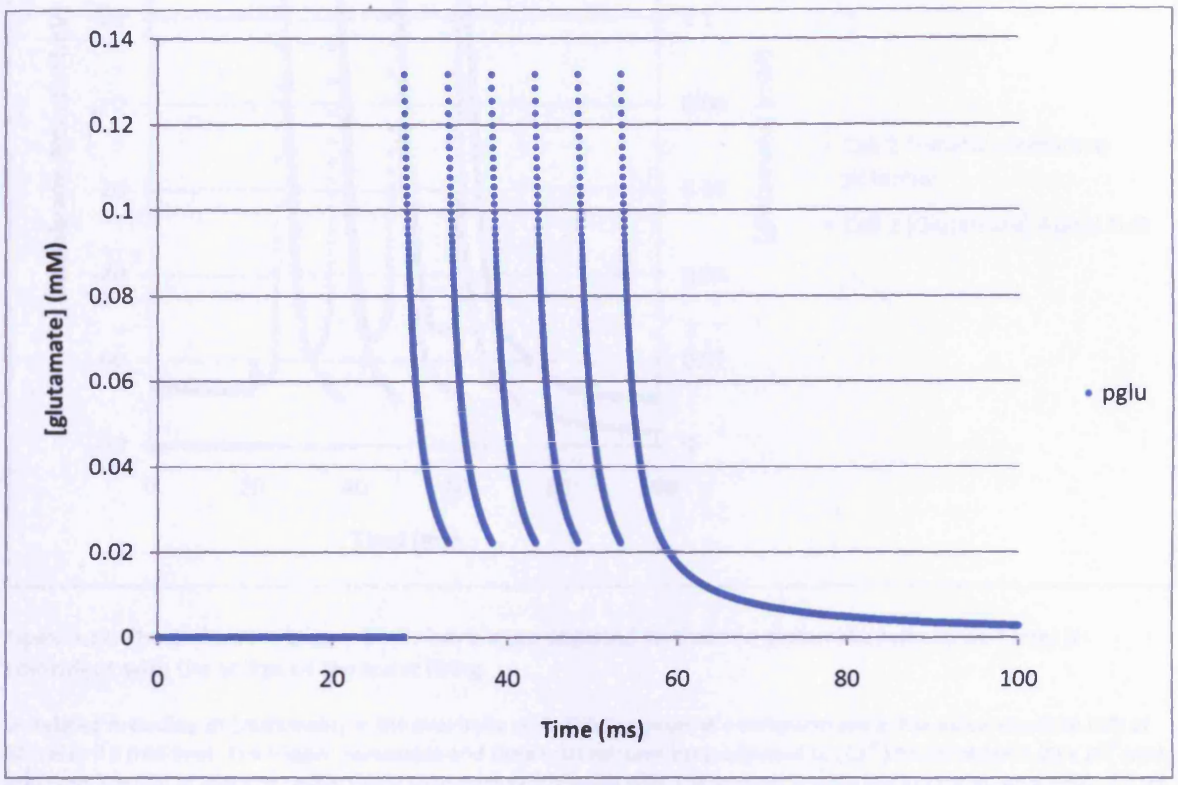

Figure 8.11: The truncated glutamate decay from Figure 8.9 has been corrected by modifying the script (see text).

Simulated recording of [glutamate] in the proximity of AMPA receptors at a compartment in the apical dendrite tuft of Mitral Cell 2. In this simulation [glutamate] decay continues after $[Ca^{2+}]$drops below a set threshold unlike Figure 7.6. See text for changes in the script that allowed this correction. A 0.07 nA current injection is given after a 20 msec delay for a duration of 0.5 msec at 20 locations in the apical dendrite tuft. Mitral Cell 2 is from Chapter 4 with fitted passive parameters to experimental recordings. It is equipped with Na, K_{dr} and K_A channels from the Migliore et al. (2005) model and L-type calcium, KCa and calcium pool from the Bhalla and Bower (1993) model. The version of the the KCa channel used is KCa_cml_vdep (see Chapter 7).

Next I adjusted the trigger parameters to fit as closely as possible the [glutamate] to the somatic membrane potential (Figure 8.12). The $[Ca^{2+}]$ trigger point was now set at 9.00 x 10^{-6} mM and the time interval to 900 x dt.

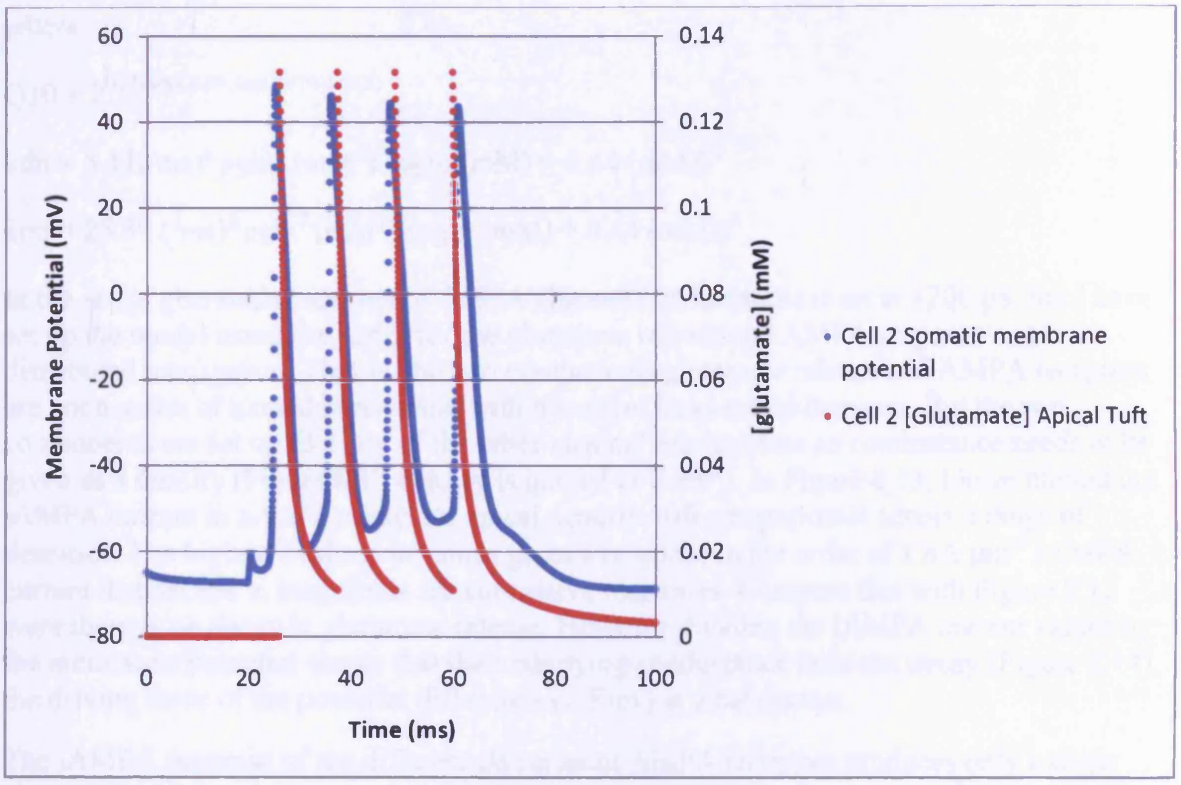

Figure 8.12: The glutamate trigger steps have been adjusted so that the glutamate release (red line) is coincident with the spikes of the burst firing.

Simulated recording of [glutamate] in the proximity of AMPA receptors at a compartment in the apical dendrite tuft of Mitral Cell 2 (red line). The trigger parameter and time interval have been adjusted to [Ca^{2+}] threshold of 9.00 x 10^{-6} mM and time interval of 900 x dt respectively to almost synchronise with the somatic membrane potential (blue line). A 0.07 nA current injection is given after a 20 msec delay for a duration of 0.5 msec at 20 locations in the apical dendrite tuft. Mitral Cell 2 is from Chapter 4 with fitted passive parameters to experimental recordings. It is equipped with Na, K_{dr} and K_A channels from the Migliore et al. (2005) model and L-type calcium, KCa and calcium pool from the Bhalla and Bower (1993) model. The version of the the KCa channel used is KCa_cml_vdep (see Chapter 7).

Modelling the AMPA auto receptors

The Saftenku (2005) implementation of the AMPA receptor mechanism uses 3 state DCO (desensitised ↔ closed ↔open) kinetics as follows:

iAMPA = (1e-6) * gampa * (v – 0 (Erev, mV))

where:

gampa = gbarampa * O * 0.46 (RelProb)

with the derivative states:

C'=Q10*(-(kdn+kon)*C+ 0.065 (/ms)*D+ 4 (/ms)*O)

D'=Q10*(- 0.065 (/ms)*D+kdn*C)

O'=Q10*(-4 (/ms)*O + kon*C)

where:

$Q10 = 2^{((35(degC)-37(degC))/10(degC))}$

$kdn = 5.11(/ms)*pglu^2\ (mM^2)/(pglu\ (mM) + 0.44\ (mM))^2$

$kon = 25.39\ (/ms)*pglu^2\ (mM^2)/(pglu\ (mM) + 0.44\ (mM))^2$

In the script gbarampa (maximum AMPA channel conductance) is set at 1200 pS, but I have set up the model using the script for the glutamate release and AMPA response as a distributed mechanism. That is, the two components glutamate release and AMPA receptors are not a series of named connection with messages links set up between. But the two components are set up like any of the other channel mechanisms so conductance needs to be given as a density (Figure 8.13 density is quoted as S/cm^2). In Figure 8.13, I have plotted out iAMPA current in nA at a particular apical dendrite tuft compartment across a range of densities. The highest of these densities gives a response in the order of 1 nA μm^{-2} iAMPA current that decays in magnitude for successive responses. Compare this with Figure 8.12 were there is no decay in glutamate release. However dividing the iAMPA current values by the membrane potential shows that the underlying conductance does not decay (Figure 8.14), the driving force of the potential difference (v-Erev) is what decays.

The iAMPA response of the different densities of AMPA receptors produces only a slight change in the burst firing seen in somatic membrane potential up to 1.2×10^{-6} mS μm^{-2} (Figure 8.15). However increasing the density an order of magnitude further to 1.2×10^{-5} mS μm^{-2}, produces extended burst firing.

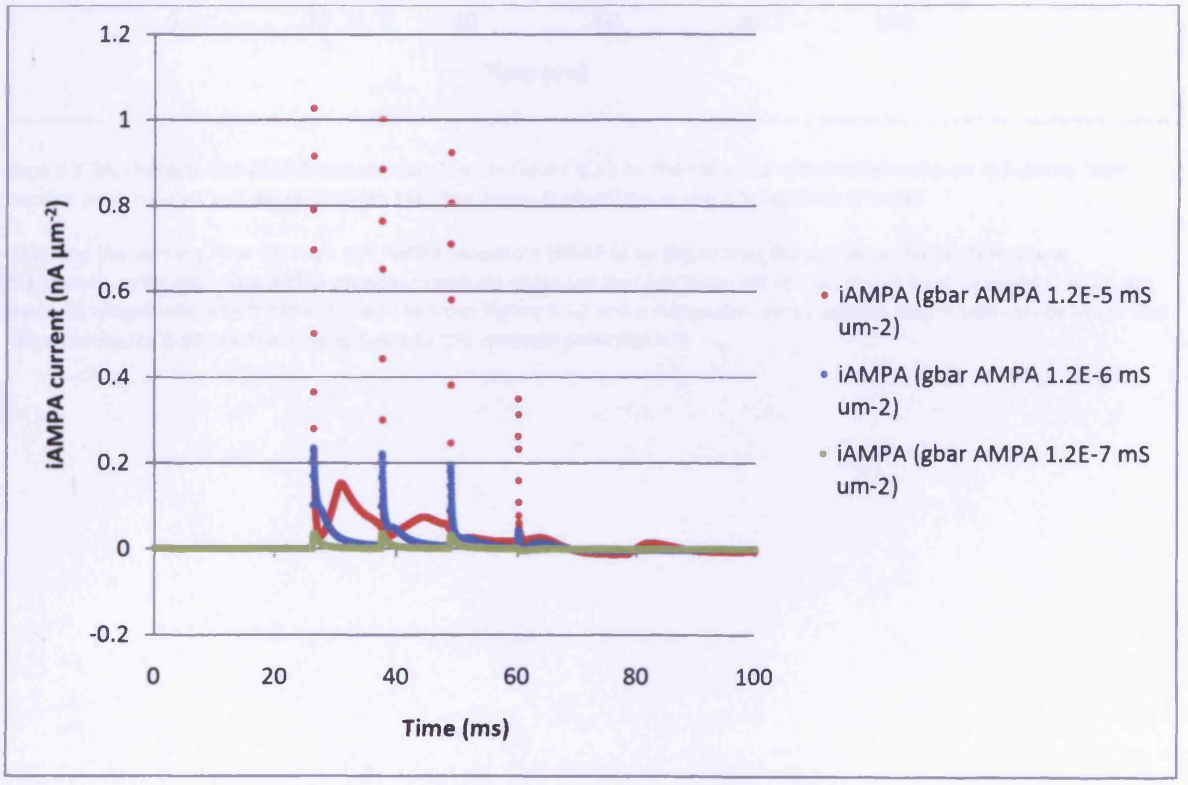

Figure 8.13: Current densities through the AMPA receptors for different densities of the receptors. Notice the decay in successive peak heights that is not a function of the glutamate release (compare Figure 8.11).

The current flow through AMPA receptors in a compartment of the apical dendrite tuft of Mitral Cell 2 in response to the glutamate release depicted in Figure 8.12 at decreasing densities of AMPA receptors. Glutamate release is controlled by a $[Ca^{2+}]$ threshold of 9.00×10^{-6} mM and a time interval of 900 x dt between quanta of glutamate released. The rising $[Ca^{2+}]$ is evoked initially by a 0.07 nA current injection is given after a 20 msec delay for a duration of 0.5 msec at 20 locations in the apical dendrite tuft. Mitral Cell 2 is from Chapter 4 with fitted passive parameters to experimental recordings. It is equipped with Na, K_{dr} and K_A channels from the Migliore et al. (2005) model and L-type calcium, KCa and calcium pool from the Bhalla and Bower (1993) model. The version of the the KCa channel used is KCa_cml_vdep (see Chapter 7).

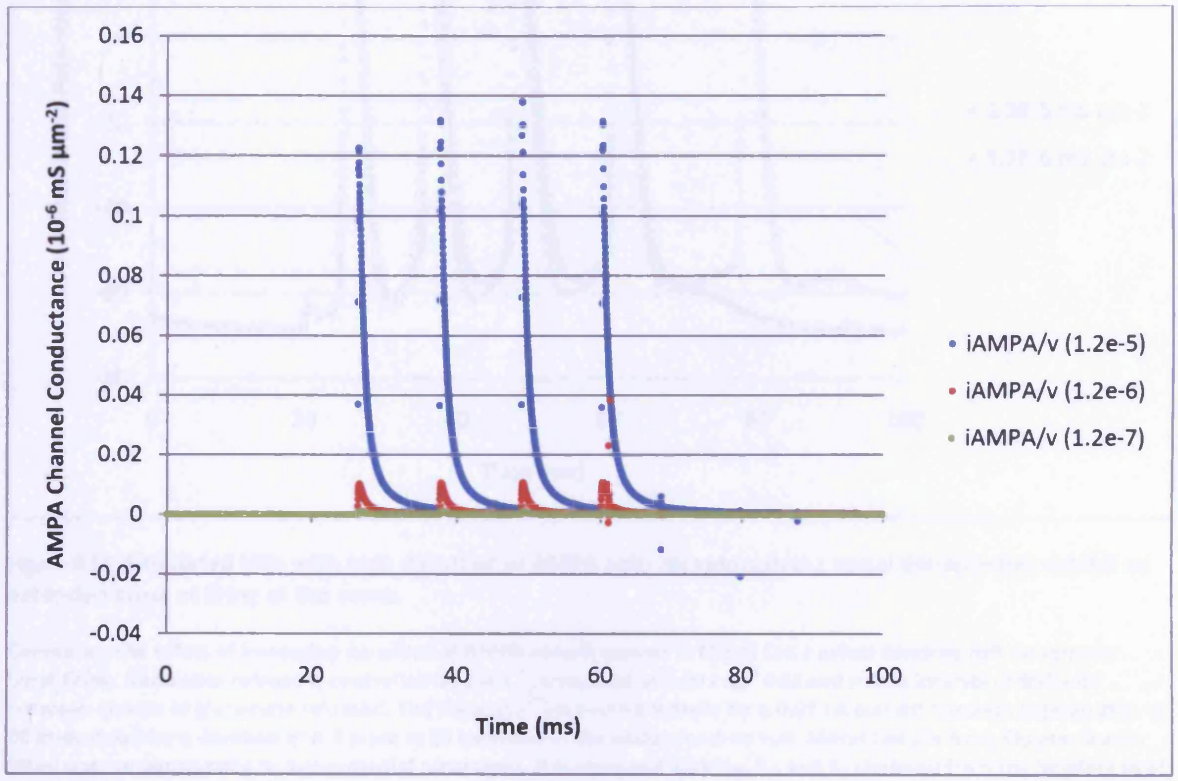

Figure 8.14: Dividing the AMPA current densities in Figure 8.12 by the Membrane Potential removes the decay from succive peak heights and demonstrates that the decay is afunction of the driving force (v-erev)

Dividing the current flow through the AMPA receptors (iAMPA) by the driving force (the potential difference: membrane potential – the AMPA receptor reversal potential that has been set at 0 produces a set of peaks that do not decay in magnitude. The iAMPA values are from Figure 8.13 and a noticeable decay in peak magnitude can be seen. The values in Figure 8.14 are the driving force as the reversal potential is 0.

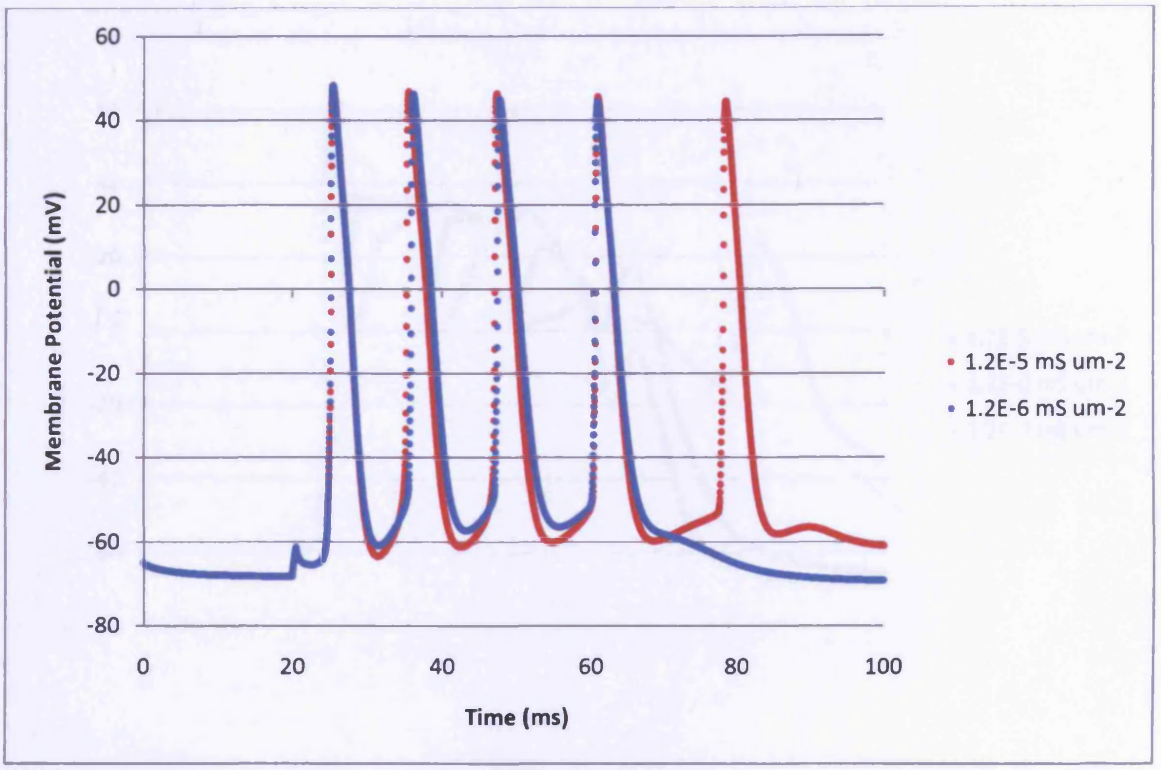

Figure 8.15: Simulated MCs with high densities of AMPA auto receptors in the apical dendrite tuft exhibit an extended burst of firing at the soma.

Comparing the effect of increasing densities of AMPA auto receptors in Mitral Cell 2 apical dendrite tuft on somatic burst firing. Glutamate release is controlled by a $[Ca^{2+}]$ threshold of 9.00×10^{-6} mM and a time interval of 900 x dt between quanta of glutamate released. The rising $[Ca^{2+}]$ is evoked initially by a 0.07 nA current injection is given after a 20 msec delay for a duration of 0.5 msec at 20 locations in the apical dendrite tuft. Mitral Cell 2 is from Chapter 4 with fitted passive parameters to experimental recordings. It is equipped with Na, K_{dr} and K_A channels from the Migliore et al. (2005) model and L-type calcium, KCa and calcium pool from the Bhalla and Bower (1993) model. The version of the the KCa channel used is KCa_cml_vdep (see Chapter 7).

Looking at synchronisation in apical dendrite tuft gap-junction connected networks of mitral cells, the membrane potential in the apical dendrite tuft must also be considered. Here the effects of the AMPA auto receptors become evident at lower densities (Figure 8.16). At an AMPA receptor density of 1.2×10^{-6} mS μm^{-2} there is clear segmentation of the apical dendrite tuft membrane potential fluctuations into responses for individual action potentials at the soma. Maybe this segmentation will aid synchronisation across a gap-junction network, so I will use this density as a starting point for use in my 6 mitral cell model simulations.

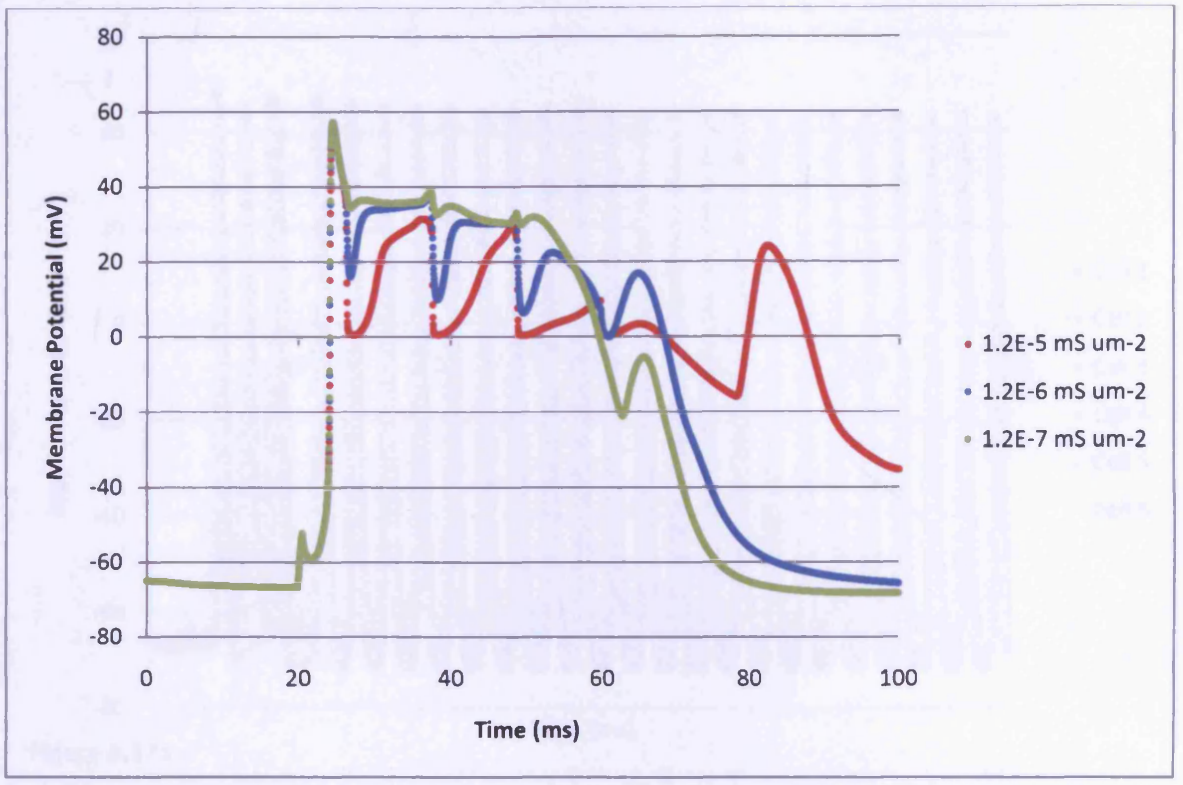

Figure 8.16: Increasing the density of AMPA auto receptors in the apical dendrite tuft of a simulated MC causes the tuft membrane potential to become more segmented before becoming erratic.

Comparing the effect of increasing densities of AMPA auto receptors in Mitral Cell 2 apical dendrite tuft on membrane potential in a compartment of the apical dendrite tuft. Glutamate release is controlled by a $[Ca^{2+}]$ threshold of 9.00×10^{-6} mM and a time interval of 900 x dt between quanta of glutamate released. The rising $[Ca^{2+}]$ is evoked initially by a 0.07 nA current injection is given after a 20 msec delay for a duration of 0.5 msec at 20 locations in the apical dendrite tuft. Mitral Cell 2 is from Chapter 4 with fitted passive parameters to experimental recordings. It is equipped with Na, K_{dr} and K_A channels from the Migliore et al. (2005) model and L-type calcium, KCa and calcium pool from the Bhalla and Bower (1993) model. The version of the the KCa channel used is KCa_cml_vdep (see Chapter 7).

Network Simulations

Auto exciting AMPA receptors were now incorporated in the apical tufts of the six MC gap-junction connected model. The mechanism was first set up as discussed in the first part of Chapter 7 with an AMPA receptor density of 1.2×10^{-6} mS μm^{-2}, the $[Ca^{2+}]$ threshold for glutamate release set to 0.9×10^{-5} mM and time interval between quanta of glutamate release set to 900 x dt. Short pulse current injections (0.5 nA, 0.5 ms after 10 ms delay cell in 2 and after 20 ms i n cell 3) produced loosely grouped firing for about the first 50 ms. This is followed by synchronised self propagating firing from all the cells (Figure 8.17). The mechanism for self propagating firing can be seen when the local $[Ca^{2+}]$ in the apical tuft is plotted (Figure 8.18). The AMPA receptors depolarise the cell sufficiently to produce a further influx of calcium ions through the L-type calcium channels. This lifts the $[Ca^{2+}]$ above the the glutamate release threshold producing a further round of AMPA receptor activation.

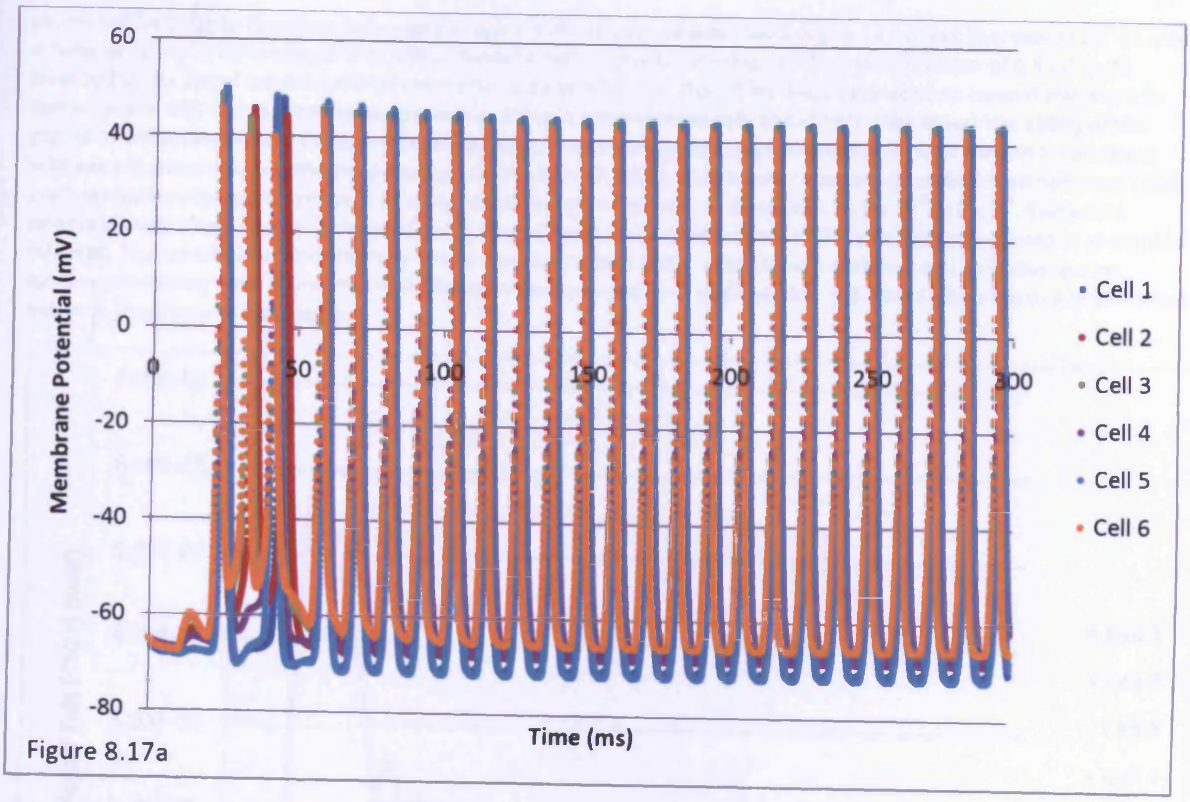

Figure 8.17a

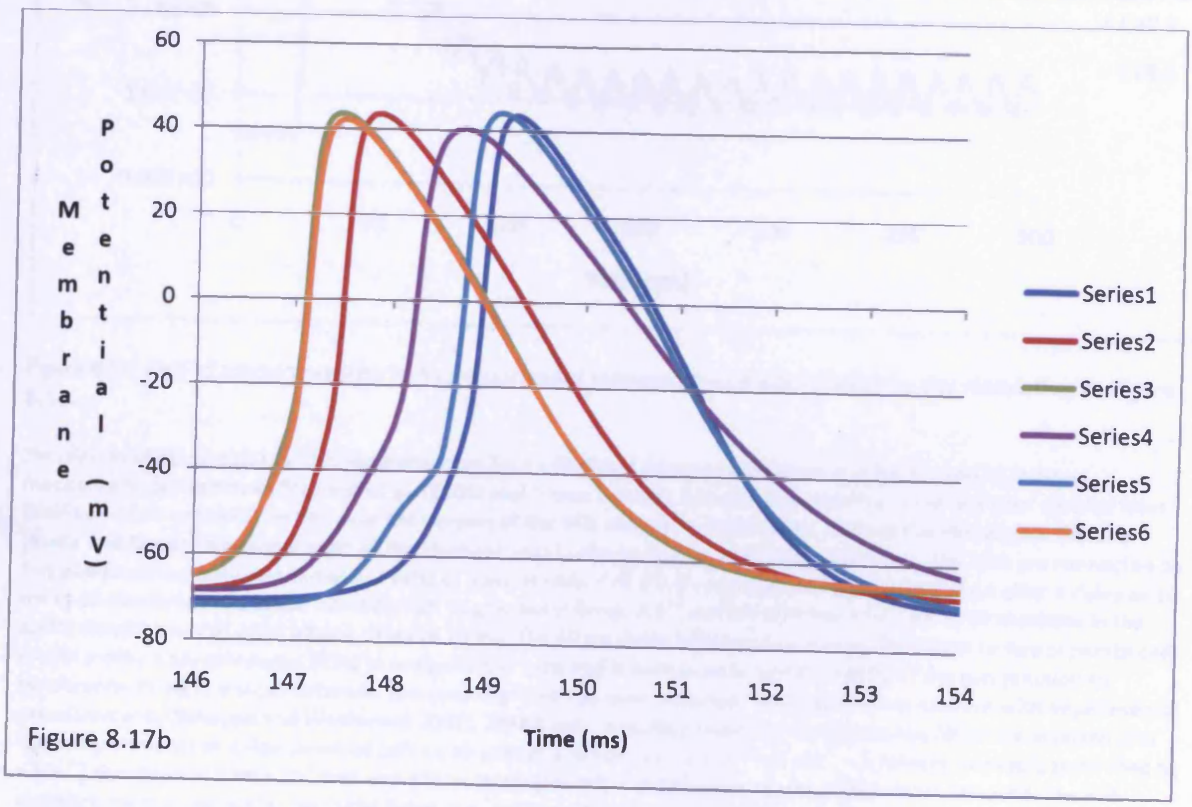

Figure 8.17b

Figure 8.17: Incorporating AMPA auto receptors into the apical dendrite tufts of simulated MCs in a gap junction connected network produces a period of burst firing followed by self propagating synchronised repetitive firing.

Simulation of somatic membrane potential in reconstructed MCs with fitted passive parameters and Na, K_{dr} and K_A channel mechanisms derived from Migliore et al. (2005) and L-type calcium, KCa and sub-membrane calcium pool derived from Bhalla and Bower (1993). In this case the version of the KCa channel is fitted to the response of the original Genesis Bhalla and Bower implementation of the channel, that I refer to as KCa_cml_Vdep in the text. The MCs are

connected by 100 gap-junctions between the apical tufts of pairs of cells. Cell 2 is given a current injection of 0.5 nA after a delay of 10 ms to 20 locations in its apical dendrite tuft to give burst firing. A 2nd current injection of 0.5 nA to 20 locations in the apical dendrite tuft of cell 3 after a delay of 20 ms. The 10 ms delay between two current injections to two separate cells would produce asynchronous firing in unconnected cells and is here used to test the ability of the gap-junction to synchronise firing in a small network. The coupling ratio has been adjusted ~0.025 which is consistent with experimental measurements (Schoppa and Westbrook 2002). AMPA auto receptors (modified from Saftenku 2005) are inserted into the compartments of apical dendrite tuft on all cells at a density of 1.2×10^{-6} mS μm^{-2}. Glutamate release is controlled by a $[Ca^{2+}]$ threshold of 0.90×10^{-5} mM and a time interval of 900 x dt between quanta of glutamate released. The current injections initially evoke loosely grouped firing, which then transforms into self propagating synchronised firing after 50 ms. Figure 8.16b shows an enlarged time scale version of 8.16a to allow the size of the offset between the traces to be viewed.

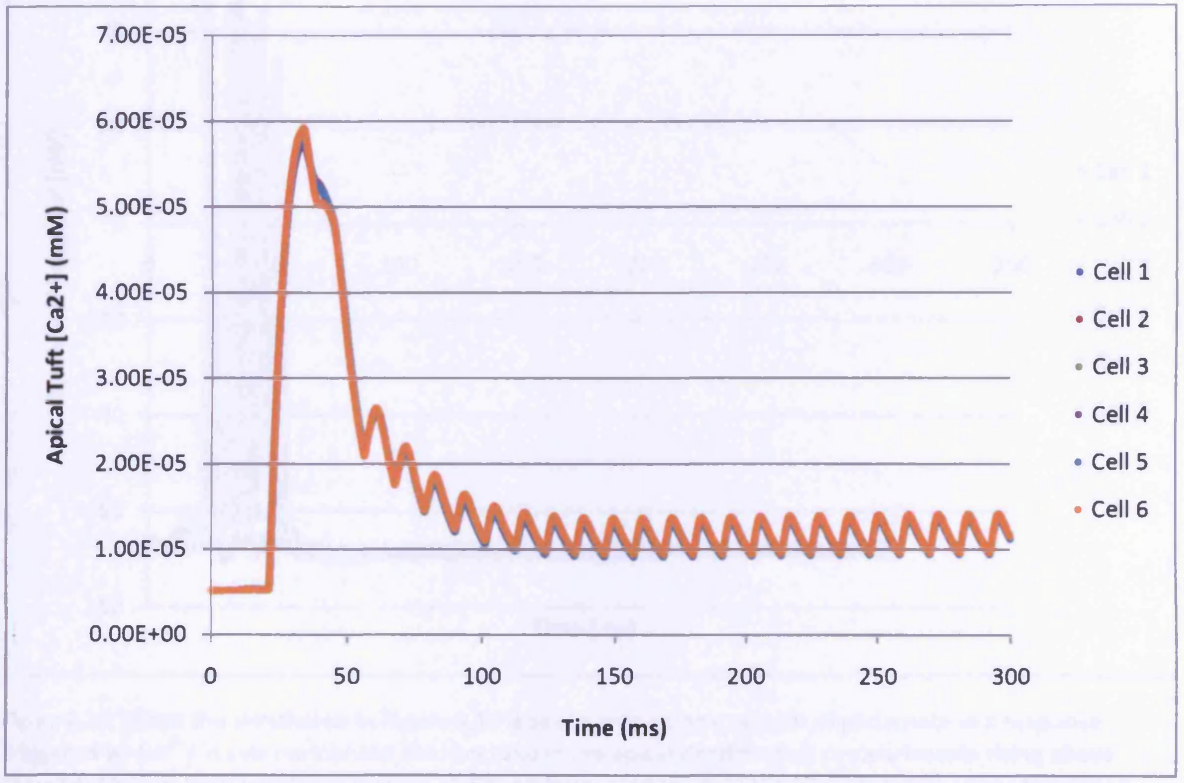

Figure 8.18: Plot of apical dendrite tuft compartment sub-membrane pool [Ca2+] for the simulation in Figure 8.16.

Simulation of apical tuft $[Ca^{2+}]$ in reconstructed MCs with fitted passive parameters and Na, K_{dr} and K_A channel mechanisms derived from Migliore et al. (2005) and L-type calcium, KCa and sub-membrane calcium pool derived from Bhalla and Bower (1993). In this case the version of the KCa channel is fitted to the response of the original Genesis Bhalla and Bower implementation of the channel, that I refer to as KCa_cml_Vdep in the text. The MCs are connected by 100 gap-junctions between the apical tufts of pairs of cells. Cell 2 is given a current injection of 0.5 nA after a delay of 10 ms to 20 locations in its apical dendrite tuft to give burst firing. A 2nd current injection of 0.5 nA to 20 locations in the apical dendrite tuft of cell 3 after a delay of 20 ms. The 10 ms delay between two current injections to two separate cells would produce asynchronous firing in unconnected cells and is here used to test the ability of the gap-junction to synchronise firing in a small network. The coupling ratio has been adjusted ~0.025 which is consistent with experimental measurements (Schoppa and Westbrook 2002). AMPA auto receptors (modified from Saftenku 2005) are inserted into the compartments of apical dendrite tuft on all cells at a density of 1.2×10^{-6} mS μm^{-2}. Glutamate release is controlled by a $[Ca^{2+}]$ threshold of 0.90×10^{-5} mM and a time interval of 900 x dt between quanta of glutamate released. The cell depolarisation produced by the initial firing seen in Figure 8.17 produces an influx of calcium ions through L-type calcium channels. This increase in $[Ca^{2+}]$ produces AMPA activation that produces further depolarisation that results in a self propagating sequence of $[Ca^{2+}]$ AMPA activation and action potentials.

If the mechanism that produces further quanta of glutamate every 900 x dt is removed the AMPA activation is only triggered by the $[Ca^{2+}]$ moving above threshold. As discussed earlier in this chapter, the local $[Ca^{2+}]$ in the apical tuft remains above threshold during burst

firing. Without a mechanism to reset the glutamate release in the programming a single release of glutamate is produced (Figures 8.19 and 8.20). This may seem like a somewhat artificial situation but for comparison purposes allows the effect of the repeated quanta of glutamate to be assessed. With a single quanta release of glutamate the MCs continue at resting potential after the initial current injection evoked burst of firing. Here there is no longer the self propagating sequence of activation depolarisation and calcium influx.

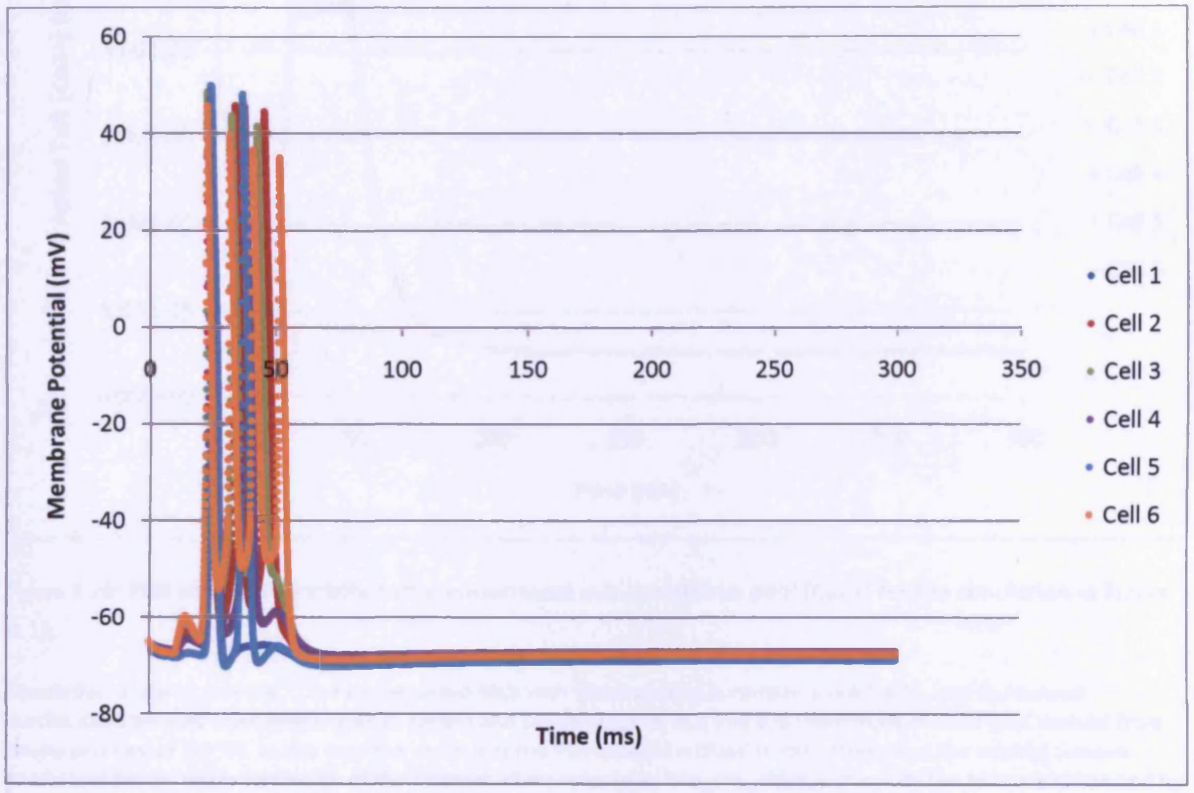

Figure 8.19: When the simulation in Figure 8.16 is set to give a single release of glutamate in a response triggered by [ca^{2+}] in sub-membrane calcium pool in the apical dendrite tuft compartments rising above threshold rather than repetitive release at a fixed time interval while the [Ca^{2+}] remains above threshold, the episode of burst firing is not followed by self propagating synchronised repetitive firing as in Figure 8.16.

Simulation of somatic membrane potential in reconstructed MCs with fitted passive parameters and Na, K_{dr} and K_A channel mechanisms derived from Migliore et al. (2005) and L-type calcium, KCa and sub-membrane calcium pool derived from Bhalla and Bower (1993). In this case the version of the KCa channel is fitted to the response of the original Genesis Bhalla and Bower implementation of the channel, that I refer to as KCa_cml_Vdep in the text. The MCs are connected by 100 gap-junctions between the apical tufts of pairs of cells. Cell 2 is given a current injection of 0.5 nA after a delay of 10 ms to 20 locations in its apical dendrite tuft to give burst firing. A 2nd current injection of 0.5 nA to 20 locations in the apical dendrite tuft of cell 3 after a delay of 20 ms. The 10 ms delay between two current injections to two separate cells would produce asynchronous firing in unconnected cells and is here used to test the ability of the gap-junction to synchronise firing in a small network. The coupling ratio has been adjusted ~0.025 which is consistent with experimental measurements (Schoppa and Westbrook 2002). AMPA auto receptors (modified from Saftenku 2005) are inserted into the compartments of apical dendrite tuft on all cells at a density of 1.2×10^{-6} mS μm^{-2}. Glutamate release is controlled by a [Ca^{2+}] threshold of 0.90×10^{-5} mM. Unlike Figure 8.17 here there is no mechanism to reset glutamate release when [Ca^{2+}] remains above threshold so a single quanta of glutamate is released when [Ca^{2+}] moves above threshold. In this case the simulation does not move into a self propagating sequence of activation to produce an extended series of synchronised action potentials. All the MCs settle at their resting potentials after their initial bursts of firing.

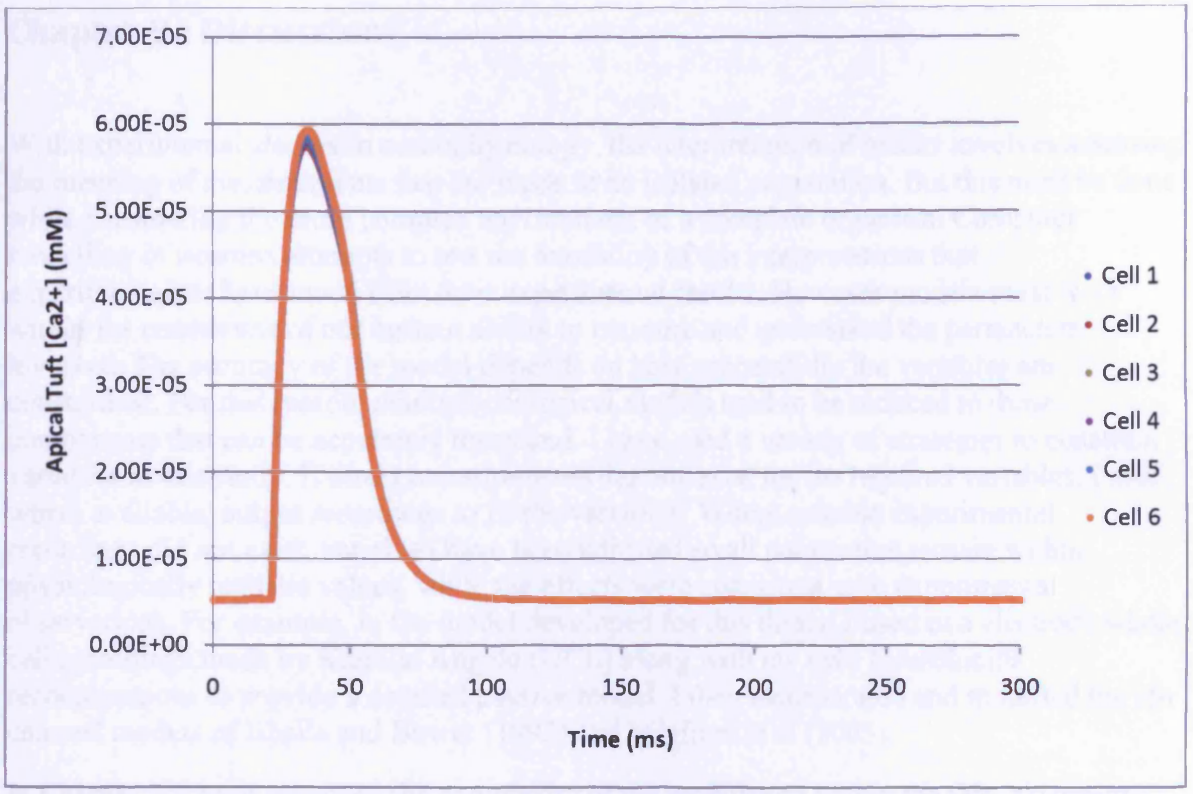

Figure 8.20: Plot of apical dendrite tuft compartment sub-membrane pool [Ca2+] for the simulation in Figure 8.18.

Simulation of apical tuft [Ca^{2+}] in reconstructed MCs with fitted passive parameters and Na, K_{dr} and K_A channel mechanisms derived from Migliore et al. (2005) and L-type calcium, KCa and sub-membrane calcium pool derived from Bhalla and Bower (1993). In this case the version of the KCa channel is fitted to the response of the original Genesis Bhalla and Bower implementation of the channel, that I refer to as KCa_cml_Vdep in the text. The MCs are connected by 100 gap-junctions between the apical tufts of pairs of cells. Cell 2 is given a current injection of 0.5 nA after a delay of 10 ms to 20 locations in its apical dendrite tuft to give burst firing. A 2nd current injection of 0.5 nA to 20 locations in the apical dendrite tuft of cell 3 after a delay of 20 ms. The 10 ms delay between two current injections to two separate cells would produce asynchronous firing in unconnected cells and is here used to test the ability of the gap-junction to synchronise firing in a small network. The coupling ratio has been adjusted ~0.025 which is consistent with experimental measurements (Schoppa and Westbrook 2002). AMPA auto receptors (modified from Saftenku 2005) are inserted into the compartments of apical dendrite tuft on all cells at a density of 1.2 x 10^{-6} mS μm^{-2}. Glutamate release is controlled by a [Ca^{2+}] threshold of 0.90 x 10^{-5} mM. Unlike Figure 8.18 here there is no mechanism to reset glutamate release when [Ca^{2+}] remains above threshold so a single quanta of glutamate is released when [Ca^{2+}] moves above threshold. In this case the simulation does not move into a self propagating sequence of activation to produce an extended series of [Ca^{2+}] fluctuations. All the MCs settle at their resting [Ca^{2+}] after the initial surge of calcium ion influx.

Chapter 9 : Discussion

With experimental studies in neurophysiology, the interpretation of results involves assessing the meaning of measurements that are made in an isolated preparation. But this must be done while considering the more complex environment of a complete organism. Computer modelling of neurons attempts to test the feasibility of the interpretations that experimentalists have made from their experimental results. However models must work within the constraints of our current ability to measure and understand the parameters involved. The accuracy of the model depends on how successfully the variables are constrained. For this reason, neurophysiological models tend to be reduced to those components that can be accurately measured. I have used a variety of strategies to constrain variables in this study. If direct measurements did not exist for the required variables, I used, where available, output recordings to fit the variables. Where suitable experimental recordings did not exist, variables have been adjusted so all parameters remain within physiologically realistic values, while the effects were consistent with experimental observations. For example, in the model developed for this thesis, I used two electrode whole cell recordings made by Kamilla Angelo (UCL) along with my own Neurolucida reconstructions to provide a detailed passive model. I then incorporated and modified the ion channel models of Bhalla and Bower (1993) and Migliore et al (2005).

In Chapter 2, I have reviewed the complexity of the modulation within the OB. No recent reviews had been published in this area, so a thorough review of the literature was needed. The review (Chapter 2) has subsequently been published as O'Connor and Jacob (2009). It was important to establish what had been achieved with existing models, the data that were available for constructing my model and what the focus should be for developing a new model. The review established that OB modulations were complex and multi layered, and it became clear that a model would only be feasible for a small subset of these interactions. It was tempting to go for a feature like lateral inhibition that would be an obvious component of signal processing. However such a subject requires a clear understanding of how the interacting subunits function. This was at least a level higher than was possible for a detailed biophysical approach, until the ground work of constructing the lower level models had been completed. Models at higher levels can and have been produced, but they rely on ignoring many of the parameters and estimates of how interactions might be weighted.

Instead I chose to develop a model that addressed a single glomerulus, representing a channel for a unique olfactory receptor protein. In mammals all olfactory receptor neurons express a single type of olfactory receptor protein and all olfactory neurons that express that particular olfactory receptor protein converge on a single glomerulus per side of the OB (see Chapter 2). There have been many experimental studies that focus on a single glomerulus but for my model I have mainly focused on Schoppa and Westbrook (2002). Migliore et al. (2005) made a simple model based on Schoppa and Westbrook (2002) and my model built on their starting point. There are many neurons that comprise a single glomerular sub unit, but as all the cells are there to affect the output of the MCs, the focus of my model was these MCs.

MC Model Construction Phase 1: The Passive Cell

Passive models include a combination of the cell morphology along with values for R_m, C_m and R_i. For many years this involved complex mathematical equations that were rendered more manageable by a series of simplifications. For example a branched structure was considered as an equivalent cylinder because it was too difficult to calculate the product of all

the branches. However with the advent of compartmental models in which the neuron was divided up into a large number of compartments, each was represented as a small circuit with its own R_m, C_m and with R_i joining each compartment with the next. This innovation along with the move to using simulator programs that contain the environment for building a neuron model has done a great deal to simplify the process so that more complex passive models can be tackled. In my model I was able to use two further innovations to take the passive model of a MC to a whole new level. These innovations were the use of a combination of software and interfaced microscope to produce an accurate 3D reconstruction of the cell morphology, together with dual patch clamp recordings from MCs in a slice preparation in which ion currents had been blocked to give fitting curves that described the passive parameters of the reconstructed cell.

In Chapter 4, I have described the process of reconstructing MC morphology from fixed slice preparations and fitting the passive parameters to dual electrode experimental recordings. This was the first phase in constructing my model, and the approach reflected my belief in the fundamental importance of morphology in determining neuron properties. The importance of morphology in other neurons has been well established in earlier studies (e.g. Vetter et al. 2000, Schaefer et al. 2003). With the development of reconstruction methods and simple methods of conversion to compartmental models, the time appeared opportune to investigate the part that MC morphology played in controlling how MCs interact as a population to integrate the input from the olfactory receptor neurons. My model used my 3D Neurolucida reconstructions of the MCs that were used to make the experimental recordings. These MCs were filled with biocytin as a final step before the pipettes were withdrawn and the slice preparation was fixed. These reconstructions represented the limit of the accuracy that it was possible to achieve with current methods. Bhalla and Bower (1993) did not have access to this method and so averaged published data for the dimensions of the soma, inter-branch segments diameter of branches of MCs from rabbit, rat and mouse morphology studies. Migliore et al. (2005) chose to model simple canonical features, the apical dendrite tuft was modelled as 20 unbranched cylinders. They were assuming that they had managed to extract all the features from the morphology that imposed a control on the MC interactions. By producing accurate reconstructions I chose not to assume that I could predict what features of MC morphology were important.

As I stated in the discussion for Chapter 4, morphology is meaningless without being linked with its associated passive parameters. For this reason the estimation of the passive parameters was carried out separately for each MC. Passive parameter fitting was carried out using experimental recordings and reconstructed morphology from the same MC. Both Bhalla and Bower (1993) and Migliore et al. (2005) used a general estimate of passive parameters from experiments carried out in turtles.

The experimental recordings were carried out by Kamilla Angelo in a lab at UCL that has specialised in carrying out dual pipette patch clamp recordings in MCs. The recordings had been made prior to my interest as part of a different line of research but fortunately were exactly what was needed to allow fitting of passive parameters. I also spent considerable effort in fine tuning the protocol for parameter fitting. At first I assumed that optimising the fit by avoiding the fitting algorithm getting stuck in local minima would be a significant problem. I therefore used a synthetic annealing algorithm that slowly reduced the ability of the fitting process to bounce out of minima. However this process took tens of thousands of iterations and produced less reliable values than the far simpler PRAXIS (principle axis see Chapter 4) algorithm that is built into Neuron. The PRAXIS algorithm produced robust parameter fits in around 150 iterations that did not change when a range of different starting

points were used. The main problem was that no estimate had been produced of shrinkage factors encountered during the fixing of the slice preparations. The contribution of other sources of error had been assessed in Chapter 4, such as soma surface area and pipette location. The largest effects were observed for shrinkage correction and pipette displacement on R_i error.

It is worth noting however that slice preparations would have ripped out the lateral dendrites that were out of plane to the slice and chopped off the sides of the apical tuft. Fixing the preparation caused shrinkage and distortion. Reconstruction also relied on an estimation of a cross sectional diameter. In practise this was a difficult procedure, especially with the soma and the larger fibres. With larger structures even with the use of a binocular microscope, depth of field made estimating a diameter in 3 dimensions difficult. It also assumed that the cross section was a perfect circle. The possible errors were numerous and assessment of their contribution was made and has been discussed in Chapter 4. However although the C_m was likely to have been over estimated, the model was internally consistent. The passive parameters have been fitted within the imperfect reconstructed morphology to experimentally recorded output, so the combination of passive parameters and morphology do reproduce electrotonic properties consistent with the experimental MCs. Also, the passive model was consistent with experimental measurements of a slice preparation. A slice preparation may not have given exactly the same results as *in vivo* recordings as the cells were damaged and connections were severed. But the model was based on and was consistent with a slice preparation.

Chapter 4 finished by considering the electrotonic shape of MCs when the reconstructed morphologies were combined with the passive parameters. The neuromorphic renderings of electrotonic transformations (see methods Chapter 4) show that the apical dendrite tufts were electrotonically elongated. This had the effect of reducing the impact of single inputs on the distant soma but lent itself to the local integration of the many inputs from the olfactory receptor neurons, interneurons and gap-junctions with other MCs. In contrast the apical dendrite trunk was seen to be electrotonically much shorter so the sum of the integration it received was transferred efficiently to the soma.

MC Model Construction Phase 2: Adding ion channels to enable action potentials

The modelling of ion channels is the oldest branch of neuronal modelling and dates back to the work of Hodgkin and Huxley (Hodgkin and Huxley 1952a,b,c,d, Hodgkin, Huxley and Katz 1952). They showed that action potentials could be explained by the actions of a sodium channel and a potassium channel along with a leak channel. They carried out their work in squid giant axons that have a relatively limited range of channels. Their work still forms the basis of the set of channels that are needed to produce an action potential, but often a third ion channel is added that increases the ability to recover after the sodium channel has depolarised the cell.

Once the passive model had been constructed, the second phase, in which active properties were added to the model, was begun. This had been complicated by the two labs that were working in this area using rival simulators (see Chapters 3, 5 and 7). As I wanted to be able to use components of both the Bhalla and Bower (1993) and Migliore et al. (2005) models I decided to use neuroConstruct and convert the Genesis and Neuron scripts to ChannelML. This conversion process has been covered in Chapter 5 for the Migliore et al (2005) Neuron files for sodium and potassium ion channels. The conversion of the Bhalla and Bower (1993) calcium ion channel and KCa channel has been covered in Chapter 7, but this belonged to a

later phase in construction of the model, when burst firing was tackled. These chapters also cover the adjustments that are made to the model to give action potentials or burst firing consistent with the published models. These adjustments were necessary because my model has different morphology and passive parameters.

It made sense to use the Migliore et al. (2005) sodium, and potassium ion channels, K_{dr} and K_A, needed for the generation of action potentials in response to input, as the K_{dr} and K_A channels were developed from experimental measurements in rat MCs (Wang et al. 1996) and the sodium channels were adjusted to work with them. However it must be noted that better experimental measurements of ion channels are needed to improve the MC model as experimental measurements of AP duration give a figure of 0.8-1.0 ms while the model generates APs with duration of ~3 ms (see Chapter 5). The time course of the sub-threshold depolarisation prior to an action potential from inputs delivered into the apical dendrite tuft was slightly slower in my model than the Migliore et al. (2005) model due to the increased distance between the apical dendrite tuft and the soma. However this difference in time course was not large enough to require any correction. The action potential threshold required the reversal potential of the leak current to be set within a range of -65 to -60 mV to avoid the MCs producing spontaneous firing. Increasing the shunt on the sodium channel by 6 mV (see Chapter 3) also raised the threshold of the action potentials above 50 mV and would be an alternative strategy for the prevention of spontaneous firing, if a higher leak reversal potential was desirable.

MC Model Construction Phase 3: Producing a gap-junction connected network of MCs

As discussed earlier in this chapter and in Chapters 1 and 2, MCs were divided into discrete populations whose apical dendrite tufts form part of a single glomerulus. As I have also said, this forms a discrete channel for the processing of the input from olfactory receptor neurons expressing a single olfactory receptor protein. In the glomerulus there are many types of interneuron that will modulate and shape the interaction between the MCs in this population. We were not at a stage where we could envisage modelling these kinds of interactions with interneurons, however the MCs were also directly connected to each other by gap-junctions (see Chapter 2). In this phase of the model construction 6 individual MCs were connected by apical dendrite gap-junctions using the Migliore et al. (2005) implementation of a gap-junction.

The Migliore et al (2005) model used two mitral cells connected by apical dendrite tuft gap-junctions. The conductance of the gap-junctions was adjusted to give a coupling ratio within the middle of 0.1-0.08 experimental measured range (Schoppa and Westbrook 2002). They found that the gap-junctions would rapidly synchronise asynchronous firing that was evoked in the two cells. I used their protocol to look at what would happen when 6 different mitral cells were connected by apical dendrite tuft gap-junctions. I did not have estimates of the number of gap-junctions so tried a series of levels including, 1, 10 and 100 randomly placed gap-junctions on the apical dendrite tuft of each MC. At each number of gap-junctions the conductance was adjusted so it came to around the mid range of cell coupling ratios. Synchronisation unsurprisingly was best when a large number of gap-junctions with a proportionally lower conductance linked the MCs. The model also performed better with 20 current injections at about 0.06 nA rather than a smaller number of larger current injections. Migliore et al. (2005) had already used 20 inputs at specific point along their 20 fibre apical dendrite tuft. Here I used a random scatter of inputs across the branching structure of the apical dendrite tuft. I therefore concluded that, synchronisation was aided by larger numbers

of smaller currents in the apical dendrite tuft both for input and gap-junctions. This conclusion reflected the purpose of the apical dendrite tuft for collecting the input from a very large number of olfactory receptor neurons and reinforced the view that morphology was an important consideration in the understanding of MC input integration and processing. This also agreed with my conclusions from the neuromorphic renderings of electrotonic transformations at the end of Chapter 4. The highly branched structure of the tuft was suited to integrating many small inputs/connections rather than a smaller number of larger inputs/connections. The axial resistance in these small fibres restricted current flow so larger input created large voltage gradients that are relatively slow to dissipate. Smaller inputs and lower conductance connections worked at a speed that was in tune with the carrying capacity of the small fibre diameters. As all the pairs of MCs were connected by 100, the resulting 1600 gap-junctions for a 6 MC network produced a very efficient synchronising mechanism. Despite all the cells having different passive parameters which produced different sub-threshold curves, the gap-junctions were able to synchronise the action potentials to tightly bunched groups.

MC Model Construction Phase 4: Adding calcium channels to produce burst firing in the MCs

The Migliore et al (2005) protocol used a continuous current injection that evoked repetitive firing at a frequency of ~50 Hz and thereby introduced an artificial source of periodicity into their MC model. However an interaction between a calcium channel and a KCa channel produced burst firing in real MCs. In Chapter 7, I inserted the required channels to produce burst firing into the model from the Bhalla and Bower (1993) model. This produced burst firing that was distinctive for each of the MCs in the model. This burst firing was generated in the soma/axon hillock and back propagated along the apical dendrite. The influence of the gap-junctions in the apical dendrite tuft was not sufficient to overcome the different driving forces in this burst firing, so no synchronisation was observed. However, if a continuous current injection was given the MCs commenced synchronous firing once the influence of the burst firing had ceased at about 120 ms. Investigation of the gating variables of the L-type calcium channels revealed that one of them has a very long time constant which prevents it from recovering to a fully open state after the initial period of burst firing. This is the reason for the absence of further episodes of burst firing after 120 ms and the observed synchronous repetitive firing is likely to be anomalous behaviour. But there is a need for experimental verification of the kinetics of this calcium channels. Comparisons with experimental recordings of MCs referred to in the introduction show that the extent of overshoot in the recovery phase of the APs is to a much lesser extent in the model. As mentioned while discussing AP duration further experimental measurements of MC ion channels kinetics and densities are needed to improve the ability of this model to give realistic firing patterns that fully reflect how the behaviour of real MCs.

Much of Chapter 7 was dedicated to the translation of the Bhalla and Bower (1993) from a Genesis script file to the ChannelML format that was used by neuroConstruct to generate Neuron mod[24] files that can be used with Migliore et al. (2005) channel mechanisms. Although this involved a lot of effort I considered the effort worth carrying out so that my model could be directly comparable with the previous models. The parameter space was also explored in an empirical fashion in order to discover how rigid the burst firing wave forms

[24] Neuron mod files are script files used by Neuron to define channel mechanisms and are written in a dedicated language called nmodl (detailed information is available on these script files on the Neuron website; this was accessed on 25/11/2010 at http://www.neuron.yale.edu/neuron/static/papers/nc2000/nmodl.htm).

were for individual MCs. I concluded from these soundings that tuning of the ion channel parameter space would not be able to influence the individual MCs burst firing wave form.

MC Model Construction Phase 5: Adding AMPA auto-excitation to the MCs

Schoppa and Westbrook (2002) suggested that AMPA auto- excitation in the apical dendrite tuft could drive correlated firing in MCs of the same glomerulus. If this were to provide a mechanism to synchronise burst firing MCs, there needed to be fine control of the glutamate release. The glutamate release was triggered by $[Ca^{2+}]$ and during burst firing the model $[Ca^{2+}]$ in a sub membrane calcium pool in the apical dendrite tuft compartments was elevated throughout the burst firing (Chapter 8). From Schoppa and Westbrook (2002) auto-excitation increased the sensitivity of the post gap-junction cell. However since the post gap-junction cell was also stimulated into burst firing the same problem of the wave form of the burst firing disrupting synchronisation would be encountered. Also, as the $[Ca^{2+}]$ remained elevated in the apical dendrite tuft throughout the burst firing there was no possibility of fine control of the timing of glutamate release from vesicles while the $[Ca^{2+}]$ remained above the release threshold. It is likely that glutamate release from MCs is not completely random as the production rate of vesicles is likely to be relatively constant at any given $[Ca^{2+}]$. I therefore chose to give the glutamate release approximately the same rate as the burst firing. But have noted in Chapter 8 that a more realistic approach to modelling glutamate release would base the release mechanism on experimental measurements of glutamate vesicle release probability over a range of $[Ca^{2+}]$.

When $[Ca^{2+}]$ threshold triggered glutamate release was incorporated into the 6 MC model another possible justification for AMPA auto-excitation was revealed. I compared a single release event with a regular release throughout the period of elevated $[Ca^{2+}]$. The regular release of glutamate produced self propagating synchronised firing in the population of mitral cells once the initial burst firing finished at about 50 ms. It was therefore possible that the burst firing was needed to produce a period of elevated $[Ca^{2+}]$ that was sufficient to push the glomerular population of MCs into self propagating AMPA auto-excitation driven synchronised firing. However there was a window of variable settings that produces this activity. Adjusting the $[Ca^{2+}]$ threshold for glutamate release affected whether the self propagating synchronised firing occurred. Altering other variables such as the rate of release events would most likely have an effect on the outcome. So we have always got to ask if the model was producing an effect that would happen in real neurons. I have not found evidence of repetitive firing in the literature for experimental MC recordings. Repetitive firing was also produced in Chapter 7 that overcomes the burst firing when a continuous current is injected in the apical dendrite tuft. However this repetitive firing was the result of the long time constant of one of the gating variables of the L-type calcium channel which is also present in the Chapter 8 models. But this self propagating synchronised firing was an interesting possibility. This possibility raises plenty more thoughts and questions:

- We know that the external tufted cells that also have dendrites in the glomerulus have a pace-making function. Perhaps this will somehow regulate the rate of glutamate release?

- An important internal source of modulation of MCs is the reciprocal synapse feedback inhibition that occurs between the MC lateral dendrites and granule cells (Chapter 2). Will this disrupt the self propagating synchronised firing or simply modify the rate?

- If the self propagating synchronised firing is a real phenomenon in MCs, what other control mechanism are needed to regulate it? Presumably there needs to be a mechanism to switch it off or does it just fade away as a result of the opposing feedback inhibition from the MCs lateral dendrites?

- Is neural plasticity and lateral inhibition involved in shaping this self propagating response?

There is plenty of scope for developing the model further to address these issues and others. However at the current state of development it is capable of informing the debate on how processes and mechanisms interact with each other. The importance of the balance between the distribution of small conductance connections in the apical dendrite tuft and other driving forces in the MCs is handled well by the model. The suggestion of Schoppa and Westbrook (2002) that AMPA auto-receptors drive correlated spiking in MCs appears plausible. But the model would suggest that at least more thought needs to be given to how such a mechanism might work. If it were a case of synchronising isolated events, the suggested auto-receptor mechanism should perform as suggested. But as burst firing produces an extended period of elevated $[Ca^{2+}]$, release of glutamate will occur at intervals over this extended period. Therefore, without a revision of the AMPA auto-receptor driven correlated spiking hypothesis, it cannot explain how the glutamate release timing would be achieved. It therefore suggests that the alternative purpose, highlighted by the model of self-propagating synchronised firing in the glomerular populations of mitral cells promoted by the auto-receptors, should be taken seriously. But effort should be made to establish the time constants for the calcium channel gating variables.

This MC network model is more powerful than those that have preceded it, which has allowed greater insight into the interactions within the network. However as experimental methods continue to improve it is important to work closely with experimentalists to produce models with better constrained variables. I have highlighted some questions that could easily be addressed by an extension of my MC network model. But equal effort should be expended into developing models that have improved constraint of variables, as and when improvements in experimental technique become available. This continuing effort to improve the models would be rewarded by increased confidence in the predictions that the models can give.

If I were given the opportunity to carry on this work with access to more experimental work, an extended series of passive MC models would produce the material for further assessment of the different kinds of MC interaction (both inter and intra glomerular). If a way could be found to identify particular glomeruli in the OB (this could be possible with accurate measurement of position and orientation of the slice of animals of the same age) and the MC models can be grouped as coming from those glomeruli, the glomerular subunits are going to be better constrained. The MCs used for the 6-MC network model in this study are obviously representative of many different glomeruli so there dimensions, orientations and passive parameters are not matched. Effort to produce a closely matched set of MCs should produce a model that is more representative of an individual glomerulus. Once more than one glomerulus has been modelled, investigation of inter-glomerular interactions such as lateral inhibition starts to become feasible.

At the same time it would increase the confidence in the results if efforts were made to control and reduce some of the sources of error. If MCs could be reconstructed from the slice preparation directly after the biocytin had been injected rather than fixing the preparation first

this would remove all the shrinkage and deformation that fixation produces. Also, methods need to be found to identify the exact location of the pipettes in the reconstruction. This, combined with collecting measurements of the pipette parameters so that they can be modelled, will reduce a second group of errors. A third group of errors that should be tackled are linked to 3D reconstruction of soma and fibre cross section. Hopefully the Neurolucida software could be developed to allow more sections of the soma to be recorded at different planes of focus thereby allowing better reconstruction of the cross sectional profile. This might also work for the trunk of the apical dendrite.

It would also be a distinct advantage if reconstructions could be produced from *in vivo* imaging, such as two photon imaging, to reconstruct the complete cell without missing lateral dendrites. But MCs are large with a lot of fine branching in the apical dendrite tuft. A combination of high resolution and deep penetration of the imaging is needed, which are beyond the scope of current methods in two photon imaging.

Experimental measurements of channel kinetics are needed for all the ion channels in MCs along with estimates of their densities in different locations. There is currently very little of this information available in the literature. The models become better able to make predictions the more data is available to constrain parameters.

Feedback inhibition from reciprocal synapses between the lateral dendrites of MCs and granule cells has not yet been attempted in my model. It would be relatively simple to construct a sequence of receptor activation that would mimic these reciprocal synapses as was done for AMPA auto-excitation in Chapter 8. This would probably be preferable to trying to reconstruct granule cells that are embedded in the tightly packed granule cell layer of the OB. Some constraining data does exist for this feedback inhibition but working with experimentalists to make extra measurements would enhance the value of this exercise. Within the mitral cell there are opposing forces one of which is this feedback inhibition. Finding out how this component interacts with the components from the apical dendrite tuft that have been modelled relies on the magnitude of these forces being correctly constrained. It would be easy to reach the wrong conclusion if something is missing from the constraint that causes an incorrect estimation of these magnitudes.

Another interaction that could be modelled and would add to the value of this model is the interaction with the pace-making external tufted cells. They are of a size and location that would respond well to reconstruction and modelling. But this would be at least as big an exercise as been carried out for this thesis to produce a reasonably constrained model.

In summary, the foundation has been laid for a single glomerulus model of the OB based on the interactions of the MCs. The model so far has suggested that the passive morphology of the apical dendrite tuft is well suited for integrating a large number of small inputs from the olfactory receptor neurones. This tuft morphology also facilitates the inter-communication of the population of MCs via gap-junctions. Burst firing is produced by influx of calcium through high threshold calcium channels that are activated by an action potential and terminated by the activation of KCa channels. This burst firing produces a sustained increase in $[Ca^{2+}]$ that provokes multiple release of glutamate from vesicles in the apical dendrite tuft. The glutamate stimulates AMPA auto-receptors which promotes self propagating synchronised firing in the glomerular MC population. The model has potential for much further development, in the first instance to verify the findings so far and then to give much greater insight into the many modulatory mechanisms that influence the behaviour of the channel subunit.

Appendix

```
//=========================================================
//original vdep version of Kca_mit_usb
//=========================================================


function make_%Name%
      float EK = -0.08
      float EREST_ACT = -0.065
      str chanpath
      chanpath = "/library/%Name%"

      if (!({exists {chanpath}}))
      create vdep_channel {chanpath}
            setfield {chanpath}    \
            Ek          {EK}  \                  //    V
            gbar        %Max Conductance Density% \  //    S
            Ik          0     \                  //    A
            Gk          0                        //    S

      create table {chanpath}/qv
      call {chanPath}/qv TABCREATE 100 -0.1 0.1
      end
            int i
            float x, dx, y
            x = -0.1
            dx = 0.2/100.0
            for (i = 0; i <= 100; i = i + 1)
                  y = {exp {(x - {EREST_ACT})/0.027}}
                  setfield {chanpath}/qv table->table[{i}] {y}
                  x = x + dx
      end

      create tabgate {chanpath}/qca

      setupgate {chanpath}/qca alpha  {5.0e5*0.015}  \
          -5.0e5 -1.0 -0.015.0 -0.0013 -size 1000 -range 0.0 0.01

      call {chanPath}/qca TABCREATE beta 1 -1 100
      setfield {chanpath}/qca beta->table[0] 50
      setfield {chanpath}/qca beta->table[1] 50

      addmsg {chanpath}/qv {chanpath}/qca PRD_ALPHA output
      addmsg {chanpath}/qca {chanpath} MULTGATE m 1
      addfield  {chanpath} addmsg1
      addfield  {chanpath} addmsg2
      setfield  {chanpath}  \
          addmsg1 "../Ca_mit_conc  qca   VOLTAGE          Ca" \
          addmsg2 "..              qv    INPUT      Vm"
end
```

```
//======================================================================
// ChannelML implementation of KCa_mit_usb
//======================================================================

<current_voltage_relation cond_law="ohmic" ion="k" default_gmax="3.6" default_erev="-80">
 <conc_dependence name="Calcium" ion="ca" charge="2" variable_name="ca_conc" min_conc="0"
max_conc="1e-7"/>
<gate name="m" instances="1">
        <closed_state id="m0"/>
        <open_state id="m" fraction="1"/>
        <transition name="alpha" from="m0" to="m" expr_form="generic" expr="( abs ( 0.015 -
(ca_conc*1e6) ) ) &lt; 1e-6 ? (exp ((v-65)/27)) * (0.65 - 250 * (0.015 - ca_conc*1e6))  : (exp ((v-
65)/27)) * (500.0*(0.015 - (ca_conc*1e6)))/( (exp ((0.015 - (ca_conc*1e6))/0.0013)) -1)" />
        <transition name="beta" from="m" to="m0" expr_form="generic" expr="0.05" />
 </gate>
</current_voltage_relation>
         <impl_prefs>
                  <table_settings max_v="50" min_v="-100" table_divisions="500"/> <!--Smaller table
settings as this is a 2D table-->
         </impl_prefs>
```

This generates the following Genesis Script in neuroConstruct:

```
function make_KCa_mit_ChannelML
    str chanpath = "/library/KCa_mit_ChannelML"
    if ({exists {chanpath}})
      return
    end
    create tab2Dchannel {chanpath}
    setfield {chanpath} \
      Ek          -0.08 \
      Ik          0 \
      Xpower      1
    setfield {chanpath} \
      Gbar 36 \
      Gk          0
    // No Q10 temperature adjustment found
    float temp_adj_m = 1
    float tab_divs = 500
    float v_min = -0.1
    float v_max = 0.05
    float v, dv, i
    // Creating table for gate m, using name X for it here
    float dv = ({v_max} - {v_min})/{tab_divs}
    // Channel is dependent on concentration of: Calcium, rate equations will involve variable:
ca_conc
    float c
```

```
    float conc_min = 0
    float conc_max = 0.09999999999999999
    float dc = ({conc_max} - {conc_min})/{tab_divs}
    float ca_conc = {conc_min}
    // Setting up the volt/conc dependent 2D table
    setfield {chanpath} Xindex {VOLT_C1_INDEX} // assumes all gates are volt/conc dep
    call {chanpath} TABCREATE X {tab_divs} {v_min} {v_max} {tab_divs} {conc_min} {conc_max}
    for (c = 0; c <= ({tab_divs}); c = c + 1)
    v = {v_min}
    for (i = 0; i <= ({tab_divs}); i = i + 1)
      // Looking at rate: alpha
      float alpha
      // Found a generic form of rate equation for alpha, using expression: ( abs ( 0.015 -
(ca_conc*1e6) ) ) < 1e-6 ? (exp ((v-65)/27)) * (0.65 - 250 * (0.015 - ca_conc*1e6))  : (exp ((v-65)/27))
* (500.0*(0.015 - (ca_conc*1e6)))/( (exp ((0.015 - (ca_conc*1e6))/0.0013)) -1)
      // Will translate this for GENESIS compatibility...
      // Equation (and all ChannelML file values) in Physiological Units but this script in SI Units
      v = v * 1000 // temporarily set v to units of equation...
      // Equation depends on concentration, so converting that too...
      ca_conc = ca_conc * 0.000001
      if ({ abs { 0.015 - {ca_conc*1e6} } } < 1e-6 )
        alpha =  {exp {{v-65}/27}} * {0.65 - 250 * {0.015 - ca_conc*1e6}}
      else
        alpha =  {exp {{v-65}/27}} * {500.0*{0.015 - {ca_conc*1e6}}}/{ {exp {{0.015 -
{ca_conc*1e6}}/0.0013}} -1}
      end
      v = v * 0.0010 // reset v
      ca_conc = ca_conc * 1000000 // resetting ca_conc
      // Set correct units of alpha
      alpha = alpha * 1000
      // Looking at rate: beta
      float beta
      // Found a generic form of rate equation for beta, using expression: 0.05
      // Will translate this for GENESIS compatibility...
      // Equation (and all ChannelML file values) in Physiological Units but this script in SI Units
      v = v * 1000 // temporarily set v to units of equation...
      // Equation depends on concentration, so converting that too...
      ca_conc = ca_conc * 0.000001
      beta = 0.05
      v = v * 0.0010 // reset v
      ca_conc = ca_conc * 1000000 // resetting ca_conc
      // Set correct units of beta
      beta = beta * 1000
      // Using the alpha and beta expressions to populate the tables
      float tau = 1/(temp_adj_m * (alpha + beta))
```

```
        setfield {chanpath} X_A->table[{i}][{c}] {temp_adj_m * alpha}
        setfield {chanpath} X_B->table[{i}][{c}] {temp_adj_m * (alpha + beta)}
        v = v + dv
    end // end of for (i = 0; i <= ({tab_divs}); i = i + 1)
        ca_conc = ca_conc + dc
    end // end of for (c = 0; c <= ({tab_divs}); c = c + 1)
    setfield {chanpath} X_A->calc_mode 1 X_B->calc_mode 1
end
```

References

Adams, D.J.; Smith, S.J.; Thompson, S.H. Ionic currents in moluscan soma. *Annu. Rev. Neurosci.* **1980**, 3, 141-167.

Adrian, E.D. Olfactory reactions in the brain of the hedgehog. *J. Physiol. (Lond.)* **1942**, 100, 459-473.

Adrian, E.D. The electrical activity of the mammalian olfactory bulb. *Electroencephalog. Clin. Neurophysiol.* **1950**, 2, 377.

Aldrich, R.W. Jr.; Getting, P.A.; Thompson, S.H. Inactivation of delayed outward current in molluscan neurone somata. *J. Physiol. (Lond.)* **1979**, 291, 507-530.

Alison, A.C.; Warwick, R.T.T. Quantitative observations on the olfactory system of the Rabbit, *Brain* **1949**, 72, 186.

Amir, S.; Caim, S.; Sullivan, J.; Robinson, B.; Stewart, J. In rats, odor-induced Fos in the olfactory pathways depends on the phase of the circadian clock. *Neuroscience Letters* **1999**, 272, 175-178.

Apelbaum, A.F.; Perrut, A.; Chaput, M. Orexin A effects on the olfactory bulb spontaneous activity and odor responsiveness in freely breathing rats. *Regulatory Peptides* **2005**, 129, 49-61.

Aroniadou-Anderjaska, V.; Ennis, M.; Shipley, M.T. Glomerular synaptic responses to olfactory nerve input in rat olfactory bulb slices. *Neuroscience* **1997**, 79, 425-434.

Aroniadou-Anderjaska, V.; Ennis, M.; Shipley, M.T. Current-source density analysis in the rat olfactory bulb. Laminar distribution of kainate/AMPA and NMDA receptor mediated currents. *Journal of Neurophysiology* **1999**, 81, 15-28.

Aroniadou-Anderjaska, V.; Zhou, F.M.; Priest, C.A.; Ennis, M.; Shipley, M.T. Tonic and synaptically evoked presynaptic inhibition of sensory input to the rat olfactory bulb via GABA(B) heteroreceptors. *Journal of Neurophysiology* **2000**, 84, 1194-203.

Aungst, J.L.; Heyward, P.M.; Puche, A.C.; Karnup, S.V.; Hayar, A.; Szabo, G.; Shipley, M.T. Centre-surround inhibition among olfactory bulb glomeruli. *Nature* **2003**, 426, 623-9.

Baker, H.; Kawano, T.; Albert, V.; Joh, T.H.; Reis, D.J.; Margolis, F.L. Olfactory bulb dopamine neurons survive deafferentation-induced loss of tyrosine hydroxylase. *Neuroscience* **1984**, 11, 605-615.

Balu, R.; Larimer, P.; Strowbridge, B.W. Phasic stimuli evoke precisely timed spikes in intermittently discharging mitral cells. *Journal of Neurophysiology* **2004**, *92*, 743-53.

Balu, R.; Pressler, R.T.; Strowbridge, B.W. Multiple modes of synaptic excitation of the olfactory bulb granule cells. *Journal of Neuroscience* **2007**, 27, 5621-5632.

Barrett, J.N.; Crill, W.E. Specific membrane properties of cat Motoneurones. *J. Physiol. (Lond.)* **1974**, 239, 301-324.

Belluzzi, O.; Puopolo, M.; Benedusi, M.; Kratskin, I. Selective neuroinhibitory effects of taurine in slices of rat main olfactory bulb. *Neuroscience* **2004**, 124, 929-944.

Bennett, M.V.; Zukin, R.S. Electrical coupling and neuronal synchronization in the mammalian brain. *Neuron* **2004**, 495-511.

Berkowicz, D.A.; Trombley, P.Q. Dopaminergic modulation at the olfactory nerve synapse. *Brain Research* **2000**, 855, 90-99.

Beshel, J.; Kopell, N.; Kay, L.M. Olfactory bulb gamma oscillations are enhanced with task demands. *Journal of Neuroscience* **2007**, 27, 8358-8365.

Bhalla U.S.; Bower J.M. Exploring parameter space in detailed single neuron models: Simulations of the mitral and granule cells of the olfactory bulb. *J. Neurophysiol.* **1993**, **69,** 1948-1465.

Bischofberger, J., and Jonas, P. Action potential propagation into the presynaptic dendites of rat mitral cells. *Journal of Physiology (Lond.)* **1997**, 504, 359-365.

Bower J.M.; Beeman D. *The Book of Genesis: Exploring Realistic Neural Models with the GEnerral Neural Simulation System.* **1998**, 2nd Edition Springer-Verlag New York, USA.

Bozza, T.C.; Mombaerts, P. Olfactory coding: revealing intrinsic representations of odors. *Curr. Biol.* **2001**, 11, 687-690.

Brashear, H.R.; Zaborszky, L.; Heimer, L. Distribution of GABAergic and cholinergic neurons in the rat diagonal band. *Neuroscience* **1986**, 17, 439-451.

Breer, H.; Shepherd, G.M. Implications of the NO/cGMP system for olfaction. *Trends in Neuroscience* 1993, 16, 5-9.

Brent, R.P. *Algorithms for minimization without derivatives.* Prentice-Hall, Englewood Cliffs, NJ, USA, **1973.**

Brennan, P.; Kaba, H.; Keverne, E.B. Olfactory recognition; a simple memory system. *Science* **1990**, 250 (4985), 1223-6.

Bressler, S.S.; Freeman, W.J. Frequency analysis of olfactory system EEG in cat, rabbit and rat. *Electroencephalogr. Clin. Neurophysiol.* **1980**, 19-24.

Brunjes, P.C.; Smith-Crafts, L.K.; McCarty, R. Unilateral odour deprivation: effects on the development of olfactory bulb catecholamines and behaviour. *Developmental Brain Research* **1985**, 22, 1-6.

Bukauskas, F.F.; Verselis, V.K. Gap junction channel gating. *Biochim. Biophys. Acta* **2004**, 1662, 42-60.

Caitlin Smith, T.; Jahr, C.E. Self-inhibition of olfactory neurons. *Nature Neuroscience* 2002, 5, 760- 766.

Cajal, R. Y. *Histologie du système nerveux de l'homme et des vertébrés*, **1911.**
Carlson, G.C.; Shipley, M.T.; Keller, A. Long-lasting depolarizations in mitral cells of the rat olfactory bulb. *Journal of Neuroscience* **2000**, 20, 2011-21.

Carnevale, N.T.; Tsai, K.Y.; Claiborne, B.J.; Brown, T.H. The electrotonic transformation: a tool for relating neuronal form to function. In: *Advances in neural information processing systems. Vol. 7*, eds Tesauro G, Touretzky DS, Leen TK MIT Press, Cambridge, MA pp. 69-76, **1995**.

Carnevale, N.T.; Tsai, K.Y.; Claiborne, B.J.; Brown, T.H. Comparative electrotonic analysis of three classes of rat hippocampal neurons. *J. Neurophysiol.* **1997**, 78, 703-720.
Castillo, P.E.; Carleton, A.; Vincent, J.D.; Lledo, P.M. Multiple and opposing roles of cholinergic transmission in the main olfactory bulb. *Journal of Neuroscience* **1999**, 19, 9180-9191.

Chabaud, P.; Ravel, N.; Wilson, D.A.; Mouly, A.M.; Vigouroux, M.; Farget, V.; Gervais, R. Exposure to behaviourally relevant odour reveals differential characteristics in rat central olfactory pathways as studied through oscillatory activities. *Chemical Senses* **2000**, 25, 561-573.

Chaput, M.A.; Holley, A. Single unit responses of olfactory bulb neurons to odour presentations in awake rabbits. *Journal of Physiology (Paris)* **1980**, 76, 551-558.

Chaput, M.A.; Holley, A. Responses of olfactory bulb neurons to repeated odor stimulations in awake freely-breathing rabbits. *Physiology and Behavior* **1985**, 34, 249-258.

Charpak, S.; Mertz, J.; Beaurepaire, E.; Moreaux, L.; Delaney, K. Odor-evoked calcium signals in dendrites of rat mitral cells. *PNAS* **2001**, 98, 1230-1234.

Chen, W.R.; Mitgaard, J.; Shepherd, G.M. Forward and backward propagation of dendritic impulses and their synaptic control in mitral cells. *Science* **1997**, **278,** 463-7.

Chen, W.R.; Shen, G.Y.; Shepherd, G.M.; Hines, M.L.; Mitgaard, J. Multiple modes of action potential initiation and propagation in mitral cell primary dendrite. *Journal of Neurophysiology* **2002**, 88, 2755-64.

Chen, Y.; Zhou, D.; Zhou, K.; Ren, Y.' Dai, W.; Xu, M.; Lu, L.; Lu, Z. Study on olfactory function in GABAC receptor/channel rho 1 subunit knockout mice. *Neuroscience Letters* **2007**, 427, 10-15.

Chen, W.R.; Shepherd, G.M. Membrane and synaptic properties of mitral cells in slices of rat olfactory bulb. *Brain Research* **1997**, 745, 189-196.

Chen, W.R.; Shepherd, G.M. The olfactory glomerulus: a cortical module with specific functions. *Journal of Neurocytology* **2005**, 34, 353-360.

Christie, J.M.; Bark, C.; Hormuzdi, S.G.; Helbig, I.; Monyer, H.; Westbrook, G.L. Connexin 36 mediates spike synchrony in olfactory bulb glomeruli. *Neuron* **2005**, *46*, 761-772.

Christie, J.M.; Westbrook, G.L. Regulation of backpropagating action potentials in mitral cell lateral dendrites by A-type potassium currents. *Journal of Neurophysiology* **2003**, 89, 2466-2472.

Christie, J.M.; Westbrook, G.L. Lateral excitation within the olfactory bulb. *J. Neurosci.* **2006**, 26(8), 2269-77.

Cleland, T.A.; Linster, C. Computation in the olfactory system. *Chemical Senses* **2005**, 30, 801-813.

Clements, J.D.; Redman, S.J. Cable properties of cat spinal motoneurones measured by combining voltage clamp, current clamp and intracellular staining. *J. Physiol. (Lond.)* **1989, 409**, 63-87.

Connors, B.W.; Long, M.A. Electrical synapses in the mammalian brain. *Annu. Rev. Neurosci.* **2004**, 27, 393-418.

Coopersmith, R.; Leon, M. Enhanced neural response to familiar olfactory cues. *Science* **1984**, 225, 849-51.

Coopersmith, R.; Lee, S.; Leon, M. Olfactory bulb responses after odor aversion learning by young rats. *Brain Res.* **1986**, 389, 271-7.

Crespo, C.; Gracia-Llanes, F.J.; Blasco-Ibanez, J.M.; Gutierrez-Mecinas, M.; Marques-Mari, A.I.; Martinez-Guijarro, F.J. Nitric oxide synthase containing periglomerular cells are GABAergic in the rat olfactory bulb. *Neuroscience Letters* **2003**, 349, 151-154.

Dahlström, A.; Fuxe, K.; Olson, L.; Ungerstedt, U. On the distribution and possible function of monoamine nerve terminals in the olfactory bulb of the rabbit. *Life Science* **1965**, 4, 2071-2074.

Das, P.; Parsons, A.D.; Scarborough, J.; Hoffman, J.; Wilson, J.; Thompson, R.N.; Overton, J.M.; Fadool, D.A. Electrophysiological and behavioural phenotype of insulin receptor defective mice. *Physiology and Behavior* **2005**, 86, 287-296.

Davila, N.G.; Houpt, T.A.; Trombley, P.Q. Expression and function of kainate receptors in the rat olfactory bulb. *Synapse* **2007**, 61, 320-334.

De Schutter, E.; Bower, J.M. A computer simulation of plateau potentials and synaptic interactions in Purkinje cell spiny dendrites. *Soc. Neurosci. Abstr.* **1991**, 21, 1383.

Desmaisons, D.; Vincent, J.D.; Lledo, P.M. Control of action potential timing by intrinsic sub-threshold oscillations in olfactory bulb output neurons. *Journal of Neuroscience* **1999**, 19, 10727-10737.

Djurisic, M.; Antic, S.; Chen, W.R.; Zecevic, D. Voltage imaging from dendrites of mitral cells: EPSP attenuation and spike trigger zones. *J. Neurosci.* **2004**, 24, 6703-6714.

Dluzen, D.E.; Muraoka, S.; Engelmann, M.; Ebner, K.; Landgraf, R. Oxytocin induces preservation of social recognition in male rats by activating alpha-adrenoceptors of the olfactory bulb. *Eur. J. Neurosci.* **2000**, 12, 760-6.

Dong, H.W.; Hayar, A.; Ennis, M. Activation of group I metabotropic glutamate receptors on main olfactory bulb granule cells and periglomerular cells enhances synaptic inhibition of mitral cells. *J. Neurosci.* **2007**, 27, 5654-63.

Egger, V. Synaptic sodium spikes trigger long-lasting depolarizations and slow calcium entry in rat olfactory bulb granule cells. *Eur. J. Neurosci.* **2008**, 27, 2066-2075.

El-Etri, M.M.; Ennis, M.; Griff, E.R.; Shipley, M.T. Evidence for cholinergic regulation of basal norepinephrine release in the rat olfactory bulb. *Neuroscience* **1999**, 93, 611-617.

Ennis, M.; Zhou, F.M.; Ciombor, K.J.; Aroniadou-Anderiaska, V.; Hayar, A.; Borrelli, E.; Zimmer, L.A.; Margolis, F.; Shipley, M.T. Dopamine D2 receptor-mediated presynaptic inhibition of olfactory nerve terminals. *Journal of Neurophysiology* **2001**, 86, 2986-97.

Ennis, M.; Zimmer, L.A.; Shipley, M.T. Olfactory nerve stimulation activates rat mitral cells via NMDA and non-NMDA receptors in vitro. *Neuroreport* **1996**, 7, 989-92.

Fadool, D.A.; Tucker, K.; Phillips, J.J.; Simmen, J.A. Brain insulin receptor causes activity-dependent current suppression in the olfactory bulb through multiple phosphorylation of Kv1.3. *Journal of Neurophysiology* **2000**, 83, 2332-2348.

Fadool, D.A.; Tucker, K.; Perkins, R.; Fasciani, G.; Thompson, R.N.; Parsons, A.D.; Overton, J.M.; Koni, P.A.; Flavell, R.A.; Kaczmarek, L.K. Kv1.3 channel gene-targeted deletion produces "Super-Smeller Mice" with altered glomeruli, interacting scaffolding proteins, and biophysics. *Neuron* **2004**, 41, 389-404.

Fadool, D.A.; Levitan, I.B. Modulation of olfactory bulb neuron potassium current by tyrosine phosphorylation. *Journal of Neuroscience* **1998**, 18, 6126-6137.

Freeman, W.J.; Skarda C.A. Spatial EEG patterns, non-linear dynamics and perception: the Neo-Sherringtonian view. *Brain Research Reviews* **1985**, 10, 147-175.

Friedman, D.; Strowbridge, B.W. Both electrical and chemical synapses mediate fast network oscillations in the olfactory bulb. *J. Neurophysiol.* **2003**, 89(5), 2601-10.

Gehlert, D.R.; Gackenheimer, S.L.; Wong, D.T.; Robertson, D.W. Localization of 5-HT3 receptors in the rat brain using [3H]LY278584. *Brain Research* **1991**, 553, 149-154.

Gerstner, W.; Naud, R. How good are neuron models? Science **2009**, 326, 379-380, 16 October 2009.

Gheusi, G.; Cremer, H.; McLean, H.; Chazal, G.; Vincent, J-D.; Lledo, P-M. Importance of newly generated neurones in the adult olfactory bulb for odor discrimination. *Proceedings of the National Academy of Sciences (USA)* **2000**, 97, 1823-1828.

Gleeson P.; Steuber V.; Silver R.A. neuroConstruct: a tool for modelling networks of neurons in 3D space. *Neuron* **2007**, 54, 219-235.

Golding, N.L.; Mickus, T.J.; Katz, Y.; Kath, W.L.; Spruston, N. Factors mediating powerful voltage attenuation along CA1 pyramidal neuron dendrites. *J. Physiol. (Lond.)* **2005**, 568, 69-82.

Golgi, C. Sulla fina struttura dei bulb olfatori, *Riv. Sper. Freniat.* **1875**, 1, 405-425.

Gonzalez, D.; Gomez-Hernandez, J.M.; Barrio, L.C. Molecular basis of voltage dependence of connexin channels: an integrative appraisal. *Prog. Biophys.Mol. Biol.* **2007**, 94, 66-106.

Granados-Fuentes, D.; Tseng, A.; Herzog, E.D. A circadian clock in the olfactory bulb controls olfactory responsivity. *Journal of Neuroscience* **2006**, 26, 12219-12225.

Griff, E.R.; Mafhouz, M.; Perrut, A.; Chaput, M.A. Comparison of identified mitral and tufted cells in freely breathing rats: I. Conduction velocity and spontaneous activity. *Chem. Senses* **2008a**, 33, 779-792.

Griff, E.R.; Mafhouz, M.; Chaput, M.A. Comparison of identified mitral and tufted cells in freely breathing rats: II. Odor-evoked responses. *Chem. Senses* **2008b**, 33, 793-802.

Gutierrez-Mecinas, M.; Crespo, C.; Blasco-Ibanez, J.M,; Gracia-Llanes, F.J.; Marques-Mari, A.I.; Nacher, J.; Varea, E.; Martinez-Guijarro, F.J. Distribution of D2 dopamine receptor in the olfactory glomeruli of the rat olfactory bulb. *European Journal of Neuroscience* **2005a**, 22, 1357-1367.

Gutierrez-Mecinas, M.; Crespo, C.; Blasco-Ibanez, J.M.; Gracia-Llanes, F.J.; Marquez-Mari, A.I; Martinez-Guijarro, F.J. Soluble guanylyl cyclase appears in a specific subset of periglomerular cells in the olfactory bulb. *European Journal of Neuroscience* **2005b**, 21, 1443-1448.

Halasz, N.; Ljungdahl, A.; Hokfelt, T. Transmitter histochemistry of the rat olfactory bulb- II. Fluorescence histochemical, autoradiographic and electron microscopic localisation of monoamines. *Brain Research* **1978**, 154, 253-271.

Hardy, A.B.; Aioun, J.; Baly, C.; Julliard, K.A.; Caillol, M.; Salesse, R.; Duchamp-Viret, P. Orexin A modulates mitral cell activity in the rat olfactory bulb: Patch-clamp study on slices, immunocytochemical localization of orexin receptors. *Endocrinology* **2005**, 146, 4042-53.

Hayar, A.; Ennis, M. Endogenous GABA and glutamate finely tune the bursting of olfactory bulb external tufted cells. *Journal of Neurophysiology* **2007**, 98, 1052-1056.

Hayar, A.; Heyward, P.M.; Heinbokel, T.; Shipley, M.T.; Ennis, M. Direct excitation of mitral cells via activation of α1-Noradrenergic receptors in rat olfactory bulb slices. *Journal of Neurophysiology* **2001**, 86, 2173-2182.

Hayar, A.; Karnup, S.; Shipley, M.T.; Ennis, M. Olfactory bulb glomeruli: external tufted cells intrinsically burst at theta frequency and are entrained by patterned olfactory input. *Journal of Neuroscience* **2004a**, 24, 1190-1199.

Hayar, A.; Karnup, S.; Ennis, M; Shipley, M.T. External tufted cells: a major excitatory element that coordinates glomerular activity. *Journal of Neuroscience* **2004b**, 24, 6676-85.

Heinbockel, T.; Laaris, N.; Ennis, M. Metabotropic glutamate receptors in the main olfactory bulb drive granule cell-mediated inhibition. *Journal of Neurophysiology* **2007a**, 97, 858-870.

Heinbockel, T.; Hamilton, K.A.; Ennis, M. Group 1 metabotropic glutamate receptors are differentially expressed by two populations of olfactory bulb granule cells. *Journal of Neurophysiology* **2007b**, 97, 3136-3141.

Heyward P.; Ennis M.; Keller A.; Shipley M.T. Membrane bistability in olfactory bulb mitral cells. *J. Neurosci.* **2001**, 21, 5311-5320.
Hines M.L.; Carnevale N.T. The Neuron simulation environment. *Neural Comput.* **1997**, 9, 1179-1209.

Hines M.L.; Carnevale N.T. Expanding Neuron's repertoire of mechanisms with NMODL. Neural Comput. **2000**, 12, 839-851.

Hines M.L.; Carnevale N.T. Neuron: a tool for neuroscientists. The Neuroscientist **2001**, 7, 123-135.

Hirano, T.; Hagiwara, S. Kinetics and distribution of voltage-gated Ca, Na, and K channels on the somata of rat cerebellar Purkinje cells. *Pfluegers Arch.* **1989**, 413, 463-469.

Hodgkin, A.; Huxley, A. Currents carried by sodium and potassium ions through the membrane of the giant axon of *Loligo*, *J. Physiol.(Lond.)* **1952a,** 116, 449-472.

Hodgkin, A.; Huxley, A. The components of membrane conductance in the giant axon of *Loligo*, *J. Physiol.(Lond.)* **1952b,** 116, 473-496.

Hodgkin, A.; Huxley, A. The dual effect of membrane potential on sodium conductance in the giant axon of *Loligo*. *J. Physiol.(Lond.)* **1952c,** 116, 497-506.

Hodgkin, A.; Huxley, A. A quantitative description of membrane current and its application to conduction an excitation in nerve. *J. Physiol.(Lond.)* **1952d,** 117, 500-544.

Hodgkin, A.; Huxley, A.; Katz, B. Measurement of current-voltage relations in the membrane of the giant axon of *Loligo*, *J. Physiol.(Lond.)* **1952,** 116, 424-448.

Hokfelt,T.; Halasz. N.; Ljungdahl, A.; Johansson, O.; Goldstein, M.; Park, D. Histochemical support for a dopaminergic mechanism in the dendrites of certain periglomerular cells in the rat olfactory bulb. *Neuroscience Letters* **1975**, 1, 85-90.

Hormuzdi, S.G.; Filippov, M.A.; Mitropoulou, G.; Monyer, H.; Bruzzone, R. Electrical synapses: a dynamic signalling system that shapes the activity of neuronal networks. *Biochim. Biophys. Acta* **2004**,1662, 113-137.

Horning, M.S.; Kwon, B.; Blakemore, L.J.; Spencer, C.M.; Goltz, M.; Houpt, T.A.; Trombley, P.Q. Alpha-amino-3-hydroxy-5-methyl-4-isoazolepropionate receptor subunit expression in rat olfactory bulb. *Neuroscience Letters* **2004**, 372, 230-234.

Huisman, E.; Uylings, H.B.M.; Hoogland, P.V. A 100% increase of dopaminergic cells in the olfactory bulb may expain hyposmia in parkinson's disease. *Movement Disorders* **2004**, 19, 687-692.

Isaacson, J.S. Mechanisms governing dendritic gamma-aminobutyric acid (GABA) release in the rat olfactory bulb. *Proc Natl Acad Sci U S A* **2001**, 98, 337-42.

Isaacson, J.S.; Strowbridge, B.W. Olfactory reciprocal synapses: dendritic signaling in the CNS. *Neuron* **1998**, 20, 749-61.

Isaacson, J.S.;Vitten, H. $GABA_B$ receptors inhibit dendrodendritic transmission in the rat olfactory bulb. *Journal of Neuroscience* **2003**, 23, 2032-2039.

Jahr, C.E.; Nicoll, R.A. Dendrodendritic inhibition: demonstration with intracellular recording, *Science* **1980**, 207(4438) 1473-5 (28 Mar 1980).

Jahr, C.E.; Nicoll, R.A. Noradrenergic modulation of dendrodentric inhibition in the olfactory bulb. *Nature **1982a**,* **297,** 227-9.

Jahr, C.E.; Nicoll, R.A. An intracellular analysis of dendrodendritic inhibition in the turtle in vitro olfactory bulb, *J. Physiol.* **1982b**, 326, 213-234.

Jo, S.M.; Won, M.H.; Cole, T.B.; Jensen, M.S.; Palmiter, R.D.; Danscher, G. Zinc-enriched (ZEN) terminals in mouse olfactory bulb. *Brain Research* **2000**, 865, 227-236.

Johnston, D.; Wu, S. M.-S. *Foundations of Cellular Neurophysiology.* **1995** MIT Press, Cambridge, MA.

Karnup, S.V.; Hayar, A.; Shipley, M.T.; Kurnikova, M.G. Spontaneous field potentials in the glomeruli of the olfactory bulb: the leading role of juxtaglomerular cells. *Neuroscience* **2006**, 142, 203-221.

Kay, L.M. Two species of gamma oscillations in the olfactory bulb: dependence on behavioural state and synaptic interactions. *Journal of Integrative Neuroscience* **2003**, 2, 31-44.

Kay, L.M.; Freeman, W.J. Bidirectional processing in the olfactory-limbic axis during olfactory behaviour. *Behav. Neurosci.* **1998**, 112, 541-553.

Keller, A.; Yagodin, S.; Aroniadou-Anderjaska, V.; Zimmer, L.A.; Ennis, M.; Sheppard, N.F. Jr.; Shipley, M.T. Functional organisation of rat olfactory bulb glomeruli revealed by optical imaging. *Journal of Neuroscience* **1998**, 18, 2602-2612.

Kirkpatrick, S.; Gelatt, C.D.; Vecchi, M.P. Optimisation by simulated annealing. *Science* **1983**, 220, 671-680.

Kishmoto, J.; Keverne, E.B.; Hardwick, J.; Emson, P.C. Localization of nitric oxide synthase in the mouse olfactory and vomeronasal system: a histochemical, immunological and in situ hybridization study. *European Journal of Neuroscience* **1993**, 5, 1684-1694.

Kosaka, T.; Kosaka, K. Neuronal gap junctions in the rat main olfactory bulb with special reference to intraglomerular gap junctions. *Neuroscience Research* **2003**, 45, 189-209.

Kosaka, T.; Kosaka, K. Neuronal gap junctions between intraglomerular mitral/tufted cell dendrites in the mouse main olfactory bulb. *Neuroscience Research* **2004**, 49, 373-378.

Kosaka, K.; Kosaka, T. Synaptic organisation of the glomerulus in the main olfactory bulb: Compartments of the glomerulus and heterogeneity of the periglomerular cells. *Anatomical Science International* **2005a**, 80, 80-90.

Kosaka, T.; Kosaka, K. Intraglomerular dendritic link connected by gap junctions and chemical synapses in the mouse main olfactory bulb: electron microscopic serial section analyses. *Neuroscience* **2005b**, 131, 611-625.

Laurent, G.; Stopfer, M.; Friedrich, R. W.; Rabinovich, M.I.; Volkovskii, A.; Abarbanel, H.D.I. Odor encoding as an active, dynamical process: experiments, computation, and theory. *Annual Review of Neuroscience* **2001**, 24, 263-297.

Linster, C.; Cleland, T.A. Cholinergic modulation of sensory representations in the olfactory bulb. *Neural Networks* **2002**, 15, 709-717.

Maher, B.J.; Westbrook, G.L. Sk channel regulation of dendritic excitability and dendrodendritic inhibition in the olfactory bulb. *Journal of Neurophysiology* **2005**, 94, 3743-3750.

Maher, B.J.; McGinley, M.J.; Westbrook, G.L. Experience-dependent maturation of the glomerular microcircuit. *PNAS* **2009**, 106, 16865-16870.

Major, G.; Larkman, A.U.; Jonas, P.; Sakmann, B.; Jack, J.J. Detailed passive cable models of whole-cell recorded CA3 pyramidal neurons in rat hippocampal slices. *J. Neurosci.* **1994**, 14, 4613-4638.

Margrie, T.W.; Sakmann, B.; Urban, N.N. Action potential propagation in mitral cell lateral dendrites is decremental and controls recurrent and lateral inhibition in the mammalian olfactory bulb. *PNAS* **2001**, 98, 319-324.

Margrie, T.W.; Schaefer, A.T. Theta oscillations coupled spike latencies yield computational vigour in a mammalian sensory system. *J. Physiol.* **2003**, 546, 363-374.

McLean, J.H.; Shipley, M.T. Serotonergic afferents to the rat olfactory bulb: 1. Origins and laminar specificity of serotonergic inputs in the adult rat. *Journal of Neuroscience* **1987**, 7, 3016-3028.

McLean, J.H.; Darby-King, A.; Hodge, E. 5-HT2 receptor involvement in conditioned olfactory learning in the neonate rat pup. *Behavioral Neuroscience* **1996**, 110, 1426-34.

McLean, J.H.; Harley, C.W.; Darby-King, A.;Yuan, Q. pCREB in the neonate rat olfactory bulb is selectively and transiently increased by odor preference-conditioned training. *Learning and Memory* **1999**, 6, 608-618.

McQuiston, A. R.; Katz. L.C. Electrophysiology of Interneurons in the Glomerular Layer of the Rat Olfactory Bulb. *Journal of Neurophysiology* **2001**, 86, 1899-1907.

Migliore, M.; Hines, M.L.; Shepherd, G.M. The role of distal dendritic gap junctions in synchronization of mitral cell axonal output. *Journal of Computational Neuroscience* **2005**, 18, 151-61.

Migliore, M.; Hoffman, D.A.; Magee, J.C.; Johnston, D. Role of an A-type K+ conductance in the back-propagation of action potentials in the dendrites of hippocampal pyramidal neurons. *J. Comput. Neurosci.* **1999**, **7**, 5-15.
Mombaerts, P. Odorant receptor gene choice in olfactory sensory neurons: the one receptor-one neuron hypothesis revisited. *Current Opinion in Neurobiology* **2004**, 14, 31-36.

Montague, A.A.; Greer, C.A. Differential distribution of ionotropic glutamate receptor subunits in the rat olfactory bulb. *Journal of Comparative Neurology* **1999**, 405, 233-246.

Mori, K.; Kogure, S.; Takagi, S.F. Alternating responses of olfactory bulb neurons to repetitive lateral olfactory tract stimulation. *Brain Research* **1977**, 133, 150-155.

Mori, K.; Nagao, H.; Yoshihara, Y. The olfactory bulb: Coding and processing of odor molecule information. *Science* **1999**, 286, 711-715.

Mori, K.; Nowycky, M.C.; Shepherd, G.M. Electrophysiological analysis of mitral cells in the isolated turtle olfactory bulb, *J. Physiol. (Lond.)* **1981a**, **314**, 281-294.

Mori, K.; Nowycky, M.C.; Shepherd, G.M. Analysis of synaptic potentials in mitral cells in the isolated turtle olfactory bulb, *J. Physiol. (Lond.)* **1981b**, **314**, 295-309.

Mori, K.; Nowycky, M.C.; Shepherd, G.M. Analysis of long duration inhibitory potential in mitral cells in the isolated turtle olfactory bulb, *J. Physiol. (Lond.)* **1981c**, **314**, 311-320.

Mori, K.; Nowycky, M.C.; Shepherd, G.M. Impulse activity in presynaptic dendrites: Analysis of mitral cells in the isolated turtle olfactory bulb, *J. Neurosci.* **1982**, 2, 497-502.

Mori, K.; Nowycky, M.C.; Shepherd, G.M. Synaptic excitatory and inhibitory interactions at distal dendritic sites on mitral cells in the isolated turtle olfactory bulb, *J. Neurosci.* **1984**, 4, 2291-2296.

Mori, K.; Shepherd, G.M. Synaptic excitation and long-lasting inhibition of mitral cells in the in vitro turtle olfactory bulb, *Brain Res.* **1979**, 172, 155-159.

Mori, K.; Takagi, S.F. Activation and inhibition of olfactory bulb neurones by anterior commissure volleys in the rabbit. *Journal of Physiology (Lond.)* ***1978,*** **279**, 589-604.

Moriizumi, T. Olfactory disturbance induced by deafferentation of serotonergic fibers in the olfactory bulb. *Neuroscience* **1994**, 61, 733-738.

Nagata, U. High voltage electron microscope studies on mitral, tufted and granule cells in the mouse olfactory bulb. *J. Electron Microsc.* **1989**, 38, 111-125.

Nagayama, S.; Takahashi, Y.K.; Yoshihara, Y.; Mori, K. Mitral and tufted cells differ in the decoding manner of odor maps in the rat olfactory bulb. *J. Neurophysiol.* **2004**, 91, 2532-2540.

Neville, K.R.; Haberly, L.B. Beta and gamma oscillations in the olfactory system of the urethane-anesthetized rat. *Journal of Neurophysiology* **2003**, 90, 3921-3930.

Nickell, W.T.; Shipley, M.T. Two anatomically specific classes of candidate cholinoceptive neurons in the rat olfactory bulb. *Journal of Neuroscience* **1988**, 8, 4482-4491.

Nicoll, R.A. GABA and dendrodendritic inhibition in the olfactory bulb, *Pharmacologist* **1970**, 12, 236.

Nicoll, R.A. Pharmacological evidense for GABA as the transmitter in granule cell inhibition in the olfactory bulb, *Brain Res.* **1971**, 35, 137-149.

Nicoll, R.A. and Jahr, C.E. Self-excitation of olfactory bulb neurones, *Nature* **1982**, 296, 441-444.

Nordin, S.; Lotsch, J.; Murphy, C.; Hummel, T.; Kobal, G. Circadian rhythm and desensitization in chemosensory event-related potentials in response to odours and painful stimuli. *Psychophysiology* **2003**, 40, 612-619.

Nowycky, M.C.; Mori, K.; Shepherd, G.M. GABAergic Mechanisms of Dendrodendritic Synapses in isolated Turtled Olfactory Bulb, *J. Neurophysiol.* **1981a**, 46, 639-648.

Nowycky, M.C.; Mori, K.; Shepherd, G.M. Blockade of Synaptic Inhibition Reveals Long-Lasting Synaptic Excitation in Isolated Turtle Olfactory Bulb, *J. Neurophysiol.* **1981b**, 46, 649-658.

Nusser, Z.; Kay, L.M.; Laurent, G.; Homanics, G.E.; Mody, I. Disruption of GABA(A) receptors on GABAergic interneurons leads to increased oscillatory power in the olfactory bulb network. *Journal of Neurophysiology* **2001**, 86, 2823-2833.

O'Connor, S.; Jacob, T.J.C. Neuropharmacology of the olfactory bulb. *Current Molecular Pharmacology* **2008**, 1, 181-190.

Okutani, F.; Kaba, H.; Takahashi, S.; Seto, K. The biphasic effects of locus coeruleus noradrenergic activation on dendrodendritic inhibition in the rat olfactory bulb. *Brain Research* **1998**, 783, 272-279.

Okutani, F.; Yagi, F.; Kaba, H. GABAergic control of olfactory learning in young rats. *Neuroscience* **1999**, 93, 1297-1300.

Osako, Y.; Otsuka, T.; Taniguchi, M.; Oka, T.; Kaba, H. Oxytocin depresses spontaneous γ-aminobutyric acid-ergic inhibitory postsynaptic currents in cultured mitral cells of the rat olfactory bulb by a presynaptic mechanism. *Neuroscience Letters* **2000**, 289, 25-28.

Osako, Y.; Otsuka, T.; Taniguchi, M.; Oka, T.; Kaba, H. Oxytocin enhances presynaptic and postsynaptic glutamatergic transmission between rat olfactory bulb neurones in culture. *Neuroscience Letters* **2001**, 299, 65-68.

Perreault, M.C.; Raastad, M. Contribution of morphology and membrane resistance to integration of fast synaptic signals in two thalamic cell types. *J. Physiol. (Lond.)* **2006**, 577, 205-220.

Pignatelli, A.; Koyabashi, K.; Okano, H.; Belluzzi, O. Functional properties dopaminergic neurones in the mouse olfactory bulb. *Journal of Physiology (Lond.)* **2005**, 564.2, 501-514.

Press, W.H.; Teukolsky, S.A.; Vetterling, W.T.; Flannery, B.P. *Numerical recipes in C: The art of scientific computing.* 2nd edition Cambridge University Press, Cambridge UK. **1992**
Price, J.L. The termination of centrifugal fibres in the olfactory bulb. *Brain Research* **1968**, 7, 483-486.

Price, J.L.; Powell, T.P.S. The morphology of the granule cells of the olfactory bulb, *J. Cell Sci.* **1970a**, 7, 91-123.

Price, J.L.; Powell, T.P.S. The mitral and short axon cells of the olfactory bulb, *J. Cell Sci.* **1970b**, 7, 631-651.

Proust, M. *Du côté de chez Swann.* **1913**.

Puche, A.C.; Shipley, M.T. Odour-induced, activity-dependant transneuronal gene induction in vitro: mediation by NMDA receptors. *Journal of Neuroscience* **1999**, 19, 1359-1370.

Puopolo, M.; Belluzzi, O. Inhibitory synapses among interneurons in the glomerular layer of rat and frog olfactory bulbs. *Journal of Neurophysiology* **1998**, 80, 344-349.

Rall, W. Branching dendritic trees and motoneuron membrane resistivity. *Exp. Neurol.* **1959**, 1, 491-527.

Rall, W.; Shepherd, G.M.; Reese, T.S.; Brightman, M.W. Dendrodendritic synaptic pathway for inhibition in the olfactory bulb, *Exp. Neurol.* **1966**, 14, 44-56.

Rall, W.; Shepherd, G.M. Theoretical reconstruction of field potentials and dendrodendritic synaptic interactions in olfactory bulb, *J. Neurophysiol.* **1968**, 31, 884-915.

Rash, J.E.; Davidson, K.G.; Kamasawa, N.; Yasumura, T.; Kamasawa, M.; Zhang, C.; Michaels, R.; Restrepo, D.; Ottersen, O.P.; Olson, C.O.; Nagy, J.I. Ultrastructural localization of connexins (Cx36, Cx43, Cx45), glutamate receptors and aquaporin-4 in rodent olfactory mucosa, olfactory nerve and olfactory bulb. *J. Neurocytol.* **2005**, 34, 307-341.

Ravel, N.; Chabaud, P.; Martin, C.; Gaveau, V.; Hugues, E., Tallon-Baudry, C.; Bertrand, O.; Gervais, R. Olfactory learning modifies the expression of odour-induced oscillatory responses in the gamma (60-90Hz) and beta (15-40Hz) bands in the rat olfactory bulb. *European Journal of Neuroscience* **2003**, 17, 350-358.

Roth, A.; Häusser, M. 2001 Compartmental models of rat cerebellar Purkinje cells based on simultaneous somatic and dendritic patch-clamp recordings. *J. Physiol. (Lond.)* **2001**, 535, 445-472.

Saftenku, E.E. Modeling of slow glutamate diffusion and AMPA receptor activation in the cerebellar glomerulus. *J. Theor. Biol.* **2005**, 234(3), 363-82.

Sahara, Y.; Kubota, T.; Ichikawa, M. Cellular localization of metabotropic glutamate receptors mGluR1, 2/3, 5 and 7 in the main and accessory olfactory bulb of the rat. *Neurosci. Lett.* **2001,** 312, 59-62.

Schaefer, A.T.; Larkum, M.E.; Sakmann, B.; Roth, A. Coincidence detection in pyramidal neurons is tuned by their dendritic branching pattern. *J. Neurophysiol.* **2003**, 89, 3143-3154.

Schaefer, A.T.; Angelo, K.; Spors, H.; Margrie, T.W. Neuronal oscillations enhance stimulus discrimination by ensuring action potential precision. *PLoS Biol* **2006**, 4(6), 1010-1024.

Schoppa, N.E. AMPA/kainite receptors drive rapid output and precise synchrony in olfactory bulb granule cells. *Journal of Neuroscience* **2006**, 26, 12996-13006.

Schoppa, N.E.; Kinzie, J.M.; Sahara, Y.; Segerson, T.P.; Westbrook, G.L. Dendrodendritic inhibition in the olfactory bulb is driven by NMDA receptors. *Journal of Neuroscience* **1998**, 18, 6790-6802.

Schoppa, N.E.; Westbrook, G.L. Regulation of synaptic timing in the olfactory bulb by an A-type potassium current. *Nature Neuroscience* **1999**, 2, 1106-13.

Schoppa, N.E.; Westbrook, G.L. Glomerulus-specific synchronization of mitral cells in the olfactory bulb. *Neuron* **2001**, 31, 639-651.

Schoppa, N.E.; Westbrook, G.L. AMPA autoreceptors drive correlated spiking in olfactory bulb glomeruli. *Nature Neuroscience* **2002**, 5, 1194-1202.

Segev, I.; Rinzel, J.; Shepherd, G.M. The theoretical foundation of dendritic function: Selected papers of Wilfrid Rall with commentaries. **1995**, MIT Press, Cambridge, MA, USA.

Shen, G.Y.; Chen, W.R.; Mitgaard, J.; Shepherd, G.M.; Hines, M.L. Computational analysis of action potential initiation in mitral cell soma and dendrites based on dual patch recordings. *J. Neurophysiol.* **1999**, 82(6), 3006-20.

Shepherd, G.M. Neuronal systems controlling mitral cell excitability, *J. Physiol (Lond.)* **1963**, 168, 101-117.

Shepherd, G.M. Physiological evidence for dendrodendritic synaptic interactions in the rabbit's olfactory glomerulus. *Brain Research* **1971**, 32, 212-217.

Shepherd, G.M.; Greer, C.A. Olfactory Bulb in *The Synaptic Organization of the Brain.* 4th edition Edited by Shepherd, G.M. O.U.P. **1998.**

Sobel, E.C.; Tank, D.W. Timing of odor stimulation does not alter patterning of olfactory bulb unit activity in freely breathing rats. *Journal of. Neurophysiology* **1993**, 69, 1331-1337.

Stopher, M.; Bhagavan, S.; Smith, B.H.; Laurent, G. Impaired odour discrimination on desynchronization of odour-encoding neural assemblies. *Nature* **1997**, 390, 70-74.

Stuart, G.; Spruston, N. Determinants of voltage attenuation in neocortical pyramidal neuron dendrites. *J. Neurosci.* **1998**, 18, 3501-3510.

Sullivan, R.M., Wilson, D.A., and Leon, M. Norepinephrine and learning-induced plasticity in infant rat olfactory system. *Journal of Neuroscience* **1989**, 9, 3998-4006.

Sullivan, R.M.,; Stackenwalt, G.; Nasr, F.; Lemon, C.; Wilson, D.A. Association of an odor with activation of the olfactory bulb beta-receptors or locus coeruleus stimulation is sufficient to produce learned approach responses to that odor in neonatal rats. *Behavioral Neuroscience* **2000**, 114, 957-962.

Tillerson, J.L.; Caudle.; W.M.; Parent, J.M.; Gong, C.; Schallert, T.; Miller, G.W. Olfactory discrimination deficits in mice lacking the dopamine transporter or the D2 dopamine receptor. *Behavioral Brain Research* **2006**, 172, 97-105.

Thurbon, D.; Lüscher, H.R.; Hofstetter, T.; Redman, S.J. Passive electrical properties of ventral horn neurons in rat spinal cord slices. *J. Neurophysiol.* **1998**, 79, 2485-2502.

Traub, R. D. Simulations of intrinsic bursting in CA3 hippocampal neurons . *Neuroscience* **1982**, 7, 1233-1242.

Trombley, P.Q. Norepinephrine inhibits calcium currents and EPSPs via a G-protein-coupled mechanism in olfactory bulb neurons. *Journal of Neuroscience* **1992**, 12, 3992-3998.

Trombley, P.Q.; Shepherd, G.M. Noradrenergic inhibition of synaptic transmission between mitral and granule cells in mammalian olfactory bulb cultures. *Journal of Neuroscience* **1992**, 12, 3985-3991.

Trombley, P.Q.; Shepherd, G.M. Glycine exerts potent inhibitory actions on mammalian olfactory bulb neurons. *Journal of Neurophysiology* **1994**, 71, 761-767.

Trombley, P.Q.; Westbrook, G.L. Excitatory synaptic transmission in primary cultures of rat olfactory bulb, *Journal of Neurophysiology **1990,** **64**, 598-606.

Tucker, K.; Fadool, D.A. Neurotrophin modulation of voltage-gated potassium channels in rat through TrkB receptors is time and sensory experience dependent. *Journal of Physiology (Lond.)* **2002**, 542, 413-429.

Urban, N.N.; Sakmann, B. Reciprocal intraglomerular excitation and intra- and iterglomerular lateral inhibition between mouse olfactory bulb mitral cells. *J. Physiol.* **2002**, 542, 355-367.

Vetter, P.; Roth, A.; Häusser, M. Propagation of action potentials in dendrites depends on dendrite morphology. *Journal of Neurophysiology **2001,** **85(2)**, 926-37.

Von Baumgarten, R.; Bloom, F.E.; Oliver, A.P.; Salmoiraghi, G.C. Response of individual olfactory nerve cells to microelectrophoretically administered chemical substances, *Pflügers Arch. Ges. Physiol.* **1963**, 277, 125-140.

Wang, X.Y.; McKenzie, J.S.; Kemm, R.E. Whole-cell K+ currents in identified olfactory bulb output neurones of rats. *J. Physiol.* **1996**, 490, 63-77.

Weaver, C.M.; Wearne, S.L. The role of action potential shape and parameter constraints in optimisation of compartment models. *Neurocomputing* **2006**, 69, 1053-1057.

Wilson, D.A.; Sullivan, R.M. The D2 antagonist spiperone mimics the effects of olfactory deprivation on mitral/tufted cell odour response patterns. *Journal of Neuroscience* **1995**, 15, 5574-5581.

Wilson M.A.; Bhalla U.S.; Uhley J.D.; Bower J.M. GENESIS: A system for simulating neural networks. In: *Advances in Neural Information Processing Systems*. D. Touretzky, editor. **1989**, Morgan Kaufmann, San Mateo, CA. pp. 485-492.

Wu, C.; Yoder, E.J.; Shih, J.; Chen, K.; Dias, P.; Shi, L.; Ji, X-D.; Wei, J.; Conner, J.M.; Kumar, S.; Ellisman, M.H.; Singh, S.K. Development and characterization of monoclonal antibodies specific to the serotonin 5-HT 2A receptor. *The Journal of Histochemistry & Cytochemistry* **1998**, 46, 811–824.

Xiong, W.; Chen, W.R. Dynamic gating of spike propagation in the mitral cell lateral dendrites. *Neuron* **2002**, 34, 115-126.

Yamada, W.M.; Koch, C.; Adams, P.R. Multiple channels and calcium dynamics. In: *Methods in Neuronal Modelling: From synapses to Networks*, edited by Koch, C.; Segev, I. MIT Press, Cambridge, MA **1989**.

Yu, G.Z.; Kaba, H.; Okutani, F.; Takahashi, S.; Higuchi, T. The olfactory bulb: a critical site of action for oxytocin in the induction of maternal behaviour in the rat. *Neuroscience* **1996**, 72, 1083-1088.

Yuan, Q.; Harley, C.W.; McLean, J.H. Mitral cell beta1 and 5-HT2A receptor colocalization and cAMP coregulation: a new model of norepinephrine-induced learning in the olfactory bulb. *Learning and Memory* **2003**, 10, 5-15.

Zaborszky, L.; Carlsen, J.; Brashear, H.R. Heimer, L. Cholinergic and GABAergic afferents to the olfactory bulb in the rat with special emphasis on the projection from the horizontal limb of the diagonal band. *Journal of Comparative Neurology* **1986**, 243, 488-509.

Zador, A.M.; Agmon-Snir, H.; Segev, I. The morphoelectrotonic transform: A graphical approach to dendritic function. *J. Neurosci.* **1995**, 15, 1669-1682.